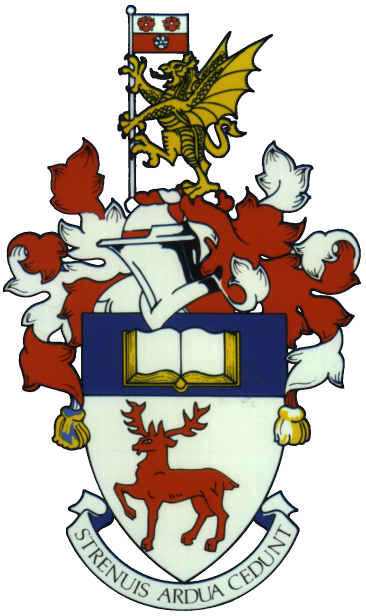

University of Southampton

Faculty of Engineering and Physical Sciences
School of Physics and Astronomy

Optically Trapped Polariton Condensates as Dissipative Coupled Oscillator Networks

by

Stella Louise Harrison

MPhys

ORCiD: 0000-0002-0302-728X

A thesis for the degree of
Doctor of Philosophy

Under the supervision of Prof. Pavlos Lagoudakis

June 2022

University of Southampton

Abstract

Faculty of Engineering and Physical Sciences
School of Physics and Astronomy

Doctor of Philosophy

Optically Trapped Polariton Condensates as Dissipative Coupled Oscillator Networks

by Stella Louise Harrison

The semiconductor-microcavity polariton is the resulting quasi-particle from strong coupling between a quantum well exciton and cavity photon. With the cavity wavelength similar to that of the photon, the exciton-polariton (herein polariton) eigenstates come into play. Due to their light effective mass alongside the particle's bosonic nature, polaritons undergo Bose-Einstein condensation (BEC) at high densities when below the critical condensation temperature. Unlike the traditional BEC phase transition of an atomic gas, the BEC of polaritons can be attained at much higher temperatures of 4 K up to room temperature. The work in this thesis specifically studies polariton condensates formed in inorganic semiconductor microcavities optically imprinted with ring or elliptical shaped traps. Such an excitation profile creates a potential minimum at the centre which is radially fed by polaritons. The polaritons build in population and undergo a quantum phase transition to form a polariton condensate spatially separated from the excitation profile.

In this thesis, optically trapped polariton condensates are used to create a synchronised condensate network, which is initially characterised using two ground state condensates to map out regions of in-phase and anti-phase synchronisation, and through describing the system as a Stuart-Landau network, the system presents as a robust optical analogue simulator of the XY Hamiltonian. The system is then used to approximately solve the NP-hard max-3-cut graph problem through minimising the XY Hamiltonian, and the minor embedding technique is explored and characterised by mapping arbitrarily connected dense graphs to experimentally-achievable planar networks of Stuart-Landau oscillators. Next, the optically trapped first excited state polariton condensate is explored via a rotating quasi-elliptical trap where quantised vortices are observed with a deterministic rotation direction, as well as a continuous chain of excited-state condensates which exhibit geometric frustration described using Bloch's theorem and likened to twisted states from the Kuramoto model, where the network of excited state condensates has potential as a 4D analogue simulator.

Contents

List of Figures

Publications

- S. L. Harrison, H. Sigurdsson, and P. G. Lagoudakis, *Synchronization in optically trapped polariton Stuart-Landau networks*, Phys. Rev. B **101**, 155402 (Apr. 2020).
- S. L. Harrison, H. Sigurdsson, S. Alyatkin, J. D. Töpfer, and P. G. Lagoudakis, *Solving the max-3-cut problem with coherent networks*, Phys. Rev. Applied **17**, 024063 (Feb. 2022).
- S. L. Harrison, H. Sigurdsson, and P. G. Lagoudakis *Minor embedding with Stuart-Landau oscillator networks*, arXiv:2109.10142 (Sept. 2021) [under consideration with Commun. Phys.].
- S. L. Harrison, H. Sigurdsson and P. G. Lagoudakis, *Twisted states in polariton Stuart-Landau networks* [in preparation].
- I. Gnusov, S. L. Harrison, H. Sigurdsson, S. Alyatkin, K. Sitnik, J. T. Töpfer, and P. G. Lagoudakis, *Vortex formation in optically stirred polariton condensates* [under consideration with Nature].

Declaration of Authorship

I declare that this thesis and the work presented in it is my own and has been generated by me as the result of my own original research.

I confirm that:

1. This work was done wholly or mainly while in candidature for a research degree at this University;
2. Where any part of this thesis has previously been submitted for a degree or any other qualification at this University or any other institution, this has been clearly stated;
3. Where I have consulted the published work of others, this is always clearly attributed;
4. Where I have quoted from the work of others, the source is always given. With the exception of such quotations, this thesis is entirely my own work;
5. I have acknowledged all main sources of help;
6. Where the thesis is based on work done by myself jointly with others, I have made clear exactly what was done by others and what I have contributed myself;
7. Parts of this work have been published as: S. L. Harrison *et al.*, Synchronization in optically trapped polariton Stuart-Landau networks. *Phys. Rev. B* **10**, 155402 (2020) [2], and S. L. Harrison *et al.*, Solving the Max-3-Cut Problem with Coherent Networks. *Phys. Rev. Applied* **17**, 024063 (2022) [4].

Signed:..... Date:.....

Acknowledgements

First and foremost, I want to thank Prof. Pavlos Lagoudakis for not only introducing me to the field of polaritonics, but for creating such a brilliant research group which I've now been a part of for nearly five years. The fact I've chosen to stay in the team for so long is a testament for your hard work as a group leader and supervisor. Thank you for bringing me into the Hybrid Photonics Group and introducing me to the polaritonics community. Polaritonics is such an interesting and fast developing field and I'm so grateful to be immersed into the world of analogue computing and for having the opportunity to travel to conferences in Russia and France. I also want to say a huge thank you to Dr Helgi Sigurdsson for co-supervising me. You've taught me everything I know as a theoretician, where at the start of my PhD you showed me how to perform a numerical simulation and have since guided me as I've developed the skills and confidence to perform my own investigations and analysis, and remained patient despite the (many) mistakes I've made along the way. Not only have you taught me how to think like a theoretician, but you've shown me how to be a successful researcher, for which I'm incredibly grateful.

During my brief spell as an experimentalist, I was so fortunate to be introduced to the optics labs and taught how to correctly run an experiment by Dr Lucy Pickup. Without a doubt Lucy, you are a brilliant and patient teacher who explains everything so clearly and passionately. To all the inorganics experimentalists in the group who helped me during my time in the lab: Lucy, Julian, Tamsin, Anton and Giannis, thank you for helping me align and run experiments when I was a confused first year, as well as teaching me your own tips and tricks for running an experiment. Arguably most importantly, I would like to thank the Hybrid Photonics Group as a whole, both past and present (including but not limited to): Lucy, Tamsin, Julian, Helgi, Giacomo, Chris, Giannis, Anton, Alexis, Dima and Nick. Thank you for all the fantastic pub trips, coffee breaks and lockdown video calls: for all the times we've had a drink in hand together and for all the fruitful discussions that followed. I am so fortunate to be part of a research group with such lovely people whom I can call my friends. Aside from physics, I've learnt so much from you, including how to make an espresso (with Passalacqua coffee, of course).

To all my friends outside of physics, particularly to the music crowd, I am so grateful for you too. Over the past few years I've been a member of Southampton University Brass Band, Southampton University Symphonic Wind Orchestra, Ocean Brass and Putney & Wimbledon Brass Band, where everyone in these groups has made me feel part of a community of fun like-minded people, and with whom I share so many brilliant memories. It is so important to have some respite away from work, and I feel so fortunate to be part of the brass banding community and have a close group of loving friends. To Will, Paddy, Sophie, Ed, Bex, Pete and Joe: thank you for always being there. Our weekly video chats always bring a smile to my face, even after a stressful day and particularly in the depths of lockdown.

To Mum and Dad, you have supported me throughout my life in everything I have done and I cannot express how grateful I am for that. It is from you that I've learnt that hard work pays off, but also that alongside working hard, it's so import to play hard and have fun! Finally, to my rock, thank you Giannis for the unconditional support, love and encouragement that you provide me at every hurdle in life. I'm so happy that you are by my side to light up my life.

Preface

I don't know how many times I've heard people say that we've been living through "strange times" these past couple of years, but that is for sure the understatement of the century. Completing a PhD during a global pandemic has definitely had its hurdles. From going in to an office full of other PhD students and postdocs everyday for the first year and a half of my PhD journey, sharing ideas over coffee breaks, having group trips out for lunch or to the pub, to working from home and legally not being allowed to leave the house for anything more than exercise or essential groceries. This for sure has taken its toll both scientifically and emotionally. Seeing my first paper get published in the first few weeks of lockdown really motivated me to press on with the next project, which certainly took longer than expected and in fact has only just been published. Without the bustle of colleagues around you when working from home, there is no yardstick to compare if you're working long enough or hard enough and there were times in the depths of lockdown where I felt so detached from the research group, but also like I should be working at all times, as my desk was sitting pride of place in the living room. Having spoken to others about their lockdown experiences, it is clear that these feelings were pretty widespread and for me they are definitely dissipating now that we are able to meet in-person again.

I am very fortunate that as a numerical modeller and theoretician, my ability to work has not physically been hindered by working from home, as I know has been the case for so many friends and colleagues. That being said, research is a group activity that thrives on continuous conversation which without the water cooler (or rather coffee machine) chat, we have all missed out on scientific advances in our fields. Now in March 2022, compulsory mask wearing has been dropped, but we are still swabbing our nose and throat out of fear of spreading the virus to the vulnerable. This month I have also had my first in-person meeting with Pavlos and the Southampton group in two years, though I am still working from home despite these occasional trips to Southampton. The world is slowly re-setting to its new-normal, but for sure, these are still "strange times".

Abbreviations

AFM	Antiferromagnetic
AlAs	Aluminium arsenide
AOM	Acouto-optic modulator
BEC	Bose-Einstein condensate
BH	Basin hopping
BS	Beam splitter
CMOS	Complementary metal-oxide-semiconductor
CPU	Central processing unit
CVM	Constrained via minimisation
CW	Continuous wave
cGLE	Complex Ginzburg-Landau equation
DBR	Distributed Bragg reflector
dGPE	Driven-dissipative Gross-Pitaevskii equation
GPE	Gross-Pitaevskii equation
GS	Gerchberg Saxton
FM	Ferromagnetic
FWHM	Full width at half maximum
GaAs	Gallium arsenide
hh	Heavy hole
InGaAs	Indium gallium arsenide
LCD	Liquid crystal display
LCOS	Liquid crystal on silicon
LED	Light emitting diode
LG	Laguerre-Gaussian
lh	Light hole
LP	Lower polariton
M2C	Maximum-2-cut
M3C	Maximum-3-cut
M4C	Maximum-4-cut
MRAF	Mixed region amplitude freedom
NA	Numerical aperture
ND	Neutral density

NP	Nondeterministic-polynomial-time
NR	Noise region
NRMSE	Normalised root mean square error
OAM	Orbital angular momentum
P	Polynomial-time
PBS	Polarising beam splitter
PL	Photoluminescence
RAM	Random access memory
SL	Stuart-Landau
SLM	Spatial light modulator
SR	Signal region
Std	Standard deviation
UP	Upper polariton
QW	Quantum well
VCSEL	Vertical cavity surface emitting laser

Chapter 1

Introduction to Polaritonics

1.1 Exciton-Polaritons

In 1972, Charles H. Henry worked on the fabrication of optical circuits and integrated chips, a field in which waveguides were commonly used. At this time, waveguides were a purely optical tool until Henry made the discovery that a sandwich of semiconductors (or "heterostructure") was not only a waveguide for light, but also for electrons. Drawing upon the principles of quantum mechanics, he made the complete analogy between the confinement of light by a waveguide and the confinement of electrons by the potential well formed by the difference in bandgap energies of the different heterostructure layers [5]. The electron wavefunction also showed discrete unique energy modes, as seen with confined light, with observable energy level splitting when the heterostructure active layer was just a few tens of nanometres thick [5]. This structure is now known as a "quantum well", and although Henry developed the first patented quantum effect heterostructure [6], it was in fact simultaneously first proposed in 1963 by Herbert Kroemer (in Proceedings of the IEEE [7]) as well as Zhores Alferov and Rudolf Kazarinov (for the USSR [8]), where both Kroemer and Alferov received a Nobel Prize in 2000 for this invention [9].

Semiconductor heterostructures are common place in modern day solid state physics and underpin many modern technologies such as laser-based communication, LEDs and bipolar transistors. In fact, in Alferov's Nobel, he pointed out that at turn of the century, semiconductor heterostructures made up two-thirds of the research matter in semiconductor physics [10]. When quantum wells (QWs) are sandwiched within a miniature Fabry-Pérot cavity, such that the cavity spacer confinement length is equivalent to the wavelength of light (less than 100 μm [1]), the resulting 'microcavity' leads to the formation of the exciton-polariton (herein polariton) quasi-particle [1]. Due to the strong coupling of the cavity photon and QW exciton, both confined within the microcavity, the two particles undergo normal mode splitting and result in the upper

and lower polariton eigenstates. Each are displaced in energy by $\pm\hbar\Omega$ respectively from the bare exciton and cavity photon modes, where Ω is the Rabi frequency of the energy splitting [11]. This chapter sets out the building blocks of microcavity polaritonics starting from the confinement of the quasi-particle's constituent parts, to the 2D Bose-Einstein condensation of planar microcavity polaritons.

1.1.1 Electrons in a Solid

The energy of electrons within an ideal crystaline solid with a periodic atom arrangement is described by a Hamiltonian that includes the kinetic energy of every electron and nucleus, plus the potential energy of all electron-electron interactions, electron-nucleus interactions and nucleus-nucleus interactions following [12],

$$H = -\sum_i \frac{\hbar^2}{2m_e}\nabla_i^2 - \sum_a \frac{\hbar^2}{2M}\nabla_a^2 + \frac{1}{2}\sum_{i\neq j} U_1(\mathbf{r}_i - \mathbf{r}_j) + \sum_{i,a} U_2(\mathbf{r}_i - \mathbf{R}) + \frac{1}{2}\sum_{a\neq b} U_3(\mathbf{R}_a - \mathbf{R}_b) \tag{1.1}$$

where U_n for $n \in \{1, 2, 3\}$ are the three respective potentials mentioned above. For the electron and nucleus respectively, their masses are m_e and M with position vectors $\mathbf{r}$ and $\mathbf{R}$ and particle labels i, j and a, b. Note that the factor of $1/2$ in the terms containing U_1 and U_3 is simply to counteract the fact that each inter-particle interaction is counted twice in the sum of each term.

Clearly, it is not possible to solve Equation 1.1 for macroscopic quantities of a crystal (around $N \simeq 10^{23}$ atoms), as the dimension of the Hilbert space of the electrons grows $\mathcal{O}(2^N)$ (compared to $\mathcal{O}(N)$ for classical interacting bodies). However, by applying the Born-Oppenheimer approximation [13] and the Hartree-Fock method of the self-consistent field approximation [14, 15], this reduces to[1]:

$$-\frac{\hbar^2}{2m_e}\nabla^2\psi + \mathcal{U}(\mathbf{r})\psi = E\psi \tag{1.2}$$

where $\mathcal{U}(\mathbf{r})$ is some periodic potential with height $\mathcal{U}_0$ that results from the interaction of each valent electron with every other valent electron and every ion in the crystal lattice.

Considering a 1D structure, due to the periodic potential of $\mathcal{U}(x)$ with lattice constant a, the potential satisfies the translation $x \to x + a$, such that $\mathcal{U}(x) = \mathcal{U}(x + a)$ [12], as

[1] The Born-Oppenheimer approximation gives the assumption that the mass of the nucleus is much larger than the mass of the electron such that the nuclei are considered to be stationary. The self-consistent field approximation assumes that under certain conditions, a problem containing many particles can be reduced to a set of single particle problems.

shown in blue in Figure 1.1. The Schrödinger equation under this translation becomes:

$$-\frac{\hbar^2}{2m_e}\nabla^2\psi(x+a)+\mathcal{U}(x)\psi(x+a)=E\psi(x+a) \tag{1.3}$$

where the solutions of Equation 1.3 and Equation 1.2 satisfy the same Schrödinger equation with the same eigenvalues E. If the eigenvalues are non-degenerate, then $\psi(x)$ and $\psi(a+x)$ can only differ by some constant coefficient $\psi(x+a)=c\psi(x)$, which when both wavefunction are normalised becomes $|c|^2=1$. That is to say, the probability of finding a particle at some position Δx from x is the same as finding a particle at position Δx from $x+a$, therefore the spatial distribution of particles is periodic with the same lattice constant a [12].

Considering now two translations of a, we have:

$$\psi(x+a_1+a_2)=c_1c_2\psi(x)=c_{1+2}\psi(x) \tag{1.4}$$

as $a_n=na$ and $a_1+a_2=a_3$. This gives the solution $c_n=e^{ika_n}$, where k can take any value. In other words, the eigenfunction of a Hamiltonian with periodic potential is a plane wave modulated by the same lattice constant a (Bloch's theorem) [1, 12, 16, 17].

In reciprocal space, the lattice periodicity is given by the reciprocal lattice vector $g=\frac{2\pi}{a}$. Due to the system's translational symmetry, if any two wavevectors in reciprocal space differ by $k_i-k_j=\frac{2\pi}{a}n$ (where n is an integer), then they are equivalent. Therefore, any interval of k with width $\frac{2\pi}{a}$ contains the full set of non-equivalent wavevectors and is known as the "Brillouin zone" [12, 16, 17]. This is shown by the grey region in Figure 1.2. Typically the Brillouin zone is chosen such that the ion cores are at the zone boundaries ($k=\pm\frac{\pi}{a}$), at which point the electron wave propagations are reflected. In turn, the electron wavefunction is a standing wave due to the many forwards and backwards propagating electrons from the many reflections in the periodic structure [17].

To solve the Schrödinger equation for this periodic potential, the wavefunction can no longer be treated as a plane wave, but instead a sum of plane waves with a set of amplitudes $\{c_{-\infty},\cdots,c_0,c_1,c_2,\cdots,c_\infty\}$,

$$\psi=\sum_{p=-\infty}^{\infty}c_pe^{ipx} \tag{1.5}$$

where the amplitudes c_p and the corresponding energies for each of the allowed wavefunctions of the periodic lattice can be calculated. By substituting Equation 1.5 into Equation 1.2 and by multiplying by $\int e^{-ikx}dx$, through orthogonality of plane waves we see that wave k is now coupled to the waves $k\pm g$ with coupling strength $\mathcal{U}_0$

(the height of the periodic potential) [17],

$$Ec_k = \frac{\hbar^2 k^2}{2m} c_k + \mathcal{U}_0(c_{k-g} + c_{k+g}). \tag{1.6}$$

For the forward propagating wave (k) and back reflected wave ($k-g$), their energies are the same at the edge of the Brillouin zone [17]. The wave energies are described by the Schödinger equations,

$$\left(\frac{\hbar^2 k^2}{2m} - E\right) c_k + \mathcal{U}_0 c_{k-g} = 0, \tag{1.7}$$

$$\left(\frac{\hbar^2 (k-g)^2}{2m} - E\right) c_{k-g} + \mathcal{U}_0 c_k = 0, \tag{1.8}$$

which in matrix form are written as

$$\begin{pmatrix} \frac{\hbar^2 k^2}{2m} - E & \mathcal{U}_0 \\ \mathcal{U}_0 & \frac{\hbar^2 (k-g)^2}{2m} - E \end{pmatrix} \begin{pmatrix} c_k \\ c_{k-g} \end{pmatrix} = 0 \tag{1.9}$$

with eigenenergies,

$$E = \frac{1}{2}\left(\frac{\hbar^2 k^2}{2m} + \frac{\hbar^2 (k-g)^2}{2m}\right) \pm \sqrt{\left(\frac{\hbar^2 k^2}{2m} - \frac{\hbar^2 (k-g)^2}{2m}\right)^2 + \mathcal{U}_0^2}. \tag{1.10}$$

If the two bare wave energies are equal, such as at the Brillouin zone edges with $\frac{\hbar^2 k^2}{2m} = \frac{\hbar^2 (k-g)^2}{2m}$, their eigenenergies become $E_\pm = \frac{\hbar^2 k^2}{2m} \pm \mathcal{U}_0$ with $k = \frac{g}{2} = \frac{\pi}{a}$. That is to say, two free electrons with the same kinetic energy will undergo an energy splitting of $\pm\mathcal{U}_0$ at the Brillouin zone boundaries in the bulk structure due to the steep periodic potential from the ion cores. This leads to a forbidden zone of height $2\mathcal{U}_0$ in energy at the Brillouin zone edges in which no propagating waves can exist. These two energy

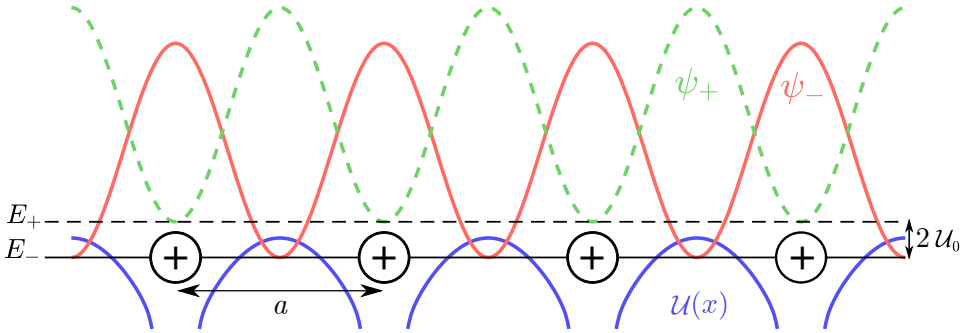

FIGURE 1.1: Schematic of a 1D crystal with lattice constant (nuclei spacing) a showing the periodic ionic potential (blue), and the spatial wavefunctions of the electron bands ψ_+ (green) and ψ_- (red) that are split in energy by $2\mathcal{U}_0$.

states correspond to the standing waves with electrons most probable at the ion cores (ψ_-), or in-between the ions (ψ_+), as shown in Figure 1.1. The former is lower in energy as the electrons see a larger electrostatic potential attraction, whereas the latter leaves the electrons feeling a weaker attraction leading to a higher energy [17].

The electron energy spectrum consists of bands separated by forbidden zone gaps (see Figure 1.2). Depending on the electron occupancy in each band, different material properties are achieved. For a partially filled band, the material has metallic properties. For a fully occupied or completely free band, the material has dielectric properties as electrons cannot provide conductivity due to the Pauli exclusion principal (one electron per state) [12, 17]. If such a dielectric material is excited with energy $\geq 2\mathcal{U}_0$ (e.g. from thermal or photonic excitation), an electron can be removed from the lower band and excited to the higher energy band, leaving behind an electron "hole" characterised by a positive charge $+e$. In this case, the material is classed as a semiconductor. In a semiconductor, the highest energy fully occupied band is labelled as the valence band, and the lowest energy band that is not fully occupied is the conduction band. The interval between the top of the valence band, E_v, and bottom of the conduction band, E_c, is labelled as the bandgap energy E_g. If $E_{v,c}$ occur at the same k, the material is said to have a direct-bandgap [12].

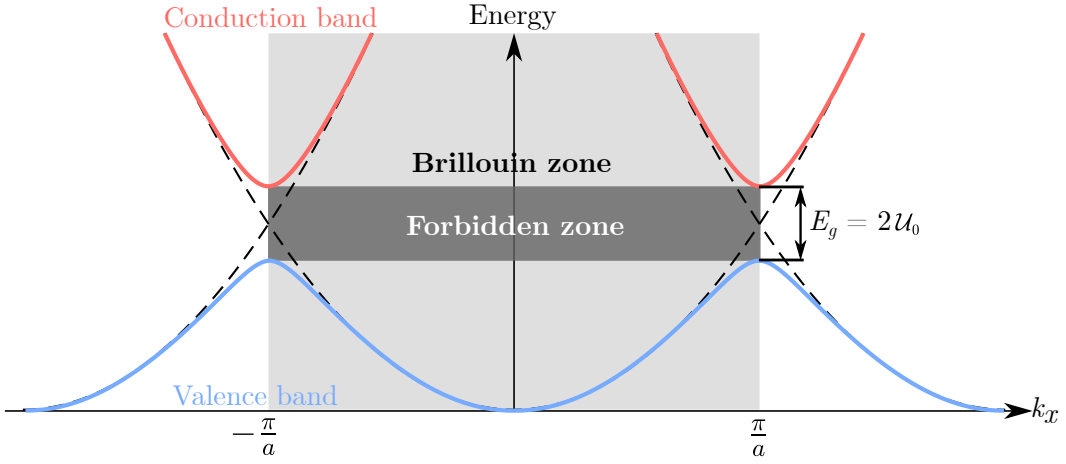

FIGURE 1.2: Dispersion of the valence band (blue) and conduction band (red) within the Brillouin zone (light grey region), which are split away from the bare electron dispersions (dashed black parabolas) by $2\mathcal{U}_0$ at the edges of the Brillouin zone, corresponding to the bandgap energy of a semiconductor, E_g. The forbidden zone is shown in dark grey and maps out the region where no electron branch exists between the top of the valence band and bottom of the conduction band.

1.1.2 Excitons

In order to study the dynamics of large many particle systems more easily, ensembles of interacting particles are often replaced with a smaller number of non-interacting quasi-particles [12]. In semiconductor physics, the exciton is a quasi-particle formed

from the Coulomb coupling of a conduction band electron and valence band hole within a semiconductor, where the classification of an exciton is further made depending on the strength of the Coulomb interaction.

In the case of strong Coulomb coupling between the electron and hole (binding energy typically 0.1 - 1 eV), the quasi-particle is classed as a "Frenkel Exciton" [18]. This strong coupling results in a tightly bound exciton with a radius comparable to the atomic spacing of the semiconductor lattice. Frenkel excitons are common in ionically bonded compounds, halides or organic semiconductors [1]. "Wannier-Mott excitons" on the other hand have a binding energy much less than that of a hydrogen atom (on the order of 0.01 eV) and span across multiple lattice sites [19, 20]. As the exciton is not localised it can propagate across a lattice [1]. In turn, the Wannier-Mott exciton corresponds to a Hydrogen-like bound state with a comparable Hamiltonian [12]:

$$H = -\frac{\hbar^2}{2m_e^*}\nabla_e^2 - \frac{\hbar^2}{2m_h^*}\nabla_h^2 - \frac{e^2}{\varepsilon|\mathbf{r}_e - \mathbf{r}_h|} \tag{1.11}$$

with effective electron and hole masses $m_{e,h}^*$, electron and hole separation distance $|\mathbf{r}_e - \mathbf{r}_h|$ and dielectric constant $\varepsilon \neq 1$. Drawing a further comparison to the Hydrogen atom, the exciton can be described by a Bohr-like radius $\alpha_B = \frac{(m_e^*+m_h^*)^2}{m_e^{*2}m_h^{*2}}\frac{\varepsilon\hbar^2}{e^2}$ and Rydberg energy (minimum energy required to ionise the exciton) $R_\chi = \frac{e^2}{2\varepsilon a_B}$ [12, 1]. Due to the neutral charge of the exciton, the free motion of the quasi-particle with effective mass $m_\chi = m_e^* + m_h^*$ follows:

$$E_{\chi_n}(k) = E_g - \frac{R_\chi}{n^2} + \frac{\hbar^2 k^2}{2m_\chi}, \tag{1.12}$$

where k is the momentum of the propagating exciton through the bulk semiconductor.

1.1.2.1 Excitons in Quantum Wells

As mentioned at the start of this chapter, QWs are heterostructure consisting of a thin semiconductor layer sandwiched within a higher bandgap material in order to confine carriers perpendicular to the slice, but allowing free propagation in the 2D plane of the QW. The bulk structure of GaAs (a semiconductor material commonly used in inorganic polaritonics with a direct bandgap) leads to an exciton Bohr radius of ~12.5 nm, making it possible to create a periodic potential of a similar size, thus confining excitons in three dimensions. For a GaAs QW however, there are two main excitonic differences to the bulk structure. Firstly, size. The GaAs exciton diameter is smaller when confined within a QW of a few tens of nanometres. Interestingly, the exciton is in fact smaller in the plane of the QW too, as this requires a lower kinetic energy than a pancake-shaped exciton [21]. Taking the 2D limit of the hydrogen atom

and assuming infinitely high potential confinement in the QW, the resulting exciton diameter is reduced by a half [1, 22]. Secondly, due to the close proximity of the electron and hole in 2D, the binding energy of the 2D exciton is four times stronger than in 3D [1, 22]. This results in an exciton wavefunction that has a tighter overlap between the electron and hole counterparts, leading to a well-defined exciton resonance [21].

1.1.2.2 Exciton Spin-Orbit Coupling

For zincblende semiconductors (2 face-centred cubic structures displaced by $\frac{a}{4}(\hat{x},\hat{y},\hat{z})$) with a direct bandgap near the centre of the Brillouin zone [1, 21], such is the case for a GaAs QW, the electrons form an S-like conduction band and the holes configure into two P-like valence bands with azimuthal quantum numbers $\ell = 0$ and 1 for the S-like and P-like bands respectively, where both electrons and holes have the same spin $s = 1/2$. Considering first the conduction band, the total angular momentum of the electrons is $j = |\ell + s| = |\ell - s| = 1/2$, with the projection along the z-axis of $m_j = \pm 1/2$. Taking into account the spin orbit coupling of the valence bands, the resulting total angular momenta of the electron holes are $j = 3/2$ and $j = 1/2$ with $m_j = \{\pm 3/2, \pm 1/2\}$ and $m_j = \{\pm 1/2\}$ respectively. The states $|j; m_j\rangle = |1/2; \pm 1/2\rangle$ (known as the "split off" band) are at a lower energy so have negligible interaction with the conduction band and will be neglected for the rest of the discussion on excitons. The states $|3/2; \pm 3/2, \pm 1/2\rangle$, (labelled as heavy holes (hh) with $m_j = \{\pm 3/2\}$ and light holes (lh) with $m_j = \{\pm 1/2\}$) do however interact with the conduction band and play a vital role in exciton formation. Each $|j; m_j\rangle$ state of the conduction and valence bands interacts (see Figure 1.3), where the resulting state is given by the sum of the m_j components of each particle. However only the resulting states with $m_j = \{\pm 1\}$ can be excited by light or can recombine by emitting a photon ($m_j = \pm 1$) and thus are labelled "bright excitons" (coloured arrows in Figure 1.3). The other states ($m_j = \{0, \pm 2\}$) are categorised as "dark excitons" as they are optically inactive and do not efficiently couple to light [23, 24] (black arrows in Figure 1.3).

For example, the coupling of lh state $|3/2; 1/2\rangle$ with electron state $|1/2; 1/2\rangle$ leads to the lh exciton state $|3/2; +1\rangle$, which can couple to right-circularly polarised light with $m_j = +1$. Alternatively, hh state $|3/2; -3/2\rangle$ and electron state $|1/2; -1/2\rangle$ lead to the hh exciton state $|3/2; -2\rangle$. As $m_j = -2$, it is not able to couple to a photon (with $m_j = \pm 1$), and so we label it as a "dark exciton". As a result, these states will also be neglected for rest of this discussion, as in subsection 1.1.4 we will be considering the coupling of excitons with microcavity photons. Note that the resulting spin projections are integers for both dark and bright excitons, indicating that the strong dipole coupling of the fermionic electron and hole (characterised by half-integer spin) results in a quasi-particle that is bosonic in nature.

At $k = 0$ in the dispersion, within a bulk material the hh states (with $m_j = \{\pm 3/2\}$) and lh states (with $m_j = \{\pm 1/2\}$) are degenerate [21, 25, 26]. However in the 2D limit, such is the case with QWs, the degeneracy is lifted due to the quantum confinement in the growth direction and the band mixing between the two states results in a hh-lh energy splitting Δ_{hh-lh}, where the lh band drops below the hh band in energy. The system undergoes the phenomenon of "mass reversal" where the hh and lh characteristics are reversed, in other words the hh states have a smaller effective mass of in-plane motion compared to the lh states [25, 26, 27]. As such, only the hh band is occupied as it is closer to the conduction band in energy [27], i.e. only the hh exciton states $|3/2; \pm 1\rangle$ make up the optically-active exciton spectrum.

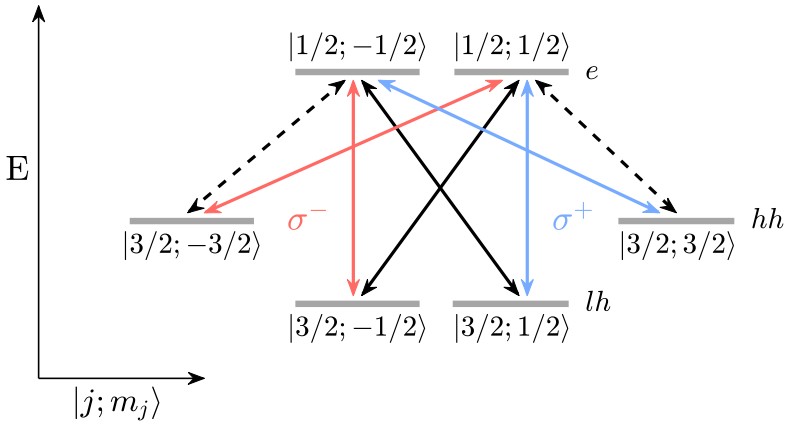

FIGURE 1.3: QW transition between conduction band electrons (e) in top row with valence band heavy holes (hh) and light holes (lh) in lower row with total angular momentum j and angular momentum projected along the z-axis m_j. Optically active exciton quasi-particles (i.e. with $m_j = \pm 1$) are indicated by red and blue arrows respectively, with a corresponding ability to couple with $\sigma^{\pm}$ polarised light. Dark excitons shown by black arrows, where solid and dashed lines represent $m_j = 0$ and $|m_j| = 2$ respectively.

1.1.3 Cavity Photons

This work concerns 1D confinement within a Fabry-Pérot cavity, although confinement is possible in up to three dimensions [1]. The Fabry-Pérot cavity is an optical resonator where the cavity length is equivalent to its confinement wavelength. In order to have a high level of confinement, the reflectivity of the cavity walls must be maximised where silver mirrors, which are used for standard reflection processes, are not sufficient. Instead distributed Bragg reflectors (DBRs) are used and consist of stacked pairs of thin layers of material alternating in relatively high and low refractive indices ($n_{h,l}$) in order to maximise the magnitude of the reflection coefficient at the layer interfaces (see Figure 1.4(d)), where each layer has an optical thickness of $\frac{\lambda_{Bragg}}{4}$. Here, λ_{Bragg} is the central wavelength that the DBRs are designed to confine and the whole region of wavelengths that experience high reflectivity from the DBR is known

as the photonic stopband (central ∼100 nm region at centre of Figure 1.4(a-c)). Light of wavelength λ_{Bragg} will reflect at each DBR boundary, where at the interfaces of high-to-low refractive indices it will gain a π phase shift (interpreted as a negative reflection coefficient, as shown in Figure 1.4(c)). Therefore, the round-trip of the light through one DBR layer is $\frac{\lambda_{Bragg}}{2}$ where the reflection of each stacked DBR layer interferes constructively and the overall reflectivity can be increased to nearly 100% if many DBRs are stacked together, as shown in Figure 1.4(a).

By bringing two DBR stacks together, separated by a cavity spacer with optical length $L_c = n_c d_c$, refractive index n_c and thickness d_c, certain wavelengths will resonate within the cavity. These resonant cavity modes, defined by $\lambda_m = 2L_c/m$ ($m \in \mathbb{Z}^+$), will experience strong suppression in reflectivity within the cavity stopband, as shown by the sharp dip at 807nm in Figure 1.4(b). The energy gap between the resonant modes is inversely proportional to the cavities optical length following $\Delta\omega_c = c\pi/L_c$, therefore the use of cavities with a small optical length, or "microcavities", ensures that only one resonant mode is present within the DBR stopband [1]. The width of the resonance peak is defined by Q-factor $Q = \omega_c/\delta\omega_c$ where $\delta\omega_c$ is the FWHM of the mode. Although this microcavity structure confines quantised wavevectors at a normal to the DBR surface ($k_\perp$), a continuous range of wave vectors are accessible in-plane to the microcavity ($k_\parallel = \sqrt{k_x^2 + k_y^2}$) and map out a parabolic dispersion with varying $k_\parallel$, which indicates that the cavity photons have gained an effective mass due to the confinement in the microcavity's growth direction.

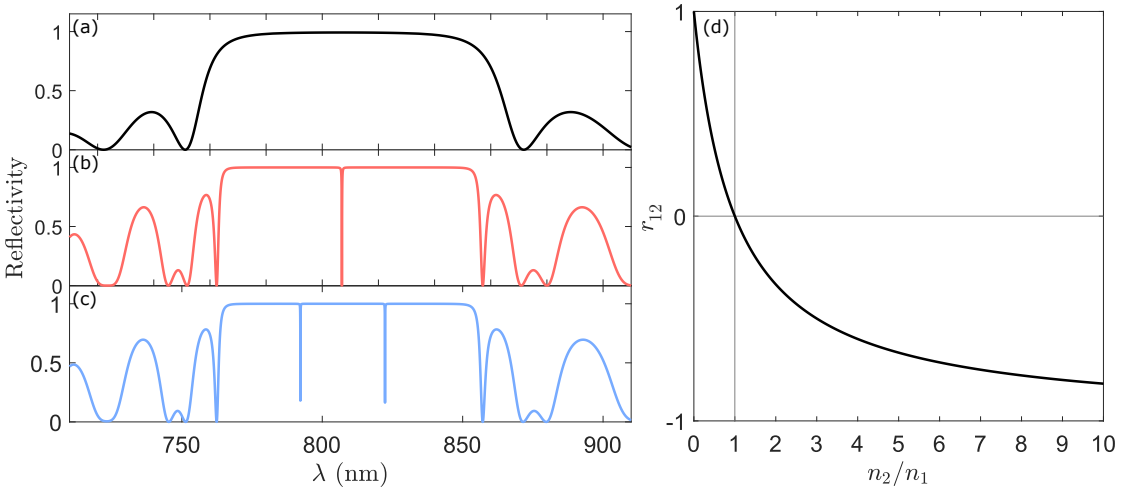

FIGURE 1.4: Reflectivity spectra of (a) DBR of 20 pairs of GaAs and AlAs layers with $\lambda_{Bragg} = 807$nm, (b) $\frac{5\lambda_{Bragg}}{2}$ GaAs Fabry-Pérot cavity confined by two stacks of the 20 DBR pairs, and (c) same cavity as (b) with an InGaAs QW at the centre. (d) Amplitude reflection coefficient, r_{12}, at interface of materials transferring from refractive index n_1 to n_2, where $r_{12} = \frac{n_1 - n_2}{n_1 + n_2}$ [1].

The reflectivity spectra in Figure 1.4 are calculated using the transfer matrix method [1, 28] by multiplying the reflection matrices from each interface of material i to j (T_{ij}) and propagation matrices through each layer of material i (T_i) following [29]:

$$T_{ij} = \frac{1}{1+r_{ij}} \begin{pmatrix} 1 & r_{ij} \\ r_{ij} & 1 \end{pmatrix} \tag{1.13}$$

$$T_i = \begin{pmatrix} e^{i\phi_i} & 0 \\ 0 & e^{-i\phi_i} \end{pmatrix} \tag{1.14}$$

where r is the amplitude-reflection coefficient giving the ratio of reflected and incident amplitudes of light, and $\phi_i = \frac{2\pi d n_i}{\lambda}$ is the phase rotation gained by the light with wavelength λ propagating over distance d through material i with refractive index n_i. The effective transfer matrix T_M is the resultant product of all the matrices across all N layers and $N-1$ interfaces:

$$T_M = \begin{pmatrix} t_{11} & t_{12} \\ t_{21} & t_{22} \end{pmatrix} = T_N T_{N-1,N}, \cdots, T_{1,2} T_1 \tag{1.15}$$

giving the final reflectivity $R = |r|^2 = \left|\frac{t_{21}}{t_{22}}\right|^2$ at wavelength λ [1, 29].

1.1.4 Light Matter Coupling

So far we have studied the one-dimensional confinement of excitons in a QW and the confinement of cavity photons in a Fabry-Pérot microcavity separately. By bringing both components together through placing QWs inside the microcavity, the exciton and cavity photon interact and light-matter coupling comes into play. The exciton and cavity photon couple with a coupling strength [30],

$$\kappa = \sqrt{\frac{1+\sqrt{R}}{\sqrt{R}} \frac{c\Gamma_\chi}{n_{cav} L_{eff}}} \tag{1.16}$$

where R is the total reflectivity power of the microcavity [1], Γ_χ is the radiative exciton decay rate at $k_x = 0$ in a single QW, n_{cav} is the refractive index of the cavity spacer and $L_{eff} = L_{cav} + L_{DBR}$ is the effective cavity length including the penetration depth into DBR mirrors given by $L_{DBR} = \frac{\lambda_{Bragg} n_l n_h}{2(n_h - n_l)}$ [1, 30, 31].

Due to this coupling, the system can be described by the two-coupled oscillator problem with a non-Hermitian Hamiltonian (describing a classical oscillator coupling) and characteristic polynomial [1, 30]:

$$H = \hbar \begin{pmatrix} \omega_\chi - i\gamma_\chi & \kappa \\ \kappa & \omega_c - i\gamma_c \end{pmatrix} \tag{1.17}$$

$$\implies (\omega_\chi - i\gamma_\chi - \omega)(\omega_c - i\gamma_c - \omega) = \kappa^2 \tag{1.18}$$

where $\hbar(\omega_{c,\chi} - i\gamma_{c,\chi})$ are the complex eigenenergies of the cavity photon and QW exciton (in the absence of exciton-photon coupling) with photon and exciton decay rates $\gamma_{c,\chi}$ respectively. The eigenfrequencies, $\omega_\pm$, can be solved using the quadratic formula,

$$\omega_\pm = \frac{\omega_\chi + \omega_c}{2} - \frac{i(\gamma_\chi - \gamma_c)}{2} \pm \sqrt{\kappa^2 + \left(\frac{\omega_\chi - \omega_c}{2}\right)^2 - \left(\frac{\gamma_\chi - \gamma_c}{2}\right)^2 + \frac{i}{2}(\omega_\chi - \omega_c)(\gamma_\chi - \gamma_c)}. \tag{1.19}$$

When $\omega_c - i\gamma_c = \omega_\chi - i\gamma_\chi$, this gives an energy splitting of $\Omega = \pm\sqrt{4\kappa^2 - (\gamma_\chi - \gamma_c)^2}$ from the bare exciton and cavity photon modes. Ω is considered as a vacuum-field Rabi splitting that can reach 4-15 meV in GaAs-based QW microcavities [1, 31].

However, Ω can only be real if

$$\kappa > \left|\frac{\gamma_\chi - \gamma_c}{2}\right|. \tag{1.20}$$

Equation 1.20 is in fact the requirement for strong coupling, such that mode splitting will only occur if and when the coupling rate is much faster than the decay channels of the system. In the weak coupling regime, the imaginary valued Ω corresponds to system losses and will not result in an energy splitting. In the strong coupling regime, two distinct modes manifest labelled as the upper polariton (UP) and lower polariton (LP) branches and are evidenced by two sharp resonances in the QW microcavitie's reflectivity spectrum shifted from the bare cavity mode by $\pm\Omega$ respectively [1], as shown in Figure 1.4(c). Explicitly, the strong coupling regime gives rise to the polariton quasi-particle resulting from the Rabi oscillation of energy between a QW exciton and cavity photon confined within a QW semiconductor microcavity.

Considering just the real components of the eigenfrequencies and using $E_{c,\chi} = \hbar\omega_{c,\chi} = \frac{\hbar^2 k_\parallel^2}{2m_{c,\chi}}$, we can define the UP and LP eigenenergies from Equation 1.19:

$$E_{UP,LP}(k_\parallel) = \frac{E_\chi(k_\parallel) + E_c(k_\parallel)}{2} \pm \frac{1}{2}\sqrt{\left(E_\chi(k_\parallel) - E_c(k_\parallel)\right)^2 + 4\hbar^2\Omega^2} \tag{1.21}$$

which correspond to the UP and LP dispersions plot in Figure 1.5(a-c). Depending on the difference in energy between the bare cavity photon and QW exciton modes at $k_\parallel = 0$ (known as cavity detuning, δ) and the resulting difference in exciton and cavity photon bare energies at any $k_\parallel$ given by $\Delta E(k_\parallel) = E_\chi(k_\parallel) - E_c(k_\parallel)$, the photonic and excitonic fractions of the lower-branch polaritons are defined by the Hopfield coefficients respectively (as shown in Figure 1.5(d-f)):

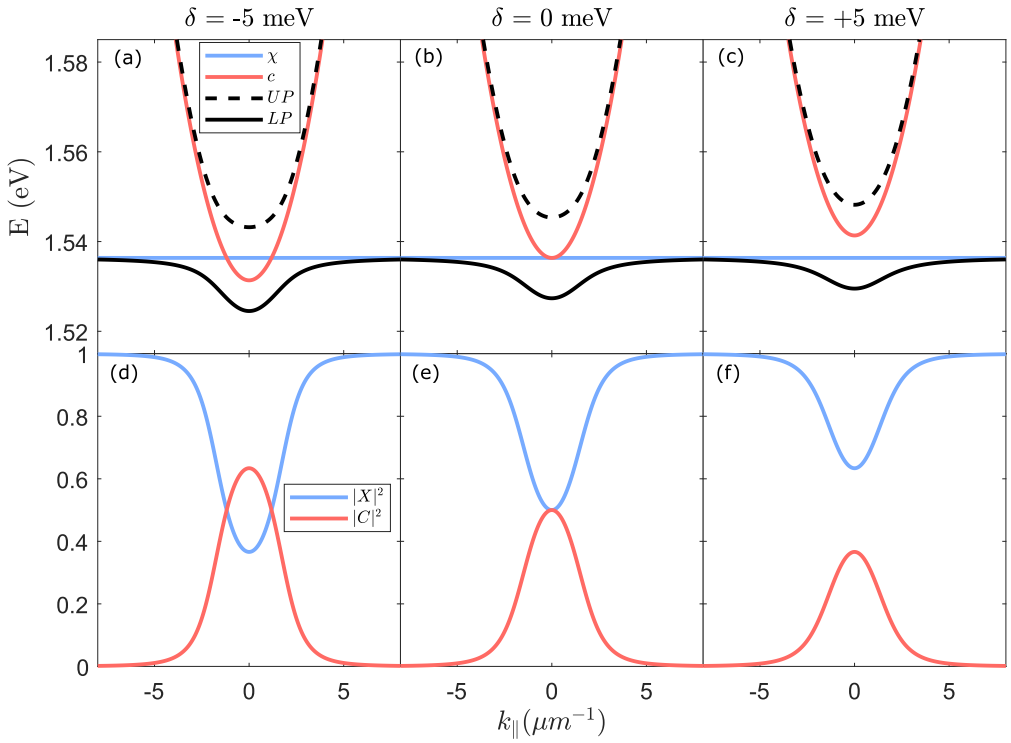

FIGURE 1.5: Dispersions of QW exciton (χ), cavity photon (c), UP and LP branches at a cavity detuning of (a) -5 meV, (b) 0 meV and (c) +5 meV, with (d-f) respective excitonic and photonic Hopfield coefficients $|X|^2, |C|^2$ for a single GaAs QW sandwiched within a $\frac{5\lambda_{Bragg}}{2}$ microcavity with $\lambda_{Bragg} = 807\ nm$.

$$|C(k_\parallel)|^2 = \frac{1}{2}\left(1 + \frac{\Delta E(k_\parallel)}{\sqrt{\Delta E(k_\parallel)^2 + 4\hbar^2\Omega^2}}\right) \tag{1.22}$$

$$|X(k_\parallel)|^2 = \frac{1}{2}\left(1 - \frac{\Delta E(k_\parallel)}{\sqrt{\Delta E(k_\parallel)^2 + 4\hbar^2\Omega^2}}\right). \tag{1.23}$$

$|C|^2$ and $|X|^2$ give the fraction of the quasi-particle from the photon and exciton respectively, and can also be thought of as the probability of observing an LP branch polariton in the photonic or excitonic state, where $|C|^2 + |X|^2 = 1$. Note how the LP dispersion has a steeper gradient around $k_\parallel = 0$ with negative cavity detuning, indicating that the effective LP mass is reduced. This makes a negative detuning more desirable for studying polariton condensates, and the critical temperature of condensation will increase, which is discussed further in section 1.2. Additionally, the negatively detuned microcavity gives rise to a larger photonic component around $k_\parallel = 0$, which results in a larger photon emission thus making it easier to measure experimental observables of the system.

In order to efficiently access a variety of cavity detunings in experiment, the QW microcavity sample is grown with a wedge-shaped cavity spacer, thus altering the

photonic confinement wavelength depending on the location at which it is optically excited. The work in thesis concerns non-resonant laser excitation, which rather than exciting the microcavity sample at its confinement wavelength, the laser is instead tuned to the first minimum energetically above the reflectivity stopband [1].

1.2 Bose-Einstein Condensation

Following on from the work of Bose on the distribution of quantum particles [32], Einstein made the proposition that an ideal gas of non-interacting bosons could experience a quantum phase transition, characterised by a build up in occupation at the ground state of a bosonic system. This macroscopic population of coherent bosons in the same quantum state has since been coined a "Bose-Einstein condensate" (BEC) [33]. For this phase transition to occur, particle separation must be at most comparable to the particle de Broglie wavelength, such that the particle wavefunctions overlap. It wasn't until 1995 that the first BECs were experimentally realised using rubidium-87 [34], sodium [35] and Lithium-7 [36] as dilute atomic gasses cooled below the critical condensation temperature.

This section discusses the BEC of an ideal quantum gas and makes comparisons to the 2D condensation of polaritons in a QW microcavity.

1.2.1 Ideal Gas of BECs

Identical quantum particles are indistinguishable within an ensemble. That is, if two particles labelled 1 and 2 were swapped, there would be no change to any measured observable of the system. For example, the energy of the system under this particle exchange stays the same:

$$\hat{H}\psi(1,2) = E\psi(1,2) \quad \text{and} \quad \hat{H}\psi(2,1) = E\psi(2,1), \tag{1.24}$$

where E is the same energy in both equations. This swapping can be written as an exchange operator, $\hat{P}_{12}\psi(1,2) = \psi(2,1)$. $\hat{P}_{12}$ has two possible eigenvalues, $\lambda = \pm 1$, as applying the operator twice gives back the original wavefunction following $\psi(1,2) = \lambda^2\psi(1,2)$. These two outcomes correspond to the respective symmetric and antisymmetric wavefunctions, with single-particle wavefunctions $u_{a,b}$ swapping between states $1, 2$ (e.g. swapping position or spin):

$$\psi_+(1,2) = \frac{u_a(1)u_b(2) + u_a(2)u_b(1)}{\sqrt{2}} \rightarrow \text{Symmetric} \tag{1.25}$$

$$\psi_-(1,2) = \frac{u_a(1)u_b(2) - u_a(2)u_b(1)}{\sqrt{2}} \rightarrow \text{Antisymmetric.} \tag{1.26}$$

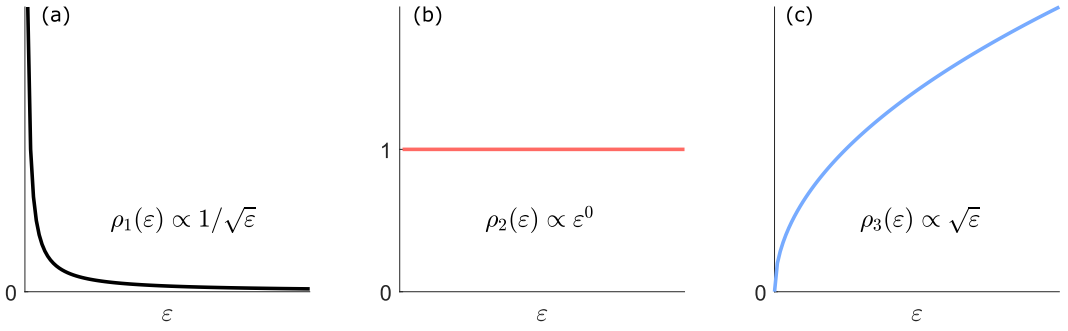

FIGURE 1.6: Trend in density of states ρ_d as a function of energy ε in (a) 1, (b) 2 and (c) 3 dimensions.

The wavefunction describing two identical particles can exist in only one of these two states. Specifically, particles with symmetric wavefunctions are *bosons* and particles with anti-symmetric wavefunctions are *fermions*. This is verified when considering two particles in the same quantum state $u_a = u_b$, then the antisymmetric wavefunction vanishes (a mathematical statement of the Pauli exclusion principle), whereas the symmetric wavefunction does not, thus showing that multiple bosons can share the same quantum state [37].

Each single particle quantum state has a possible occupation number of $n = \{0, 1, \cdots, \infty\}$ for bosons and $n = \{0, 1\}$ for fermions and depends on the energy ε, temperature T and chemical potential μ of the state, where the occupation number of fermions and bosons follow the Fermi-Dirac and Bose-Einstein distributions respectively for the ± 1 in the denominator:

$$n(\varepsilon, T, \mu) = \frac{1}{e^{\beta(\varepsilon-\mu)} \pm 1} \tag{1.27}$$

where $\beta = \frac{1}{k_B T}$ and k_B is Boltzmann's constant. As this section concerns the condensation of bosons, fermions will no longer be discussed. The total number of particles in the system N can be determined by integrating the product of n with the density of states in 3D, ρ_3, over all energies from the ground state, ε_0, upwards:

$$N = \int_{\varepsilon_0}^{\infty} n(\varepsilon)\rho_3(\varepsilon)d\varepsilon. \tag{1.28}$$

The trend between $\rho_d(\varepsilon)$ and ε changes over $d = \{1, 2, 3\}$ dimensions, as shown in Figure 1.6, but for $d = 3$ it is defined for particles with mass m_p and system volume V as [38],

$$\rho_3(\varepsilon) = \sqrt{\varepsilon}\frac{V}{4\pi^2}\left(\frac{2m_p}{\hbar^2}\right)^{\frac{3}{2}}. \tag{1.29}$$

For BECs, we consider the occupation in the ground state $n_0 = \frac{1}{e^{\beta(\varepsilon_0-\mu)}-1}$. If the chemical potential does not follow $\mu < \varepsilon_0$, then n_0 will be negative and the occupation

n_0 grows with μ up to an asymptote at $\mu = \varepsilon_0$. The definition of the critical temperature for 3D condensation requires that the number of particles in excited states N_{ex} (i.e. particles with $\varepsilon > \varepsilon_0$) is equal to the total number of particles N when $\varepsilon_0 = 0 (= \mu)$:

$$N = N_{ex} = \frac{V}{4\pi^2}\left(\frac{2m_p}{\hbar^2}\right)^{\frac{3}{2}} \int_{\varepsilon_0+\delta\varepsilon}^{\infty} \frac{1}{e^{\beta\varepsilon}-1} d\varepsilon \tag{1.30}$$

where $\varepsilon_0 + \delta\varepsilon \simeq \varepsilon_0$ as $\delta\varepsilon$ is infinitesimally small [38]. Note that in Figure 1.6(c), the 3D density of states converges to 0 as $\varepsilon \to 0$, whereas the 2D and 1D cases remain constant and tend to ∞ respectively. The consequence of this behaviour is that a finite BEC threshold temperature exists for a 3D system only. By using the known relation $\frac{1}{e^x-1} = \sum_{n=1}^{\infty} e^{-nx}$ with $x = \beta\varepsilon$, and introducing the Riemann zeta and Gamma functions $\zeta(\frac{3}{2}) = \sum_{n=1}^{\infty} n^{-\frac{3}{2}}$ and $\Gamma(\frac{3}{2}) = \int_0^{\infty} e^{-t}\sqrt{t}dt$, we can evaluate the integral in Equation 1.30:

$$N = \frac{V}{4\pi^2}\left(\frac{2m_p}{\beta\hbar^2}\right)^{\frac{3}{2}} \zeta\left(\frac{3}{2}\right)\Gamma\left(\frac{3}{2}\right). \tag{1.31}$$

The particles can be considered as a wave with a thermal de Broglie wavelength λ_{dB}. This can be derived by evaluating the partition function of the system and relating it to $\frac{V}{\lambda_{dB}}$ to get $\lambda_{dB} = \sqrt{\frac{2\pi\hbar^2}{m_p k_B T}}$ [39]. Therefore, the BEC critical density is,

$$n_c = \frac{N}{V} \simeq \frac{2.612}{\lambda_{dB}^3}. \tag{1.32}$$

Since $n_c^{-\frac{1}{3}}$ corresponds to the average spacing between particles, qualitatively the BEC phase transition occurs when the particle separation distance is equivalent to the de Broglie wavelength [38]. The condensation threshold condition can thus be re-written in terms of a critical temperature following,

$$T_c = \frac{2\pi\hbar^2}{m_p k_B}\left(\frac{1}{2.612}\frac{N}{V}\right)^{\frac{2}{3}}. \tag{1.33}$$

When the density is above n_c or equivalently the temperature below T_c, the population of particles at ε_0 grows to form a BEC alongside the population of thermal particles with $\varepsilon > 0$:

$$N = N_0 + N_{ex}. \tag{1.34}$$

For N_{ex} at $T < T_c$, the relation in Equation 1.32 holds following $n_{ex}\lambda_{dB}(T)^3 = 2.612$, but there is no integral that represents N_0. Given that at the critical temperature, $n = n_c$ and by equating $n_{ex}\lambda_{dB}(T)^3$ to Equation 1.32, the fractional number density of

particles in the excited state can be expressed as,

$$\frac{n_{ex}}{n} = \frac{\lambda_{dB}(T_c)}{\lambda_{dB}(T)} = \left(\frac{T}{T_c}\right)^{\frac{3}{2}} \tag{1.35}$$

giving the fractional number density of the ground state,

$$\frac{n_0}{n} = \frac{n - n_{ex}}{n} = 1 - \left(\frac{T}{T_c}\right)^{\frac{3}{2}} \tag{1.36}$$

where $n_0 \to n$ as $T \to T_c$, i.e. below critical temperature, the majority of particles occupy the ground state resulting in a Bose-Einstein condensate [37].

1.2.2 BECs in Two-Dimensions

In a 2D system of an ideal non-interacting bosonic gas, the density of states does not converge to zero as $\varepsilon \to 0$ (Figure 1.6(b)), therefore in the 2D limit, the integral in Equation 1.28 diverges. The maximum number of particles in the excited state is therefore infinite and it is not possible to reach the condensation threshold for finite T_c, even if the particle separation distance is comparable to λ_{dB}. This is also the case for the ideal interacting Bose gas as long range order cannot appear in a 2D ideal Bose gas.

However, in the presence of a trapping potential, the density of states drastically changes and 2D BECs can indeed exist [1, 40]. For example, with a symmetric harmonic trapping potential $U(x, y) = \frac{m_p\omega^2}{2}(x^2 + y^2) = \frac{2m_p\pi^2c^2}{\lambda^2}(x^2 + y^2)$, the density of states becomes $\rho_2(\varepsilon) = \frac{\varepsilon}{\hbar^2\omega^2}$, which converges to zero as $\varepsilon \to 0$. The corresponding critical temperature is calculated following the same method as the 3D case to give [40],

$$T_c = \sqrt{\frac{6N}{\pi^2}}\hbar\omega_c \tag{1.37}$$

and the fractional number density of particles in the ground state follows,

$$\frac{n_0}{n} = \frac{n - n_1}{n} = 1 - \left(\frac{T}{T_c}\right)^2. \tag{1.38}$$

With bosonic condensation now proved to be possible in a finite 2D system of a weakly interacting Bose gas confined by a harmonic potential, the QW microcavity polariton offers to be an ideal system for experimentally observing such a phase transition. Due to the polariton's relatively light effective mass (typically $\sim 10^{-5}m_e$ [1]) compared to a dilute atomic gas, the critical temperature of a QW microcavity polariton is typically a few Kelvin, which is experimentally far easier to maintain than the micro-Kelvin temperatures required by atomic condensates.

The original experiments in search of the Bose-Einstein condensation of polaritons were mainly held back by the cavity photon lifetime of the samples, where clouds of polaritons were unable to thermalise within the cavity lifetime. It was not until 2006 that Kasprzak et al. [41] reported experimental observations of a coherence build-up across a cloud of polaritons, thus demonstrating long range order, marking the first official sighting of polariton Bose-Einstein condensates.

There is some contention within the condensate community whether this coherence build up in polariton systems qualifies as a BEC, as a condensate of polaritons varies from a traditional BEC in a number of ways. The points of contention include:

- **Polariton condensates are in two dimensions.** As discussed above, both the cavity photons and QW excitons are confined in a 2D plane, thus the resulting condensate is also two dimensional;
- **Polaritons require continuous pumping.** Due to the relatively short lifetime of the cavity photon, polaritons are in quasi-equilibrium of continuous decay and formation;
- **Excitons undergo a Mott transition.** At high densities, excitons dissociate and become a metallic plasma of electrons and holes as the constituent exciton components experience repulsion and attraction from the neighbouring particles. Due to the now fermionic characteristics of the system, coherence deteriorates across the exciton cloud. This issue is overcome by placing multiple QWs around the anti-nodes of the microcavity, such that each QW produces excitons below the Mott transition density, but the overall contribution of excitons is high [1];
- **Polaritons are blue-shifted from LP branch.** Due to the strong polariton-polariton repulsion at high densities, condensed polaritons are shifted from the LP branch to a slightly higher energy, which increases with the excitonic fraction of the polaritons $|X|^2$ [11].

However, with the system showing long range order (first predicted in 1956 [42] and demonstrated in 2006 [41]) and a non-linear emission in response to varying pump power [1], the community has settled on the nomenclature of “polariton condensate” and will be refereed to as such herein.

1.2.3 Polariton Condensate or Laser?

Although the structure of the QW microcavity is identical to that of a vertical-cavity surface emitting laser (VCSEL), the behaviour is intrinsically very different. In a VCSEL, lasing occurs via population inversion, where many pairs of electrons and holes are optically excited. The light is amplified by the recombination of electron-hole

pairs, where the coherence of emitted light comes directly from the relaxation from the inverted state. Polaritons however undergo stimulated cooling from a hot exciton reservoir through many phonon emissions down the LP branch, losing all phase information from the initial optical stimulation. Coherence builds spontaneously for particles at the bottom of the LP branch, below the exciton energy of the VCSEL [11].

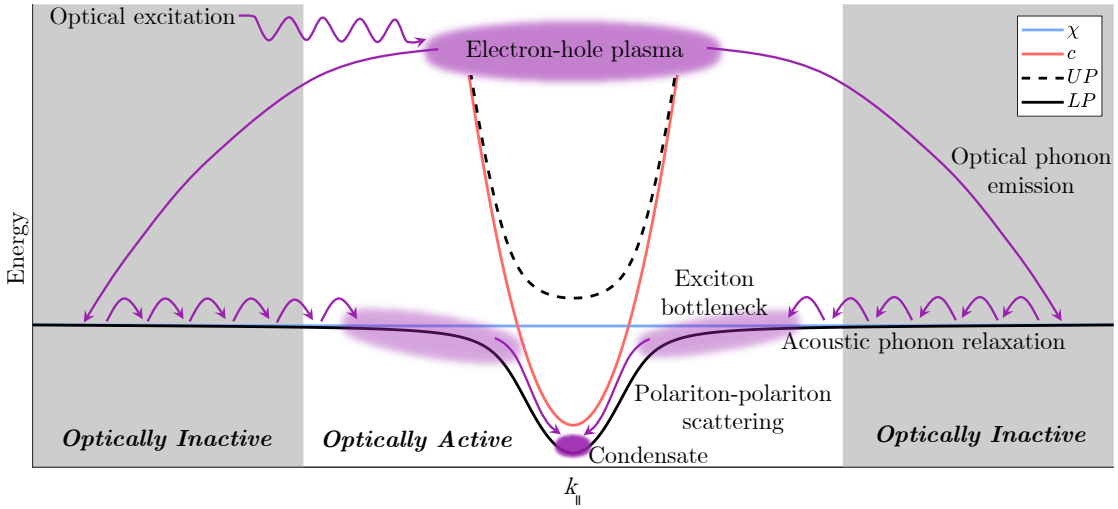

FIGURE 1.7: Schematic of the polariton condensation process in terms of the energy dispersion, with (blue) exciton dispersion, (red) cavity photon dispersion, (dashed black) UP branch, (solid black) LP branch, (purple arrows) dynamics of the condensation process in the (grey background) optically inactive and (white background) optically active regions. The optical excitations creates a relatively high energy hot electron-hole plasma that, through optical phonon emission, forms high energy optically inactive excitons at with large $|k_{\|}|$ on the LP branch. These excitons reduce in energy via many small acoustic phonon relaxations, thus losing all phase properties of the initial optical excitation. As the excitons become optically active and couple to photons, an exciton bottleneck builds up, from which the polaritons undergo polariton-polariton scattering and relax into the LP ground state, gaining a global phase coherence thus forming the polariton condensate.

1.2.4 Non-resonant Excitation

A population of polaritons are introduced into the microcavity through optical excitation, typically using a laser. When a microcavity is excited by a non-resonant pump laser, a high energy ($\sim$ 100 meV above the bottom of the LP branch) electron-hole plasma is injected into the sample at high momenta on the LP branch. This plasma dissipates energy first through longitudinal-optical phonon emission in the first picosecond to form excitons, followed by acoustic phonon relaxation after $\sim$1 ns [43]. As acoustic phonon interactions are inefficient, it requires many emissions for the excitons to relax down the LP branch towards the edge of the light cone, in turn losing all original phase of the laser. Once the difference between the exciton and photon momentum is comparable to the Rabi splitting energy, the phonon density of states reduces considerably making cooling less efficient and excitons are then able to couple

to cavity photons. This introduces radiative decay into the system such that a bottleneck of incoherent excitons builds to a macroscopic population and stimulated cooling (polariton-polariton scattering) takes over as the dominant cooling process. For two polaritons in the bottleneck region, one scatters to twice the bottleneck momentum, whilst the other scatters to $k_{\parallel} = 0$ (where population builds up). The polaritons spontaneously occupy the same quantum state above condensation density [11]. Figure 1.7 is a schematic representation of this condensation mechanism in the view of the system's dispersion.

As the exciton diffusion length is so small at cryogenic temperatures, the resulting potential landscape that confines the polariton condensate follows the spatial geometry of the hot exciton reservoir, as dictated by the incident laser excitation profile. This gives rise to two optical confinement regimes, the first being optically pumped ballistically expanding condensates, which form at the spatial location of the pumping profile (e.g. using a profile consisting of Gaussian spots), as depicted in Figure 1.8(left) [41, 44, 45]. The steep potential formed by the pump profile causes condensed polaritons to ballistically propagate away from the condensate centre in a radial direction with non-zero momentum on the free LP dispersion. The other regime creates optically trapped condensates, where the condensate is spatially displaced from the excitation profile as polaritons ballistically propagate down the potential landscape and build in density at a potential minima to above the condensation threshold, as shown in Figure 1.8(right). Optically trapped condensates are excited using a tight profile that prevents polaritons from radially propagating away using pump geometries such as an annulus (ring) or a tightly packed lattice of Gaussian spots [46, 47, 48, 49, 50, 51, 52]. The system of an optically trapped condensate can be

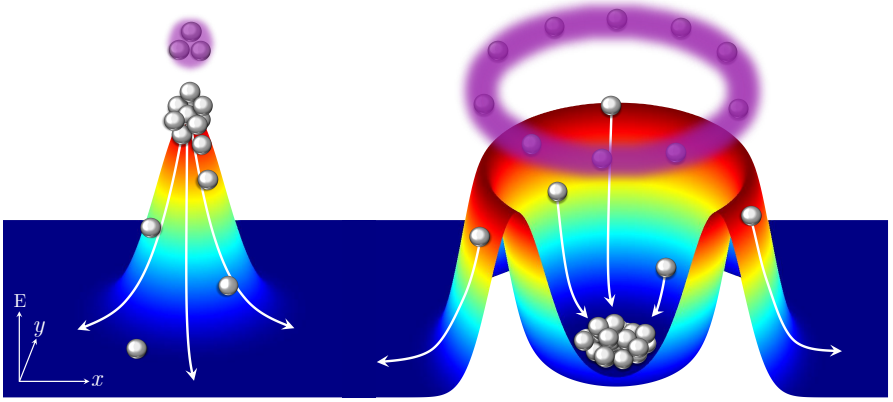

FIGURE 1.8: Pumping schematics for the (left) ballistically expanding and (right) optically trapped polariton condensates, showing the (purple) Gaussian spot and ring shaped pump profiles, (rainbow landscape) the corresponding potential landscape mapped out by the active exciton reservoir and (silver balls) the ballistically propagating polaritons (left) at the Gaussian pump site and (right) trapped within the centre of the annular (ring-shaped) pump profile. White arrows indicate the flow of polaritons.

interpreted as a particle in a finite box, where the allowed energy modes are comparable to Hermite-Gaussian modes [46, 47, 50], such that the lowest threshold mode has the highest gain from having the largest overlap with the exciton reservoir. The resulting condensate has a momentum around $k_{||} = 0$, such that the condensed state is not on the free LP dispersion, but rather within the U-shaped slope of the dispersion. If the optical trap is of high enough intensity, multiple energy modes can be occupied, such that the resulting condensate is given by the superposition of the condensed trap modes.

1.3 Interacting Polariton Condensates

When two optically pumped polariton condensates are brought together, the ballistically propagating polaritons expanding from each condensate centre interact and interference fringes form between them, as schematically depicted in Figure 1.9. These interference modes take the form of symmetric (bright fringe at centre) and antisymmetric (dark fringe at centre) modes, likened to the ferromagnetic (even parity) and antiferromagnetic (odd parity) states in classical magnetism [44]. As the distance between the two condensates is scanned, the coupling contributions cycle between a dominant odd and even parity mode [45], such that the relative phase difference between the condensate centres is 0 or π radians for a dominant even or odd parity coupling respectively.

As the condensate excitation profile is much smaller than the total size of the propagating condensate, the polariton density is very low away from the excitation site. Thus, polaritons no longer experience a strong repulsion and the cylindrically symmetric outflow of polaritons from a single condensate centre can be analytically

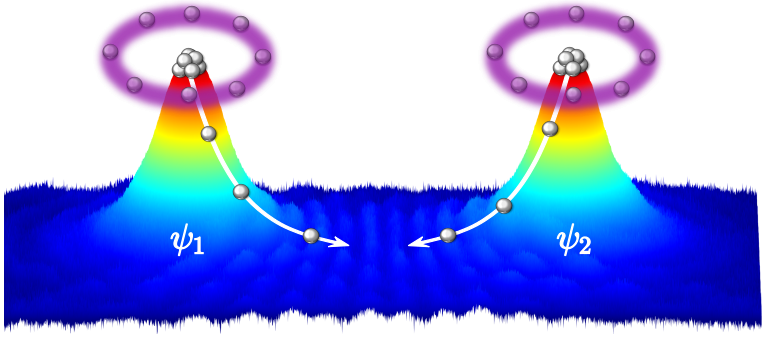

FIGURE 1.9: Schematic to show the dissipative coupling mechanism between two optically trapped polariton condensates. The two condensates, labelled ψ_1 and ψ_2, optically trapped by annular pumping profiles (shown by purple rings) dissipate polaritons (shown by silver balls) which ballistically propagate away from the condensate centres and interfere with the neighbouring condensate. The superposition of ψ_1 and ψ_2 leads to interference fringes as a result of this dissipative coupling mechanism. The 3D real-space profile is taken from Figure 3.2(a).

described by the 0-order Hankel function of the first kind[2] $\psi_n(r) = H_0^{(1)}(k_c r)$ [53], such that the coupling strength J_{nm} between a pair of polariton condensates n and m is described by the Bessel function of the first kind[2] dependent on the product of condensate separation distance d_{nm} and complex outflow polariton wavenumber k_c [54]. The complex wavevector encompassing the real energy blue shift of the condensate from the LP branch and the imaginary gain from the confinement potential [53], leads to a complex inter-condensate coupling strength where positive J_{nm} corresponds to purely ferromagnetic dissipative coupling and negative J_{nm} to purely antiferromagnetic dissipative coupling, such that if a system of condensates are ferromagnetically coupled to nearest neighbours, the condensates will arrange to have the same phase. Inversely, if antiferromagnetically coupled, the neighbouring condensates will not have the same phase where, depending on the connectivity, a non-trivial frustrated state can occcur [44].

As the polaritons ballistically propagate down the potential landscape mapped out by the cloud of hot excitons to an energy minimum, the relative phase of the resulting network of M condensates minimises the energy of the XY Hamiltonian given by [54, 55, 56, 57],

$$H_{XY} = -\sum_{n=1,n<m}^{N} J_{nm}\cos(\theta_n - \theta_m) \tag{1.39}$$

where θ_n is the phase of the n^{th} condensate centre. The minimised solution of the XY Hamiltonian is given by the condensate state with a phase configuration that carries the highest number of particles (N_0 is maximised, as discussed in section 1.2), where in order to reach the global XY minimum value, all condensates must have the same energy and polariton density. This is achieved through gain feedback, where the optical pump intensity exciting each condensate is adjusted in order to balance the intensities of all the condensates in the system [56]. This technique is discussed further, and numerically implemented in subsection 5.4.3.

Maximising the particle number leads to the minimisation of the XY Hamiltonian following on from the definition of the maximum particle number in real-space or Fourier space [44, 54]:

$$N = \int |\tilde{\Psi}(\mathbf{r})|^2 d^2\mathbf{r} = \frac{1}{(2\pi)^2}\int |\hat{\Psi}(\mathbf{k})|^2 d^2\mathbf{k} \tag{1.40}$$

[2]The Bessel function is given by the solutions of the Bessel equation: $x^2y'' + xy' + (x^2 - a^2)y = 0$. The solutions to which can take two forms. The first kind, denoted $J_a(x)$, is finite at the origin ($x = 0$) for $a \in \mathbb{Z}^+$, or diverges for negative non-integers of a. The second kind, denoted $Y_a(x)$, has a singularity at $x = 0$. The Hankel function is given by the a linear summation of the Bessel function of the first and second kinds, where the Hankel function of the first and second kinds are respectively given by $H_a^{(1,2)}(x) = \underbrace{J_a(x)}_{\text{Real}} \pm \underbrace{iY_a(x)}_{\text{Imaginary}}$.

where $\tilde{\Psi}(\mathbf{r})$ is the total condensate wavefunction in real-space and the hat ($\hat{}$) denotes the Fourier transform. In the case of M condensates located at $\mathbf{r} = \mathbf{r}_n$, $\tilde{\Psi}(r)$ can be approximately described by the sum of the individual condensate wavefunctions $\psi_n(\mathbf{r})$ with phase θ_n at the condensate centres,

$$\tilde{\Psi}(\mathbf{r}) = \sum_{n=1}^{M} \psi_n(\mathbf{r} - \mathbf{r}_n) e^{i\theta_n}. \tag{1.41}$$

All condensates are continuously pumped and produce a radial outflow of polaritons from the condensate centres at $\mathbf{r}_n$, where constructive and destructive interference of propagating polaritons results in interference fringes between the condensate centres, visible in real-space and Fourier-space. By writing the separation distance between any two condensates as $\mathbf{d}_{nm} = \mathbf{r}_m - \mathbf{r}_n$ with a relative phase difference $\theta_{nm} = \theta_m - \theta_n$, the total number of polaritons is then given by:

$$N = \frac{1}{(2\pi)^2} \int \sum_{n=1}^{M} |\hat{\psi}_n(\mathbf{k})|^2 + \sum_{n<m=1}^{M} \hat{\psi}_n^* \cdot \hat{\psi}_m e^{i(\mathbf{k}\cdot\mathbf{d}_{nm} + \theta_{nm})} d^2\mathbf{k} \tag{1.42}$$

$$= \sum_{n=1}^{M} N_n + \frac{1}{(2\pi)^2} \int \sum_{n<m=1}^{M} \hat{\psi}_n^* \cdot \hat{\psi}_m e^{i(\mathbf{k}\cdot\mathbf{d}_{nm} + \theta_{nm})} d^2\mathbf{k} \tag{1.43}$$

where N_n is the total number of polaritons in a bare un-coupled condensate ψ_n, and the second term corresponds to the polaritons in the interference fringes. Assuming that $\psi_n(\mathbf{r})$ is cylindrically symmetric, we can describe the complex outflow of polaritons from the condensate centres using the 0-order Hankel function [53]. The corresponding Fourier-space wavefunction (which is also cylindrically symmetric) can then be written as $\hat{\psi}_n(\mathbf{k}) = |\hat{\psi}_n(k)|e^{i\phi_n(k)}$ where $\hat{\psi}_n(k) = 2\pi \int_0^\infty \psi_n(r - r_n) e^{i\theta_n} J_0(kr_n) r dr$ [44, 54], then the total number of polaritons becomes:

$$N = \sum_{n=1}^{M} N_n + \sum_{n<m=1}^{M} \frac{1}{\pi} \int_0^\infty |\hat{\psi}_n^*(k) \cdot \hat{\psi}_m(k)| J_0(k d_{nm}) k \cos(\theta_{nm} + \phi_{nm}) dk. \tag{1.44}$$

Here, J_0 is the Bessel function of the first kind and $\phi_{nm} = \phi_m - \phi_n$ is the k-dependent phase difference between $\hat{\psi}_{n,m}$. In the limit of equally pumped condensates, $\hat{\psi}_n = \hat{\psi}_m \to \hat{\psi}$, this can be simplified further to give:

$$N = MN_0 + \sum_{n<m=1}^{M} \underbrace{\frac{1}{\pi} \int_0^\infty |\hat{\psi}|^2 J_0(k d_{nm}) k dk}_{J_{nm}} \cos(\theta_{nm}) \tag{1.45}$$

which shows that the state containing the maximum number of particles corresponds to the XY Hamiltonian ground state [54].

By assuming that all condensates have the same natural frequency and the energy line-width of the system is infinitesimal such that $|\hat{\psi}|^2 \simeq k_c|\hat{\psi}(k_c)|^2\delta(k-k_c)$, the coupling strength J_{nm} between condensates $\psi_{n,m}$ follows the Bessel function with $J_{nm} \simeq \frac{k_c|\hat{\psi}(k_c)|^2}{\pi} J_0(k_c d_{nm})$ when solved analytically [44, 54]. This assumption removes the integral in Equation 1.45:

$$N = MN_0 + \sum_{n<m=1}^{M} \frac{k_c|\hat{\psi}(k_c)|^2}{\pi} J_0(k_c d_{nm}) \cos(\theta_{nm}). \tag{1.46}$$

As the separation distance between two optically pumped condensates is scanned, the spectral weight of an even and odd parity modes oscillates, where each have a distinct unique energy (see Figure 3 in [45]). By the above definition, the minimisation of the XY Hamiltonian is achieved through a system of single-energy condensate interactions, which corresponds to a purely imaginary inter-condensate coupling strength [45]. However, the separation distances corresponding to single energy states are not equal in energy, thus a system with grater than two optically pumped coupled condensates does not in general minimise the XY Hamiltonian. Luckily we have not reached a dead end as this dilemma is tackled in the work of chapter 3 (and published in [2]).

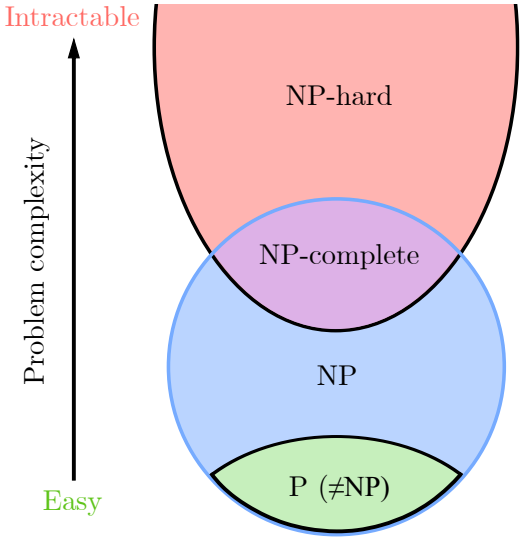

FIGURE 1.10: Schematic to show the different classes of computational complexity, where P and NP-complete are subsets at opposite ends of the complexity spectrum of the NP class (shown by the blue ring), and NP-hard is at least as complex as NP-complete, where the upper limit corresponds to intractable problems. Note that in general, it is accepted that P≠NP.

1.4 Computational Complexity

The complexity of computational problems is measured by its dependence on time compared to the size of a problem or the number of operations required to solve it. Starting at the simplest end of the spectrum building upwards, this dependence could be linear, quadratic, higher order polynomial, exponential or even factorial in time as the problem grows in size. At the extreme complex end of the spectrum lies the computationally intractable problems, which cannot be tackled (or an algorithm cannot be applied) in an efficient way in order to find a solution. It is for this reason that there is a keen interest among many scientific disciplines to seek out heuristic algorithms to solve complex problems in a reasonable timescale, whereby heuristic solvers use a practical method to approximate solutions through the inherent physical property of the system - for example, the network of coupled condensates minimising the XY Hamiltonian.

The complexity class P corresponds to the problems for which there exists a polynomial time algorithm for finding a solution. If there exists a polynomial time algorithm to verify a solution to a problem with binary decision variables (i.e. "yes" or "no" answers), but not solve it, then it belongs to the non-deterministic polynomial-time class, NP. It is generally believed that P$\neq$NP, however this still remains an unsolved problem. The hardest set of problems that belong to NP are labelled as NP-complete, for which it's possible to reduce any NP-complete problem to another NP problem in polynomial time, such that if a deterministic polynomial time algorithm exists to solve an NP-complete problem, then every NP class problem can be solved in polynomial time.

NP-hard is used to describe the set of problems that are at least as hard as the NP-complete class, where instead of a simple binary result, the solution takes a specific value. For example, the task of answering "is the XY ground state of this condensate network less than -3 (in arbitrary units of energy)?" is NP-complete, but "what is the XY ground state of this polariton graph" is NP-hard. A diagram of complexity classes is shown in Figure 1.10.

Chapter 2

Techniques in Simulation and Experiment

2.1 Numerical Modelling

At low temperatures, the polariton condensate contains thousands of weakly interacting polaritons where the global energy is described by the Hamiltonian containing the kinetic and potential energy of every polariton, plus the interactions with every other polariton on the system. It is impossible to analytically solve the individual polariton energies in the system. In the cold temperature limit $T \to 0$, all particles are assumed to be in the ground state, i.e. the condensate, such that a mean field approximation (system average) can be applied. This approximation allows us to describe all the polaritons in a coherent quantum state by a single wave, known as the order parameter. This treatment results in a differential equation known as the generalised Gross-Pitaevskii equation (GPE) or nonlinear Schrödinger equation, which through numerical integration can be used to simulate the dynamics of polariton condensates.

For over 70 years, this model has existed where the equation was first proposed by Vitaly Ginzburg and Lev Landau in 1950 in order to describe type-I semiconductors without having to probe their microscopic properties. As such it was named the complex Ginzberg-Landau equation (cGLE) [58]. The superfluid counterpart was first proposed in 1961 the form of the GPE [59, 60]. Note that the cGLE and GPE give analogous results when adapted for driven-dissipative polariton condensate systems [61]. In order to extract steady state solutions of the polariton condensate system, a quasi-equilibrium between the pumping rate and polariton decay rate must be maintained. The GPE only considers particles within the condensate and so is not able to simulate the phase transition of polaritons into the condensate [62, 63].

2.1.1 Gross-Pitaevskii Equation

A dilute weakly interacting Bose gas can be described by the Hamiltonian [62, 63, 64, 65]

$$\hat{H} = \int \hat{\Psi}^\dagger(\mathbf{r},t)\hat{H}_0(\mathbf{r})\hat{\Psi}(\mathbf{r},t)d\mathbf{r} + \frac{1}{2}\int\int \hat{\Psi}^\dagger(\mathbf{r},t)\hat{\Psi}^\dagger(\mathbf{r}',t)\hat{V}_{int}(\mathbf{r}-\mathbf{r}')\hat{\Psi}(\mathbf{r}',t)\hat{\Psi}(\mathbf{r},t)d\mathbf{r}d\mathbf{r}' \tag{2.1}$$

which is written in the occupation number representation of the Schrödinger picture[1], exploiting the indistinguishability of the particles [65]. The Bose field operators $\hat{\Psi}(\mathbf{r}',t)$ and $\hat{\Psi}^\dagger(\mathbf{r}',t)$ represent the creation and annihilation operators of the field at some position $\mathbf{r}$ and time t and the operator $\hat{H}_0(\mathbf{r})$ represents the single-particle Hamiltonian of a non-interacting particle following $\hat{H}_0(\mathbf{r}) = -\frac{\hbar^2\nabla^2}{2m_p} + \hat{V}_{ext}(\mathbf{r})$, where m_p is the particle mass and $\hat{V}_{ext}(\mathbf{r})$ is the external confining potential of the system. $\hat{V}_{int}(\mathbf{r}-\mathbf{r}')$ is the two-body inter-particle potential, assuming that the likelihood of a collision between more than two particles is negligible. The factor of $\frac{1}{2}$ at the start of the second ensures that each inter-particle interaction is only counted once.

At the low temperature limit in a weakly interacting Bose gas, the two-body potential can be replaced by a perfectly elastic collision term [64, 65]:

$$\hat{V}_{int}(\mathbf{r}-\mathbf{r}') = \alpha\delta(\mathbf{r}-\mathbf{r}') \tag{2.2}$$

where α is the effective interaction strength between two particles given by the scattering energy within the condensate [62] and δ is the Kronecker-Delta function such that binary collisions occur at $\mathbf{r} = \mathbf{r}'$. The Hamiltonian Equation 2.1 then follows:

$$\hat{H} = \int \hat{\Psi}^\dagger(\mathbf{r},t)\hat{H}_0(\mathbf{r})\hat{\Psi}(\mathbf{r},t)d\mathbf{r} + \frac{\alpha}{2}\int \hat{\Psi}^\dagger(\mathbf{r},t)\hat{\Psi}^\dagger(\mathbf{r},t)\hat{\Psi}(\mathbf{r},t)\hat{\Psi}(\mathbf{r},t)d\mathbf{r}. \tag{2.3}$$

The system dynamics can be explored through the standard commutation relation of the Hamiltonian operator with a general operator $\hat{O}$, where the general equation of motion in the Heisenberg picture[1] obeys,

$$i\hbar\frac{\partial\hat{O}}{\partial t} = [\hat{O}(t),\hat{H}]. \tag{2.4}$$

[1] Two formulations of quantum mechanical states considered here are called the "Schödinger representation" (or picture) and the "Heisenberg representation" (or picture). In the Schrödinger picture, time evolution exists within the state vector $|\psi(t)\rangle$, where some operator $\hat{\Omega}$ has no dependence on time. In contrast, the Heisenberg picture assumes that the state vector is independent of time, where the time evolution is solely contained by the operator. Here, time evolution can be considered as a rotation in the Hilbert space due to a unitary time evolution operator $\hat{U}(t) = \sum_j |E_j\rangle\langle E_j|e^{-iE_jt/\hbar}$, where $|E_j\rangle$ is the eigenvector of state j with an eigenenergy of E_j. If both the the state vectors and the operators are both time dependent, then the system is being analysed in the "interaction representation" [65]

Equation 2.4 can be expanded with the creation Bose field operator, and by using the commutation relations $[\hat{\Psi}(\mathbf{r},t),\hat{\Psi}^{\dagger}(\mathbf{r}',t)]=\delta(\mathbf{r}-\mathbf{r}')$ this becomes [65]:

$$i\hbar\frac{d\hat{\Psi}(\mathbf{r},t)}{dt}=[\hat{\Psi}(\mathbf{r},t),\hat{H}(\mathbf{r}')]=\hat{\Psi}(\mathbf{r},t)\hat{H}(\mathbf{r}')-\hat{H}(\mathbf{r}')\hat{\Psi}(\mathbf{r},t) \tag{2.5}$$

$$\begin{aligned}&=\hat{\Psi}(\mathbf{r})\left(\int\hat{\Psi}^{\dagger}(\mathbf{r}')\hat{H}_0(\mathbf{r}')\hat{\Psi}(\mathbf{r}')d\mathbf{r}'\right)-\left(\int\hat{\Psi}^{\dagger}(\mathbf{r}')\hat{H}_0(\mathbf{r}')\hat{\Psi}(\mathbf{r}')d\mathbf{r}'\right)\hat{\Psi}(\mathbf{r})\\&+\frac{\alpha}{2}\left[\hat{\Psi}(\mathbf{r})\left(\int\hat{\Psi}^{\dagger}(\mathbf{r}')\hat{\Psi}^{\dagger}(\mathbf{r}')\hat{\Psi}(\mathbf{r}')\hat{\Psi}(\mathbf{r}')d\mathbf{r}'\right)-\left(\int\hat{\Psi}^{\dagger}(\mathbf{r}')\hat{\Psi}^{\dagger}(\mathbf{r}')\hat{\Psi}(\mathbf{r}')\hat{\Psi}(\mathbf{r}')d\mathbf{r}'\right)\hat{\Psi}(\mathbf{r})\right]\end{aligned} \tag{2.6}$$

$$=\int[\hat{\Psi}(\mathbf{r}),\hat{\Psi}^{\dagger}(\mathbf{r}')]\hat{H}_0(\mathbf{r}')\hat{\Psi}(\mathbf{r}')d\mathbf{r}'+\frac{\alpha}{2}\int[\hat{\Psi}(\mathbf{r}),\hat{\Psi}^{\dagger}(\mathbf{r}')\hat{\Psi}^{\dagger}(\mathbf{r}')]\hat{\Psi}(\mathbf{r}')\hat{\Psi}(\mathbf{r}')d\mathbf{r}' \tag{2.7}$$

$$i\hbar\frac{d\hat{\Psi}(\mathbf{r},t)}{dt}=\left(\hat{H}_0(\mathbf{r})+\alpha\left|\hat{\Psi}(\mathbf{r},t)\right|^2\right)\hat{\Psi}(\mathbf{r},t). \tag{2.8}$$

Note that the time dependence is dropped in the interim equations for compactness and readability only. It is now that we consider the definition of the creation (annihilation) Bose field operator as $\hat{\Psi}^{(\dagger)}(\mathbf{r})=\sum_i\phi_i^{(*)}(\mathbf{r})\hat{a}_i^{(\dagger)}$, where ϕ_i are the single particle states and $\hat{a}_i^{(\dagger)}$ is the creation (annihilation) operator of a single particle. In other words, the field operator can be split into the condensed particles and thermal fluctuations (non-condensed particles) following,

$$\hat{\Psi}(\mathbf{r},t)=\hat{\psi}(\mathbf{r},t)+\hat{\delta}(\mathbf{r},t) \tag{2.9}$$

where $\hat{\psi}(\mathbf{r},t)=\phi_0(\mathbf{r},t)\hat{a}_0$ is the condensate operator corresponding to the particles in the condensed ground state of the system and $\hat{\delta}(\mathbf{r},t)=\sum_{i\neq0}\phi_i(\mathbf{r},t)\hat{a}_i$ is the non-condensed particle operator. In the low temperature limit for a system with many particles, most particles are assumed to be in the condensed state, i.e. $N_0\simeq N$, such that the creation and annihilation of a particle has no effect on the system (known as the "Bogoliubov approximation" [66]) which implies that that the states $|N\rangle,|N-1\rangle,|N+1\rangle$ are equivalent. This assumption allows us to perform the Bogoliubov replacement of $\hat{a}_0\simeq\sqrt{N_0}$ [1], which replaces the condensate operator $\hat{\psi}(\mathbf{r},t)$ with the complex number $\psi(\mathbf{r},t)=\sqrt{N}\phi_0(\mathbf{r},t)$ [65]. As such, all operator dependence of the Bose field operator is governed by the fluctuation term $\hat{\delta}(\mathbf{r},t)$.

We can substitute $\hat{\Psi}(\mathbf{r},t)=\sqrt{N}\phi_0(\mathbf{r},t)+\hat{\delta}(\mathbf{r},t)$ into Equation 2.8, where in the $T=0$ limit all the particles are in the condensate such that $\hat{\delta}(\mathbf{r},t)=\hat{\delta}^{\dagger}(\mathbf{r},t)=0$ and

$\hat{\Psi}^{(\dagger)}(\mathbf{r},t) \rightarrow \psi^{(*)}(\mathbf{r},t)$. This leads to the Gross-Pitaevskii equation (GPE), describing the mean-field dynamics of the condensed particles:

$$i\hbar\frac{\partial\psi(\mathbf{r},t)}{\partial t} = \left[-\frac{\hbar^2\nabla^2}{2m} + \hat{V}_{ext}(\mathbf{r},t) + \alpha|\psi(\mathbf{r},t)|^2\right]\psi(\mathbf{r},t). \tag{2.10}$$

In order to simulate the dynamics of polariton condensates, the GPE has been adapted to better match the system's open-dissipative nature, due to the polariton's finite lifetime, as continuous pumping is required in order to reach a steady state. This generalised GPE was first adapted in 2007 to include the continuous pumping and decay, as well as coupling to a pairs of rate equations describing the active and inactive reservoirs of uncondensed particles that feed the condensate [67]:

$$i\hbar\frac{\partial\psi}{\partial t} = \left[-\frac{\hbar^2\nabla^2}{2m} + \hat{V}_{ext}(\mathbf{r}) + G(n_A+n_I) + \alpha|\psi|^2 + \frac{i\hbar}{2}(Rn_A-\gamma)\right]\psi(\mathbf{r},t), \tag{2.11}$$

$$\frac{\partial n_A}{\partial t} = -(\Gamma_A + R|\psi|^2)n_A + Wn_I, \tag{2.12}$$

$$\frac{\partial n_I}{\partial t} = -(\Gamma_I + W)n_I + P(\mathbf{r},t). \tag{2.13}$$

Here $n_A(\mathbf{r},t)$ is reservoir of active exciton that experience bosonic stimulated scattering into the condensate. These excitons have low momentum and are inside the light cone of the cavity, thus couple to light and form polaritons. The active reservoir is maintained by $n_I(\mathbf{r},t)$, the inactive exciton reservoir and consist of a cloud of higher momentum excitons that are outside the lightcone so do not couple to light, hence "inactive". These excitons are still classified as bright excitons due to their projected spin $m_j = \pm 1$ and are still physically able to couple with light when relaxed to a lower momentum. Additionally, G is the polariton-reservoir interaction strength, R is the rate of stimulated scattering of polaritons in to the condensate from n_A, γ is the polariton decay rate, $\Gamma_{A,I}$ are radiative and nonradiative exciton reservoir decay rates, W is the conversion rate between inactive and active reservoir excitons, and $P(\mathbf{r},t)$ is the non-resonant pump profile that both feeds and traps the condensate.

In polaritonics, $\hat{V}_{ext}(\mathbf{r})$ represents any potential patterning on the microcavity, but will be neglected for the remained of this thesis where only plain cavities are studied. The condensate wavefunction ψ, plus both of the exciton reservoirs $n_{A,I}$, depend on position and time, which have been dropped in the above equations for compactness. Due to the confinement of polaritons in the z-direction of the microcavity, the position vector r refers to the x, y-coordinates of in-plane location to the microcavity.

To model the condensate dynamics under a specific pumping regime $P(\mathbf{r},t)$, Equations 2.11-2.13 are numerically integrated in time using a linear multistep method. The

polariton occupation number of the condensate at a given time is defined as $N = \int |\psi(\mathbf{r},t)|^2 d^2\mathbf{r}$. At the start of the simulation $N \simeq 0$ and over some integration period this should grow until the system reaches a quasi-equilibrium of polariton creation and decay. At which point, $\psi(\mathbf{r},t)$ represents a steady state solution of the condensate system. However, if the pumping profile does not supply sufficient gain to the system, a condensate will not form as the polariton density is below condensation threshold, where the threshold for condensation is given by the pump intensity that creates a steady state condensate with an occupation number of 1.

2.1.1.1 Choosing the GPE Parameters

The parameters for the numerical integration of Equations 2.11-2.13 are chosen to match the properties of the 2λ microcavity used in the corresponding experiments [3]. Using the best of our current understanding of the microcavity system, the parameters are enumerated with $G = 2g|X|^2$ and $\alpha = g|X|^4$, where g is the exciton-exciton dipole interaction strength, which is typically $g \simeq 1$ μeV μm^2 in GaAs-type quantum wells. The polariton mass it taken to be $m_p = 5.64{\times}10^{-5} m_0 \simeq 0.288$ meV ps^2, where m_0 is the mass of a free electron. As $|X|^2$ is the excitonic Hopfield coefficient of polaritons at the bottom of the LP branch, it depends on the cavity detuning which is matched to the experimental value. In this thesis, the experimental range of cavity detuning is -5 meV to -3.2 meV. From these values, $|X|^2$ can be calculated following Equation 1.23, using the sample's Rabi splitting of $2\hbar\Omega = 8$ meV [3]. The polariton lifetime follows the cavity lifetime of the sample, where with a cavity reflectivity $> 99.9\%$ [54], we use $\frac{1}{\gamma} = 5.5$ ps [3, 68]. Due to the photonic component of the polariton, the quasi-particles undergo fast thermalisation and decay from the condensate to the exciton background at a rate of γ [53]. However, the optically inactive exciton recombination rate is taken to be much smaller than the condensate decay rate, with $\Gamma_I = 0.01\gamma$. The rate of optical coupling of the nonradiative exciton reservoir, W, and the rate of stimulated scattering of radiative excitons to the condensate, R, are not directly measurable, but are calculated through fitting the GPE results to experimental data, where $R < W < \gamma$. As the understanding of the exact values of these parameters is continually improving, some simulations in this thesis use slightly different parameter values. However, these minor changes do not affect the general results of the condensate system.

2.1.2 Stuart-Landau Model

In the case of many interacting polariton condensates, equations 2.11-2.13 can be simplified and generalised to a discretised version fo the driven-dissipative GPE that does not depend on complicated degrees of freedom. Instead, only the weak nonlinear effects on the condensate saturation are considered assuming that the characteristic

reservoir lifetimes are much shorter that those of the condensate [69]. Under these assumption, the condensate wavefunction can be written as $\psi(\mathbf{r},t) = \sum_n \varphi_n(\mathbf{r})\psi_n(t)$, where $\varphi_n(\mathbf{r})$ vary little from the particle interactions, such that each condensate is described by a complex single point value that varies over time and equation n is coupled to each other equation m by coupling strength J_{nm}.

This model describes a Stuart-Landau network [70, 71, 72] of dissipative non-linear coupled oscillators $\psi_n(t)$,

$$\frac{d\psi_n}{dt} = \left[P_n - i\omega_n - (R_s + ig)|\psi_n|^2\right]\psi_n + \sum_{m=1}^{N} J_{nm}\psi_m \tag{2.14}$$

where P_n denotes the net gain of each oscillator, e.g. for polariton condensates this is given by the non-resonant pumping of the microcavity at each condensate centre, ω_n is the natural frequency of oscillator n, R_s is the particle saturation rate and g is the real energy shift due to the nonlinear interactions of the system, such that $\alpha = g - iR_s$ in polariton condensate systems corresponds to the polariton-polariton interaction strength. J_{nm} is the coupling strength between each pair of oscillators, which for polaritons is a function of the propagating particle momentum and condensate separation distance [54].

The Stuart-Landau model describes a plethora of nonlinear oscillator networks (not only polariton condensate systems) and can be derived from the normal form of the Hopf bifurcation [73, 74]. The Hopf bifurcation describes a dynamical transition in nonlinear oscillating systems where the stable solutions transition from a fixed point to a limit cycle, or equivalently, the eigenvalues cross the imaginary axis. For example, if we consider a nonlinear oscillating system in polar coordinates with the following equations of motion:

$$\dot{r} = r(\mu - r^2) \tag{2.15}$$

$$\dot{\theta} = \omega + br^2 \tag{2.16}$$

where μ, ω and b are free parameters. From the Jacobian matrix of the Cartesian form of these equations, we can easily calculate that the eigenvalues are $\lambda = \mu \pm i\omega$. Clearly, $r = 0$ is a fixed point solution of this system and marks the origin of the dynamics. If $\mu < 0$, then $r = 0$ is a stable attracting fixed point and all trajectories in the system will spiral towards it (Figure 2.1(a)). However if $\mu > 0$, then the fixed point is unstable and the trajectories instead converge to the limit cycle centred at $r = 0$ with an amplitude of $r = \sqrt{\mu}$ (Figure 2.1(b)). For small μ, this limit cycle will have an oscillation period close to $\frac{2\pi}{\omega}$. This drastic change in the system dynamics is labelled as a Hopf bifurcation, where the bifurcation point in this example is at $\mu = 0$. If we instead look at the eigenvalue picture of this transition (Figure 2.1(c)), we can see that

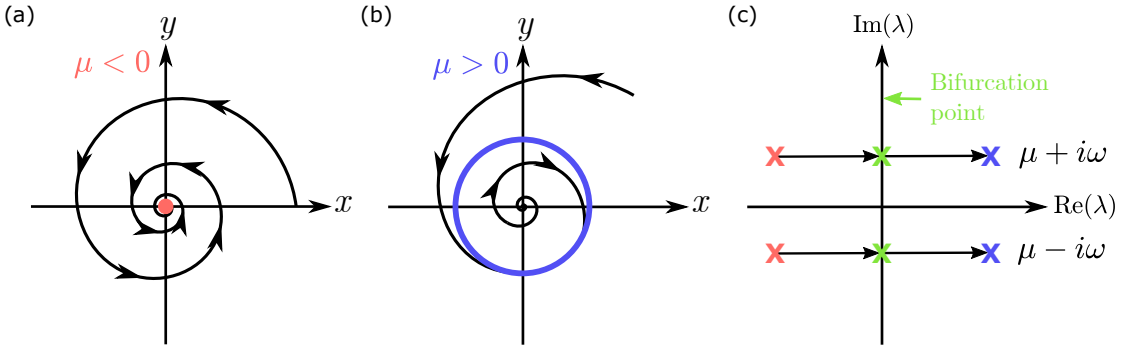

FIGURE 2.1: Figure to show (a) $\mu < 0$ and (b) $\mu > 0$, corresponding to a stable fixed point (unstable limit cycle) and unstable fixed point (stable limit cycle) respectively. The transition between these two behaviours is called the "Hopf bifurcation". The eigenvalues for $\mu < 0$ and $\mu > 0$ are shown in the complex plane by the red and blue crosses in (c) respectively, which uniformly approach and cross the imaginary axis in turn reaching the bifurcation point at $\mu = 0$ (green crosses) where the bifurcation occurs.

as μ is increased from a negative to positive value (red crosses to blue crosses), the two eigenvalues symmetrically approach and cross the imaginary axis, where the point at which they cross the imaginary axis marks the bifurcation point (green crosses with $\mu = 0$), in turn shifting the system trajectory from a real focus to a closed limit cycle [75, 76].

For the case of a network of coupled oscillators, the dynamics follow the general form:

$$\dot{x}_n = f_n(x_n) + \epsilon_n g_n(x_1, \ldots, x_N, \epsilon, t), \quad n = 1, 2, \ldots, N, \tag{2.17}$$

where N is the number of oscillators, x_n is the state of the n^{th} oscillators, making $\mathbf{x} = \{x_1, x_2, \ldots, x_N\}$ the state vector of the whole network. Here, f_n is a smooth function describing the dynamics of uncoupled oscillator n, but now we include the coupling strength and dynamical interactions with the other oscillators in the system with the addition of ϵ_n and smooth function g_n respectively.

When approaching the bifurcation point, the combination of functions f_j and g_n for each oscillator can be approximated using a pair of equations [73, 74, 77]:

$$\dot{x}_n = a_n x_n - b_n y_n \mp (c_n x_n - d_n y_n)(x_n^2 + y_n^2) + \sum_{m=1}^{N} J_{nm} x_m \tag{2.18}$$

$$\dot{y}_n = a_n y_n + b_n x_n \mp (c_n y_n + d_n x_n)(x_n^2 + y_n^2) + \sum_{m=1}^{N} J_{nm} y_m \tag{2.19}$$

where the last term in each equation corresponds to g_n and all prior terms to f_n. Here, J_{nm} is the coupling strength between oscillators n and m. These equations follow the

Jacobian matrix

$$A = \begin{pmatrix} a & -b \\ b & a \end{pmatrix} \tag{2.20}$$

with eigenvalues $\lambda_{1,2} = a \pm ib$, similarly to the example of Equations 2.15–2.16. Here, a_j, b_j, c_j, d_j are all nonnegative coefficients. The $\mp$ symbols determine whether the bifurcation is supercritical (stable limit cycle, unstable fixed point) or subcritical (unstable limit cycle, stable fixed point) respectively. In this thesis, the networks of dissipative coupled oscillators (such as polariton condensates) undergo a supercritical bifurcation, and from now on only the negative sign will be considered. By introducing complex parameter $z = x + iy = \rho e^{i\theta}$, we can re-write Equation 2.18 and Equation 2.19 as a single complex function,

$$\dot{z}_n = \Big[(a_n + ib_n) - (c_n + id_n)|z_n|^2\Big] z_n + \sum_{m=1}^{N} J_{nm} z_m, \tag{2.21}$$

Clearly Equation 2.21 is equivalent to Equation 2.14 with $a_n \to P_n$, $b_n \to \omega_n$, $c_n \to R_s$ and $d_n \to g$. In polar coordinates this becomes,

$$\dot{\rho}_n = (P_n - R_s|\rho_n|^2)\rho_n + \sum_{m=1}^{N} J_{nm}\rho_m\rho_n \cos(\theta_m - \theta_n) \tag{2.22}$$

$$\dot{\theta}_n = \omega_n - g|\rho_n|^2 + \sum_{m=1}^{N} J_{nm}\frac{\rho_m}{\rho_n}\sin(\theta_m - \theta_n). \tag{2.23}$$

And so, the Stuart-Landau equation is derived from the normal form of the Hopf bifurcation. Interestingly, the phase dynamics fo the Stuart-Landau oscillators (Equation 2.23) is the generalisation of the well-known Kuramoto model when $\rho_n = \rho_m = \rho$ (i.e. oscillator densities are uniform) and Equation 2.22 have reached a steady state.

It is worth noting that the Stuart-Landau model can always be scaled in time and amplitude in order to reduce the equation by up to two parameters. This is beneficial when numerically simulating the Stuart-Landau equation over a large parameter space, as removing two parameters drastically reduces the number of simulations that need to be run. For example, with the scaling of $t \mapsto \tau / P_n$ and $\psi \mapsto \tilde{\psi}\sqrt{P_n/R_s}$, parameters R_s and P_n can be removed from the equation with the additional redefinitions $\tilde{\omega}_n \mapsto \omega_n/P_n$, $\tilde{g} \mapsto g/R_s$ and $\tilde{J}_{nm} \mapsto J_{nm}/P_n$, to give,

$$\dot{\tilde{\psi}}_n = [1 - i\tilde{\omega}_n - (1 + i\tilde{g})|\tilde{\psi}_n|^2]\tilde{\psi} + \sum_{m=1}^{N} \tilde{J}_{nm}\tilde{\psi}_m. \tag{2.24}$$

The Stuart-Landau model results into two classes of solutions, the stationary state with $\rho_n = 0$ (i.e. the trivial solution) and the oscillatory state with $\rho_n \neq 0$. In the case of polariton systems, the latter corresponds to above threshold condensates such that the particle number $N_n = \sum_n^N |\psi_n|^2 > 0$. If we consider just some uniform pumping parameter $P_n = P_m = P$ and coupling terms J_{nm} following,

$$\dot{\psi}_n = P\psi_n + \sum_{nm} J_{nm}\psi_m \tag{2.25}$$

then the network Hamiltonian is simply,

$$\hat{H} = P\mathbb{I} + \hat{J} \tag{2.26}$$

with $\mathbb{I}$ representing the $N \times N$ identity matrix and operator $\hat{J}$ describing the coupling matrix between all the oscillators. Let the eigenvalues of $\hat{J}$ be $\{\lambda_1, \lambda_2, \ldots, \lambda_N\}$, then the eigenvalues of $\hat{H}$ are simply $\{\lambda_1 + P, \lambda_2 + P, \ldots, \lambda_N + P\} = \{h_1, h_2, \ldots, h_N\}$.

If all $h_n < 0$, then the system is below condensation threshold ($P < P_{th}$), however P can be increased until one of the eigenvalues h_n becomes positive. At this point, $P = P_{th}$ and $\rho_n = 0$ is *not* the steady state, but instead the oscillatory state comes into play, characterised by a particle number $N = \sum_n |\psi_n|^2 > 0$. Additionally, we could consider $P_n \neq P_m$, where P is a row vector containing all P_n, which physically corresponds to non-uniform pumping across the condensates. This may be considered when balancing the condensate PL across a lattice or condensate network [56, 78].

2.2 Experiment

Before commencing this section, I would like to clarify that although I undertook the experimental work of [2], the optical setup was designed and built by former experimentalists of the Hybrid Photonics Group in Southampton. By the end of my first year as a PhD student, my research had become solely theoretical and I have not set foot in the laboratory since July 2019. This section sets out the fundamental aspect of the experimental work of this thesis, although this was not a key aspect of my PhD journey.

2.2.1 Sample

The microcavity used in the experimental work of this thesis has a $2\lambda_{Bragg}$ confinement length with a central confinement wavelength of $\lambda_{Bragg} = 854$ nm. The microcavity Q-factor is high enough ($\sim 1.2 \times 10^4$) to ensure that multiple absorbtions and emissions occur before the photon escapes, which is achieved through using 23 and

26 GaAs/AlAs DBR pairs at the top and bottom of the microcavity respectively. Due to the lattice constant mismatch between the two DBR materials, strain can build up during the growth process from the stacking of many DBR layers and can lead to defects in the sample structure. To avoid this, strain compensation is achieved by using GaAs/$AlAs_{0.98}P_{0.02}$ DBR layers, where the phosphorous doping compensates for the lattice constant mismatch. The cavity spacer contains three pairs of InGaAs QWs around the antinodes of the confined light, plus an additional QW at each of the outer confined nodes, and results in a Rabi splitting of 8 meV. This placing ensures that each QW produces excitons below the Mott transition density, but with many QWs a large population of excitons is achieved. This sample is described in detail in the work of Cilibrizzi et al. [3].

2.2.2 Beam Sculpting

Throughout the research in this thesis, the polariton condensate trapping geometries are controlled through non-resonant laser excitation (as described in subsection 1.2.4), in order to shape the hot exciton reservoir into a potential landscape following the incident laser geometry. Other than using an optical pump, the condensate confinement potential can also be mapped out using chemically etched pillars, strips and 2D lattices [79, 80, 81, 82, 83, 84], piezo electric acoustic lattices [85] or thin metal film deposition [86, 87]. However, the etching and metal films permanently fix the potential landscape so do not allow for the continuous arbitrary control of the trapping potential, and the acoustic excitation is restricted to confining condensate lattices. On the other hand, an optical pump is fully controllable and can map out any arbitrary confinement potential.

In 2D simulations of the condensate system, the pump profile can take any arbitrary shape dictated by $P(\mathbf{r}, t)$ in Equation 2.13. In experiment, this arbitrary control is achieved using a spatial light modulator (SLM). An SLM is a computer controlled device that can either modulate the amplitude or phase of an incident beam using a programmable translucent liquid crystal display (LCD) of reflective liquid crystals on silicon (LCOS). An amplitude modulating SLM masks the beam profile in transmission whereas phase modulating SLM imprints a specific phase pattern onto the wavefront in Fourier-space, which in turn gives full control of the real-space patterning without masking out a substantial portion of the beam intensity. As used in the experimental work of this thesis, a reflective SLM connects to a computer like any ordinary screen where each pixel is assigned an 8-bit grey level, corresponding to the voltage applied to the liquid crystal cell (which has a horizontal director axis). As the voltage is ramped from 0 V to V_{max}, the long-axis orientation of the liquid crystal molecules rotate from parallel to perpendicular to the screen surface (rotation in the x-z plane), in turn creating a varying optical thickness to incident light that is horizontally polarised

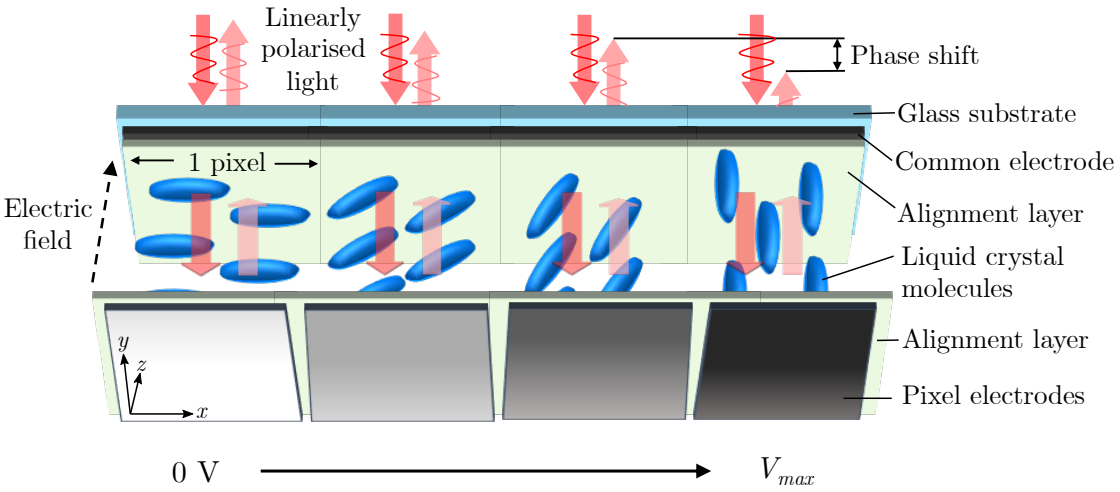

FIGURE 2.2: Schematic of an SLM, showing that as a voltage is applied to each pixel electrode between 0 volts and V_{max} volts, the liquid crystals rotate in to an angle in the plane of the electric field, relative to the horizontal plane of the pixels (x-z plane). This is achieved from inducing a variable-voltage electric field through the liquid crystal layer. The crystal rotation is proportional to the applied voltage, which in-turn controls the applied phase-shift of the reflected beam. Here, the darkness of the electrodes represents the magnitude of the applied voltage, the liquid crystals are shown by blue ovals, the incident beam to the SLM screen is shown in red and the reflected beam in a lighter shade of red. The height difference between the incident and reflected beam arrows at the top of the figure represents the phase shift applied to the beam due to the liquid crystal rotation. All components of the SLM follow the labelling on the right of the figure.

(linear polarisation parallel to the director axis), thus applying a phase delay to the reflected beam in 256 linear steps between 0 and 2π radians. This process is schematically depicted in Figure 2.2 [88]. The imprinted beam then diffracts off the SLM, such that the first-order diffraction is the highest intensity sculpted beam, and so the higher orders and zeroth-order diffracted (a.k.a. reflected) beams are blocked off with an iris.

2.2.2.1 Kinoform Calculation

Although the SLM in principle allows for complete arbitrary control of the pumping profile, in practice it is a complex task to calculate the exact phase map that needs to be imprinted onto the laser profile in order to achieve the desired spatial sculpting. The image that is displayed on the SLM screen to impose a specific phase map is called a kinoform, and this can be calculated using two possible methods.

More simple beam structures can be shaped using an analytically solvable kinoform, which consists of a single analytical solution or a sum of multiple solutions modulated between 0 and 2π. For example, applying a horizontal or vertical phase grating to a Gaussian laser beam will shift the beam in the vertical or horizontal direction respectively. So, a desired Gaussian beam geometry can be achieved through the

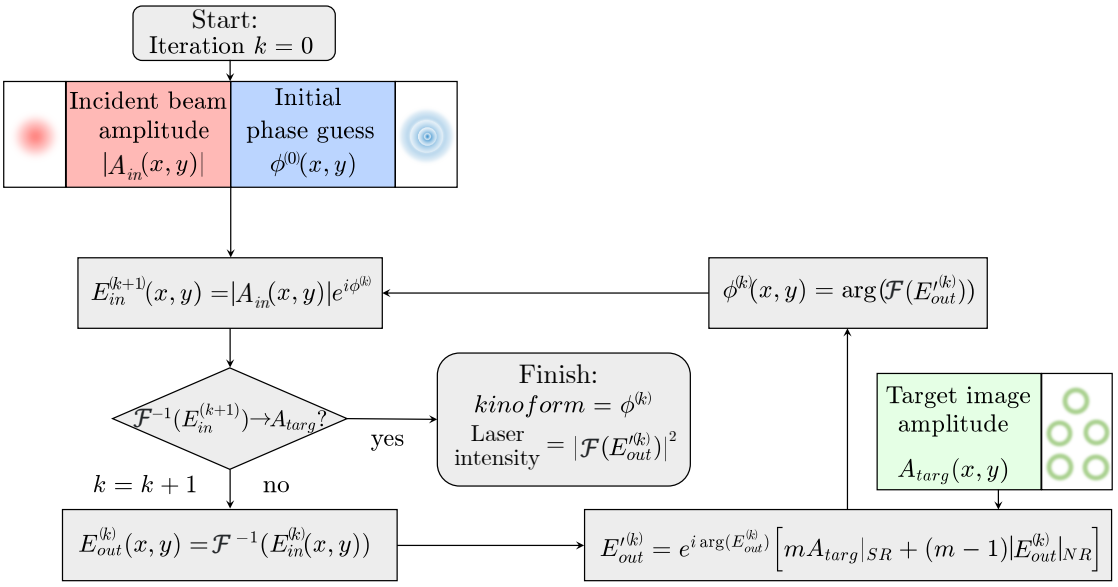

FIGURE 2.3: Flow chart showing the iterative steps of the MRAF algorithm. The loop is stopped when the real-space picture of the algorithmically calculated hologram image, $\mathcal{F}^{-1}(E_{in}^{(k+1)}(x,y))$, converges to the target image amplitude, $A_{targ}(x,y)$.

summation of linear gratings each corresponding to the steered beam location of the individual spot sites. Additionally, if a phase delay is radially applied from the centre of an incident Gaussian beam (i.e. a continuous-phase diffractive axicon), an annulus-shaped profile is sculpted in real-space, where the inverse of the radial phase period corresponds to the annulus diameter [89]. If the continuous-phase axicon is binarised to 0 and π radians phase delay, the resulting annulus is more uniform and symmetric in intensity. As analytical kinoform solutions can be combined, the summation of the axicon and the vertical gratings that horizontally displace the beam by differing amounts will shape a Gaussian laser beam into two spatially separated annuli. This exact kinoform was used in the experiments of chapter 3.

For more complex beam patterns, an iterative algorithm is used to approximate the kinoform based on the incident beam profile and a target image depicting the desired beam profile. The most commonly used approximation methods are the Gerchberg Saxton algorithm (GS), which was first developed for electron microscopy in 1971 [90], and the mixed-region amplitude freedom algorithm (MRAF), which uses the same approach as GS but by splitting the target image into a signal region (SR) (region of interest) and a noise region (NR) (the background) more complex profiles can be formed (albeit more slowly) [91]. In the MRAF technique, the weighting of the signal and noise regions in each loop of the iteration is controlled by the mixing parameter m, where by setting $m = 1$, MRAF makes an equivalent kinoform approximation to GS. For a target image that is not a simple array of Gaussian spots, the MRAF algorithm produces a smoother more uniform beam profile than the GS method, however the MRAF algorithm takes longer to converge to the target image and results in a lower optical efficiency. The detailed steps of the MRAF iterative algorithm are mapped out

as a flow chart in Figure 2.3, following the procedure discussed in [91]. The MRAF algorithm is the method used for creating the kinoform for the work in chapter 4, there the target laser profile was five annuli arranged into a house configuration, and in chapter 7 where the target image consisted of two spatially separated ellipses.

Additionally, first order Zernike polynomials are applied to both analytically and iteratively solved kinoforms to act as a grating in order to displace the first-order diffracted beam from the reflected zeroth-order beam.

2.2.2.2 Temporal Sculpting

The sample is sensitive to extreme heat and is prone to burning if a highly focussed laser is held on the sample surface for too long. In order to avoid such overheating, the continuous wave (CW) monomode laser with a narrow linewidth, which is used to excite the microcavity, is passed through an acousto-optic modulator (AOM). This chops the beam, creating a pulse at a repetition rate of 10 kHz and duty cycle of a few percent, thus creating a ≈ 1 µs pulse every 100 μs. These timescales are many orders of magnitude longer than the polariton lifetime and dynamics of the polariton system, and so the this excitation is still considered to be CW, although it is often classed as quasi-CW or quasi-pulsed.

2.2.2.3 Intensity Stabilisation

Due to the non-uniformities in the sample structure and the incident beam profile, plus any small misalignment of the optics, the calculated kinoform will never create condensates with the ideal relative intensities of the target image. As all project in this thesis that study multiple coupled condensates rely on the system to minimise the XY Hamiltonian, it is important that the network of condensates experimentally produced are equal in intensity and in energy. This is achieved through an intensity stabilisation procedure, whereby the pumping profile of each condensate is adjusted in order to compensate for any deviation between the relative integrated intensity of condensates and the target image pump sites. A new kinoform based on the adjusted target image is iteratively approximated and displayed on the SLM.

By repeating this intensity correction iteratively, it is possible to create a lattice of over 100 optically pumped polariton condensates with a relative standard deviation in intensity of less than 1% [78].

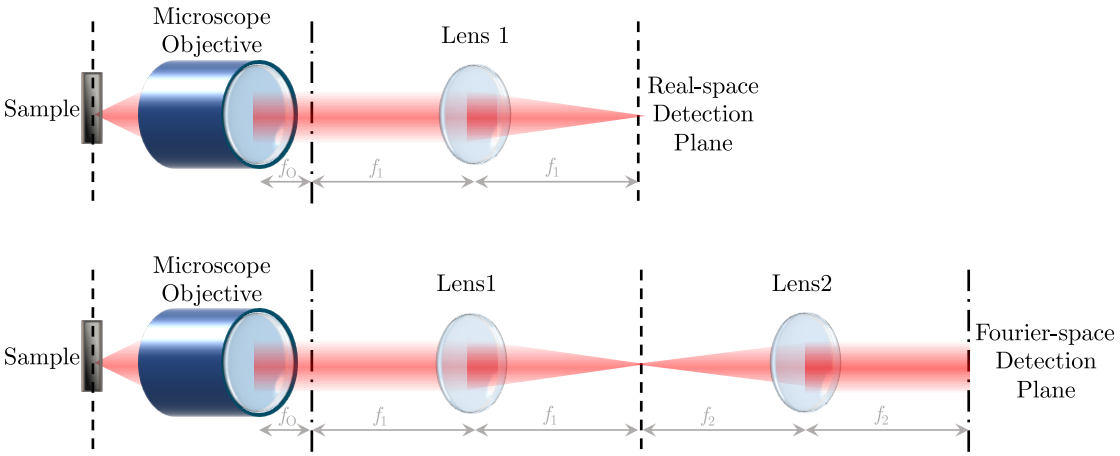

FIGURE 2.4: Schematic of (top) real-space an (bottom) Fourier-space imaging of the sample PL using a microscope objective with focal length f_O and lenses $1, 2$ with focal lengths $f_{1,2}$ respectively. The vertical dashed and dot-dashed black lines represent the real and imaginary planes respectively.

2.3 Measurements

As the radiated photoluminescence (PL) from the microcavity sample encodes the state of the condensed polaritons from before they decayed, a variety of measurements can be carried out in order to fully analyse the condensate system. The emitted condensate PL is a propagating beam of photons that carries both phase an amplitude information from the now decayed polaritons. The direct detection of these photons when focussed at the real or imaginary plane of a lens only shows the spatial distribution of the polariton intensity within the sample (or "real-space" profile) or the intensity of the momentum distribution (or "Fourier-space" profile), respectively. However, by manipulating the PL before detection opens up the measurement of other condensate parameters. This section will discuss the variety of measurements considered throughout the work of this thesis both in experiment and in simulation.

2.3.1 Real-space and Fourier-space

As mentioned above, "real-space" imaging refers to the spatial intensity distribution of condensate PL, as emitted from the surface of the sample. This is a achieved experimentally using a microscope objective to focus the PL emitted from the sample surface at infinity, followed by a lens to focus the collimated beam at its focal length, as shown in the top row of Figure 2.4. In simulations, the same profile corresponds to the intensity of the condensate order parameter, $|\psi|^2$.

"Fourier-space" imaging, also known as "k-space" imaging, corresponds to the beam profiles when the real-space is focussed at infinity and maps out the Fourier transform of the real-space wavefront. In polaritonics, it is often labelled as k-space as instead of

mapping out the spatial x, y profile of the condensate PL, it maps out the wavevectors k_x and k_y with $k_x \equiv k_y = 0$ at the centre. Thus, the Fourier-plane of the PL encodes the energy information of the condensates in terms of the distribution in polariton momentum. Experimentally, this is imaged using an additional lens to real-space PL imaging, placed between the microscope objective and lens 1 following a $4f$ optical alignment depicted in the bottom schematic of Figure 2.4. In simulation, the k-space profile is given by $|\hat{\psi}|^2$, where $\hat{\psi}$ is the Fourier transform of the condensate wavefunction ψ.

2.3.2 Phase-space

As the condensate wavefunction is complex, it is possible to measure both the real and Fourier space. When the real-space is measured experimentally, the camera/detector maps out the PL intensity while the phase information is lost. However, the argument of the real-space condensate wavefunction maps out the phase-space of the condensate system. In simulation it is simple to define $\arg(\psi)$, but in experiment a more complex optical setup is required.

Experimentally, interferometric analysis is required to reconstruct the condensate phase-map. As discussed above, a network of condensates are pumped and confined by a quasi-CW beam shaped using an SLM, but in addition to this, a second low-intensity narrow-linewidth "seed" laser is used, focussed to a Gaussian spot with 2 μm FWHM. The seed laser is resonant with the condensate PL and is chopped synchronously to form an identical quasi-pulse to the condensate pump profile. It is then focussed through the same microscope objective onto the sample surface, such that the seed spatially overlaps with one of the condensates. This in turn fixes the phase of one of the condensates. The condensate PL is then collected and interfered with the expanded seed beam (used as a reference) using a Mach-Zehnder interferometer, which is then detected using a 2D detector. The recorded data is analysed using off-axis digital holograph [92, 93], whereby the first diffraction order of the interference pattern in the Fourier plane is filtered and the inverse Fourier transform is digitally performed. From this analysis, the expanded reference beam is subtracted and results in the reconstructed condensate phase-map [94].

2.3.3 Spectroscopy

The PL is spectrally resolved using a high resolution 750 mm spectrometer with a 1800 grooves per mm grating. By focussing the PL Fourier-space onto the horizontal spectrometer slit, a near linear profile about $k_x = 0$ is spectrally resolved and the polariton dispersion is directly measurable. If the real-space is focussed onto the slit, a vertical narrow profile of real-space is spectrally resolved. In simulations, by taking a

line profile in real-space (or k-space) at each integration time step, the Fourier transform of the temporal stack leads to the polariton dispersion (or spectrally-resolved real-space).

Chapter 3

Synchronisation in Polariton Stuart-Landau Networks

By bringing two optically trapped polariton condensates together, we demonstrate tunable dissipative interactions between them. The condensates are both pumped and confined using annular shaped non-resonant optical traps. The coupling between the pair is realised through the finite escape rate of polaritons which ballistically propagate from the condensate centres, such that phase locking is observed, akin to what is observed with optically pumped condensates in the work of Ohadi et al. [44]. Through tuning the condensate separation distance, we map out regions of strong and weak dissipative coupling, where the strong coupling regimes are characterised by clear in-phase or anti-phase synchronisation. The condensate trapping potential is used to finely tune the bare condensate energies, such that robust single energy is maintained within the condensate system irrespective of the condensate coupling, as governed by the dissipative coupling of the optically trapped polariton condensates. As a result, we present a system that offers a potential optical platform for the minimisation of both sparse and dense randomly connected XY Hamiltonians. The work presented in this chapter follows the findings published in Physical Review B [2] and is the combined research effort of myself, Helgi Sigurdsson and Pavlos Lagoudakis. In the undertaking of the experiment, I was offered technical support from Julian Töpfer and Giannis Chatzopoulos. I carried out all experiments and simulations throughout this chapter, except for the Hankel function fitting in Figure 3.4 which was performed by Helgi. The initial discussion of controlling the natural frequencies of ballistically expanding condensates took place between Pavlos Lagoudakis and Nikolay A. Gippius and was important to the development of this research project.

3.1 Introduction

Limit cycle oscillators are dynamical systems with two dimensional phase (which can be described by a rotating phasor) with an isolated closed phase trajectory, such that at least one other phase trajectory spirals into it over time [95]. If neighbouring trajectories spiral into the same limit cycle as $t \to \infty$, they are said to be stable or attracting.

Dynamical systems in nature generally come about from dissipative oscillators, where without a driving force, motion would cease. System dissipation can arise from friction, heat loss, emission of particle or electromagnetic radiation or even material degradation. Dissipation and driving forces tend to reach an equilibrium irrelevant of the initial system transients and the system settles into a typical dynamical behaviour. The set of states in phase-space towards which the system evolves for a wide variety of initial states are labelled as attractors, where stable limit cycles are a specific example [96]. Attractors are characterised by self-sustained oscillations with perfectly periodic trajectories and can return to the limit cycle trajectory should a small perturbation occur. Real-world examples of a limit cycle are all around us, such as the cycle of day to night, moon cycles, seasons, tides, the beating of a wing, as well as the pendulum [97]. However, the ideal pendulum is not a limit cycle oscillator as there exist multiple concentric limit cycles in the system each with a different period, as such the orbits are not attractors. The physical pendulum experiences damping from friction and air-resistance making the stationary state of the pendulum a fixed-point attractor [98].

Many disciplines study instabilities, synchronisation and pattern formation in systems of limit cycle oscillators, such as hydrodynamics, biological ensembles, neural networks, nonlinear optics, Josephson junctions and coupled BECs [99, 100, 101]. Condensates of microcavity polaritons [102] are found to follow similar oscillatory dynamics due to their dissipative nature and give rise to a powerful experimental platform to study nonlinear and out-of-equilibrium dynamics at the macroscopic quantum level [1] even at room temperature [103].

The dynamics between multiple coupled polariton condensates can be described using a discretised version of the driven-dissipative Gross-Pitaevskii equation (dGPE) [104, 105, 106],

$$i\frac{d\psi_n}{dt} = [\Omega_n + \alpha|\psi_n|^2]\psi_n + \sum_{\langle nm\rangle} J_{nm}\psi_m \tag{3.1}$$

where ψ_n is a complex number describing the density and phase of oscillator n, with complex self energy $\Omega_n = \omega_n + i(p_n - \gamma_n)$, nonlinearity $\alpha = g - iR_s$ and coupling to neighbouring condensate J_{nm}. Physically, $\gamma_n, p_n > 0$ denote the linear losses and gain of the condensate respectively, g and R_s correspond to the real energy of the

condensate from the exciton dipole interaction strength and polariton saturation rate, and ω_n is the natural frequency of the oscillator. For a single condensate, the oscillator density $|\psi|^2$ coincides with that of the Landau equation, describing the dynamics of disturbances in the smooth laminar flow of fluids following $\frac{\partial|\psi|^2}{\partial t} = k_1|\psi|^2 + k_2|\psi|^4$, where $k_{1,2}$ are real constants [107, 72]. When condensates are coupled, i.e. $J_{nm} \neq 0$, Equation 3.1 can be regarded as the discretised form of the complex Ginzberg-Landau equation [108] to describe a system of coupled limit-cycle oscillators labelled as a *Stuart-Landau networks*. It is worth noting that the complex Ginzberg-Landau equation differs from the dGPE only in its historical origin and intent [61].

Recent studies of dissipative optical networks of limit cycle oscillators have shown regimes with strong phase-space attractors in systems of limit-cycle oscillators, where the relative phase arguments between stable oscillator pairs, $\theta_{nm} = arg(\psi_n^*\psi_m)$, correspond to the ground state of the XY Hamiltonian [54, 55, 56] and the Ising Hamiltonian [109, 110, 111]. However, in order for the system of optical oscillators to reach this minimum energy fixed point attractor, the oscillator natural frequencies ω_n need to be resonant with each other ($\omega_n = \omega_m$), and the coupling strengths J_{nm} need to be imaginary in value in order to ensure dissipative coupling between oscillators resulting in a fixed definite phase relationship [57]. The relative phase arguments of a desynchronised system are meaningless, as the steady state attractor does not correspond to a spin Hamiltonian. From an experimental stand point, it is paramount to possess enough control over the network parameters (such as the trapping potential and condensate separation distance) for the system to remain in the synchronised regime in order to extract relative condensate phases, particularly in the case of time averaged experiments.

In this chapter, limit-cycle oscillators within an optical platform are experimentally demonstrated and analysed through controlling J_{nm} and fixing the global oscillator natural frequencies $\omega_n = \omega_m \doteq \omega$ using optically trapping polariton condensates. We demonstrate regimes of clear synchronisation and map the couplings to weights of the XY Hamiltonian. The experimental results are corroborated by numerical simulations of both the continuous and discrete dGPE, for which we benchmark the performances at finding the XY ground state.

In studies of optically pumped ballistically expanding polariton condensates, it was revealed that a strong re-normalisation of condensate energies occurs when coupled together, where two energy branches of the condensate system are populated simultaneously [45]. We show that this multimodal behaviour can be quenched by optically confining the polariton condensates within an annular trap [46, 47, 50], thus limiting their state space and favouring synchronisation. Optically trapped condensates have a relatively lower pump intensity at condensate threshold, compared to the ballistically expanding state, as the condensate does not form at the spatial location of the pump, but instead non-condensed polaritons propagate away from the pump

location such that a population of polaritons builds at the centre of the annular trap, where above some critical density they form a polariton condensate. This trapping process is described in more detail in subsection 1.2.4. Due to their non-equilibrium behaviour, polaritons can diffuse away from their pumping spots through transferring their potential energy into kinetic energy [45, 112, 113], where such a flow of coherent polaritons with tunable cavity in-plane momentum results in interference and robust phase locking between spatially separated condensates [53, 114, 115, 116, 44].

The phase locking of the condensates can be detected through the observation of interference fringes in the cavity real-space and reciprocal-space photoluminescence (PL), which has been achieved over a condensate separation distance greater than 100 μm [45, 78, 117]. More importantly, optically trapped polariton condensates show a coherence time of several nanoseconds [52], which is an increase by a factor of 100 compared to ballistically expanding condensate [118, 119], thus allowing for greater scalability of the system compared to optically pumped polariton condensates. Through scaling the a network of polariton condensates intercalated with optical potential barriers [94], we propose a robust platform on which to imprint arbitrary weights of an XY Hamiltonian into a polariton condensate system for heuristic computation of the XY ground state.

3.2 Experimental Method

A pair of optically trapped polariton condensates are realised using a strain-compensated 2λ sample outlined in subsection 2.2.1 and characterised in [3]. The sample is held in a cold finger cryostat, supplying a continuous flow of liquid helium to cool the sample to a few Kelvin and is nonresonantly pumped at a cavity detuning of around -5 meV by right-circularly-polarised light from a CW monomode laser, tuned to the first minimum in reflectivity energetically above the stopband ($\lambda = 780$ nm). To avoid sample heating, the CW laser is modulated to a quasi-CW beam through the use of an AOM at a repetition rate of 10 KHz and duty cycle of 5%. The annular shape of the beam is achieved by focussing the Gaussian beam onto the surface of a phase-modulating SLM, displaying an analytically solved phase kinoform (see subsubsection 2.2.2.1 for details). The resulting pump profiles consist of two annular traps, each described by $P(r) = P_0 e^{-(r-r_0)^2/2\sigma^2}$, where P_0 denotes the pump amplitude, r scans the radial distance from each trap centre, r_0 marks the individual trap radius of 9.4 μm, and σ corresponds to the 2 μm diffraction-limited full width at half-maximum of each annulus (or the "thickness" of each ring). An example of a single laser profile used to optically trap the condensates is shown in Figure 3.2(d). The rings are adjusted in relative intensity in order to balance the height and energy of the resulting condensate pair [120], where a knife edge is used to cut the excitation profile of each ring in turn in order to characterise the individual bare condensates.

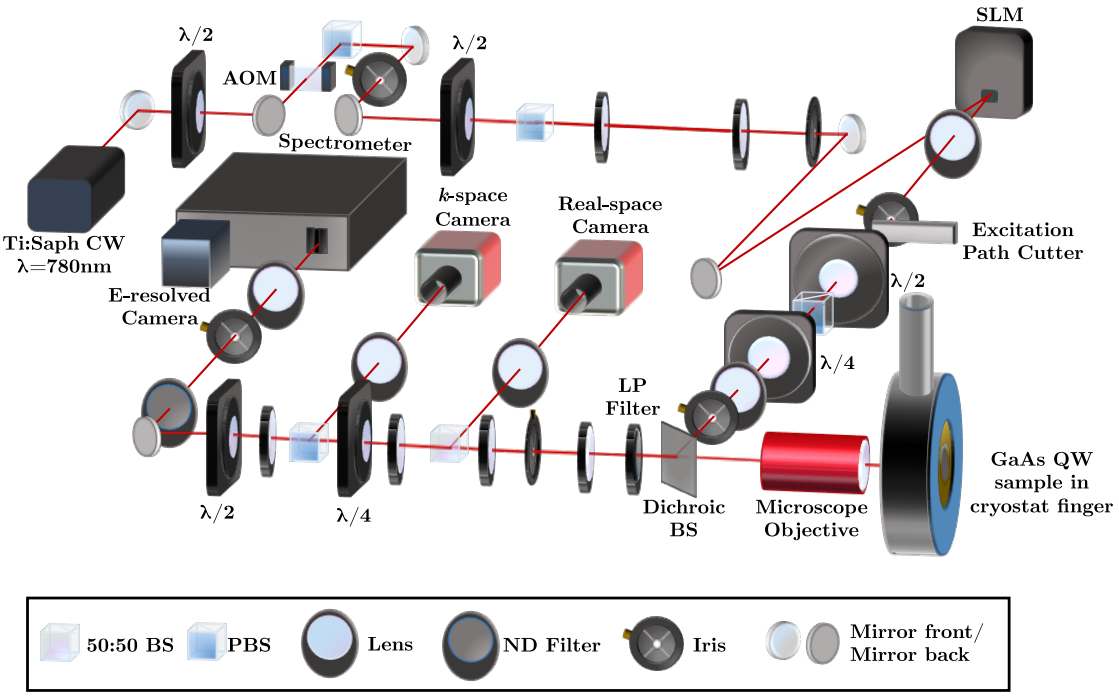

FIGURE 3.1: Schematic to show the optical setup of this experiment, where horizontally polarised light is focussed in the Fourier-plane on the surface of the SLM, which imprints a phase profile onto the beam, thus sculpting it in real-space into two rings. The beam is focussed in real-space on the surface of the sample cooled to ∼4 K using a liquid helium cryostat. The resulting condensate PL is emitted from the sample with circular polarisation and is imaged simultaneously in real-space and Fourier-space (k-space). The vertically polarised component of the PL is focussed on the vertical spectrometer grating and the beam is imaged as energy-resolved k-space and energy-resolved real-space through the addition or removal of the penultimate lens. All optical components are labelled or shown in the boxed key.

The modulated and balanced beam is then focussed on the surface of the sample using two lenses and a high numerical aperture microscope objective (NA = 0.4). The PL emission is collected through the same objective and passes through an 808 nm long pass filter, in order to cut out the excitation laser beam. As well as being measured in real-space and reciprocal-space, the PL is spectrally resolved with an 1800 grooves/mm grating in a 750 mm spectrometer, centred at 875 nm. The schematic for this optical setup is shown in Figure 3.1.

3.3 Numerical Spatiotemporal Simulations

The condensate dynamics are also modelled using the mean-field theory approach, where by the condensate order parameter $\Psi(\mathbf{r}, t)$ is described as a two-dimensional semi-classical wave equation, known as the generalised GPE, whose derivation is outlined in section 2.1, coupled to an active and inactive exciton reservoir [67],

$$i\frac{\partial\psi}{\partial t} = \left[-\frac{\hbar\nabla^2}{2m_p} + G(n_A + n_I) + \alpha|\psi|^2 + \frac{i}{2}(Rn_A - \gamma)\right]\psi(\mathbf{r},t), \tag{3.2}$$

$$\frac{\partial n_A}{\partial t} = -(\Gamma_A + R|\psi|^2)n_A + Wn_I, \tag{3.3}$$

$$\frac{\partial n_I}{\partial t} = -(\Gamma_I + W)n_I + P(\mathbf{r},t). \tag{3.4}$$

Here, the active reservoir describes the density of excitons n_A that experience bosonic scattering into the condensate and the inactive reservoir describes the density of excitons n_I that sustain the active reservoir [104, 121]. m_p is the effective polariton mass in the LP branch, α describes the system's non-linearity as a result of the inter-particle interaction strength, R is the rate of stimulated scattering of polaritons into the condensate from the active reservoir, γ is the polariton decay rate, $\Gamma_{A,I}$ are the active and inactive reservoir exciton decay rates, W is the conversion rate between the inactive and active exciton reservoirs and $P(\mathbf{r})$ describes the nonresonant CW pump profile which, which in this case is two spatially separated annular traps.

Eqs. (3.2 - 3.4) are numerically integrated using a linear multistep method in time and spectrally resolved. Many parameters used in these simulations are based off the sample properties with $m_p = 0.28$ meV ps^2, $\gamma = \frac{1}{5.5}$ ps^{-1}, $\hbar\alpha = 3.5$ μeV μm^2 and $G = 10\alpha$. The nonradiative recombination rate of inactive reservoir excitons is taken to be much smaller than the condensate decay rate such that $\Gamma_I = 0.01\gamma$, as opposed the the active reservoir decay rate which is considered to be comparable to the condensate decay rate, $\Gamma_A = \gamma$, due to the fast themalisation to the exciton background [53]. The remaining parameters are determined through fitting to experimental data, where we use the values $\hbar R = 99$ μeV μm^2 and $W = 0.035$ ps^{-1}.

The pump profile used to trap the condensates consists of two rings each with a diameter of 7 μm and FWHM of 2 μm, pumped with a height to induce condensation just above threshold and scanned over a range of separation distances from 20 μm to 80 μm.

3.4 Results and Discussion

In experiment, above threshold power the condensates form at the centre of the optical traps as a single Gaussian ground state mode. In Figure 3.2(a,b), we show the real-space and reciprocal-space condensate PL with visible interference fringes in both, as evidenced in the white line profiles, thus indicating that the condensates are phase-locked. The faint outer ring in the reciprocal-space realisation corresponds to the radial outflow of coherent polaritons from the pump sites, where the bright centre is a result of the polaritons localised within the traps. Figure 3.2 is created by stacking

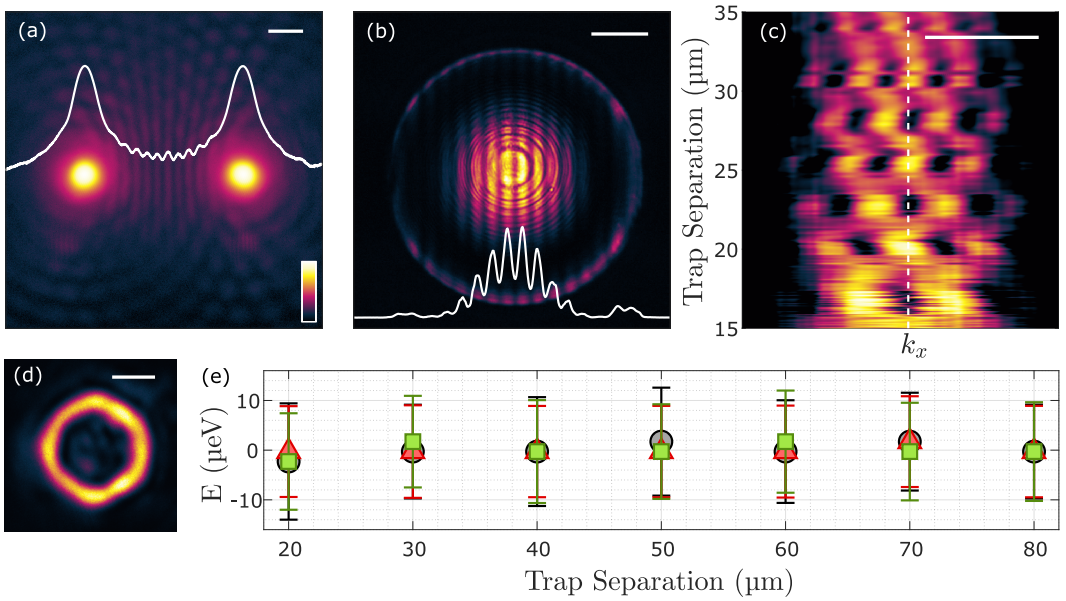

FIGURE 3.2: (a) Real-space and (b) Fourier-space experimentally realised condensate PL from two annular traps with $d = 50$ μm separation, with logarithmic and linear integrated line profiles shown in white. (c) Horizontal line profiles from Fourier-space PL (i.e., at $k_y = 0$) for varying trap separation, with dashed white line to mark $k_x = 0$. (d) Laser profile of annular pump with 12 μm diameter, used to trap each condensate. (e) Energies of the condensates with varying trap separation, with red triangles and green squares corresponding to the uncoupled left and right condensates and black circles corresponding the coupled condensate system respectively. Error bars shown the FWHM of the energy linewidth and zero energy corresponds to 0.796 meV above the bottom of the lower polariton branch. White scale-bars represent (a) 10 μm, (b,c) 0.5 μm^{-1} and (d) 5 μm. The same linear colour scale is used in (a-d).

the reciprocal space slices through $k_y = 0$ over a range of condensate separation distances between 15 μm and 35 μm. As the separation distance is increased, addition fringes appear, where a bright or dark central fringe indicates even (in-phase) and odd (anti-phase) parity respectively. Such phase-locking means that the coupling between optically trapped condensates is finite and therefore normal mode splitting is to be expected, such that the energy modes of the coupled system are shifted from the bare modes. Surprisingly, due to the system's dissipative behaviour, this is not what we observe. For optically trapped condensates, the coupled condensates remain synchronised with the same observed energy as the bare condensates [shown in Figure 3.2(e)]. This observation can be understood by considering the interacting condensates at a zero-detuned two-level system in the linear regime, with states $|\psi_1\rangle$ and $|\psi_2\rangle$ and energy $\omega_1 = \omega_2 \doteq \omega$. The coupling is then realised as an operator of the form $\hat{\mathcal{J}} = Je^{i\beta}\hat{\sigma}_1$ with $J > 0$ and the non-Hermitian classical Hamiltonian,

$$\mathcal{H} = \omega\hat{\sigma}_0 + \hat{\mathcal{J}} = \begin{pmatrix} \omega & Je^{i\beta} \\ Je^{i\beta} & \omega \end{pmatrix}. \tag{3.5}$$

Here, $\hat{\sigma}_n$ are the 2×2 Hermitian unitary Pauli matrices, with $n = 0$ corresponding to

the identity matrix. The even-parity and odd-parity eigenmodes of Equation 3.5 (corresponding to in-phase and anti-phase configurations) are written as $\Psi = (1, \pm 1)^T/\sqrt{2}$ and have the eigenfrequencies $\omega_{A,B} = \omega \pm Je^{i\beta}$. However, as we experimentally observe a monomode state in the coupled condensate system, we consider the case where the modes are degenerate in real frequency, which occurs when $\beta = \pm\pi/2$, but the imaginary frequency is split by $\Delta = i2J$. This imaginary frequency splitting corresponds to different linewidths of the two degenerate modes, where the parity state will follow the eigenstate with the largest imaginary energy component, which physically corresponds to increased scattering from the reservoir of uncondensed polaritons, thus gains population during the condensation process. Therefore, although the real energy splitting is within the system linewidth, the dissipative splitting still has great impact on the parity forming process, as evidenced by the clear interference fringes of definite parity in Figure 3.2(a-c).

Between the regions of clear parity in Figure 3.2(c), there are separation distances that result in blurred regions with no clear parity. These appear periodically with separation distance (as do the regions fo clear parity), which stems from the fact that the polariton outflow is dictated by the time-independent cylindrical wave equation (Helmholtz equation) outside of the annular pumps, whose solutions follows the Hankel function [53]. This results in J_{nm} spiralling in the complex plane as a function of polariton outflow momentum and condensate separation distance [55, 54]. In the cases where the coupling is predominantly imaginary with $\beta = \pm\pi/2$, the fringes and parity become clear due to the deterministic condensation into the highest gain modes. However, in the inverse case with $\beta = [0, \pi]$, both parity modes are degenerate in gain and so are occupied stochastically with each realisation in either even or odd parity. As the experimental realisations are time integrated over many realisations, the regions of stochastic parity occupation average out and result in the periodic "blurred" regions in Figure 3.2(c).

These findings are corroborated with numerical simulations using the 2DGPE, where in agreement with experiment, the energy of the simulated optically trapped condensate wavefunction maintains an energy of ∼0.782 meV above the bottom of the LP branch, where parity switching is also observed as a function of condensate separation distance in both real- and reciprocal-space. The steady state example of an even and odd parity realisation are shown in Figure 3.3(a-d). Again, we stack the $k_y = 0$ line profiles over a range of condensate separation distances and averaged over 20 independent simulation realisations, where in agreement to the experimental findings, we see periodic regions of clear and smeared-out parity corresponding to strong and weak dissipative coupling [Figure 3.3(e)].

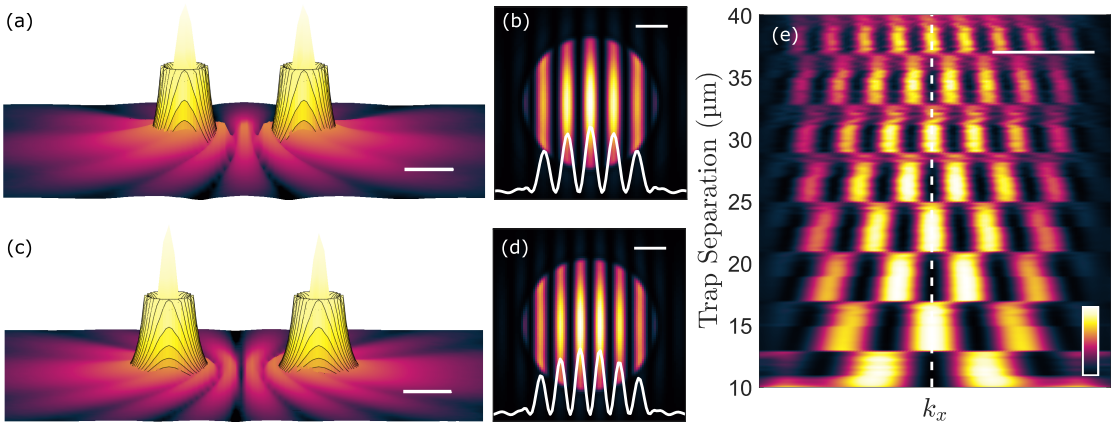

FIGURE 3.3: Numerically simulated (a,b) real-space PL and pump profiles (black contours) and (c-d) Fourier-space PL from two annular pump profiles with 7 μm diameter with (a,c) 23.2 μm and (b,d) 26.6 μm trap separation. White lines in (b,c) show the horizontal line profiles at $k_y = 0$. (e) Horizontal line profiles from Fourier-space PL (i.e., at $k_y = 0$) for varying trap separation, with dashed white line to mark $k_x = 0$. All plots shown on the same normalised linear colourscale and whote scale-bars to shown (a,c) 10 μm and (b,d,e) 0.5 μm^{-1}.

3.4.1 Hankel Function Polariton Outflow

In order to determine the inter-condensate coupling strength between neighbouring condensates, we first plot the steady state solution of Eqs. (3.2 - 3.4) trapped by an annular shaped pump profile for the wavefunction outside of the trapping potential. By fitting this data with the zeroth-order Hankel function of the first kind, we see that the steady-state condensate follows the same solution of the Helmholtz equation as expected [53] [Figure 3.4(a)].

To determine the coupling strength between two optically trapped condensates, we write a Hamiltonian to describe the two individual condensates following the condensate order parameters $\psi_{1,2}(\mathbf{r}) = c_{1,2}\varphi_{1,2}(\mathbf{r})$,

$$Ec_1\varphi_1(\mathbf{r}) = \left[-\frac{\hbar^2\nabla^2}{2m_p} + V_1(\mathbf{r}) \right] c_1\varphi_1(\mathbf{r}), \tag{3.6}$$

$$Ec_2\varphi_2(\mathbf{r}) = \left[-\frac{\hbar^2\nabla^2}{2m_p} + V_2(\mathbf{r}) \right] c_2\varphi_2(\mathbf{r}), \tag{3.7}$$

such that $\langle\varphi_1|\varphi_2\rangle \simeq 0$ and $\langle\varphi_1|\varphi_1\rangle = \langle\varphi_2|\varphi_2\rangle = 1$ with a total wavefunction $\Psi(\mathbf{r}) = c_1\varphi_1 + c_2\varphi_2$. The global Hamiltonian becomes

$$i\hbar\frac{d\Psi}{dt} = \left[-\frac{\hbar^2\nabla^2}{2m_p} + V_1 + V_2 \right] \Psi. \tag{3.8}$$

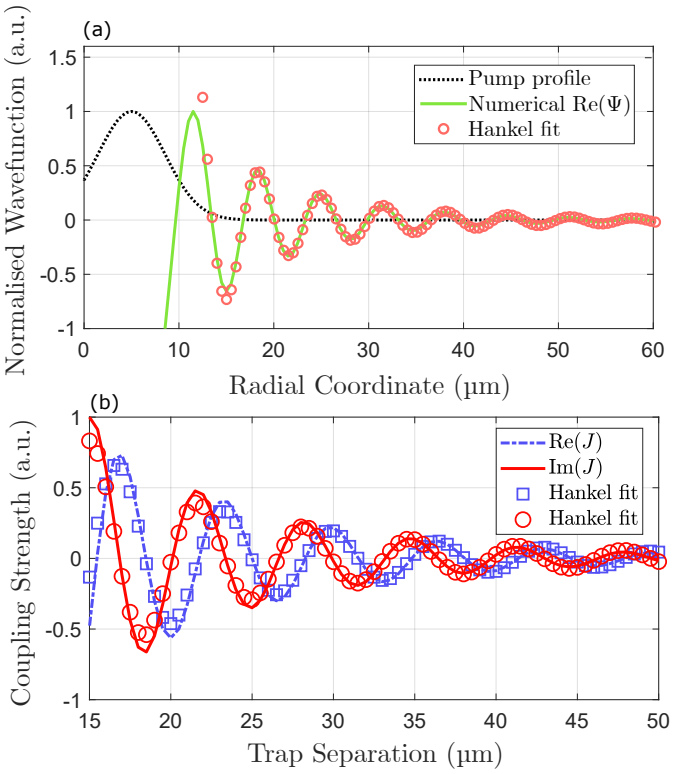

FIGURE 3.4: (a) Cross section of nonresonant pump profile (black dotted line), real part of the numerically obtained condensate wavefunction (green), and a fitted zeroth-order Hankel function of the first kind, $\psi(\mathbf{r}) = Ae^{i\phi}H_0^{(1)}[k(r-r_0)]$, where A and ϕ are real fitting parameters. Radial coordinates correspond to r. $r_0 = 11$ μm is adjusted to where the particles escape the trap. (b) Real (blue line) and imaginary (red line) part of Equation 3.16 for wavefunctions separated by $d = |\boldsymbol{d}|$. As the magnitude of the distance is increased, the integral expectedly decreases as the overlap diminishes. The circle and square markers are a fit to the data using a Hankel function $J = J_0 e^{i\phi}H_0^{(1)}[k(d-d_{\text{trap}})]$. $d_{\text{trap}} = 10$ μm is the diameter of the trap used in this simulation. For (a,b) $k = k_c + i\kappa$, where $k_c = 0.96$ μm^{-1} and $\kappa = m_p\gamma/2\hbar k_c$.

By multiplying through by $\int \varphi_1^*$, this becomes

$$\int \varphi_1^* i\hbar\frac{d\Psi}{dt}d\mathbf{r} = i\hbar\frac{dc_1}{dt}\underbrace{\int |\varphi_1|^2 d\mathbf{r}}_{=1} + i\hbar\frac{dc_2}{dt}\underbrace{\int \varphi_1^*\varphi_2 d\mathbf{r}}_{\simeq 0} \tag{3.9}$$

$$= \int \varphi_1^*\left[-\frac{\hbar^2\nabla^2}{2m_p} + V_1 + V_2\right](c_1\varphi_1 + c_2\varphi_2)d\mathbf{r}. \tag{3.10}$$

By grouping together the kinetic and potential energies of each condensate, this can be written as,

$$\begin{aligned} i\hbar\frac{dc_1}{dt} = \int \varphi_1^*\left[-\frac{\hbar^2\nabla^2}{2m_p} + V_1\right]c_1\varphi_1 d\mathbf{r} + \int \varphi_2^*\left[-\frac{\hbar^2\nabla^2}{2m_p} + V_2\right]c_2\varphi_2 d\mathbf{r} \\ + c_1\int \varphi_1^* V_2\varphi_1 d\mathbf{r} + c_2\int \varphi_1^* V_2\varphi_2 d\mathbf{r} \end{aligned} \tag{3.11}$$

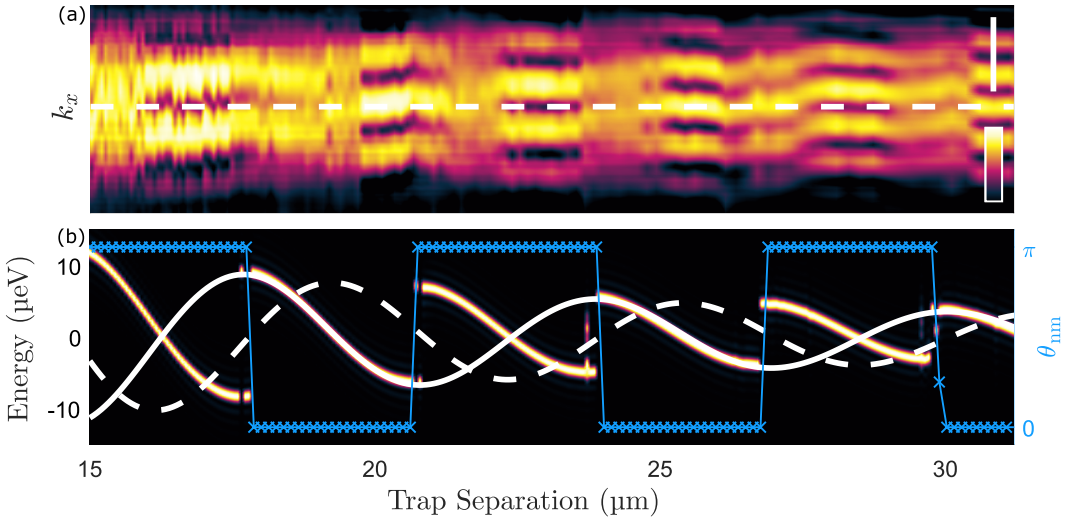

FIGURE 3.5: Experimental reciprocal-space PL as shown in Figure 3.2(d), with a dashed white line to show $k = 0$ μm^{-1}. (b) The colourmap shows the spectral intensity (real energy) from simulation of two condensates as a function of distance d using Equation 3.1 and with coupling as defined by Equation 3.17. Blue crosses show the steady-state relative phase θ_{12} from the simulation. Solid and dashed white lines correspond to the real and imaginary parts of Equation 3.17 respectively. Parameters: $k_c = 1.04$ μm^{-1}, $d_{\text{trap}} = 9.4$ μm, $m_p = 0.28$ meV ps^{-2} μm^{-2}, $\omega_n = 0$, $\gamma_n^{-1} = 5.5$ ps, $p_n/\gamma_n = 1.65$, $R_s = 0.005$ ps^{-1}, and $g/R_s = 0.02$.

$$= c_1 E \underbrace{\int |\varphi_1|^2 d\mathbf{r}}_{=1} + c_2 E \underbrace{\int \varphi_1^* \varphi_2 d\mathbf{r}}_{\simeq 0} + c_1 \underbrace{\int V_2 |\varphi_1|^2 d\mathbf{r}}_{\simeq 0} + c_2 \int \varphi_1^* V_1 \varphi_2 d\mathbf{r} \tag{3.12}$$

$$= E c_1 + c_2 \int \varphi_1^* V_1 \varphi_2 d\mathbf{r}. \tag{3.13}$$

As the equivalent expression exists for the other condensate through simply swapping the labels 1 and 2 in Equation 3.13, this result can be written in matrix form with the diagonal term corresponding to the condensate self energies and off-diagonal terms to the inter-condensate interactions,

$$i\hbar \frac{d\mathbf{c}}{dt} = i\hbar \frac{d}{dt} \begin{pmatrix} c_1 \\ c_2 \end{pmatrix} = \begin{pmatrix} E & J_{12} \\ J_{21} & E \end{pmatrix} \begin{pmatrix} c_1 \\ c_2 \end{pmatrix}, \tag{3.14}$$

and thus the definitions of the inter-condensate coupling strengths become

$$J = J_{12} = J_{21} = \int \varphi_1^* V_1 \varphi_2 d\mathbf{r} = \int \varphi_2^* V_2 \varphi_1 d\mathbf{r}. \tag{3.15}$$

We then use this result to calculate the coupling strength between two condensates with the overlap integral of the 2DGPE steady-state solution of a single condensate

wavefunction ($\psi(\mathbf{r})$) with its itself displaced over a range of spatial displacements $\mathbf{d}$ ($\psi(\mathbf{r}-\mathbf{d})$) and a single trapping potential $V(\mathbf{r})$,

$$J = \int \psi^*(\mathbf{r}) V(\mathbf{r}) \psi(\mathbf{r}-\mathbf{d}) d\mathbf{r}. \tag{3.16}$$

The resulting integration of Equation 3.16 as a function of condensate separation distance $d = |\mathbf{d}|$ is shown in Figure 3.4(b) as separate components of real and imaginary coupling strength, which are fit with the Hankel function of the first kind as shown by the overlayed red circles and blue squares respectively. This result confirms that the precise pump shape does not play a significant role on the coupling strength, where the qualitative analytical form can be obtained from considering the wave function outside of the pumping potential only. We use this result to describe these findings using Equation 3.1 through adiabatically eliminating the dynamics of the exciton reservoirs feeding the condensates [122] and applying a tight-binding method on the localised dissipative condensates [123, 106]. Using the notation of the coupling strength used in the coupling operator combined with the Hankel function behaviour we can write,

$$J_{nm} = |J_{nm}| e^{i\beta_{nm}} = J_0 e^{i\phi} H_0^{(1)}[k(d - d_{\text{trap}})]. \tag{3.17}$$

Here J_0 is the magnitude of the coupling strength, ϕ is the phase adjustment parameter to match the coupling strength with the experiment results, $k = k_c + \frac{i m_p \gamma}{2\hbar k_c}$, where k_c is the outflow polariton momentum [53], m_p is the effective polariton mass and d_{trap} is the trap diameter. Two interacting polariton condensates are then modelled using Equation 3.1 for $p_n > \gamma_n$ and the resulting real energies are plot in Figure 3.5(b) across the condensate separation distances of 15 μm to 40 μm. The overlayed blue crosses correspond to the relative condensate phases $\theta_{12} = \arg(\psi_1^* \psi_2)$ and show a step-function transition from in-phase to anti-phase locking. Figure 3.5(a) shows a section from Figure 3.2(c) for ease of simple comparison between theory and experiment. The spectrum shows discontinuous jumps where the imaginary (dissipative) component of J_{nm} changes sign and corresponds to the parity switching of the lowest threshold mode of the condensates. This result shows that a system of two coupled optically trapped polariton condensates robustly occupy the highest gain energy mode dictated by the imaginary part of J_{nm}.

3.4.2 Sparsely Connected Chains

The relative phase between two condensates can be controlled experimentally using an optical potential barrier between the condensate pair [94], such that J_{nm} can be programmed to nearly arbitrary values, with phases chosen as $\beta_{nm} \simeq \pm\pi/2$. This makes it possible to create a randomly connected network of dissipatively coupled

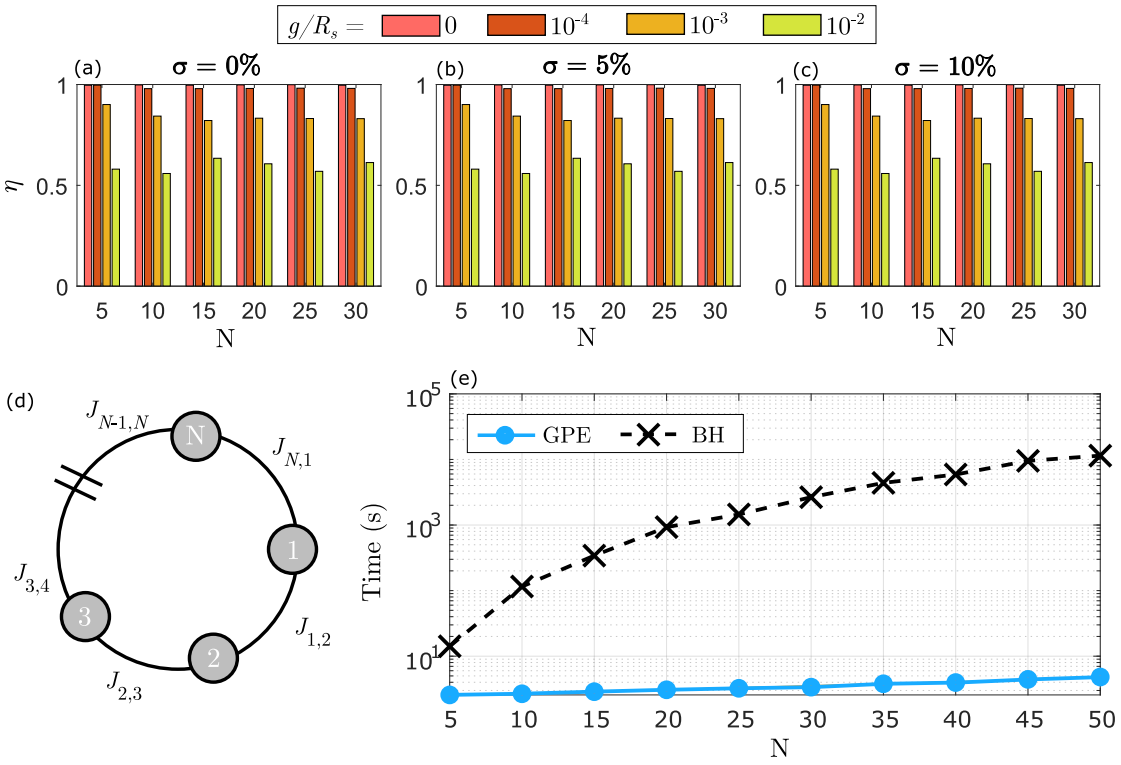

FIGURE 3.6: (a-c) Average ratio of minimised XY Hamiltonian energy between the dGPE and BH method, $\eta = E_{\text{GPE}}/E_{\text{BH}}$, for 20 random realisations of couplings J_{nm}. Performance is shown for different network sizes N, values of g/R_s and σ. Part (d) shows a schematic of the randomly connected continuous-chain lattice tested with dGPE and BH methods. (e) Elapsed computation time taken to find a local minimum energy phase configuration using the dGPE and BH methods.

polariton Stuart-Landau oscillators for the simulation of an arbitrary XY Hamiltonian [55, 54, 57]. The idea is to numerically integrate Equation 3.2 initially with $p_n - \gamma_n$ negative enough such that $\psi_n = 0$ is the only stable solutions, corresponding to pumping below the condensation threshold density. Then, by adiabatically increasing p_n, the trivial solution of ψ_n becomes unstable and the system undergoes a non-linear transient process know as a Hopf bifurcation into the condensed steady state with $|\psi_n| > 0$ and whose phase configuration correlates to that of the XY ground state.

Using a similar technique to [124, 57], we verify the performance of Equation 3.1 and test its ability to find the XY Hamiltonian ground state against a global classical optimiser, the basin hopping (BH) method [125] for randomly connected closed chains of dissipative coupled oscillators [see schematic in Figure 3.6(d)], following $H_{XY} = -\sum_{nm} \text{Im}(J_{nm}) \cos(\theta_{nm})$. Since no cavity system is ideal, we additionally test the dGPE over values of β_{nm} deviated from the ideal $\pm\pi/2$. Additionally, we investigate the ratio of the two nonlineatities g/R_s, where g dictates the real energy shift of each condensate and R_s corresponds to the polariton saturation rate.

For each set of undirected couplings J_{nm}, the energy found using the BH method and the dGPE are denoted as E_{BH} and E_{GPE}, where in Figs. 3.6(a-c), we plot

$\eta = E_{GPE}/E_{BH}$ averaged over 20 random coupling configurations of the closed chains over various numbers of oscillators N. The ideal case of $\beta_{nm} = \pm\pi/2$ is shown in Figure 3.6(a), whereas Figure 3.6(b,c) correspond to $J_{nm} = |J_{nm}|(e^{\pm i\pi/2}) \pm \sigma$, where $\sigma > 0$ introduces a small real component to the coupling strength. With $g/R_s = 10^{-4}$, the performance does not drop below $\eta = 0.96$, and we see that while $g \leq R_s$, the energy ratio η remains above 0.78 and does not vary significantly with σ. However, increasing g below this value considerably reduces the accuracy of the dGPE at minimising the XY Hamiltonian. The time taken to compute the XY energies for the BH and dGPE methods over a range of N is shown in Figure 3.6(e), where the classical solver takes non-polynomial time to compute the solution. Each minimisation method is considered using a single coupling configuration for each graph on a single core of the same Intel(R) Xeon(R) W3520 @ 2.67 GHz CPU. The computation time of the dGPE increases by just 2.5 s as the system scales in size by a factor of 10, whereas the time taken by classical BH method grows by more than three orders of magnitude over the same scaling of size.

To summarise, this investigation shows that the XY Hamiltonian of randomly weighted chains of dissipatively-coupled Stuart-Landau oscillators is approximately minimised to within 96% of the ground state when using physically realistic values of g/R_s for dissipative polariton systems. The performance of this polaritonic optimiser also does not significantly vary when a small component of weakly-dissipative coupling is introduced.

3.4.3 Densely Connected Graph

In addition to spare chains of oscillators, we also compare the robustness of the dGPE against the BH method for random all-to-all connected polariton graphs of N condensates, where again we plot $\eta = E_{GPE}/E_{BH}$ over a range of realistic and unrealistic polariton-polariton interaction strengths and a small real coupling strength contribution. These results are shown in Figs. 3.7(a-c), which show that the dGPE of Stuart-Landau oscillators is able to minimise the XY energy of any lattice configuration, although some configurations are not experimentally realistic. The phases of a chain of 10 all-to-all randomly connected oscillators after finding the XY ground state is illustrated as phasors in Figure 3.8 for both the dGPE and BH methods and shows that both methods are able to locate the same ground state configuration.

The average standard deviation between the dGPE and BH methods is written as

$$\Delta = \frac{1}{M}\sum_{m=1}^{M} \min\sqrt{\frac{1}{2N}(\mathbf{x}_{\mathrm{dGPE}} - \mathbf{x}_{\mathrm{BH}}^{(\pm)})^{\dagger}(\mathbf{x}_{\mathrm{dGPE}} - \mathbf{x}_{\mathrm{BH}}^{(\pm)})}, \tag{3.18}$$

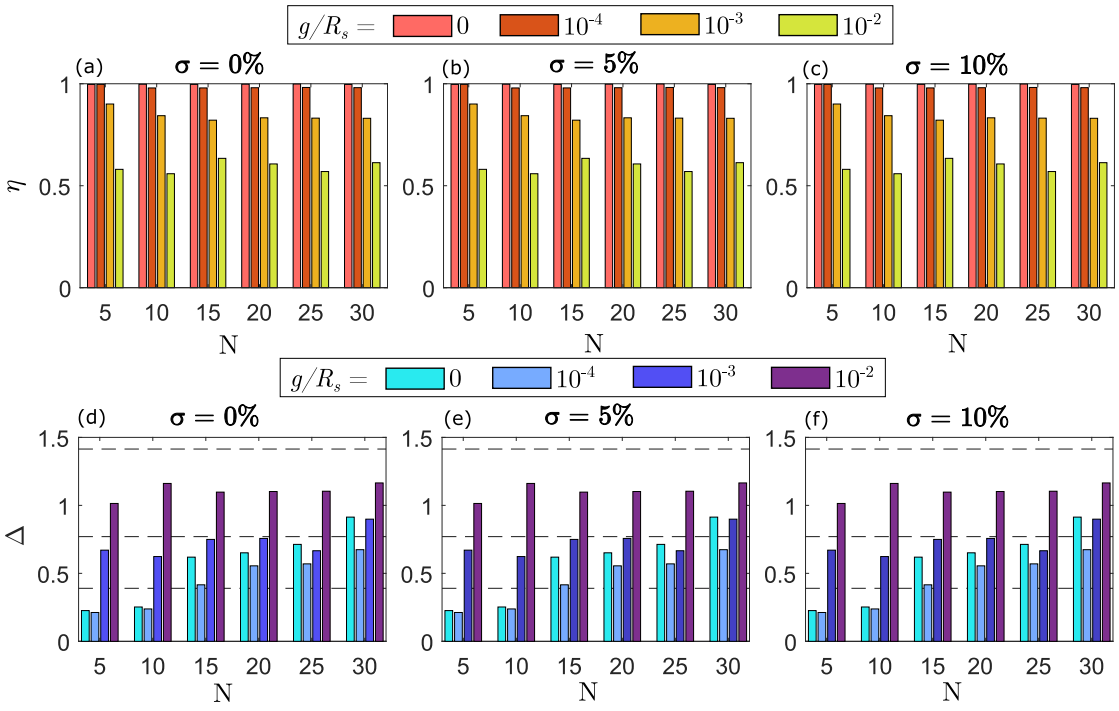

FIGURE 3.7: (a-c) Measure of $\eta = E_{\text{dGPE}}/E_{\text{BH}}$ for a range of polariton-polariton interaction strengths g/R_s, and a fraction of nondissipative coupling strength $\sigma = 0\%$, 5% and 10% respectively for a range of N densely and randomly coupled spins. (d-f) Average standard deviation Δ ($M = 20$) between minimised spins using the dGPE and BH methods for and $\sigma = 0\%$, 5% and 10% respectively, for varying g/R_s and N. Grey horizontal lines represent the standard deviation in Euclidean distances corresponding to the relative phases of $\frac{\pi}{8}$, $\frac{\pi}{4}$ and $\frac{\pi}{2}$.

where $\mathbf{x}_{\text{dGPE}} = \{e^{i\theta_n}\}_{n=1}^{N}$ and $\mathbf{x}_{\text{BH}}^{(\pm)} = \{e^{\pm i\theta'_n}\}_{n=1}^{N}$ are the complex state vectors coming from each method with phases θ_n and θ'_n respectively. The global gauge is fixed by rotating the state vectors such that $\theta_1, \theta'_1 = 0$ in each method. The "min" operation is added since the XY Hamiltonian is invariant by an overall sign factor, i.e., $H_{XY} = -\sum_{nm} \text{Im}(J_{nm}) \cos[\pm(\theta_n - \theta_m)]$. The integer M denotes the number of different networks tested. For $M = 20$, we plot Δ over a range of N in Figs. 3.7(d-f). The coupling strengths are defined as $J_{nm} = |J_{nm}|(e^{\pm i\pi/2 \pm \sigma})$ such that the choice of $\pm$ is chosen randomly for each coupling, where in Figure 3.7(d) $\sigma = 0$ (describing the ideal case) but for Figs. 3.7(e,f), a real coupling component is included (i.e. $\sigma > 0$).

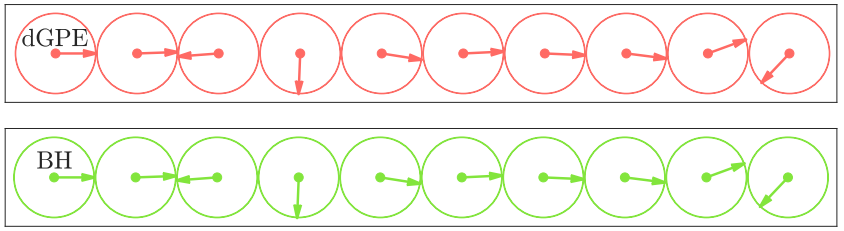

FIGURE 3.8: Relative phases of 10 randomly and densely connected spins minimising the XY Hamiltonian achieved by (top) the dGPE and (bottom) the basin hopping method. In the minimisation shown, $g/R_s = 1 \times 10^{-4}$ and $\sigma = 0\%$.

Overall, these results show that the XY energies solved using the BH and dGPE method deviate as both g and σ increase and correspond to the desynchronisation of the Stuart-Landau oscillators.

3.5 Conclusions

The work in this chapter demonstrates the robust synchronisation between optically trapped polariton condensates, a phenomenon attributed to the dissipative mechanism from the mutual condensate interference. The coupled condensates do not exhibit noticeable normal mode splitting in experiment due to the linewidth of the polaritons, yet at the same time the system is able to synchronise over a range of separation distances where dissipative coupling is dominant. The single-mode operation of the polariton condensate system is paramount in order to read out the relative phase configurations between steady-state condensates, particularly in time averaged measurements. This result offers up the system of synchronised polariton condensate networks as an optical platform for physically realising the recently proposed gain-dissipative Stuart-Landau oscillators, which can be used to heuristically solve dense randomly connected spin Hamiltonians on the ultrafast timescale.

Chapter 4

Solving the Max-3-Cut Problem with Coherent Networks

There exist many computational problems that are intractable through classical computing and, as transistors cannot be miniaturised any further (or in other words, Moore's law is drawing to a halt), will remain unsolved unless a new computational solving technique is developed. This has led to a growing demand for alternative and unconventional computing techniques to tackle these complete and intractable problems. In this chapter, a liquid light machine is used to approximate solutions to the NP-hard max-3-cut problem based on networks of synchronised exciton-polaritons. Through using the continuous phase degree of freedom of polariton condensates, we overcome the binary limitations of the decision variable in Ising machines. As the dynamical transients of the condensate network provide fast annealing of the XY Hamiltonian, we can apply the Goemans and Williamson random hyperplane technique to discretise the steady-state phases of the condensates to ternary spins that serve as decision variables for an approximate optimal solution of the max-3-cut problem, for which we shown successful results in theory and experiment. In addition to applying this phase binning and spin mapping, we present applications of this technique to the tasks of image segmentation and circuit design using coherent networks of polariton condensates.

The work presented in this chapter is published in Physical Review Applied [4], and is the joint work of myself, Helgi Sigurdsson, Sergey Alyatkin, Julian Töpfer and Pavlos Lagoudakis. The simulations in this chapter were performed by me, following the guidance of Helgi, who carried out the statistical benchmarking of Figure 4.5, and Pavlos. The experiments were carried out by Sergey, using an optical setup developed by him and Julian.

4.1 Introduction

In nature, complexity is as widespread as it is diverse. With the turn of the computing age, there has been a rapid rise in non-Boolean strategies designed to tackle complex computational problems that are simply too cumbersome for conventional Turing-based computers. Such computing architecture cannot simultaneously process an *instruction fetch* and *data operation* due to having a common bus, thus restricting and limiting the performance of a computer, labelled as the *Von-Neumann bottleneck* as coined by John Backus in 1978 [126, 127]. In addition to the bottleneck, CMOS architectures are reaching their limits as transistors cannot be made any smaller without introducing quantum effects.

Many scientific fields depend on the development of more powerful computing platforms and a new method of computing in order to tackle intractable problems such as climate change [128, 129], drug design [130], and the development of new materials and batteries [131] (to name a few). These types of problems are often approached using approximation algorithms or heuristic non-conventional solvers such as semidefinite programming [132, 133], genetic algorithms [134], and nature inspired heuristic algorithms [135, 136]. As opposed to building an optimiser for the minimisation of some cost function, instead a problem can be mapped to the Hamiltonian of a physical system that relaxes to the ground state of its energy landscape corresponding to the global minimisation of the Hamiltonian, thus implicitly optimising the cost function. Coherent networks are widely considered as the next possible generation of quantum [137] and classical computational devices [138], and have gained much interest in the field of photonic-based classical annealers, which have been realised for both Ising [109, 110, 139, 140, 141, 142, 143, 144, 145] and XY spin Hamiltonians [54, 55, 146, 147, 148], waveguide networks for the subset sum problem [149], and digital degenerate cavity lasers for the phase retrieval problem [150].

Here, we test a liquid light machine based on a planar network of exciton-polariton condensates and demonstrate its ability to optimise the maximum-3-cut (a.k.a. max-3-cut and M3C) computational problem compared to the brute force method, with a focus on two applications of image segmentation and constrained-via-minimisation in circuit design. Through applying the recent developments of connecting the dissipative nature of condensate dynamics to the minimisation of the XY Hamiltonian [54, 55, 57, 2] we apply a random hyperplane technique to bin the continuous condensate phases (corresponding to the XY ground state) to ternary decision variables [132, 151]. In the following steps, we map the NP-hard M3C optimisation problem [152] to the minimisation of a ternary phase-discretised XY Hamiltonian, which is near-optimally solved using the decision variables extracted from the standard XY model. Max-cut based problems have many real-world applications

such as in social network modelling [153], statistical physics [154], portfolio risk analysis [155], circuit design [156], image-segmentation [157], and more [158, 159, 160].

Unlike Ising machines which are limited to binary decision variables and thus restricted to just the max-2-cut problem [154, 109], the continuous degree of freedom of the variables (spins) of the XY model makes it possible to bin their phases into higher dimension decision variables, where a direct mapping exists for the max-2-cut and max-3-cut problems. However, the continuous phases of the XY model give new perspectives on whether the higher order max-k-cut problems can be approximated through discretising the phases to k decision variables. The discussed method can be applied to any system of interacting oscillators such as electronic circuits, laser systems and condensates. However, polariton condensate systems have a potential advantage over other optical optimisers [161, 162, 148, 163, 164, 111] due to the continuous-phase-locking capabilities of the condensates, strong nonlinearities, the ability to arbitrarily control polariton graph geometries and coupling strengths [94], their long coherence length (reported up to 120 μm [78]), their robust network synchronization resulting from the ballistic nature of the condensate interaction mechanism [44, 45], plus the robustness of the inorganic semiconductor microcavity [3].

4.2 Mapping the M3C Problem to the Ternary XY Model

The M3C problem is as follows: given an undirected graph $\mathcal{G} = (\mathcal{V}, \mathcal{E})$, the M3C is the partition of vertices $\mathcal{V}$ into three subsets, such that the sum of all edge weights $\mathcal{E}$ that connect between different subsets is maximised. We denote the number of vertices with $|\mathcal{V}|$. Following similar arguments presented by Barahona for an Ising spin system [156] we will show a map from minimising the energy of a ternary XY spin system to the maximisation of a M3C problem. The ternary spin system is written as follows,

$$\mathbf{s} = \begin{pmatrix} \cos(\theta) \\ \sin(\theta) \end{pmatrix}, \qquad \theta \in \left\{0, \frac{2\pi}{3}, \frac{4\pi}{3}\right\}. \tag{4.1}$$

Here, $\mathbf{s} \in \mathbb{R}^2$ is a vector that can pick up three distinct orientations. We can label these vectors as "spins" in analogy to Ising spin systems which are binary in comparison (i.e., $\theta \in \{0, \pi\}$). For a set of spins and a set of couplings $J_{ij} = J_{ji} \in \mathbb{R}$ we define a Hamiltonian,

$$H = -\sum_{ij} J_{ij} \mathbf{s}_i \cdot \mathbf{s}_j. \tag{4.2}$$

Here, $\mathbf{s}_i \cdot \mathbf{s}_j$ is the dot product between the spins. It is easy to see that, in our ternary system, for any two spins we have $\mathbf{s}_i \cdot \mathbf{s}_j = \cos(\theta_i - \theta_j) \in \left\{1, -\frac{1}{2}\right\}$ (for comparison, the spins in an Ising system would be binary in orientation with $\theta \in \{0, \pi\}$, resulting in

$\mathbf{s}_i \cdot \mathbf{s}_j \in \{-1, 1\}$). This model is also known as the $q = 3$ vector Potts model which has been studied in statistical mechanics and quite recently in the context of exciton-polariton condensates [56]. When $\theta_i \in [-\pi, \pi)$ then Equation 4.2 is just the standard XY model,

$$H_{XY} = -\sum_{ij} J_{ij} \cos(\theta_i - \theta_j), \qquad \theta_i \in [-\pi, \pi). \tag{4.3}$$

Let us now define an undirected graph $\mathcal{G} = (\mathcal{V}, \mathcal{E})$ with edges $\mathcal{E}$ connecting vertices $\mathcal{V}$, where $\mathcal{V}$ contains the ternary spins $\mathbf{s}$ from Equation 4.1. Each edge connecting vertex $\mathcal{V}_i$ and $\mathcal{V}_j$, with corresponding spins s_i and s_j, is assigned a weight J_{ij}. We define three sets of spins corresponding to the three orientations of θ_i,

$$\mathcal{V}_n = \left\{ i \in \mathcal{V} \mid s_i = \frac{2\pi n}{3} \right\}, \qquad n = 0, 1, 2. \tag{4.4}$$

Let us define $\mathcal{E}_n$ as the set of edges connecting spins within each set $\mathcal{V}_n$ and $\delta\mathcal{E}$ as the set of edges connecting spins between different sets of vertices. We can then rewrite Equation 4.2 in the following manner,

$$H = -\sum_{i,j \in \mathcal{E}_n} J_{ij} + \frac{1}{2} \sum_{i,j \in \delta\mathcal{E}} J_{ij}. \tag{4.5}$$

By defining the sum total of all the edges $C = \sum_{ij \in \mathcal{E}} J_{ij}$, we then have,

$$H + C = \frac{3}{2} \sum_{i,j \in \delta\mathcal{E}} J_{ij}. \tag{4.6}$$

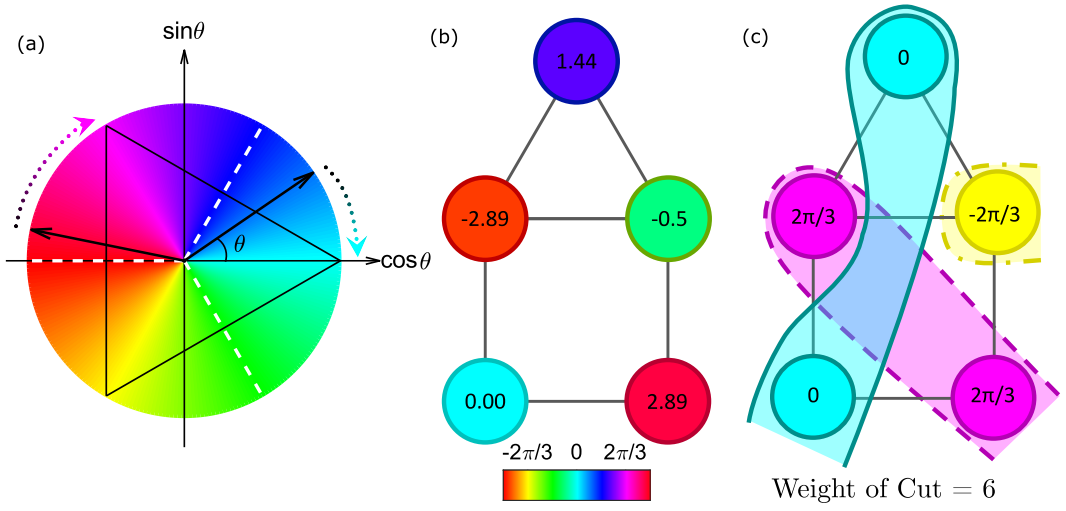

FIGURE 4.1: (a) Schematic of a chosen binning boundary (dashed white lines) projecting spins into the corners of the circumscribed triangle. (b) The XY ground state of the house configuration with numbers representing the angles (phases) θ_i of the vertices in radians; (c) the ternary mapping of the phases in (b).

Since C is invariant on the spin configuration, it can be seen that minimising Equation 4.2 is the same as maximising a M3C problem by redefining $J_{ij} = -\mathcal{W}_{ij}$, where $\mathcal{W}_{ij}$ is the weight of the edge connecting $\mathcal{V}_i$ and $\mathcal{V}_j$,

$$\min\left[-\sum_{ij} J_{ij}\mathbf{s}_i \cdot \mathbf{s}_j\right] \quad \leftrightarrow \quad \max\left[\sum_{i,j\in\delta\mathcal{E}} \mathcal{W}_{ij}\right]. \tag{4.7}$$

In the polariton network, the interacting quantities in question are nonlinear oscillators (the condensates) each characterised by a complex-valued number $\psi_i = \rho_i e^{i\theta_i}$, where ρ_i gives the condensate particle density and θ_i defines the phase of the condensate. In this sense, the phasors of the condensates then take the role of interacting two-dimensional pseudospins $\mathbf{s}$ which dynamically experience a gradient descent towards the ground state of H_{XY} [54].

As pointed out by Frieze and Jerrum [165], a mapping exists between a max-k-cut problem and the ground state of a system of spins residing at the vertices of an equilateral simplex in $\mathbb{R}^{k-1}$. For the max-2-cut problem the corresponding simplex is a line with vertices $\theta = \{0, \pi\}$ which is the reason an Ising system ground state maps directly to the max-2-cut [154]. For the M3C problem the simplex is an equilateral triangle inscribed by the unit circle like in Equation 4.2 and shown in Figure 4.1(a). For the max-4-cut the problem maps to the ground state of the Heisenberg spin system where the simplex is an equilateral tetrahedron inscribed by the unit sphere, and so on. To reiterate, this means that the continuous-phase XY ground state can be binned to binary and ternary decision variables, which directly map to solutions of the max-2-cut and max-3-cut graph problems respectively.

4.2.1 The random hyperplane technique

In order to approach the ground state of the ternary Hamiltonian of Equation 4.2, the spins in the XY Hamiltonian of Equation 4.3 that correspond to the ground state configuration $\{\mathbf{s}_1, \mathbf{s}_2, \dots\}$ are projected onto their closest ternary counterpart through binning the phases to the unit complex triangle, as inscribed on Figure 4.1(a). This technique of discretising the continuous phases onto binary or ternary decision variables creates a semidefinite relaxation program[1] which has previously been studied

[1] Semidefinite programming refers to an area of optimisation mathematics following a linear objective (cost) function that is subject to convex constraints. Semidefinite programs are the name given to optimisation problems consisting of a linear function of a variable $x \in \mathbb{R}^m$ following: $\min\left(c^T x\right)$ subject to $F(x) \geq 0$, where $F(x) = F_0 + \sum_{i=1}^{M} x_i F_i$.

The problem data is given by $c \in \mathbb{R}^m$ and the $m+1$ symmetric matrices $F_0, \dots F_m \in \mathbb{R}^{n\times n}$, where $F(x)$ is positive semidefinite meaning that it is Hermitian (it is its own conjugate transpose) and has non-negative eigenvalues. Many real-world problems can be approximated as a semidefinite program, where a mathematical program (or algorithm) is used to optimise the problem, which is in general NP-hard [166].

by Goemans and Williamson [151, 132] and is referred to at the *random hyperplane technique* in mathematical computer science.

In this project, we focus on the M3C problem, for which the ternary decision variables are selected through discretising the phases following the binning boundary depicted in Figure 4.1(a) (similarly to [151]). An approximate solution to Equation 4.2 is obtained through the random sampling of many different orientations of the triangular binning boundary, with respect to one of the XY phases (hence the label of "random" hyperplane technique). We point out that the minimisation of the ternary Hamiltonian (Equation 4.2) and continuous Hamiltonian (Equation 4.3) following the same relaxation procedure as a semidefinite program, thus underpinning the common point of finding the ground state of both systems [132, 133].

4.2.2 The house graph

The procedure of this technique is shown for the example of the anti-ferromagnetic (AFM) house graph in the XY ground state (Figure 4.1(b)), which is binned to ternary spins (Figure 4.1(c)), thus obtaining the M3C solution with a weight of cut equal to 6, as all adjacent graph vertices belong to a non-similar subset (depicted by the different colours). The AFM house graph has also been recently studied using degenerate laser cavities to find the XY ground state energy [148]. Here, AFM refers to a negative value coupling strength $J_{ij} < 0$ in Equation 4.2 and Equation 4.3, giving a preferential spin alignment of $\theta_i - \theta_j = \pi$ between a pair of condensates or dissipative coupled oscillators. On the contrary, ferromagnetic (FM) coupling strengths following $J_{ij} > 0$ lead to a preferential phase alignment of $\theta_i - \theta_j = 0$ for a pair of coupled oscillators. For brevity, we use $J = -1$ in dimensionless units. We first calculate the ground state XY energy of the AFM house graph using the basin hopping method (a classical optimiser) [125], with angles (phases) θ_i given in radians inside the discs. A variety of binning boundary rotations are tested to find the orientations that gives the minimal XY energy. From which, the phases are binned to their ternary counterparts (Figure 4.1(c)) in order to calculate the subsets for the encoded max-3-cut problem, where the ternary energy of the cuts gives the "weight of cut".

To illustrate that the maximum cut weight has been obtained, in Figure 4.2(a) we plot the M3C weight (dashed black line) against the distribution of possible cut weights (blue bars) from 100 random samplings of θ_i each tested over 100 random hyperplane orientation. This shows that the random stochastic sampling gives a wide spread of weights with a modal cut weight of 5, maximum cut weight of 6 and minimum cut weight of 2. This result underlines that even when many different boundaries are tested, the M3C cannot be found from random data. Additionally, the XY energy of these random stochastic realisations are shown by the blue bars in Figure 4.2.

4.3 Polariton Dynamics

4.3.1 Polariton Theory

To investigate the applicability of our method to polariton condensate networks, we start by performing numerical simulations of the generalised 2DGPE coupled to an (active) exciton reservoir $n(\mathbf{r}, t)$, which experiences bosonic scattering into the condensate:

$$i\frac{\partial \Psi}{\partial t} = \left[-\frac{\hbar\nabla^2}{2m_p} + G\left(n + \frac{P(\mathbf{r})}{W}\right) + \alpha|\Psi|^2 + \frac{i}{2}\left(Rn - \gamma\right)\right]\Psi, \tag{4.8}$$

$$\frac{\partial n}{\partial t} = -\left(\Gamma + R|\Psi|^2\right)n + P(\mathbf{r}). \tag{4.9}$$

Here, m_p is the effective mass of a polariton in the lower dispersion branch, α is the interaction strength of two polaritons in the condensate, G is the polariton-reservoir interaction strength, R is the rate of stimulated scattering of polaritons into the condensate from the reservoir, γ is the polariton decay rate, Γ is the decay rate of the reservoir excitons, W quantifies the population ratio between low-momentum excitons that scatter into the condensate and those which reside at higher momenta (so called inactive excitons), and $P(\mathbf{r})$ is the non-resonant continuous wave (CW) pump profile.

The condensates are pumped using five synchronised annular optical traps in the AFM house configuration, as shown in Figure 4.3(a), where the coupling to first nearest neighbours is purely imaginary following the techniques described in chapter 3 [2]. The

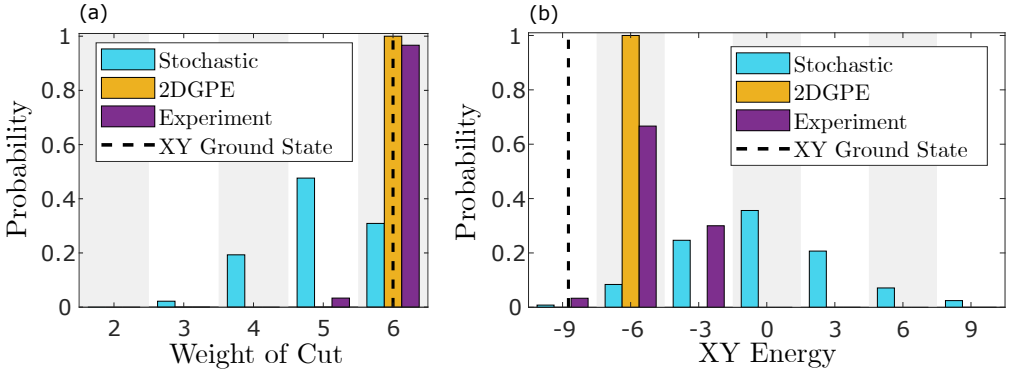

FIGURE 4.2: (a,b) histograms of the M3C weights and XY energies respectively from the corresponding house graph of (blue) 1000 random samples of partitioning, (yellow) 2DGPE simulations and (purple) experiment. Dashed black lines show the XY ground state on spectra, not discretized to the histogram bins (white and gray background stripes). Weight of cuts in (a) represent the optimum cut for each data set sampled across 100 uniformally spaced binning boundaries (different rotations of the unit triangle).

cluster of annular rings making up the pump profile of $P(\mathbf{r})$ is given by

$$P(\mathbf{r}) = P_0 \sum_i p(\mathbf{r} - \mathbf{r}_i). \tag{4.10}$$

Here, P_0 denotes the laser power density and the function $p(\mathbf{r})$ corresponds to the 2D annular shaped profile of a single laser incident to the microcavity plane and the coordinates $\mathbf{r}_i$ are the locations of the vertices in the polariton graph. The annular shaped pump profiles optically trap each condensate, yet allow for coherent transport of particles between nearest neighbours, consistent with those described in [2].

In the 2DGPE simulations, the parameters are taken such that the polariton mass and lifetime are based on the properties of a laboratory InGaAs microcavity sample: $m_p = 0.28$ meV ps^2 μm^{-2} and $\gamma = \frac{1}{5.5}$ ps^{-1}. We choose values of interaction strengths typical of InGaAs based systems: $\hbar\alpha = 3.5$ μeV μm^2, $G = 10\alpha$. The reservoir decay rate is taken comparable to the condensate decay rate $\Gamma = \gamma$ due to fast thermalisation to the exciton background. Although physically the loss rate of optically active excitons in the polariton bottleneck is comparable to the condensed polariton decay rate, there is an argument that Γ should be chosen to more effectively model the rapid relaxation of the exciton reservoir dynamics [67, 53]. However, as the numerical simulations consider only the steady state of the condensate system, we stick with the definition of $\Gamma = \gamma$. The final two parameters are then found by fitting to experimental results where we use the values $\hbar R = 98.9$ μeV μm^2, and $W = 0.035$ ps^{-1}.

The laser driven condensate system is simulated close to, but above, condensation density threshold where the interacting condensates (optically trapped by each annular pump) spontaneously self-organise in phase in order to maximise particle number, which in turn minimises the XY Hamiltonian (see section 1.3) [54, 55].

For each steady state realisation of the AFM polariton house graph, 100 random binning boundaries are tested in order to find the M3C. The weight of cuts and XY energy are plot as yellow bars in Figure 4.2(a,b), showing that the simulations robustly give the correct M3C weight = 6, while closely approximating the minimum XY energy as indicated by the dashed black line.

4.3.2 Experiment

We experimentally inject five exciton-polariton condensates in the AFM house configurations in a semiconductor microcavity, following a similar technique to chapter 3 [2], and measure their relative phase configurations using a homodyne technique [94].

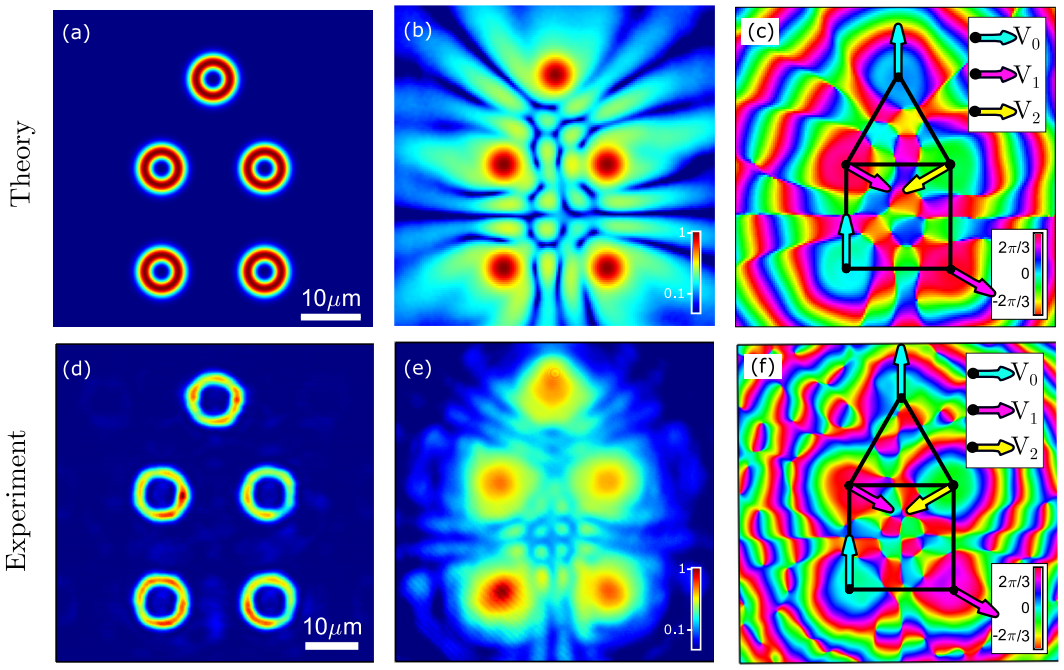

FIGURE 4.3: (a, d) Optical pump profile $P(\mathbf{r})$; (b, e) condensate density $|\Psi(\mathbf{r})|^2$, and (c, f) condensate phase map $\theta(\mathbf{r})$ from 2DGPE simulation and experiment, respective to each row, of optically trapped polariton condensates [2] in the AFM house configuration, with arrows in (c, f) showing the discretised XY phase into subsets $\mathcal{V}_{0,1,2}$

The GaAs-based microcavity is cooled down to ∼4 K in a closed-cycle helium cryostat and pumped non-resonantly with a CW single-mode laser at a negative exciton-photon detuning of -4.2 meV. In order to shape the excitation profile, a programmable reflective phase-only spatial light modulator (SLM) is used and the SLM kinoform is calculated using the MRAF iterative algorithm (as detailed Figure 2.3 and subsubsection 2.2.2.1). The laser pump pattern is focused onto the sample using a 50× microscope objective with a numerical aperture of 0.42. The separation distance between pumping rings (20.5 μm) and their diameter (7.8 μm) is chosen such that any pair of the nearest trapped polariton condensates in a square geometry demonstrates AFM coupling [see Figure 4.4(a,b)]. The excitation geometry defines the range of the excitation intensity per single pumping ring, where the trapped condensates maintain AFM coupling. Therefore for the house configuration, the excitation power is proportionally increased to ensure AFM coupling between nearest condensates. The results presented in Figure 4.3(e,f) correspond to excitation conditions supporting only single energy (i.e. stationary) states above condensation threshold. Time-averaged measurements of real-space condensate PL are performed under CW excitation, acousto-optically modulated in time with square pulses at a frequency of 5 kHz and duty cycle of 1%. To implement the relative phase readout between the nodes in the house configuration we utilize a homodyne interferometric technique [94], which is discussed in more detail in subsection 6.3.3. Each reconstructed phase map is extracted from a single-shot measurement in a Mach-Zenhder interferometer. The excitation pulse-width in all single-shot measurements is 100 μs.

Using this technique, we record 60 experimental realisations of the AFM house graph of polariton condensates. Each time, we extract the XY energy from the condensate phases, giving the distribution shown in Figure 4.2(b) by the purple bars. This result confirms that polariton condensates favour the phase configurations corresponding to the small XY energies, as pointed out by [54], but not necessarily the XY ground states as the system can relax to a local energy minima of the potential landscape, or even a non-stationary stationary state of θ_i whose XY energy has no physical meaning. Despite this energy discrepancy however, the resulting M3C weights from the experiment (purple bars in Figure 4.3(a)) indicate very good performance, implying that the approximate solutions to the continuous variable problem of minimising the XY Hamiltonian can indeed give good results to the M3C problem. This is an important result that emphasises that coherent networks of dissipatively coupled oscillators, such as polariton condensates, can potentially perform as heuristic solvers for the NP-hard M3C problem.

In Figure 4.3(a,d) we show the real-space map of the theoretical and experimental excitation profiles respectively. The coupled strength between nearest neighbour condensates is selected to be uniform across the graph and FM, such that $J_{ij} = J < 0$, where the condensate separation distance is chosen to correspond to a single-mode occupation of the system, as discussed in chapter 3 [2]. In Figure 4.3(b,e) and Figure 4.3(c,f) the theoretically and experimentally realised condensate densities $|\Psi(\mathbf{r})|^2$ and corresponding phase maps $\arg(\Psi(\mathbf{r}))$ are shown for their condensate wavefunctions $\Psi(\mathbf{r})$, respectively. In Figure 4.3(e), the polariton density is averaged over many condensate realisations to improve the visibility of the inter-condensate interference fringes, but we also show the equivalent "single-shot" plot in Figure 4.4(c) for consistency with the single shot theoretical density map. The clear interference fringes between the condensates in both theory and experiment show that the condensates are synchronised, meaning we can extract their phases such that $\theta(\mathbf{r}_i) = \theta_i$. The presented phase-maps in Figure 4.3(c,f) both give the ternary phase configurations that matches the M3C, shown in Figure 4.1(c).

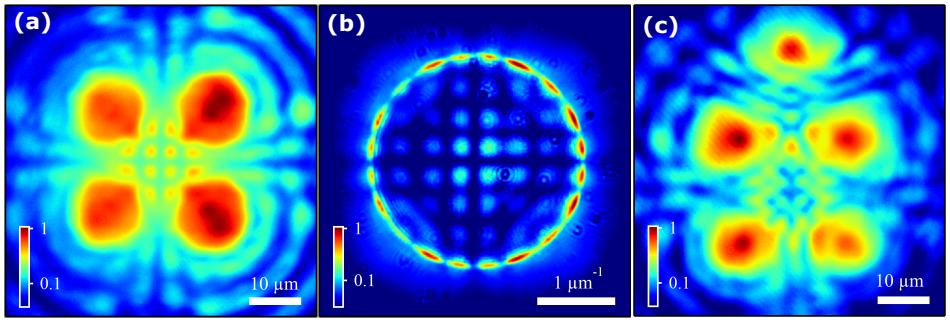

FIGURE 4.4: Time integrated (a) real-space and (b) reciprocal-space polariton PL for the square cell of trapped condensates sustaining AFM coupling. (c) Single shot realization of the polariton PL in real space for the AFM house graph.

4.3.3 Benchmarking phase-and-amplitude oscillators

In the previous subsection, we showed results that underscore the potential of dissipative coupled oscillator systems to solve graph problems, such as the M3C. But to understand the quantitative ability of this method, we look into the statistics by many different all-to-all connected graph configurations $\mathcal{G}$ with randomly chosen edge weights $\mathcal{W}_{ij}$. We test the performance of our method to solve the M3C by comparing the maximum weight of cut solved using brute force compared to networks of Stuart-Landau (SL) phase-and-amplitude dissipative coupled oscillators (for speediness compared to the classical basin hopping optimisation method [2, 125]). This SL model is simpler and more general than the GPE as it does not depend on the spatial degree of freedom, but rather the inter-oscillator coupling strength. It describes the dissipative coupling between non-linear oscillators $\psi_n = \rho_n e^{i\theta_n}$, with density ρ_n and phase θ_n. The dynamics of these oscillators follow the SL model,

$$\frac{d\psi_n}{dt} = \left[P - |\psi_n|^2\right]\psi_n + \sum_m J_{nm}\psi_m \tag{4.11}$$

where P denotes the oscillator "gain" and J_{nm} is the inter-oscillator coupling strength. In chapter 3, we saw that such networks show good performance at minimising the dense and sparse randomly connected XY Hamiltonian [2]. These simulations start with initial background noise as we numerically integrate Equation 4.11 in time using a linear multistep method and once the oscillators reach a steady state, we extract their phases $\theta_n = \arg(\psi_n)$ in order to obtain the approximate ground state of Equation 4.3.

We then compare the weight-of-cuts obtained from these phase configurations of SL oscillators W_{SL} against the correct minimum (maximum) cut weights obtained using brute force $W_{BF}^{min(max)}$, where we define the normalised error as,

$$S_W = \frac{W_{\mathrm{BF}}^{\max} - W_{\mathrm{SL}}}{W_{\mathrm{BF}}^{\max} - W_{\mathrm{BF}}^{\min}}. \tag{4.12}$$

For this metric, $S_W = 0$ means that the oscillator system has found the best cut, whereas $S_W = 1$ is the worst possible cut. In Figure 4.5, we use 1000 random all-to-all connected graphs, with $\mathcal{W}_{ij}$ selected from a normal distribution centred at zero, we numerically model the SL network dynamics and extract S_W from the synchronised steady state solutions corresponding to the fixed points of $\psi_n^*\psi_m$. By increasing the number of binning boundaries tested (different binning orientations), we see an intuitive increase in performance, understood from the fact that Equation 4.3 is independent of a global rotation in phase $\theta_i \to \theta_i + \phi$ such that the procedure of binning the XY spins to evaluate Equation 4.2 is not. This is because the continuous phases are always binned to $\{0, 2\pi/3, 4\pi/3\}$ irrespective of ϕ, where varying ϕ can lead to an alternative (non-maximum) weight of cut. This is why several binning

orientations need to be tested in order to minimise the XY energy in order to successfully solve the M3C thus minimising S_W. The results in Figure 4.5(a-c) show very good performance with mean errors of $\bar{S}_W = 0.53\%$, 1.38% and 1.86% for graphs containing $|\mathcal{V}| = 6$,12 and 18 vertices, which is well below today's best error guarantree of 16.40% in [151] and 19.98% in [165]. For reference, the average errors for the theoretically and experimentally calculated M3C weights of the AFM house graph in Figure 4.2(a) are $\bar{S}_W = 0$ and $\bar{S}_W = 0.83\%$ respectively.

We additionally investigate whether the performance of the system depends on the energy gap between the ground states of the ternary spin system and continuous XY spin system, i.e. $\min(H_{XY}) - \min(H_T)$. Results in Figure 4.5(d) show the mean error for different energy gaps, indicating good performance with no significant dependence on the ground state energy gap between the two Hamiltonians.

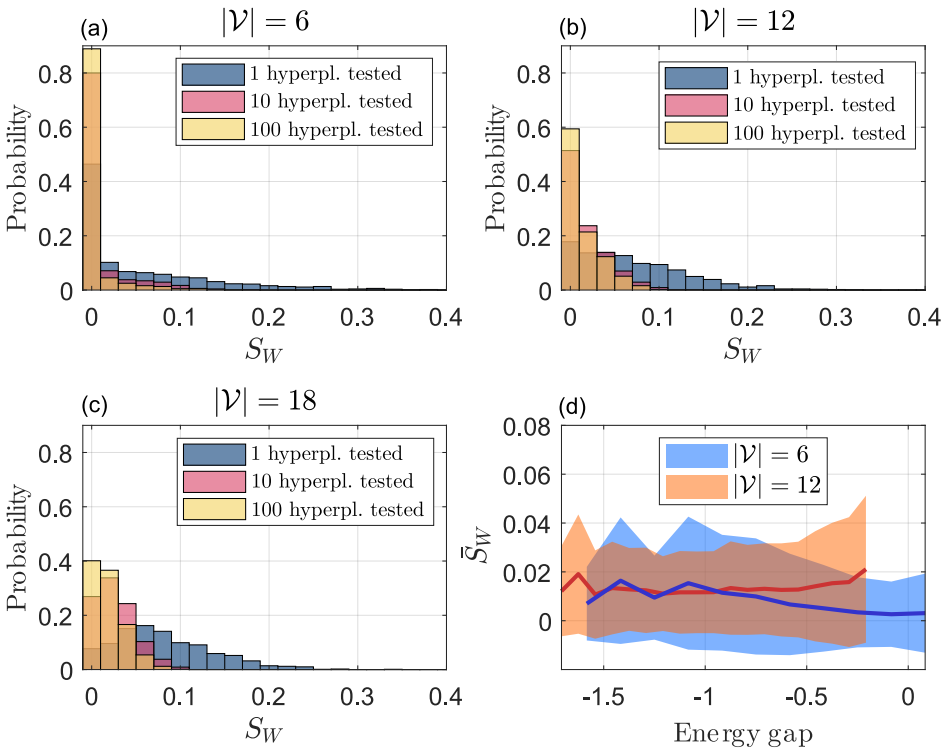

FIGURE 4.5: (a,b,c) Performance of $|\mathcal{V}| = 6, 12, 18$ vertex graphs, respectively, showing an expected drop with graph size yet still maintaining peak probability around zero error ($S_W = 0$). The mean errors are $\bar{S}_W = 0.53\%$, 1.38%, and 1.86%. With more random binning boundaries tested [different rotations of the triangle in Figure 4.1(a)] the probability of finding the correct solution increases. (d) Mean error $\bar{S}_W$ (whole lines) plotted against the ground state energy gap, $\min(H_{XY}) - \min(H_T)$, indicating weak dependence when the energies between the ternary and continuous spin systems are different. Shaded area denotes the standard deviation. Here, $\min(H_{XY})$ is estimated using the Stuart Landau network (as opposed to e.g. the basin hopping method) for computational speediness, whereas $\min(H_T)$ is found using brute force. Horizontal axis is given in units of $|\mathcal{V}|\sigma$ where σ is the standard deviation of $\mathcal{W}_{ij}$.

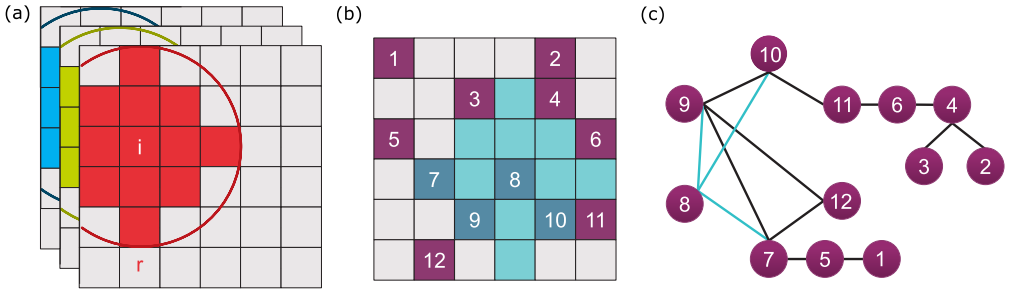

FIGURE 4.6: (a) Each small square represents a pixel in a colored image with i labelled and the surrounding patch colored according to RGB color layer. Radius r shows the maximum distance of pixel connectivity where only pixels within the ring have an edge weight connecting $\mathcal{V}_i$ and $\mathcal{V}_j$, otherwise $\mathcal{W}_{ij} = 0$; (b) $m = 12$ random pixels are selected and transformed into a graph (c).

4.4 Applications

4.4.1 Image Segmentation

The M3C problem can be used to segment an image into 3 objects or regions [40]. When formulating a graph from an image, the vertices and edges represent pixels and their relative similarity respectively. When selecting vertices, all pixels or a smaller sample can be included, with connectivity to neighbours within a given radius. To define the edge weights, a weighted average is taken over properties such as colour, brightness, texture, spatial proximity and number of sharp edges between pixels, in addition to setting a threshold weight [40, 167, 168, 169]. In this work, we consider colour, brightness and spatial proximity using a variety of procedures to enumerate the edge weights for the M3C problem.

For a coloured image, we randomly sample m pixels. For each colour layer (formed by separating an image into the three RGB layers), we consider each sampled pixel i and define a local "patch" encompassing it and its (up to) eight nearest neighbours, as depicted in Figure 4.6. We define the total brightness of the N pixels in a patch as,

$$p_i = \sum_{i=1}^{N} i, \tag{4.13}$$

where p_i is calculated for all pixels in the image and are normalised over each colour layer [170]. In addition to this local weight, we assign a global colour weight, $c_i = M_A/M$, to each pixel according to its colour frequency in the image, where A is the colour of pixel i, M_A is the number of pixels with colour A, and M is the total number of pixels. We define the edge weight connecting pixels i and j as $\mathcal{W}_{ij}$, which is equal to 0 if the pixel separation is greater than r. Otherwise, we define five methods for enumerating $\mathcal{W}_{ij}$ based on a variety of techniques described in

literature [171, 170, 172, 173, 174, 175],

$$\text{Method 1:} \quad \mathcal{W}_{ij} = \exp\left(\frac{|p_i - p_j|^q}{\sigma}\right); \tag{4.14}$$

$$\text{Method 2:} \quad \mathcal{W}_{ij} = \exp\left(\frac{|c_i p_i - c_j p_j|^q}{\sigma}\right); \tag{4.15}$$

$$\text{Method 3:} \quad \mathcal{W}_{ij} = \exp\left(\frac{|c_i - c_j|^q}{\sigma}\right); \tag{4.16}$$

$$\text{Method 4:} \quad \mathcal{W}_{ij} = \exp\left(\frac{|i - j|^q}{\sigma}\right); \tag{4.17}$$

$$\text{Method 5:} \quad \mathcal{W}_{ij} = \exp\left(\frac{|ic_i - jc_j|^q}{\sigma}\right). \tag{4.18}$$

Here, σ is the standard deviation in brightness across each patch, q is a free parameter and $\mathcal{W}_{ij}$ is averaged over each colour layer. To find the results of the image segmentation, we find the M3C of the graph $\mathcal{G} = (\mathcal{V}, \mathcal{W})$, with $|\mathcal{V}| = m$ vertices representing the sampled pixels with weights $\mathcal{W}_{ij}$ connecting vertices i and j. We will show that the partition of the continuous phases in a polariton condensate graph (just as we demonstrated in Figure 4.1 for the house graph) into a ternary phase configuration, acting as decision variables for the M3C, can segment different objects within an image. Figure 4.8 shows a schematic of the mapping process from an image to a graph.

We show 3-region image segmentation, using simple pictures of an apple and a tree, performed by solving the M3C problem for each graph using the same procedure as described in Figure 4.1. This time however, the XY ground state is approximated using the Stuart-Landau model detailed in Equation 4.11. In order to approach the ground state phase configuration, we use a bottom-up approach [55] to physically replicate a slow pump-up in laser power beyond polariton condensate threshold in order to produce measurable PL from the system. This is achieved through increasing P linearly in time from $P(t = 0) = -\lambda_{max}$ to $P(t = T) = \lambda_{max}$, where T is the total integration time needed to reach a steady state and $\lambda_{max} > 0$ is the largest eigenvalue of the coupling matrix $\mathbf{J} = \{J_{nm}\} \in \mathbb{R}^{N \times N}$.

The apple and tree images are shown in Figure 4.7, overlaid with the resulting ternary spins using each of the five methods of enumerating $\mathcal{W}_{ij}$. By eye, it is clear that each subset of spins of the M3C correctly locate objects and regions within each of the images. The weight enumeration methods that combine both local (relative pixel or

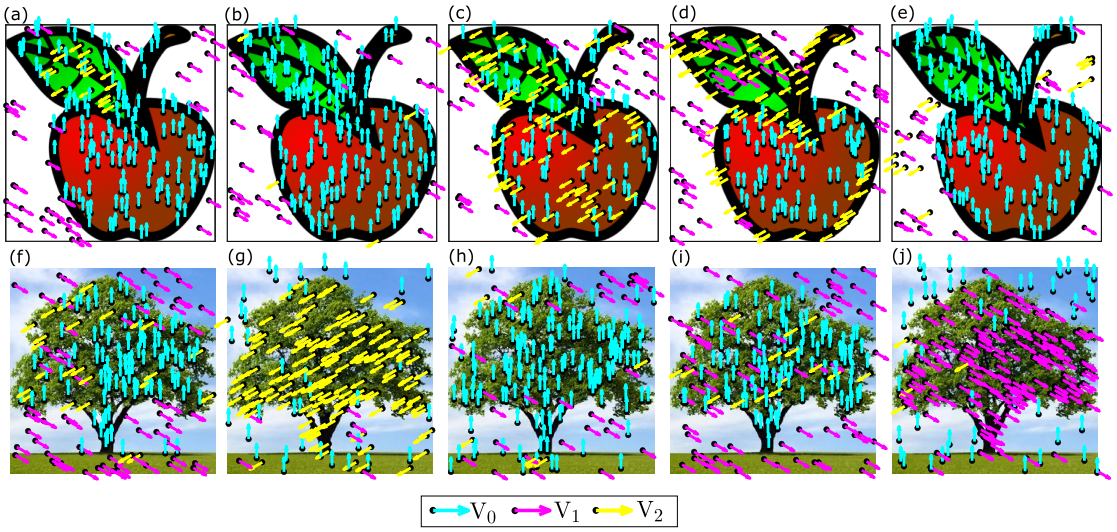

FIGURE 4.7: Images of an apple and a tree, with image segmentation results (a-e, f-j) using the Stuart-Landau network for methods (Equation 4.14-4.18) respectively, with $m = 200$, $r = 400$, $q = 0.1$ for (a-e) and $q = 0.2$ for (f-j). The cyan, magenta and yellow arrows represent the subsets $\mathcal{V}_{0,1,2}$ respectively.

patch brightness) and global properties (colour frequency in the image), whose results are shown in Figure 4.7(b,e,g,j), best locate a single object and a background by predominantly cutting the graph into just two spin subsets. In the apple image for example, this is a result of the similar-valued edge weights between pixels within the red, black and green regions.

However, the methods that only consider local pixel values (relative patch and pixel values, with results shown in Figure 4.7(a,d,f,i)) segment the images into multiple same spin regions. This is seen most clearly for the simpler apple image, where the local methods are able to correctly locate the white background, red apple, green leaf and black outline. As this figure consists of mainly four block colours, a single spin subset must represent two image regions as there are only three subsets in the M3C problem, such is the case for $\mathcal{V}_0$ in Figure 4.7(a) which represents both the red and black regions in the image.

Finally, by considering just the global properties (colour frequency) as shown in Figure 4.7(c,h), the images are again segmented into an object and background, but this time through locating the dominant colours in the image, as Method 3 only includes the global weighting of each colour in the image when enumerating the edge weights (Equation 4.16). Here, some objects are located by multiple subsets. Again, this is an artefact from having only three subsets with which to segment an image containing additional colour regions or objects. In Figure 4.7(c) for example, the red part of the apple is represented by both $\mathcal{V}_0$ and $\mathcal{V}_2$ which indicates that the steady state phases of the oscillators lies close to the binning boundary between these two segmentations.

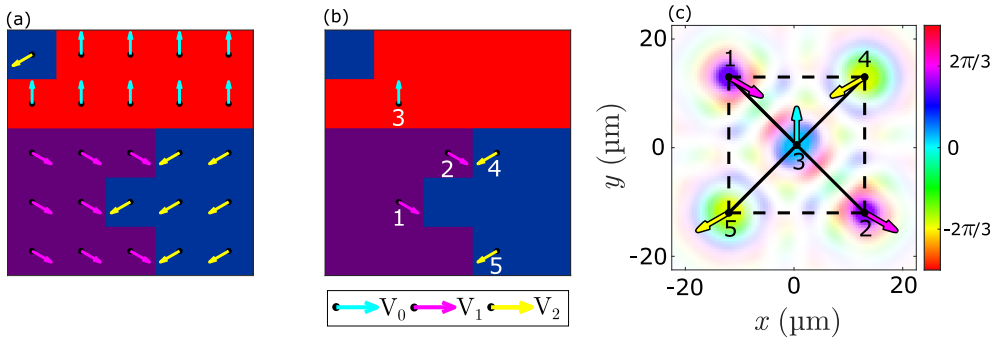

FIGURE 4.8: Simple colored image (a,b) showing image-segmentation using the Stuart-Landau network for the phase-discretised XY ground state of the graphs following Eq. (4.17), with $r = 4$, $q = 0.01$ for (a) $m = 25$ and (b) $m = 5$. (c) Shows the condensate phase map $\arg(\Psi(\mathbf{r}))$ obtained from 2DGPE simulation solving the set of pixels given by (b) with transparency proportional to the polariton density $|\Psi(\mathbf{r})|^2$. Projecting the phase of each condensate into its ternary counterpart is given by the cyan, magenta and yellow arrows, representing the subsets $\mathcal{V}_{0,1,2}$ respectively. Solid and dashed black lines represent $\mathcal{W}_{ij} = 1.0$ and $\mathcal{W}_{ij} = 0.8$ (rounded to 1 decimal place) respectively.

Through adjusting the segmentation parameters (m, r, q, σ) and choosing different methods (Equation 4.14-4.18), image segmentation using dissipative coupled oscillators can be achieved to match a wide range of image segmentation requirements.

We additionally consider a much simpler coloured image containing 25 pixels (shown in Figure 4.8) to demonstrate image segmentation using a planar graph. We first find the image segmentation using the SL network, with all-to-all coupling (i.e. $r \geq 5\sqrt{2}$) between all pixels (Figure 4.7) and a subset of sampled pixels (Figure 4.7), where both cases correctly locate the different block colours in the image.

4.4.2 Constrained Via Minimisation

In this section, we discus the application of the M3C (solved using coherent networks) to constrained-via-minimisation (CVM) in circuit design. In order to optimise space in commercial electronic devices, often components are split over multiple layers of circuit board. For example, circuits in the average smart phone are often split over 12 layers and professional circuit board manufacturers boast to produce multilayer circuit boards with close to 100 layers [176]. Multiple layers are achieved through drilling holes, known as "vias", that are lined with an electrically conductive coating to allow the connectivity of the components to span many layers of board. However, the addition of vias increases fabrication time, complexity and cost, making it desirable to minimise the number of vias in the design of each multilayer circuit board.

For CVM, the circuit board components are already laid out and split into clusters called "cells" (sections of fixed circuit layout, shown as grey areas in Figure 4.9(a)), which are pre-placed with vertical and horizontal tracks already routed under the

assumption that all pin connections are bipartite (i.e. a single track connects two pins), but layer assignment is not yet performed. Segments of track that overlap are labelled as critical segments (solid lines in Figure 4.9(a)) which cannot be on the same layer of circuit board. Free segments of track (dashed lines in Figure 4.9(a)) have no overlaps with other tracks and these are the regions of track on which a via can be placed. We demonstrate CVM through reducing the task to a M3C problem [156], which we then solve through simulation of coherent networks of polariton condensate. We demonstrate CVM on up to 3 layers, where the max-k-cut corresponds to CVM with up to k layers of circuit board. It is worth noting that the exact CVM problem we tackle has previously been studied in the work of [156] with the max-2-cut problem, so we have prior knowledge that the minimum number of vias for the circuit board in Figure 4.9(a) requires just two layers of circuit board, such that the solution to the M3C problem will only incorporate two out of the three possible spin subsets.

For the circuit in Figure 4.9(a), we define the layout graph $\mathcal{G} = (\mathcal{V}, \mathcal{E})$. Each critical segment is represented by a vertex $\mathcal{V}$, where pairs of vertices are connected by either a conflict edge $\mathcal{A}$ (when a pair of critical segments cross paths) or by a continuation edge $\mathcal{B}$ (when a pair of critical segments are connected by a free segment), such that $\mathcal{E} = \mathcal{A} \cup \mathcal{B}$, where the layout graph of the example circuit is shown in Figure 4.9(b). The reduced layout graph $\mathcal{V} = (\mathcal{S}, \mathcal{T})$ arbitrarily selects a vertex v_i in $\mathcal{V}_i$ to represent critical region i, such that $\mathcal{S} = \{v_i, \ldots, v_z\}$. $\mathcal{T}$ contains the edges linking v_i and v_j for $i \neq j$, if and only if $\mathcal{G}$ contains a continuous edge connecting some vertex in $\mathcal{V}_i$ to some vertex in $\mathcal{V}_j$ (i.e. connecting different cells).

The edges of $\mathcal{R}$ in Figure 4.9(c) have weights $(\alpha_{ij}, \beta_{ij})$, as contained in $\mathcal{T}$, such that:

$\alpha_{ij} =$ Minimum number of vias needed between $\mathcal{V}_i$ and $\mathcal{V}_j$ should v_i and v_j be assigned the same layer, i.e. sum of all free segments between $\mathcal{V}_i$ and $\mathcal{V}_j$ that connect a pair of critical segments with different orientations (horizontal and vertical);

$\beta_{ij} =$ Minimum number of vias needed between $\mathcal{V}_i$ and $\mathcal{V}_j$ should v_i and v_j be assigned different layers, i.e. sum of all free segments between $\mathcal{V}_i$ and $\mathcal{V}_j$ that connect a pair of critical segments with the same orientation.

The partition of this graph into $\mathcal{S}_n$, $n = 0, 1, 2$, corresponds to the assignment of each critical region to layer n. For such a partition, the number of vias required is:

$$\mathrm{VIA}(\mathcal{S}_n) = \sum_{v_i v_j \in T_n} \alpha_{ij} + \sum_{v_i v_j \in \delta\mathcal{T}} \beta_{ij} \tag{4.19}$$

where edges $\mathcal{T}_n$ connect critical regions assigned the same layer and $\delta\mathcal{T}$ connect critical regions assigned different layers. By defining $A = \sum_{v_i v_j \in \mathcal{T}} \alpha_{ij}$, then

$$\mathrm{VIA}(\mathcal{S}_n) - A = \sum_{v_i v_j \in \delta\mathcal{T}} (\beta_{ij} - \alpha_{ij}). \tag{4.20}$$

As A is invariant on the layer assignment, and by redefining the edge weights $\mathcal{W}_{ij} = \alpha_{ij} - \beta_{ij}$ as in Figure 4.9(d), we see that this problem follows the same form as Equation 4.6. Thus, the constrained via minimisation problem is reduced to the M3C problem of Equation 4.7,

$$\max \sum_{v_i v_j \in \delta\mathcal{T}} \mathcal{W}_{ij}. \tag{4.21}$$

The phase-discretised XY solution coming from the polariton network for our example reduced layout graph [see Figure 4.9(e,f)] partitions the vertices into just two subsets, showing that the minimum via configurations only requires two layers of circuit board. In this example, the minimised number of vias is 2, as

$$A - \sum_{v_i v_j \in \delta\mathcal{T}} \mathcal{W}_{ij} = 2 - 0$$

and thus a correct solution has been found by the polariton network.

4.5 Other Maximum Cuts

It is worth noting that the continuous-phase spins of the XY model can be projected into binary decision variables with $\theta_i = [0, \pi]$ (i.e. to 1-dimensional spins) which leads to an Ising energy function whose ground state corresponds to the max-2-cut (M2C) problem [156]. This binary projection strategy has been explored previously with coherent photonic Ising machines [139, 140, 109, 110, 141, 142, 145]. However, to the best of our knowledge, the mapping between the continuous-phase oscillator ground state to the ternary spins with $\theta_i \in \{0, 2\pi/3, 4\pi/3\}$ has not previously been studied.

We show the weight of cuts solved using the SL model compared to the brute force method for the M2C and M3C in Figure 4.10(a,b), where the error between W_{SL} and W_{BF} is negligible for M2C. This is due to the M2C only having two possible values for the decision variables, such that every oscillator has a window of 180° in which to be correctly binarised. In the case of the M3C however, the window is reduced to 120°, giving less room for error in the binning process thus leading to an increased error between W_{SL} and W_{BH}.

Furthermore, as we point out in section 4.2, the direct mapping of the ground state configuration of a spin Hamiltonian to the max-k-cut problem requires spins to belong to corners of the equilateral complex unit simplex in $\mathbb{R}^{k-1}$ dimensions. In other words, for the first few values of k, the spins must be at the corners of the unit line (M2C),

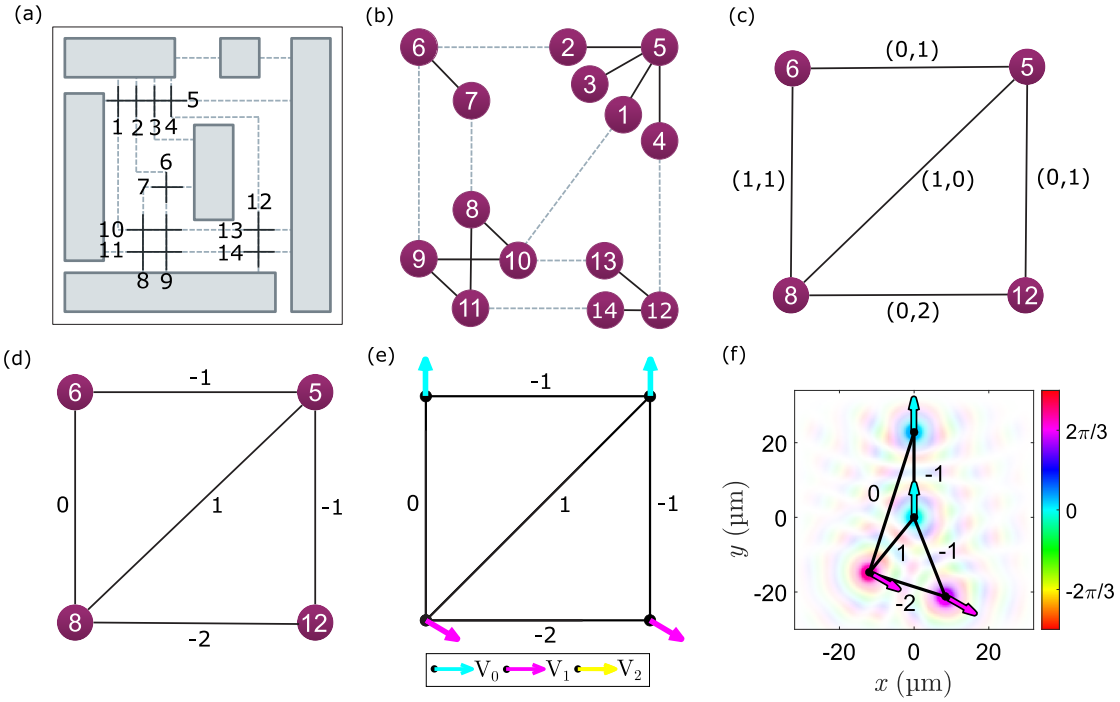

FIGURE 4.9: (a) A circuit with routing between pre-placed cells (gray areas), with critical segments of tracks numbered and shown in solid black line and free segments showed in gray dashes; (b) the layout graph of circuit (a) with critical edges shown in solid black and continuation edges in gray dashes; (c) the reduced layout graph of (b) with edges labelled $(\alpha_{ij}, \beta_{ij})$; (d) the reduced layout graph of (b) with edge weights $w_{ij} = \alpha_{ij} - \beta_{ij}$, and (e,f) ground state discretized XY phase for the M3C of graph (d), solved using the Stuart-Landau network and 2DGPEs respectively, with black numbers representing the graph edge weights w_{ij}. The cyan, magenta and yellow arrows represent the subsets $\mathcal{V}_{0,1,2}$ respectively and in (f) the transparency is proportional to the polariton density $|\Psi(\mathbf{r})|^2$.

triangle (M3C) and tetrahedron (M4C), where the mutual angles between any two spins is either 0 or a constant (which for the line is 180°, the triangle 120° and tetrahedron ∼70.53°). For this reason, projecting the two-dimensional XY ground state phases onto the quaternary decision variable with angles $\theta_i \in \{0, \pi/2, \pi, 3\pi/2\}$ about the unit circle is not the direct mapping for the M4C problem, but however is an *approximation* of the solution (though we expect a worse performance). In Figure 4.10(c) we do indeed see a greater spread in cut weights from the SL networks compared to the M4C solved using brute force.

The difference between the max-k-cut errors for $k = 2, 3, 4$ becomes more apparent in Figure 4.10(d), as the normalised mean error for $k = 2, 3$ remains constant as a function of graph size, as opposed to the growing error of the M4C with graph size. Interestingly, the error for the M2C stays practically negligible, indicating that SL systems can compete with photonic Ising machines, through the binarising of oscillator steady-state phases. The larger error of the M3C is expected due to the high partition complexity to three decision variables. We finally point out that the mean error of the

M4C remains relatively small with $\bar{S}_W < 0.05$ for $|\mathcal{V}| = 14$, despite its growth with system size.

As a result, this leads to an exciting perspective into using condensate phase dynamics to go beyond the M3C, even if a direct mapping no longer exists. We also plot the mean error of the different max-k-cut problems while scanning the number of tested binning boundaries (each with a different rotation relative to the steady-state oscillator phases) as plot in Figure 4.10(e), which shows that the error approaches some asymptotic minimum with the increase of tested binning boundaries at a similar rate, regardless of k. Notably, the asymptotic error does however increase with k.

4.6 Conclusions

Both in theory and in experiment we have shown the potential of nonlinear optical oscillators, with a focus on polariton condensates, at approximating solutions to the NP-hard max-3-cut optimisation problem. This study was prompted by recent works

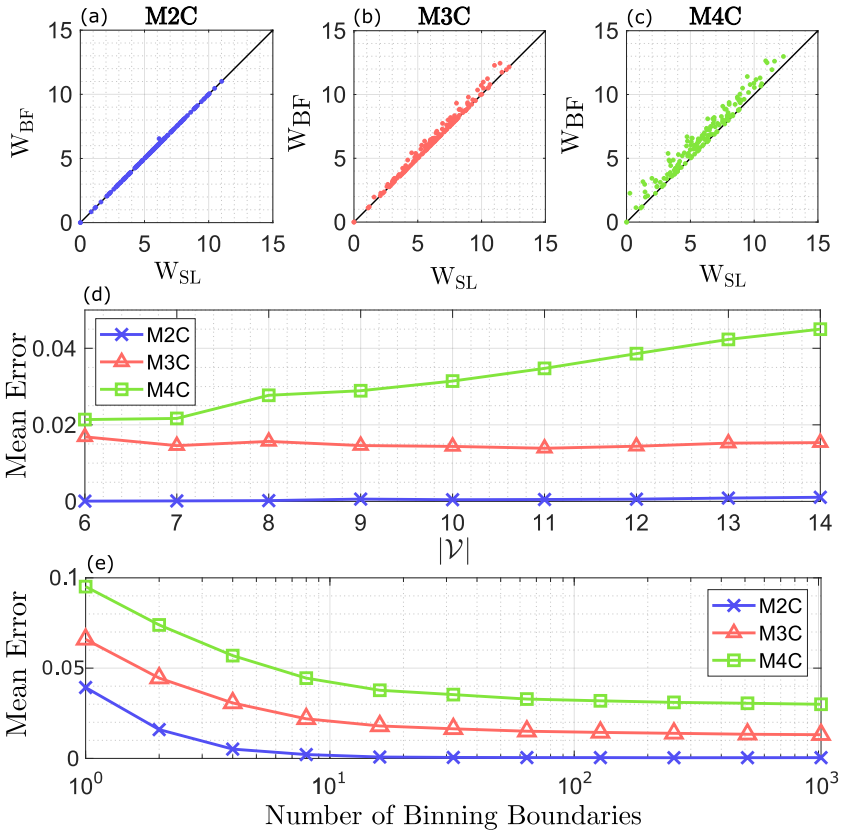

FIGURE 4.10: Obtained weights of (a) max-2-cut, (b) max-3-cut and (c) max-4-cut from 160 random graphs using the Stuart-Landau model (W_{SL}) with $|\mathcal{V}| = 10$ and 100 unique binning boundaries and the brute force method (W_{BF}). Black line indicates $W_{SL} = W_{BF}$. Comparison of the mean error $\bar{S}_W$ obtained by averaging over 160 random graphs of different max-k-cut tasks as a function of (d) network size $|\mathcal{V}|$ (tested for 100 unique binning boundaries) and (e) number of binning boundaries with $|\mathcal{V}| = 10$.

showing the gradient decent of exciton-polariton networks towards the equilibria of synchronised states with phasor configurations correlating to the XY ground state [2, 54, 56, 57].

In this work, we exploit this feature of the dynamical system in order to approximate solutions to the max-3-cut problem via two methods: Firstly, we apply the semidefinite relaxation program of Goemans and Williamson (known as the random hyperplane technique) [132, 151] which bins (projects) oscillator phasors into equally-distributed ternary decision variables. Secondly, we use the direct mapping between the q=3 vector Potts model (which we label as the "ternary XY model" in Equation 4.2) and the max-3-cut, as originally presented by Frieze and Jerrum [165], which we obtain using the aforementioned ternary decision variables.

This study provides the first experimental evidence that polariton condensate networks can potentially serve as optical annealers for the max-3-cut problem, thus opening up a new perspective for coherent nonlinear optical networks as approximate analogue solvers for complex graph-based problems, where the condensate networks arrange in phase to the XY ground state on time scales on the order of hundreds of picoseconds (dependent on system size). Although polariton interactions are restricted to inherently two-dimensional networks, there are studies beginning to investigate all-to-all connectivity [177, 178]. This dilemma will be addressed in the following chapter. Additionally, we have studied complex applications of this technique to image segmentation and CVM in circuit design, which we heuristically solve using our proposed method and simulations on both Stuart-Landau oscillator networks and polariton condensate networks.

Our technique goes beyond the previously studied Ising networks to solve the max-2-cut problem, [109, 162], by exploiting the continuous phase degree-of-freedom in oscillatory systems. Their natural ability to minimise the XY Hamiltonian can be applied to solve the M3C problem through the Goemans and Williamson inspired semidefinite programming, and applying a phase binning between k equidistant boundaries leads to the approximate solution of the max-k-cut problem, where we further explore the max-2-cut and max-4-cut.

This technique can be applied to any system of dissipative coupled nonlinear oscillators, such as laser networks and photonics condensates, but in this study we have taken a step towards realising a liquid light machine of interacting polariton condensates as a practical coherent network platform for a heuristic computational device through exploiting the ultrafast temporal dynamics, parallel interactive nature, and continuous degree of freedom that can now be accessed in state-of-the-art experiments in polariton lattices [94, 78].

Chapter 5

Solving Dense Graph Problems with Stuart-Landau Networks

In this chapter, we implement the technique of minor embedding from quantum annealing in order to simulate networks of dissipative coupled oscillators following the Stuart-Landau model for instances of all-to-all connected networks mathematically labelled as "complete graphs". Where many physical oscillator systems depend on two-dimensional networks, particularly in photonic systems, it becomes impossible to practically control all coupling strengths of a complete graph beyond a handful of nodes. By building off the triad structure minor embedding originally proposed by Choi [179, 180], which expands the densely connected complete graph to a sparse graph of nodes, we present a potential hardware layout for realising a dense graph solver using future on-ship solid state devices. Our analysis reveals that minor embedding allows for the simulation of the XY Hamiltonian of an arbitrary complete graph using the two-dimensional triad graph structure. The work in this chapter is currently under review as a journal submission with Communications Physics, and is available as a pre-print article on arXiv [181], authored by myself, Helgi Sigurdsson and Pavlos Lagoudakis. Pavlos came up with the idea to read into how graph problems are mapped to 2D networks in the field of quantum computing, but I came up with the idea to apply the triad minor embedding technique to dissipative nonlinear oscillator networks. All simulations were carried out by me under the guidance of Helgi, except from the benchmarking of the Stuart-Landau model's performance against the commercially available optimisers and the Kuramoto model (subsection 5.2.1), which was performed by Helgi.

5.1 Introduction

Dense graph combinational problems have been tackled using quantum annealing systems for over a decade, where qubits and their relative coupling strengths represent graph vertices and edge weights respectively. In order to solve such dense graph problems, the graph vertices must first be mapped onto the qubit architecture, which in general is not as densely connected as the graph problem at hand. This hurdle is overcome through a technique called *minor embedding*, where by the dense graph problem is expanded to match the connectivity of the qubit architecture [180, 182, 183, 184, 185, 162]. However, finding the simplest minor embedding of an arbitrary graph is in general an NP-hard problem, where the computational complexity grows with the number of graph vertices [182, 186]. Luckily, a standardised embedding of a complete graph has been realised, which expands the complete graph onto a sparse network based on the square lattice, labelled the *triad graph* [180, 179, 187]. An alternative embedding scheme has been developed for quantum annealers that embeds spins to fewer qubits than the triad graph [188], where each qubit represents a coupling edge between spins and has been successfully implemented with Kerr-nonlinear resonators [189] and superconducting circuits [190, 191]. However, by using qubits to represent the system interactions rather than the spin states themselves, this technique applies only to binary spin systems.

In this study, we minimise the classical XY Hamiltonian using coherent networks of Stuart-Landau oscillators of randomly-weighted complete graphs embedded to the triad structure and demonstrate through dynamical annealing that the dynamics of the triad graph can be used to solve for the XY ground state of the encoded complete graph [57, 2]. Stuart-Landau oscillators represent the graph vertices, where each oscillator is described by a complex number $\psi_n = \rho_n e^{i\theta_n}$, and the graph edges map to the inter-oscillator coupling strength J_{nm}. Recently, there have been multiple studies investigating the Start-Landau network dynamics as their fixed point attractors correlate with the minimisation of the XY Hamiltonian [57, 124, 2, 192]. This offers perspectives into realising an analogue computer based on networks of coherent oscillators to heuristically solve complex graph problems, such as the NP-hard max-3-cut problem [4] and the phase retrieval problem [193]. There are a group of optical dissipative coupled oscillator platforms that make for an ideal candidate to experimentally realise such a solvers such as polariton condensates [4, 54], photon condensates [164], non-degenerate optical parametric oscillators [194, 147], and coupled laser arrays [148]; where these optical coherent networks take advantage of the systems photonic parallelism, ultrafast computation timescales, low power consumption and their continuous-phase degree of freedom. However, many hurdles arise when experimentally realising such systems.

In order for optical coherent networks to approximate a graph problem, the coupling strength between each pair of oscillators must be tuned to match the corresponding graph edge weight. From a standard computer simulation point of view, this is not an issue [195, 143]. For the case of polariton condensate systems [54, 178, 2] (and optical coherent networks in general), tuning the inter-condensate coupling strengths has been demonstrated previously by applying a below-threshold Gaussian spot on the microcavity sample between a pair of polariton condensates [94], where this spot acts as a potential barrier to the propagating polaritons, resulting in a tunable relative phase between condensates. However, for a densely connected graph, this technique becomes impossible as there is not enough space in the system to include a tunable optical barrier between every pair of coupled condensates. Additionally, as the magnitude of the coupling strength between neighbouring condensates decays exponentially with separation distance [2], the coupling strength to condensates beyond first nearest neighbour becomes negligible, making it impossible to represent a high-weight graph edge with polariton condensates separated by a large distance. This means that beyond a handful of vertices, it becomes impossible to experimentally realise an optical heuristic solver. We tackle this problem through minor embedding all-to-all connected graph problems to the triad graph in order to overcome this connectivity issue and demonstrate the feasibility of the triad structure at numerically simulating the dynamics of its encoded complete graph for systems of nonlinear optical oscillators.

5.2 The Stuart-Landau Model

The Stuart-Landau model describes a wide variety of oscillatory systems and is formally derived from the Hopf bifurcation (see subsection 2.1.2). We apply the model to networks of dissipative coupled oscillators representing vertices of a graph problem following

$$\dot{\psi}_n = -[i\omega_n + |\psi_n|^2]\psi_n + \sum_{m=1}^{N} J_{nm}\psi_m, \tag{5.1}$$

where $\psi_n \in \mathbb{C}$ gives the dynamics of oscillator n which depends on the oscillator's natural frequency ω_n, some nonlinear interaction (second term) and its coupling to all other oscillators in the system with coupling strength J_{nm} to oscillator m. Note that in Equation 5.1, the pump P is eliminated following the rescaling of Equation 2.14 and the real energy shift from nonlinear interactions is set to $g = 0$ as the dynamics of $\dot{\psi}_n$ are topologically invariant to $g = 0$ and $g \neq 0$ [77], thus eliminating g keeps the model more general and simple.

In polar coordinates, with $\psi_n = \rho_n e^{i\theta_n}$, the density and phase dynamics can be extracted through separating the real and imaginary terms to arrive at,

$$\dot{\rho}_n = -\rho_n^3 + \sum_{m=1}^{N} J_{nm}\rho_n\rho_m \cos(\theta_m - \theta_n) \tag{5.2}$$

$$\dot{\theta}_n = \omega_n + \sum_{m=1}^{N} \frac{\rho_m}{\rho_n} \sin(\theta_m - \theta_n) \tag{5.3}$$

We see that in the last term of Equation 5.3, the phase of oscillators with small amplitudes are strongly affected by those with a greater amplitude. Notably, when all amplitudes are static and uniform, θ_n describes the generalised Kuramoto model [196, 197]. In fact, in the limit of $\rho_n = \rho_0$ and $\omega_n = 0$, the phase-locked states of the Kuramoto model are described by the energy minima of the Lyaponov potential [100],

$$\mathcal{L} = -\sum_{n,m=1}^{N} J_{nm} \cos(\theta_m - \theta_n) \tag{5.4}$$

which is equivalent to the well-known (and highly discussed in this thesis) XY Hamiltonian. Therefore, phase oscillators experience a gradient descent towards the minima of the XY Hamiltonian with $\dot{\theta}_n = -\partial\mathcal{L}/\partial\theta_n$. It has been shown that the performance of Stuart-Landau networks can be improved through the addition of an dynamic gain-feedback mechanism [57]. As such, we too investigate the addition of such a mechanism in subsection 5.4.3. However, we do not employ such a mechanism in the main study of this chapter, as we observe that the minor embedding technique itself helps the oscillator amplitudes to converge without the use of a complex dynamic pumping mechanism. There is no guarantee however that the Stuart-Landau network will relax into the XY ground state, though surprisingly, impressive results have been obtained numerically through direct simulation of Equation 5.1 [57, 2, 124]. In fact, when we compare the performance of randomly-weighted and all-to-all connected Stuart-Landau networks to two commercial optimisers at their ability to minimise the XY Hamiltonian, the Stuart-Landau model outperforms them all.

5.2.1 Benchmarking the performance of Stuart-Landau Oscillators

For this benchmarking, we investigate graphs of $N > 50$ spins (oscillators) using the commercially available GlobalSearch[1] optimiser from the Global Optimisation Toolbox[2] of Matlab^{TM}. This algorithm uses a scatter search method to generate

[1] https://uk.mathworks.com/help/gads/how-globalsearch-and-multistart-work.html
[2] https://uk.mathworks.com/help/gads/

possible trial points that are evaluated using a chosen optimisation method to find local minima.

The algorithm then iteratively analyses points that converge using a score function which continuously updates and rejects points that are unlikely to improve upon the best minimum found so far. We have decided to use two well known optimisation methods for the Global Search algorithm. **(1)** The *trust region* method since we can easily compute both the gradient and the Hessian matrix of the XY Hamiltonian (i.e., the objective function) making it quite fast and accurate and thus an appropriate choice. **(2)** The *sequential quadratic programming* (SQP) gradient descent method since it also benefits from knowing the gradient of the objective function. Our search region is bounded on $\theta_n \in [-4, 4]$ which is taken larger than the periodic range $[-\pi, \pi]$ in order to more efficiently find minima that might be close to values around $\theta_n = \pm\pi$. All other options of the gradient descent algorithm were set to default as they did not considerably improve the efficiency of the optimiser.

We then extract the resulting XY energy from each optimisation technique and quantify the performance between the Stuart-Landau model (with XY energy given by E_{SL}) to the Global Search algorithm (with XY energies E_{GS} respectively), using the ratio of their energy difference,

$$\text{Energy Difference} = \frac{E_{GS} - E_{SL}}{2E_{GS}} \tag{5.5}$$

Here, the factor of $1/2$ scales the Energy Difference to ensure that if $E_{SL} = -E_{GS}$, then the difference is exactly unity. The results of such analysis are shown in Figure 5.1, where we have averaged over 1000 randomly connected dense graphs. The

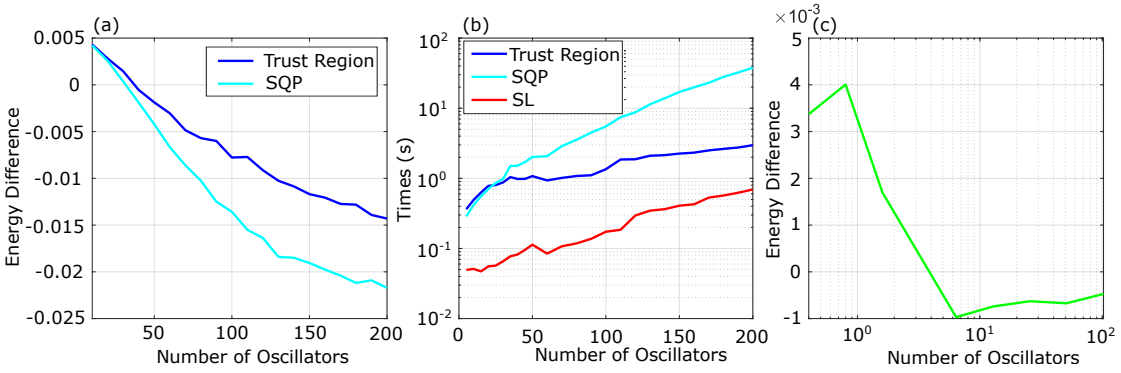

FIGURE 5.1: (a) Average energy difference between the Global Search algorithm and the SL model according to Eq. (5.5) with the GS algorithm using two different optimiser approaches, trust region and SQP. The SL model outperforms the Global Search algorithm around $N \approx 30$ spins. (b) Time taken for different methods to arrive at an answer for the XY energy. (c) Energy difference between the Kuramoto and the Stuart-Landau models [i.e., E_{GS} is replaced with E_{KM} in Eq. (5.5)]. The SL model outperforms the KM model in finding low energy values to the XY Hamiltonian at around $N \approx 30$.

edge weights are chosen on the interval of $[-1, 1]$ and up to $N = 200$ spins are considered. Amazingly, even after supplying knowledge of the gradient and the Hessian of the objective function for the commercial optimisers, the Stuart-Landau model starts to outperform the Global Search algorithm around $N \simeq 30$ spins. In Figure 5.1, we plot the computational time taken for the two algorithms to provide a solution and for the Stuart-Landau model to reach a steady state. This shows that the Stuart-Landau model is vastly more efficient as an optimisation method than the Global Search algorithm at enumerating the XY Hamiltonian.

We additionally consider the performance of the Stuart-Landau model compared to the Kuramoto model (Equation 5.3 with $\rho_n = \rho_m$) at minimising the XY Hamiltonian. In Figure 5.1(c), we show the average energy difference between the two models over 1000 randomly connected dense graphs. Amazingly, around $N \simeq 30$ spins (oscillators), the Stuart-Landau model starts to outperform the Kuramoto model - a known heuristic solver that directly maps to the minimisation of the XY energy [55]. This demonstrates that Stuart-Landau oscillators are more efficient at exploring their state space during the transient growth phase (period of small t in numerical integration where $|\psi_n|$ rapidly grows) from the initial vacuum state $|\psi_n(t = 0)| \simeq 0$, as opposed to the Kuramoto oscillators which are fixed to the complex unit circle.

5.3 Minor Embedding

5.3.1 Triad Graph

In order to create the triad graph, we must first consider the undirected all-to-all coupled graph, known mathematically as the *complete graph*, which is labelled as K_N in the case of N vertices. A schematic is shown in Figure 5.2(a) for the K_5 graph. The complete graph consists of vertex set $V(K_N)$ connected by edge set $J(K_N)$. Each vertex V_n, with assignment index n, is connected symmetrically to all other vertices in the graph, such that any two vertices V_n and V_m are connected by an edge with weight $J_{nm} = J_{mn}$.

In the process of minor embedding, we map K_N to the triad graph K_N^{emb} (Figure 5.2(c)) through expanding each vertex $V_n \in V(K_N)$ to a chain of uniformly coupled vertices of length $N - 1$, with an intra-chain edge weight of

$$J^{\text{intra}} = J_c, \qquad \text{(coloured edges)}. \tag{5.6}$$

Each vertex of the chain is adjacent to a single vertex of a another chain with inter-chain edge weights,

$$J^{\text{inter}}_{n,m} = J_{n,m}, \quad \forall\ J_{n,m} \in J(K_N), \quad \text{(black edges)}. \tag{5.7}$$

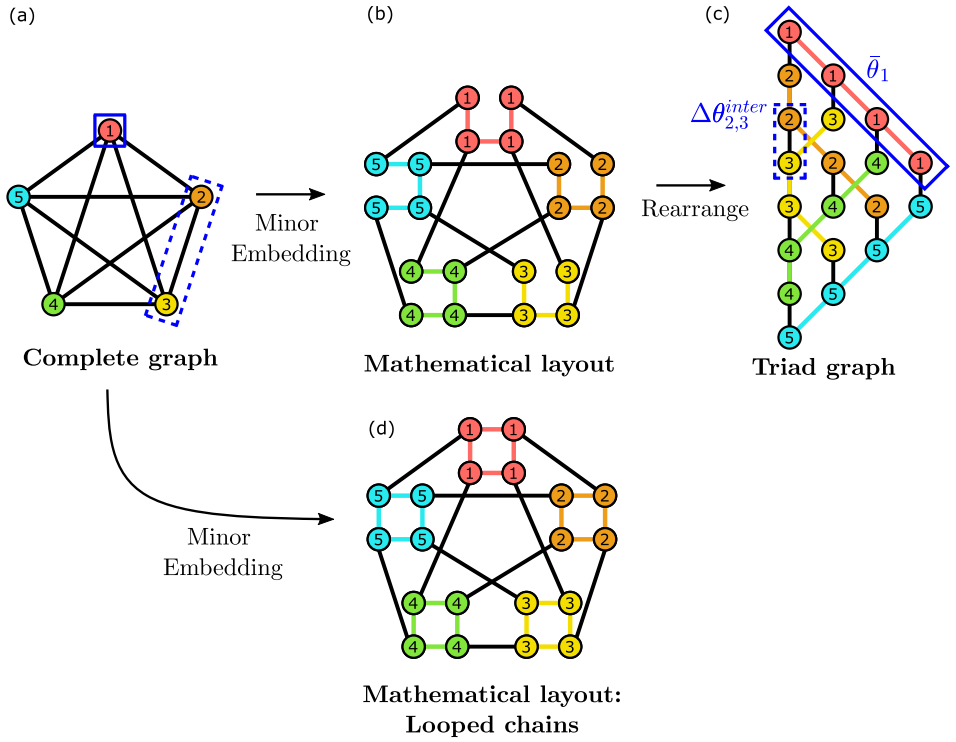

FIGURE 5.2: (a) K_5 graph mapped through minor embedding to (b) the K_5^{emb} triad graph, (c) the mathematical layout of K_5^{emb} and (d) when including N additional edges to loop the chains. In (b-d), the FM chain couplings are shown by coloured edges $J^{\text{intra}} = J_c$ and the encoded coupling strength of K_5 are shown by black edges, such that $J^{\text{inter}}_{n,m} = J_{n,m}$. The blue solid and dashed boxes overlayed on (a,b) demonstrate two possible phase extraction methods for the unembedded and embedded XY energies from the triad graph respectively.

The resulting triad graph consists of vertex set $V^{emb}(K_N^{emb})$ containing $N(N-1)$ vertices labelled V_n^{emb}, connected by edges in the set $J^{emb}(K_N^{emb})$ containing $\frac{N(N-1)}{2}$ inter-chain edges labelled J_{nm}^{inter} and $N(N-1)$ intra-chain edges J_{nm}^{intra}. Physically, $J_c > 0$ gives precedence to in-phase locking within each chain, which in the context of spin Hamiltonians is considered as an FM coupling, where the oscillator phasors $\mathbf{s}_n = [\cos(\theta_n), \sin(\theta_n)]^T$ take the role of 2D spins. The aim of the FM intra-chain coupling is to minimise the deviation of phase within each chain in order to best mimic the dynamics of complete graph K_N [162], and reduce the spread of oscillator amplitudes across the chain. In other words, the red vertex of K_5 indicated by the solid blue box in Figure 5.2(a) (described by ψ_1 in Equation 5.1) is represented by the average dynamics of the phase and amplitude oscillators making up the chain of 4 red oscillators in the triad graph (blue box in Figure 5.2(c)). Note, the number of black edges in the complete and triad graphs are the same, as they are equivalent.

In building the triad structure from a complete graph, it can be easier to visualise the process in the mathematical layout (Figure 5.2(b)), where each vertex of the complete graph is expanded to a chain of length $N-1$ about its original vertex site. The triad graph is then formed through simply rearranging the vertices onto a square lattice,

which we label as the hardware layout, as the adjacency of the mathematical layout (Figure 5.2(b)) and hardware layout (Figure 5.2(c)) are equivalent. We also consider the addition of an edge between the first and last vertices in each chain, thus "looping" the chains such that every vertex (Figure 5.2(d)) has a uniform degree of connectivity. Experimentally, this is difficult to realise in most oscillator platforms, but we theoretically compare the unlooped and looped triad graphs' synchronisation dynamics and ability to minimises the XY Hamiltonian of the encoded complete graph in order to discern how the more "symmetric" connectivity affects the performance of the triad structure.

This study works close to the system's bifurcation that separates the *normal states* $\rho_n = 0$ from the *oscillatory states* $\rho_n \neq 0$, thus we are interested in the average oscillator phase across each chain, written as

$$\bar{\theta}_n = \frac{1}{N-1} \sum_{n' \in chain}^{N-1} \theta_{n,n'} \tag{5.8}$$

where n is the index of the chain and n' denotes the location within a given chain.

We refer to the phase averaging as "unembedding", as the act of doing so reduces the minor embedded graph back down to the original K_N structure [198, 199].

5.3.2 XY Energy Extraction

Each oscillator of the complete graph is associated with some complex parameter ψ_n, which contains the state information of the n^{th} oscillator. From this, we can define the state vector $\boldsymbol{\psi} = [\psi_1, \psi_2, \ldots, \psi_N]^T$ and corresponding phasors $\boldsymbol{\theta} = [\theta_1, \theta_2, \ldots, \theta_N]^T$. The XY energy associated with complete graph K_N is written:

$$H_{XY} = -\sum_{n,m}^{N} J_{nm} \cos(\theta_m - \theta_n). \tag{5.9}$$

However, for the triad graph, we can extract the XY energy for its encoded complete graph using two methods. The first takes the average phase across each triad chain to unembed the triad graph back down to the complete graph, following Equation 5.8, as shown by the solid blue boxes in Figure 5.2(a,c). We refer to this as the "unembedded energy" and define it as,

$$H_{XY}^{unemb} = -\sum_{n,m}^{N} J_{nm} \cos(\bar{\theta}_m - \bar{\theta}_n). \tag{5.10}$$

The second method uses the relative phase $\Delta\theta_{nm}^{inter}$ between each pair of oscillators connected by a black edge, akin to $\theta_m - \theta_n$ in Equation 5.9 (see dashed blue boxes in Figure 5.2(a,c)). This is labelled as the "embedded energy" as the vertices are still in the triad structure and is written as,

$$H_{XY}^{emb} = -\sum_{n,m}^{N} J_{nm} \cos \Delta\theta_{nm}^{inter}. \tag{5.11}$$

If $J_c = 0$, the minimisation of H_{XY}^{emb} is trivial, as the graph formed is a set of individual oscillator pairs connected by J_{nm}.

The aim of this study it to compare the triad graph to its encoded complete graph at synchronisation dynamics and ability to minimise the complete graph XY Hamiltonian in order to find the parameter space for which the triad structure correctly represents its encoded complete graph.

5.4 Results

5.4.1 Coherence Properties

We numerically investigate the degree of coherence in oscillator dynamical networks in complete and triad graph structures in order to compare their ability to synchronise to inphase spin configurations. We consider the FM graph of oscillators coupled equally to all others with $J_{nm} = J > 0$. Oscillator frequencies ω_n are chosen randomly from a normal distribution $g(\bar{\omega})$, with a dimensionless standard deviation of $\sigma = 1$. Naturally, we choose a rotating frame with frequency $\bar{\omega}$ such that $\bar{\omega} = 0$ without loss of generality. The oscillator coupling matrix $\mathbf{J} = (J_{nm}) \in \mathbb{R}^{N\times N}$ always has at least one positive eigenvalue for all graphs considered in this study, which means that the trivial $\rho_n = 0$ steady state is never stable (see subsection 2.1.2 for detailed explanation), thus the phases θ_n are well defined at all times.

In order to quantify the emergent coherence properties we define a phase order parameter, commonly used in the analysis of such oscillatory systems [100], which captures the degree of coherence between the oscillators. For the complete graph, we define this order parameter as,

$$r_{\text{complete}} = \frac{1}{N}\left|\sum_{n=1}^{N} e^{i\theta_n}\right|. \tag{5.12}$$

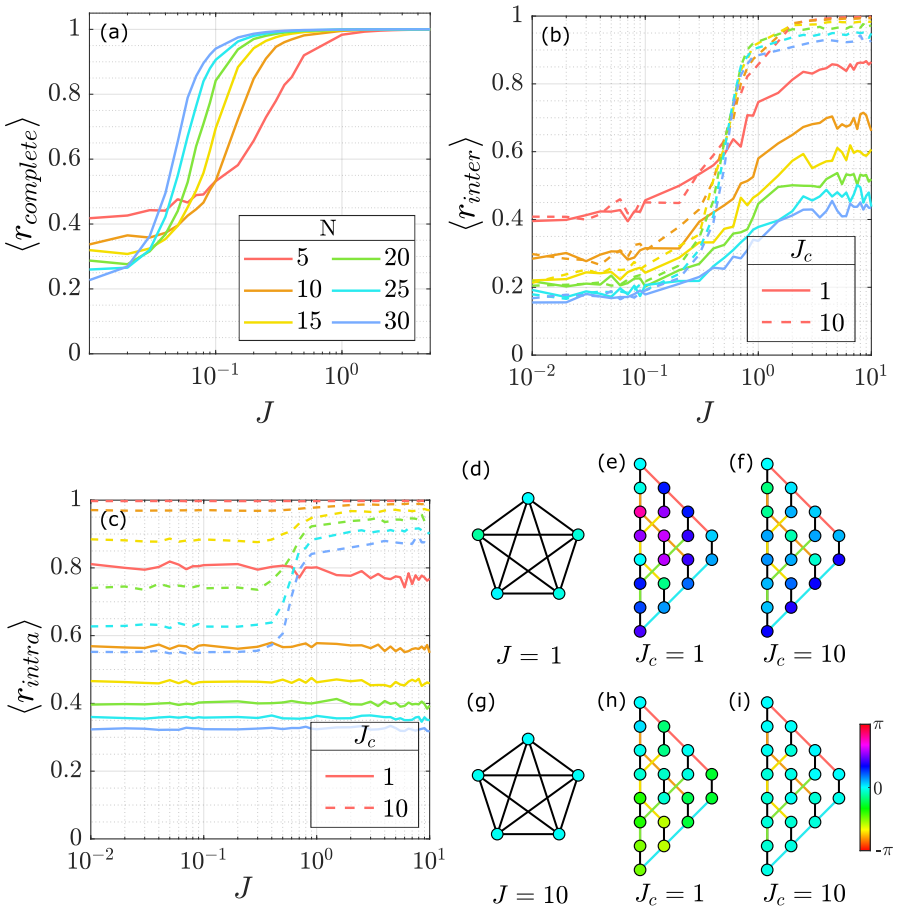

FIGURE 5.3: Coherence of (a) $\langle r_{\text{complete}} \rangle$ for uniform FM coupled complete graphs with coupling strength J, (b) $\langle r_{\text{inter}} \rangle$ and (c) $\langle r_{\text{intra}} \rangle$ for the corresponding triad graphs. All results are averaged over 160 instances of ω_n and random initial conditions. Example steady state phases of $N = 5$ oscillators in the (d,g) complete and triad structures with (e,h) $J_c = 1$ and (f,i) $J_c = 10$ for a single instance. (d-f) $J = 1$ and (g-i) $J = 10$, where the phases are indicated by vertex colour.

If all oscillators have the same phase $\theta_n = \theta_m$, then $r_{\text{complete}} = 1$. Alternatively, for infinitely many uniformly randomly-distributed phases on the interval $[0, 2\pi)$, then $r_{\text{complete}} = 0$.

We numerically integrate the Stuart-Landau model (Equation 5.1) of the FM complete graph from $t = 0 \to T \gg J^{-1}, J_c^{-1}$ and calculate the average coherence $\langle r_{\text{complete}} \rangle$ at the final time $t = T$ over 160 random realisations of ω_n and initial conditions (Monte Carlo sampling). We repeat these calculations over a range of coupling strengths J (show in Figure 5.3(a)) and observe the gradual transition from an incoherent to coherent state with increasing J.

This build up in coherence is reminiscent of the coherence bifurcation characteristic to the Kuramoto model [197, 100], where $r_{\text{complete}} = 0$ (the incoherent state) is stable below some critical coupling strength J_{crit}, defined in the limit of $N \to \infty$. As J is increased through and above J_{crit}, the system reaches a partially synchronised state with $0 < r_{\text{complete}} < 1$, for which oscillators at the centre of $g(\bar{\omega})$ are synchronised,

while those at the tails of the distribution remain incoherent, such that the system is split into two dynamical groups [200]. As J is increased further, more oscillators join the synchronised group until the entire system becomes coherent [196, 201], as we too observe with the Stuart-Landau oscillators. Finite size effects are clearly observed in Figure 5.3(a) with changing N. Notably, larger J is required in order for the system to synchronise smaller networks and leads to a finite minimum coherence as J tends to 0, which gradually decreases as N gets larger.

Now we move on to the triad graph. Similarly to the complete graph coherence defined in Equation 5.12, we define the phase order parameter to quantify the degree of coherence between the unembedded (chain-averaged) phases of the triad graph,

$$r_{\text{inter}} = \frac{1}{N}\left|\sum_{n=1}^{N} e^{i\bar{\theta}_n}\right|, \tag{5.13}$$

and the average phase coherence within each chain of the triad,

$$r_{\text{intra}} = \frac{1}{N}\sum_{n=1}^{N} \underbrace{\frac{1}{N-1}\left|\sum_{n'\in\text{chain}}^{N-1} e^{i\theta_{n,n'}}\right|}_{r_n^{\text{intra}}}. \tag{5.14}$$

All three degrees of coherence are visually presented in Figure 5.4, where the chain averaging is again represented by a blue box on the complete and triad graph and the red box indicates a chain for which we calculate its coherence in the first sum of

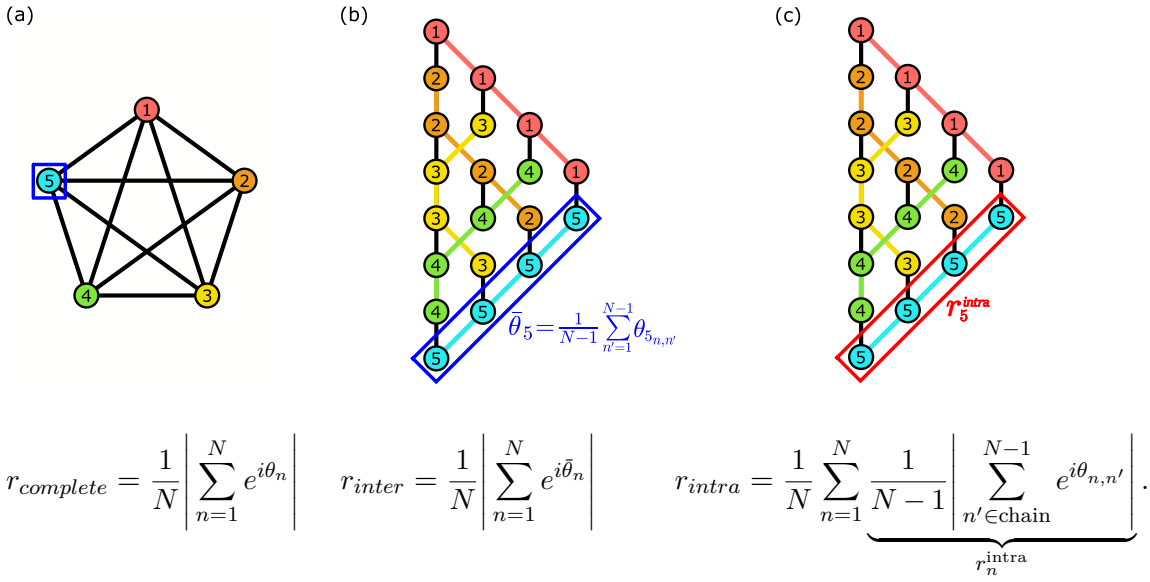

FIGURE 5.4: (a) Coherence extracted over all oscillators in the complete graph, (b) the unembedded triad coherence between the N average chain phases, plus (c) the average chain coherence. All schematics represent the K_5 and K_5^{emb} graphs with the blue boxes in (a,b) and red box in (c) representing the extraction of the average phase and coherence across chain 5 respectively.

Equation 5.14. The triad graph coherence parameters are also averaged over 160 realisations, denoted by $\langle\cdot\rangle$.

We consider two embedding parameters $J_c = \{1, 10\}$ and investigate the triad graph coherence in relation to the complete graph. Lower and higher values of J_c did not qualitatively change the findings. Oscillator frequencies ω_n are chosen randomly from $g(\bar{\omega})$ across all oscillators in order to best represent the experimental reality, such that there is no single energy across each triad chain. As seen in Figure 5.3(b,c), for smaller J_c the inter-chain and intra-chain coherences are low and show a weak dependence on coupling strength. However, for larger J_c we observe a fast inter-chain coherence transition in Figure 5.3(b), which indicates that the triad graph has managed to correctly represent the embedded complete graph under the conditions of $J/J_c < 0.1$. This figure of merit will be useful in future experimental design requirements. Interestingly, for larger J, the inter-chain coherence is smaller for larger graphs, as opposed to the smaller coherence of smaller complete graphs seen in Figure 5.3(a) (i.e. the order of the lines has flipped). This is attributed to the fact that chains themselves need to be coherent in order to correctly represent their embedded complete graphs, and as longer chains struggle to settle into a coherent phase configuration (Figure 5.3(c)), the coherence reduces with increased N for the triad graph. Overall, we see that as J and J_c are increased, both the inter-chain and intra-chain degrees of coherence converge to unity. Figure 5.3(d-i) schematically shows the simulation results of varying J and J_c, where vertex colours correspond to the steady state oscillator phases. By eye, it is plain to see that the spread of oscillator phases does reduce with increasing J_c, but is effected more significantly by the increase in J.

We repeat this study, but his time with looped triad chains (depicted in Figure 5.2(d)), where the results are shown in Figure 5.5. In comparison to the unlooped triad chains, there is a slight increase in r_{inter} and r_{intra} across varying N, which is particularly

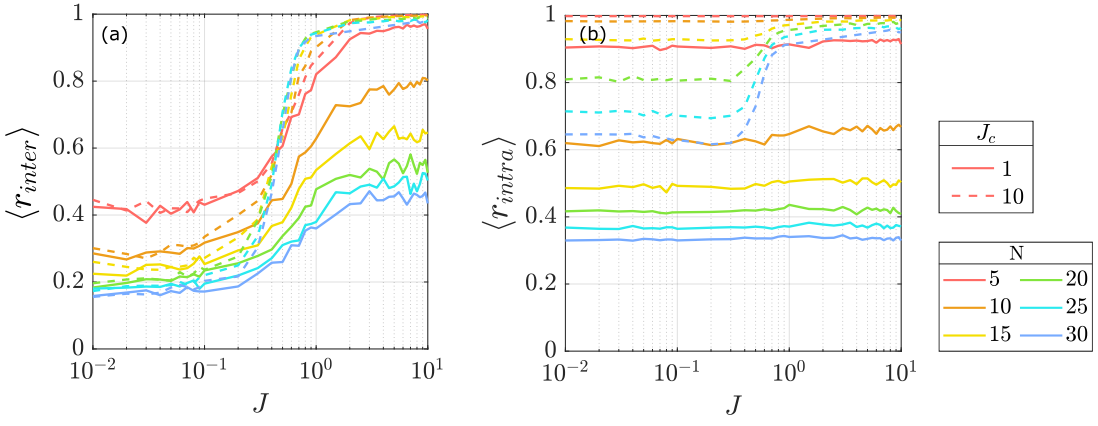

FIGURE 5.5: Coherence (a) $\langle r_{inter} \rangle$ and (b) $\langle r_{intra} \rangle$ of triad graphs corresponding to uniform FM complete graphs with looped chains and $J_c = 1$ and 10. All scanned over a range of coupling strengths J and averaged over 160 instances with standard deviation in oscillator frequencies $\sigma = 1$.

noticeable for $J_c = 10$ and larger J. Overall however, looping the triad chains introduces very minor changes to the system's coherence.

5.4.2 XY Energy

Here, we investigate the feasibility of minor embedding the complete graph to the triad graph of Stuart-Landau oscillators at optimising the XY Hamiltonian. We compare the unembedded and embedded complete graph XY energies (Equation 5.10 and Equation 5.11) extracted from the triad graph, to the ground state energy calculated using the classical basin hopping method [125]. We define the performance of the Stuart-Landau system as the normalised difference in extracted XY energies of the triad or complete graphs of Stuart-Landau oscillators, E_{SL}, compared to the complete graph XY energy solved using the basin hopping technique, E_{BH},

$$\text{Error} = \frac{E_{BH} - E_{SL}}{E_{BH}}. \tag{5.15}$$

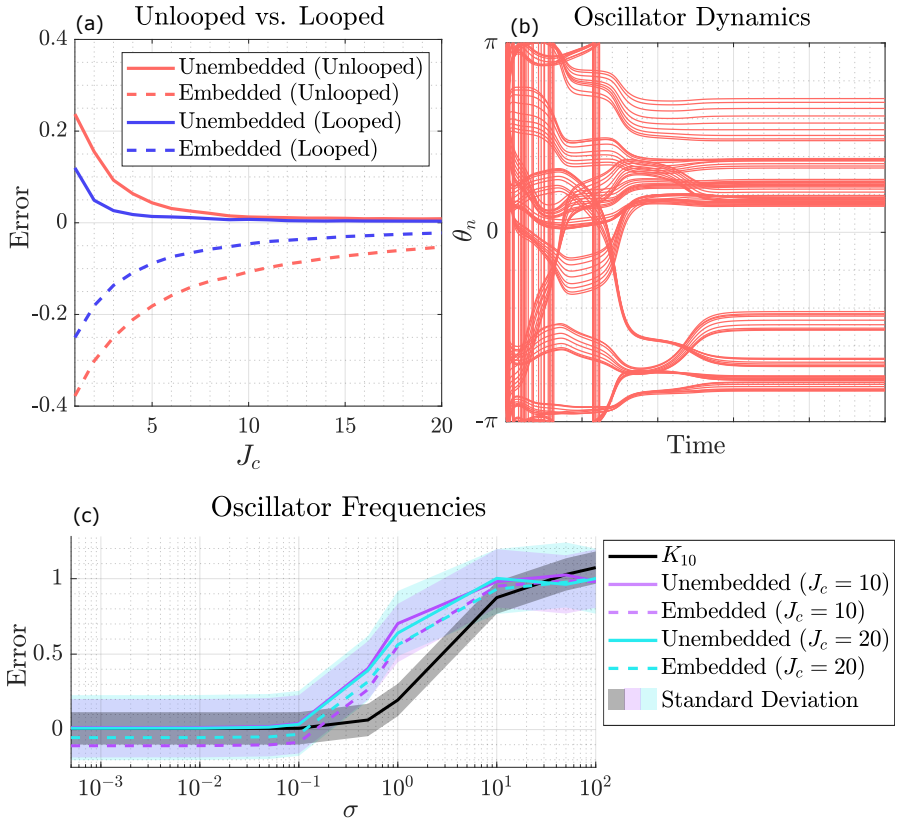

FIGURE 5.6: (a) Error between the Stuart-Landau model and the classical-basin hopping method in minimising the XY Hamiltonian on a randomly connected complete graph with $\sigma = 0$. (b) The phase dynamics of the triad graph oscillators for a single random graph with $J_c = 10$. (c) Distribution of oscillator energies with unlooped triad chains and the complete graph, with translucent surfaces to represent the standard deviation in error of the unembedded energies.

We perform this benchmarking over 160 unique complete graphs where each edge weight is randomly and independently selected from a uniform distribution $J_{nm} \in [-1, 1]$. Note that there is no qualitative difference in using a normal distribution with the same variance. To find the optimum embedding, we first consider $N = 10$ over a range of embedding parameters J_c with both unlooped and looped triad chains. These initial results are shown in Figure 5.6(a), where all oscillators are given the same natural frequency (i.e. $\sigma = 0$). Clearly, the error reduces with increasing J_c, with the unembedded energy error converging to 0 faster than the embedded error, suggesting that taking the average phase across each chain allows the triad structure to best mimic its encoded complete graph dynamics. This is an expected result, as larger J_c reduces the distribution of phase across each chain, thus achieving a better representation of the complete graph and corroborates with Figure 5.3(b). Interestingly, with the addition of looped triad chains the error reduces as a result of the reduced spread in phase distribution (and increased coherence) that we previously saw in Figure 5.5. The negative error in Figure 5.6(a) stems from the fact that $\min[H_{XY}^{emb}] < \min[H_{XY}]$ when $J_c \to 0$. In this limit, the triad graph is broken down into N independent pairs of oscillators connected only with black edges. The sum of all their XY energies is trivially minimised through setting the relative phases between oscillator pairs to $\Delta\theta_{nm} \in \{0, \pi\}$ for positive and negative couplings respectively. As we see in Figure 5.6(b), the phase dynamics of $\theta_n(t)$ over the $N(N-1) = 90$ triad oscillators split into N moving paths, each corresponding to a different triad chain.

When a random distribution of ω_n is included in the oscillator dynamics ($\sigma > 0$), the XY energy error grows with the increase in σ, as shown in Figure 5.6(c). The spread in

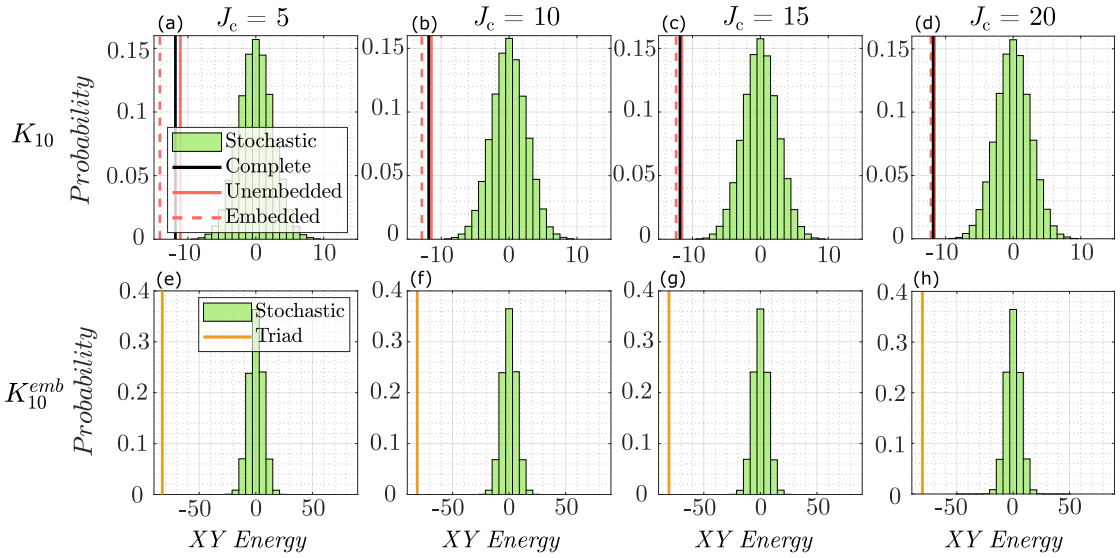

FIGURE 5.7: (a-d) XY energy from a single random K_{10} graph and extracted embedded and unembedded energies from the corresponding triad graph compared to the XY energy from 10^4 random phase configurations. (e-h) XY energy of the K_{10}^{emb} graph compared to the XY energy of 10^4 random phase configurations. Each column representing $J_c = 5, 10, 15$ and 20 respectively.

ω_n leads to oscillator desynchronisation and loss of the steady state as no well defined phase relation can enter the XY Hamiltonian. The error becomes non-negligible for $\sigma \simeq 0.1$ for both the complete and triad graphs of Stuart-Landau oscillators, showing the limit in ability of Stuart-Landau oscillators at minimising the XY Hamiltonian. We further compare the complete and triad graph energies to randomly sampled phase configurations, shown in Figure 5.7. Here, we plot histograms of complete graph XY energies extracted from K_{10} and K_{10}^{emb} for 10^4 random phase realisations alongside the extracted XY energies from the Stuart-Landau networks of complete and triad graphs with $\sigma = 0$. As J_c increases, the unembedded and embedded triad energies converge to the complete graph energy (Figure 5.7(a-d)) and the XY Hamiltonian of the entire triad graph of oscillators is minimised for all J_c (Figure 5.7(e-h)). This confirms that Stuart-Landau oscillators always minimise the XY energy of the triad graph in the limit of small σ, but the ground state triad phase dynamics converge to those of the unembedded triad graph when J_c is maximised.

Lastly, we show the triad graph's performance as minimising the complete graph XY Hamiltonian as a function of problem size (network size) N, and embedding parameter J_c (Figure 5.8). We see that the error converges to zero as J_c increases, with better performance from the unembedded XY energy. As expected, larger networks struggle to find the correct global ground state as they instead settle into the growing number of local minima in the system. Interestingly, the unembedded error from the looped triad chains (Figure 5.8(b)) plateaus beyond $J_c = 10$ and indicates that the benefit of chain looping that we noticed previously is only apparent for $N \leq 10$. This puzzling behaviour implies that looping the chains of the triad graph generates a new family of state attractors that do not correlate with the optimisation of the XY Hamiltonian. Such attractors likely correspond to the appearance of twisted states within the looped

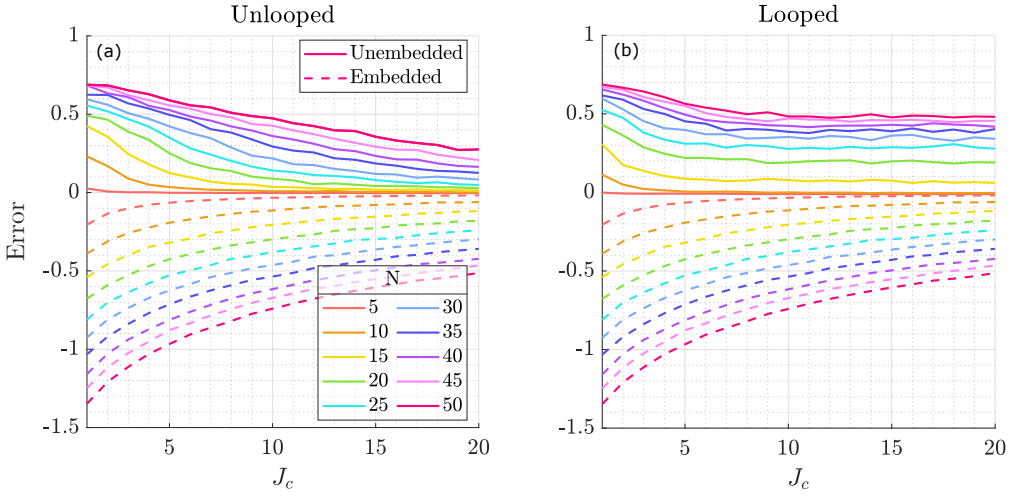

FIGURE 5.8: XY energy error from the triad structure of Stuart-Landau oscillators compared to the complete graph XY energy solved using the basin hopping method for (a) unlooped and (b) looped triad chains with $N = 5$ to 50, averaged over 160 random graphs and $\sigma = 0$.

triad chains, where such states commonly appear in large sparsely connected networks of oscillators [202].

5.4.3 Dynamic Pumping

Clearly the Stuart-Landau model is an robust heuristic minimiser for the XY Hamiltonian which can out-perform multiple other optimising algorithms and heuristic solvers [see subsection 5.2.1], but as the oscillator amplitudes are not equal across the system, the fixed point attractor of the oscillator steady state is in fact approximated and not minimised exactly. As a possible improvement, we investigate the addition of a dynamic pumping mechanism that feeds back the amplitude of each oscillator at each step in numerical integration in order to adjust the gain of each node respectively. To explore this feedback mechanism, we adjust Equation 5.1 slightly to follow:

$$\frac{d\psi_n}{dt} = [P_n(t) - i\omega_n - |\psi_n|^2]\psi_n + \sum_{m=1}^{M} J_{n,m}\psi_m. \tag{5.16}$$

Here, P_n is the pumping rate of oscillator ψ_n in arbitrary units of time, where initially all oscillators are injected equally with $P_n(0) = 0$ for all n. After the initial pumping in the first time step of integration, we apply a feedback mechanism to balance the occupation of each oscillator, following:

$$\frac{dP_n(t)}{dt} = \epsilon\left(\rho_t - \rho_n(t)\right) \tag{5.17}$$

where ϵ is the parameter that controls the rate of change of P_n such that $\epsilon = 0$ makes Equation 5.16 identical to Equation 5.1, ρ_t is the target density of the oscillators and $\rho_n(t)$ is the density of oscillator n at time t, given by $|\psi_n(t)|$. This approach is similar to the feedback mechanism of [124]. We numerically integrate Equations 5.16 and 5.17 for 100 randomly-connected complete graphs and corresponding triad graphs with varying N, with $\epsilon = 0$ and $\epsilon = 0.04$. The resulting energy error (as defined by Equation 5.15) and standard deviation of amplitudes across each oscillator network is shown for randomly connected triad graphs with $J_c = 20$ in Figure 5.9, where the results are averaged over the 100 unique graphs.

We do indeed see a drop in XY energy by less than 1% for all N when $\epsilon = 0.04$, compared to $\epsilon = 0$. From the amplitude dynamics of a K_5 random graph and corresponding K_5^{emb} in Figure 5.9, we see that the relative spread of amplitudes reduces for the triad graph compared to the complete graph when there is no feedback. Additionally, due to the large coupling strengths from the intra-chain couplings in the triad graph, the rate of change of ψ_n is increased and the steady state is reached an order of magnitude sooner than for the equivalent complete graph. When $\epsilon = 0.04$, the

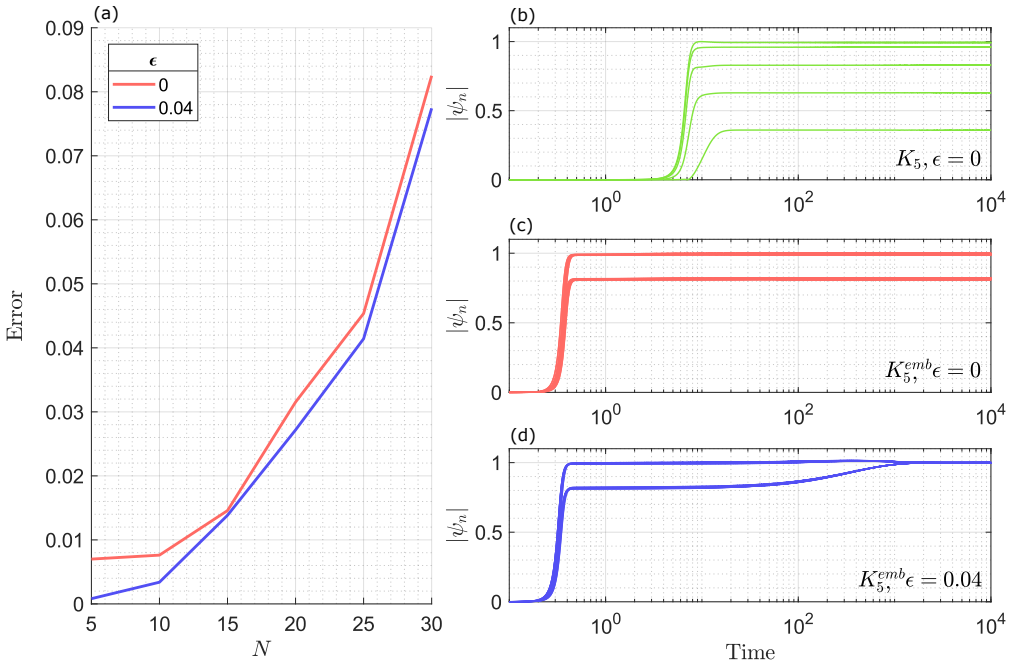

FIGURE 5.9: (a) Unembedded energy error of randomly connected triad graphs with (red) $\epsilon = 0$ and (blue) $\epsilon = 0.04$ with $J_c = 20$ over a range of N, averaged over 100 unique random graphs realisations. Oscillator amplitude dynamics for (b) a randomly connected K_5 graph with $\epsilon = 0$, and the corresponding $J_c = 20$ triad graph with $N(N-1) = 20$ vertices, for (c) $\epsilon = 0$ and (d) $\epsilon = 0.04$. Amplitudes normalised to $\max|\psi_n|$ and $\rho_t = \max|\psi_n|$.

oscillator amplitudes converge with a standard deviation of 3.84×10^{-5}, though the energy error reduces by less than 1%.

As the inclusion of ϵ has such a small effect on the XY energy of triad graphs, we argue that the inclusion of the feedback mechanism is not crucial to this investigation. The message of this study is that a technique has been found and characterised for dissipative oscillator systems to map arbitrarily-weighted complete graphs to a simple and experimentally-practical configuration, where, in practice, applying a feedback pumping mechanism greatly complicates the experimental method. Instead, this study shows that the XY energy can be optimised by increasing the intra-chain coupling strength of the minor embedded graph, which forces the chain of oscillators to follow the same phase dynamics. To top this off, we also show that the Stuart-Landau network without a feedback mechanism in fact outperforms two commercial optimisers and the Kuramoto model (whose fixed point attractor corresponds to the minimised XY energy) at minimising the XY Hamiltonian for sufficiently large networks (large N).

To summarise, the minor embedding technique applied to the randomly weighted complete graph to form the triad graph proves to be a promising method in realising the XY ground state of a complete graph using 2D optical annealing platforms, such as polariton condensates. The triad graph has best success at annealing the complete

graph XY Hamiltonian when the chain coupling strength is taken to be sufficiently large compared to the complete graph edge weights, where as the number of complete graph oscillators increases, so does the required chain coupling strength. However, the inclusion of gain feedback to balance the oscillator intensities has little affect on the triad graph's ability to minimise the XY Hamiltonian of its encoded complete graph.

5.5 Conclusions

In this chapter, it was demonstrated that the dynamics of all-to-all coupled Stuart-Landau networks can be approximated through applying a minor embedding to the triad graph. This technique is not new, but is in fact regularly used in the field of quantum annealing [180]. Here, we compare the (dense) complete graph to the (sparse) triad graph - defined by a single embedding parameter J_c - through their synchronisation dynamics and ability to minimise the all-to-all connected XY Hamiltonian. The triad graph managed to represent the encoded complete graph synchronisation dynamics under the condition of $J/J_c < 0.1$, however a greater coupling strength is required in order to fully synchronise the triad graph as the embedded chains need to first be synchronised in order to see growth in the inter-chain coherence. We show that the steady state phases in the minor embedded graph can optimise the XY Hamiltonian of the encoded complete graph and achieve good performance by simply increasing J_c. By introducing some spread in oscillator energies, the error of the Stuart-Landau network's ability to minimise the XY Hamiltonian grows and becomes non-negligible around $\sigma \simeq 0.1$ for a random uniform sampling of all $J_{nm} \in [-1, 1]$. For $\sigma = 0$, we compare Stuart-Landau networks to the classically solved ground state and stochastic random phase configurations.

When the Stuart-Landau model is benchmarked against two commercial optimisers and the Kuramaoto model at minimising the XY Hamiltonian, amazingly the Stuart-Landau networks outperformed all other optimisation techniques for sufficiently large graphs. The convergence of the triad graph dynamics to the complete graph of Stuart-Landau oscillators offers up the triad graph as a potential test-bed for which to map dense graph problems using continuous phase oscillators, such as polariton condensates, photon condensates and coupled laser arrays. This open up perspectives on designing analogue computing hardware aimed at solving dense graph problems (such as minimising the XY Hamiltonian) across a wide range of platforms in a similar spirit to superconductor quantum annealing platforms.

Chapter 6

Quantised Vortices in Optically Stirred Polariton Condensates

6.1 Introduction

Quantised vortices are topological objects representing circular motion in a fluid, characterised by integer (ℓ) multiples of 2π phase rotation about a core, where the topological charge of a vortex is represented by winding number ℓ. Unlike classical fluids, such as a cup of tea that rotates like a rigid body when stirred, superfluids of quantum matter can support these rotational flows when stirred above some critical velocity [203], where for a small enough rotation frequency, little to no motion of the fluid is observed; yet above a critical frequency, the phase singularity appears with a current proportional to its surrounding phase gradient. Such stirred quantum vortices have been observed in superfluid Helium and atomic gas condensates [204, 205], such as with ^{4}He contained in a rotating bucket, which lowers the free energy in the system through spontaneous nucleation of quantum vortices carrying $\ell\hbar$ orbital angular momentum (OAM) to match the rotation of the container [206]. However, there has been little investigation into the rotation (via optical stirring) of driven-dissipative quantum fluids, which are not dictated by the energy minimisation principles, but the balance between gain and loss instead.

Vortices have been studied in a myriad of physical systems, such as superconductors [207, 208, 209, 210], magnetic systems [211, 212] (which has led to the development of vortex based random access memory (RAM) [213, 214, 212], as controlled vortex networks can be used for the storage and processing of binary information), atomic condensates [215, 205, 216] and nonlinear optics [217, 218, 219]. More recently, there have been many studies of vortices in polariton condensate systems [220, 122, 221, 222, 223, 224, 225, 226, 227]. Polariton condensates are an ideal platform for investigating quantum vortices, which have integer phase winding ℓ and

carry $\ell\hbar$ OAM, as the excitonic component of the polariton leads to long coherence times and the photonic component allows for great dynamic optical control of the trapping potential using an SLM. Additionally, the excitonic component means that the particles interact, giving rise to strong nonlinear dynamics.

Polariton condensate vortices are classified into two groups. The first being spontaneous vortices, which arise from homogeneous or broad pumping profiles and form from fluctuation in the condensate field due to the random initial conditions in numerical simulation and optical misalignment or sample defects in experiment [220, 122, 228, 229, 227]. These spontaneous vortices form in vortex-antivortex pairs, such that the average OAM across all polaritons in the system cancels out and converges to zero. The second group corresponds to stimulated vortices which form from using a spatially inhomogeneous pump such as an annulus [230, 231, 221, 222, 223, 224, 232], an ellipse [233] or a polygon of tight Gaussian spots [234]. This group of vortices are not especially sensitive to noise, but instead the winding number ℓ and vortex location are determined by the pumping profile. However, due to pump symmetry, the sign of ℓ is stochastic with each realisation. Typically, a single vortex will form at the pump centre, but if the optical trap is spontaneously adjusted to a broad homogeneous pump, then the imprinted vortex will spiral about the condensate and potentially leave the system [223].

In this chapter, we break the axial symmetry of the annular pump and investigate a quasi-elliptical trapping profile that confines a dipole mode ψ_{10}; a ground state condensate in one direction and first excited state condensate in the perpendicular direction. This alone does not bring vorticity to the system, but as the pump is rotated about its centre with increasing rotation frequency F, the imbalance of positive and negative OAM leads to the formation of a quantised vortex within the polariton condensate and new energy modes in the system can be described following Floquet theory. By varying the rotation frequency and trap diameter, we map out regions of deterministic condensation into a vortex that co-rotates or counter-rotates with the trap rotation, regions where a quantised vortex can stochastically occupy either rotation direction and regions where no vortices are observed.

The work in this chapter is currently being collated into a manuscript for submission to a Nature-group journal and is authored by Ivan Gnusov, myself, Helgi Sigurdsson, Sergey Alyatkin, Kirill Sitnik, Julian Töpfer and Pavlos Lagoudakis. Ivan built the optical setup and carried out the experiments with the support of Sergey Alyatkin, Kirill Sitnik and Julian Töpfer, and I ran the simulations and analysis of the resulting polariton OAM with guidance from Helgi Sigurdsson, who developed the theory to describe the deterministic obervation of co-rotating and counter-rotating vortices compared to the trap rotation (subsection 6.4.3). The manuscript is being written from the perspective of the experimental work, but this chapter is written from the simulation point of view and will cover the technical numerical aspects and the criteria

for confirming a vortex sighting, as well as presenting the key experimental results and discussing the theory describing these observations.

6.2 Trapping Potential

In this study, we require an optical trapping potential that breaks axial symmetry in order to stir the condensate when rapidly rotated. The first pump profile that comes to mind is simply the elliptical ring studied previously with polariton condensates [235, 233] which is uniform in intensity about the ellipse's perimeter. However, despite previously being studied and characterised in the static regime, the experimental rotation frequency of such an excitation profile is capped by the frame rate of the SLM (∼60 Hz). The period of such a frequency is many orders of magnitude longer than the picosecond timescales of the system dynamics, and as such, a 60 Hz trap rotation will have a negligible effect on the resulting condensate.

Rapid trap rotations have previously been studied in the field of atomic condensates, where the superposition of two vortical modes modulated with a small frequency offset and difference in winding number leads to a much faster rotating trap profile [236]. We employ this technique through the combination of two annular pumps with quantised phase windings co-propagating with the same polarisation, but with differing winding numbers ℓ_1 and $\ell_2 = \ell_1 - \Delta\ell$. The recombination of these two beams leads to the constructive interference at $\Delta\ell$ azimuthal positions, such that $\Delta\ell$ equidistant petals make up the resulting beam pattern. By fine tuning the laser cavity lengths, it is possible to produce two beams with frequencies f_1 and f_2, where the frequency difference $\Delta f = f_1 - f_2$ can reach the order of hundreds of GHz. Each SLM produces a rotating phase front following $E_{1,2} \propto e^{i(\ell_{1,2}\theta - \omega_{1,2}t)}$, where θ is the angle of the trap rotation in the plane of the microcavity in the anticlockwise direction and $\omega_{1,2} = 2\pi f_{1,2}$. When both beams are recombined using a beamsplitter, the resulting profile is made up of $|\Delta\ell|$ petals (chosen to be $|\Delta\ell| = 2$ in place on an ellipse) where the frequency of pump rotation follows the expression [237],

$$F = \frac{\Delta f}{\Delta \ell} = \frac{f_1 - f_2}{\ell_1 - \ell_2} = \frac{1}{2\pi}\frac{\omega_1 - \omega_2}{\ell_1 - \ell_2} \tag{6.1}$$

where positive and negative F (in turn positive and negative θ) correspond to anticlockwise and clockwise pump rotations respectively. The superposition of two annular modes with $|\Delta\ell| = 2$ is depicted in Figure 6.1, where the top row shows a schematic of the pump profile intensity and phase used in simulation and the middle row for the experiment. In the latter, the displayed phase maps are given by the kinoforms displayed on each SLM, clearly depicting a single fork at the centre, corresponding to a charge-1 vortex core, where SLM_1 imprints phase winding (and

thus OAM) $\ell_1 = \pm 1$ and SLM_2 imprints $\ell_2 = \mp 1$ to ensure $|\Delta\ell| = 2$. The two experimental phase maps are flipped vertically form each other, such that each imprints a vortex with opposite charge. Note how the inner shape of the resulting pump profile is elliptical, but the intensity is not uniform about the azimuthal angle, which is why we label this beam shape as a "quasi-ellipse". The bottom row of Figure 6.1 schematically depicts the experimental technique where two beams recombine after being imprinted with the SLM phase profiles, to form a two-petalled beam that helically rotates in time and is focussed on the surface of the microcavity sample using a microscope objective. In both experiment and simulation, the trap diameter is set to 14 µm. This dumbbell shaped excitation profile stirs the polariton condensate like a paddle, much like the optical Ferris wheel for ultracold atoms [236]. This technique has recently been theoretically considered for polariton systems, but only for the case fo resonant excitation [238].

Due to the repulsive Coulomb interactions between the polaritons and excitons [239],

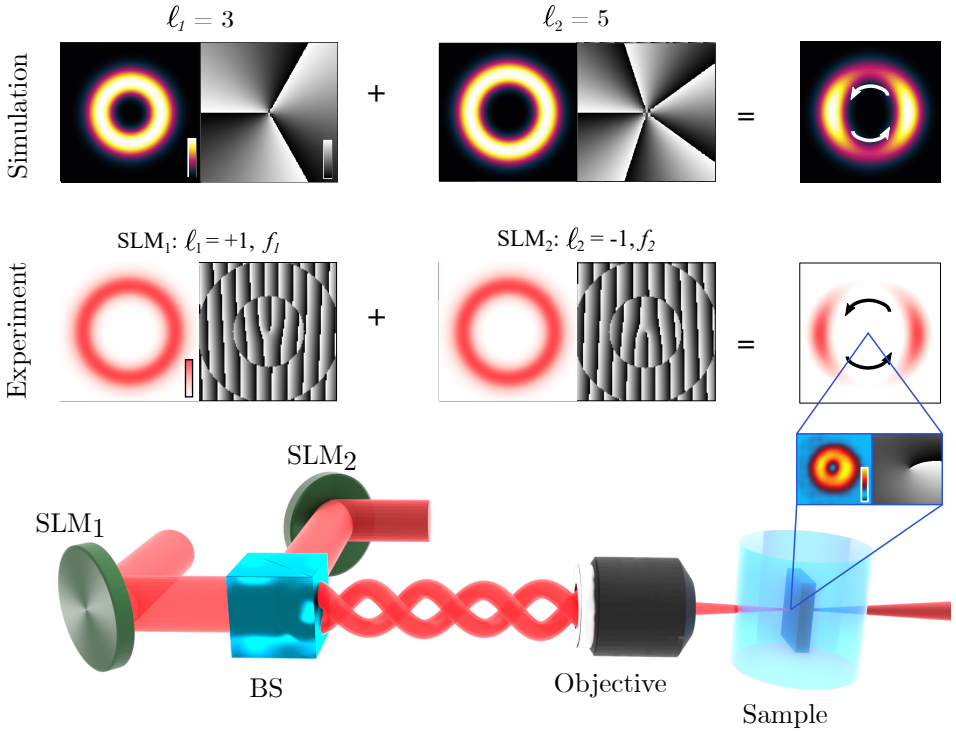

FIGURE 6.1: Numerical intensity and phase maps of excitation profiles used in (top) simulation and (middle) experiment created by the addition of two Laguerre Gaussian (LG) modes with $|\ell_1 - \ell_2| = 2$, with arrows to show direction of rotation. (Bottom) experimental schematic of the two LG modes sculpted independently by SLMs and combined with a beam splitter and focussed on microcavity sample using a microscope objective in order create a rotating quasi-ellipse that optically stirs and traps the polariton condensate. The window connecting the experimental pump profile and sample surface depicts (left) experimentally measured real-space condensate PL intensity containing a vortex at the centre as verified by (right) the corresponding phase-map. Experimental phase maps in (middle) correspond to the kinoforms displayed on each SLM. Each intensity profile is normalised independently and the phase profiles scaled between $-\pi$ and π radians. The 3D graphic was created by Ivan Gnusov.

the density gradients in the reservoir lead to an effective force pushing the polaritons from high to low pump intensity regions, where at critical pumping density, the excitons undergo stimulated scattering into the condensates [41] until the gain is clamped and the system stabilises. The ultrafast relaxation in turn allows us to use this all-optical technique to stir the condensate. If the reservoir responded more slowly to the excitations, the exciton reservoir would smear out following the time averaged excitation profile, which would lead to a cylindrically symmetric trapping potential for the polaritons. Instead, the reservoir excitons quickly thermalise into the bottleneck region of the polariton dispersion [240], to then undergo scattering into the condensate before radiatively decaying after a few picoseconds. This means that the reservoir responds quickly to the rapid changes in the pumping profile, whose dynamics are transferred to the condensate.

6.3 Methods

6.3.1 Continuous 2DGPE

The effects of the rotating pump profile on the condensate and exciton reservoirs are modelled using the mean-field theory approach, where the condensate order parameter $\Psi(\mathbf{r},t)$ describes the condensate density as a two-dimensional semi-classical wavefunction following the generalised 2DGPE coupled to an active and an inactive exciton reservoir $n_{A,I}(\mathbf{r},t)$ [67]. The active reservoir excitons undergo bosonic scattering into the condensate and the inactive reservoir sustains it (see section 2.1 for further details):

$$i\hbar\frac{\partial\psi}{\partial t} = \left[-\frac{\hbar^2\nabla^2}{2m_p} + G(n_A+n_I) + \alpha|\psi|^2 + \frac{i\hbar}{2}(Rn_A-\gamma)\right]\psi(\mathbf{r},t), \tag{6.2}$$

$$\frac{\partial n_A}{\partial t} = -(\Gamma_A + R|\psi|^2)n_A + Wn_I, \tag{6.3}$$

$$\frac{\partial n_I}{\partial t} = -(\Gamma_I + W)n_I + P(\mathbf{r},t). \tag{6.4}$$

Here, m_p is the effective polariton mass on the LP branch, $G = 2g|X|^2$ and $\alpha = g|X|^4$ are the polariton-reservoir and polariton-polariton interactions strengths respectively, where g is the exciton-exciton dipole interaction strength and $|X|^2$ is the excitonic Hopfield coefficient. Additionally, R is the rate of stimulated scattering of polaritons into the condensate from the active reservoir, γ is the polariton decay rate (inverse of polariton lifetime), $\Gamma_{A,I}$ are the active and inactive reservoir exciton decay rates, W is the inactive to active reservoir exciton conversion rate and $P(\mathbf{r},t)$ describes the nonresonant continuous-wave dynamic pumping profile.

Eqs. (6.2 - 6.4) are numerically integrated in time using a linear multistep method starting from random initial conditions. The parameters used in these simulations are based off the sample properties, with $m_p = 0.30$ meV ps^2, $\gamma = \frac{1}{5.5}$ ps^{-1}, $\Gamma_A = \gamma$ due to the fast thermalisation to the exciton background [53], whereas the nonradiative recombination rate of inactive reservoir excitons is taken to be much smaller than the condensate decay rate with $\Gamma_I = 0.01\gamma$. The remaining parameters are enumerated through fitting to experimental data, giving $\hbar R = 6.67$ μeV μm^2, $W = 0.05$ ps^{-1}, $g = 1$ μeV μm^2, and $|X|^2 = 0.35$.

$P(\mathbf{r}, t)$ is the dynamic pumping profile given by the superposition of two rotating Laguerre-Gaussian (LG) modes with $|\Delta\ell| = 2$, resulting in a two-petalled quasi-ellipse following

$$P(\mathbf{r}, t) = \mathcal{P}(r) \left| e^{i(\ell_1\theta - \omega_1 t)} + e^{i(\ell_2\theta - \omega_2 t)} \right|^2 = 4\mathcal{P}(r) \cos^2 \left[\frac{(\ell_1 - \ell_2)\theta}{2} - \frac{(\omega_1 - \omega_2)t}{2} \right], \quad (6.5)$$

where $\mathcal{P}(r)$ represents the annular intensity profiles shown in Figure 6.1, θ is the rotation angle in the plane of the microcavity and $\omega_{1,2} = 2\pi f_{1,2}$. The intensity of the pumping profile remains constant throughout each simulation and is chosen such that the system operates just above condensation threshold, with the number of polaritons in the system on the order of 10^3 for the single condensate over an area of 6.4 mm^2 .

6.3.2 Vortex Analysis: Simulations

The 2DGPE is numerically integrated for a trap rotating with a frequency $F = 2\Delta f$, which is scanned over a large range of F, where the positive and negative signs of F correspond to anticlockwise and clockwise trap rotation respectively. The probability current of the resulting condensate wavefunction, which describes the rate of flow of the condensate, is analysed following

$$j_c = \frac{\hbar}{2m_p i}(\Psi^* \nabla\Psi - \Psi \nabla\Psi^*) \quad (6.6)$$

where the location of the vortex core is attributed to the location of $\min|j_c| = \min|\Psi|$. We also look at the projection of the condensate wavefunction onto angular harmonics, where around each vortex core, the distribution of orbital angular momentum (OAM) is analysed in order to give the number of polaritons with OAM = ℓ,

$$N_\ell(t) = \frac{1}{2\pi} \left| \int \Psi^*(\mathbf{r}, t) e^{i\ell\phi} d\mathbf{r} \right|^2 . \quad (6.7)$$

Here, $\ell \in \mathbb{Z}$ and ϕ is the azimuthal angle in-plane to the microcavity about the vortex core. Note that in the analysis of the GPE, the range of ℓ is considered from -3 to 3.

The expectation value of the angular momentum for a polariton in the condensate is written as

$$\langle \ell \rangle \hbar = \frac{L_z(t)}{N(t)} \simeq \frac{1}{N(t)} \sum_{\ell=-3}^{3} \ell N_\ell(t) \tag{6.8}$$

where $L_z(t) = -i \int \Psi^*(\mathbf{r}, t)(x\partial_y - y\partial_x)\Psi(\mathbf{r}, t)d\mathbf{r}$ is the total angular momentum of the system at time t with a total number of condensed polaritons defined as $N(t) = \int |\Psi(\mathbf{r}, t)|^2 d\mathbf{r}$ [224]. Here, positive ℓ corresponds to an anticlockwise phase winding and negative ℓ to a clockwise phase winding about the vortex core.

6.3.3 Experimental Techniques

In experiment, the polariton condensate is formed in an inorganic 2λ $GaAs/AlAs_{0.98}P_{0.02}$ microcavity with embedded InGaAs quantum wells [3]. The sample is held at a cryogenic temperature of ∼4 K. For the condensate formation, we use a nonresonant excitation scheme with two frequency detuned Ti-sapphire lasers. By fine-tuning the cavity of one laser, we can control their frequency detuning such that both light sources are stabilised with a frequency jitter smaller than 20 MHz. Two high precision wave-meters allow us to measure the frequency of both lasers in real time, correcting for the slow thermal frequency drift.

Figure 6.1 schematically depicts the excitation part of the setup. The radiation from each laser (detuned in frequency by Δf) separately hits two different SLMs each displaying the analytical perfect vortex kinoform [241] that shapes each beam into an annulus with a quantised phase winding of ℓ, such that the annulus diameter and phase winding number are fully controllable through adjusting the SLM kinoforms. The resulting optical patterns of each laser are rings with corresponding topological charges, which are superposed using a beamsplitter. The resulting beating pattern appears to be rotating in time [236, 238]. The rotating nonresonant laser pattern is focussed on the surface of the sample at a cavity detuning of -3.2 meV with a diameter of 14 µm, which acts as a rotating quasi-ellipse that simultaneously confines and stirs the condensate.

We retrieve the phase of the polariton condensate utilising two interferometric techniques: the homodyne interferometry and the interference of the condensate with a retro-reflected copy of itself in Michelson interferometry. The homodyne technique is described in detail in [94]. To apply this technique, we use an external source laser at the condensate wavelength as a reference beam and interfere it with the condensate emission. The reference laser beam is greatly expanded to overlap with the whole condensate with flat phase front with respect to the condensate. To lock the phases between them, we use part of the reference beam as a seed on the sample close to the

condensate. This leads to the observation of interference fringes, thus allowing for phase retrieval.

For the interferometric technique, we do not use any external light sources but instead interfere the condensate PL with itself and spatially displace one arm of the interferometer with respect to the other (retroreflected) to observe the phase dislocation. As a result, in the interference pattern when the vortex is present, we see a vortex-antivortex pair singularity, which forms due to the angular momentum flipping caused by reflections. Given the interferograms, we can extract the phase of the condensate wavefunction by performing the 2D Fourier transform. In the frequency domain, we filter the harmonic corresponding to the interference fringes and perform an inverse Fourier transform. The resultant complex-valued array carries the information about the phase of the original condensate, given by the argument of this data.

6.3.4 Vortex Analysis: Experiment

For a perfect quantised vortex, all particles must have the same non-zero OAM, have a dark void (not ridge) in its real-space intensity and have a constant-gradient phase rotation about the phase singularity. However, it is generally accepted that there exists a vortex in a condensate system even when the phase gradient is not constant, as shown in [220, 224, 242, 227, 233]. In order to classify whether or not there exists a vortex in experiment, we first consider the analytical superposition of vortex and antivortex modes with varying weightings and analyse the azimuthal phase profile about the centre of the wavefuction as well as the real-space profile. We create the perfect vortex and antivortex modes ψ_v and ψ_{av} with an intensity profile that follows a radially symmetric Hermite polynomial (Figure 6.2(a)) and a phase-map that winds 2π radians with a constant gradient in an anticlockwise and clockwise direction for the vortex and antivortex respectively (Figure 6.2(b,c)). ψ_v and ψ_{av} are summed together with a vortex mode weighting of v, such that the resulting wavefunction is given by $\psi = \sqrt{v}\psi_v + \sqrt{1-v}\psi_{av}$. Note that the dipole orientation depends on the relative angle between the vortex and antivortex phases, where here the antivortex has a $\pi/2$ rotation compared to the vortex leading to a dipole aligned diagonally rotated $\pi/4$ to the vortex and antivortex phase jumps.

For a given vortex fraction, we take the phase profile of the azimuthal path about the centre of the resulting wavefunction (Figure 6.2(d)). This is compared to the perfect vortex phase profile (dashed black line in Figure 6.2(e)) and the absolute phase difference between the extracted and perfect vortex phase profiles at N equally spaced points along the profile, calculated as $\Delta = |\theta_\psi - \theta_{\psi_v}|$, shown in Figure 6.2(g). The azimuthal angle zero-point is chosen to be on the phase discontinuity (white/black boundary in Figure 6.2(d)) and a global phase offset is applied to the extracted phase profile in order to minimise the normalised root mean squared error (NRMSE) to the

perfect vortex phase profile. The NRMSE is defined as

$$\text{NRMSE} = \frac{1}{M}\sum_{m=1}^{M}\left[\frac{1}{4N}\sum_{n=1}^{N}|e^{i\theta_\psi} - e^{i\theta_{\psi_v}}|^2\right], \tag{6.9}$$

where θ_ψ is the phase at one point in the N-point phase profile around each condensate vortex and θ_{ψ_v} is the phase at one point along the phase profile of the ideal vortex, where N gives the number fo data points in the extracted phase profile. This error parameter describes the average normalised euclidean distance between the extracted and perfect vortex phases. An error of NRMSE = 1 corresponds to the maximum error where all data points deviate by π radians from the perfect vortex profile.

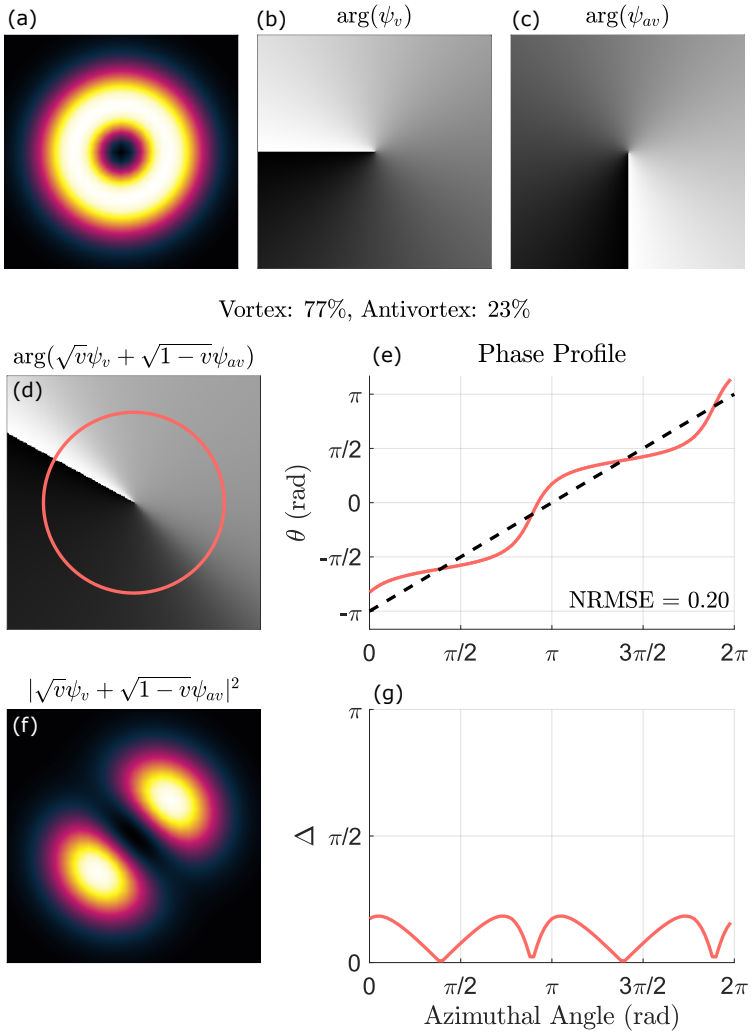

FIGURE 6.2: Numerical (a) intensity and (b,c) phase for ideal vortex (ψ_v) and antivortex (ψ_{av}) respectively. Example of resulting (d) phase profile and (f) real-space intensity profile from superposition of vortex and antivortex with fraction of vortex component $v = 0.77$ and red loop centred about vortex centre in (d). (e) Solid red line to show the 100-point phase profile about azimuthal angle of red path in (d) compared to the ideal phase about a vortex shown by dashed black line and (g) showing Δ the absolute phase difference between the red and black lines of (e), with normalised root mean squared error (NRMSE) of 0.20.

An example of this analysis in Figure 6.2(d-g) is shown for $v = 0.77$ with an $N = 100$-point phase profile and results in an NRMSE $= 0.20$. As v is increased or decreased, the corresponding NRMSE does the opposite. Additionally, we consider the real-space intensity, where there must be a zero-intensity void at the singularity site, which is present for NRMSE < 0.20. For example in Figure 6.2(f), there is a dark centre that is very faintly surrounded by a non-zero intensity perpendicularly to the dipole mode. As such, we define that if NRMSE ≤ 0.20, then there exists a vortex in the system. This is the analysis criterion we use to decide which experimental observations contain a vortex.

6.4 Results & Discussion

6.4.1 Counter-Rotating Polariton Fluid

For each rotation frequency, 40 numerical integrations of Eqs. 6.2-6.4 are performed using a 14 μm diameter pump profile as described in section 6.2, each starting from unique random initial conditions. For each F, we plot the intensity distribution of excitons in the active reservoir, $|n_A|^2$, as this both confines and stirs the polaritons in the system. When the pump profile is stationary, the active exciton reservoir follows the non-uniform quasi-elliptical profile of the pump (see Figure 6.3(a)). Interestingly, as $|F|$ increases the active reservoir becomes more uniform in intensity and the slight ellipticity smears out, where at $F = 20$ GHz the active reservoir appears completely circular and uniform in intensity, such that the condensate confined within experiences a stationary annular trapping potential (shown in Figure 6.3(a-e)).

The corresponding condensate intensity and phase profiles after 0.8 ns of numerical integration (Figure 6.3(f-j) and Figure 6.3(k-o) respectively) show that the condensate is strongly effected by the trap rotation. For $F = 0$ GHz, the condensate forms into a dipole mode, clearly indicated by the two-lobe intensity, the sharp vertical step in phase through the centre of the system and a probability current that flows away from the phase boundary. However, as the magnitude of rotation frequency increases, the vertical phase jump begins to spiral with its tail at the centre of the system, where the continuous phase that loops the singularity becomes smoother in gradient about the azimuthal angle with increasing $|F|$. Additionally, the probability current gains a circular flow as the trap is rotated, shown by the cyan arrows in Figure 6.3(f-j). At $F = 2$ GHz, the dominant flow of polaritons is still in the radial direction away from from the dark ridge that runs between the two dipole lobes in real-space, but there is indeed a rotational flow at the centre of the system, which surprisingly runs in the opposite direction (clockwise) to the optical pump (anticlockwise), however as this is a quantum fluid governed by a superposition of vortex and antivortex modes, this phenomenon is explained using a time periodic discretised dissipative GPE (see

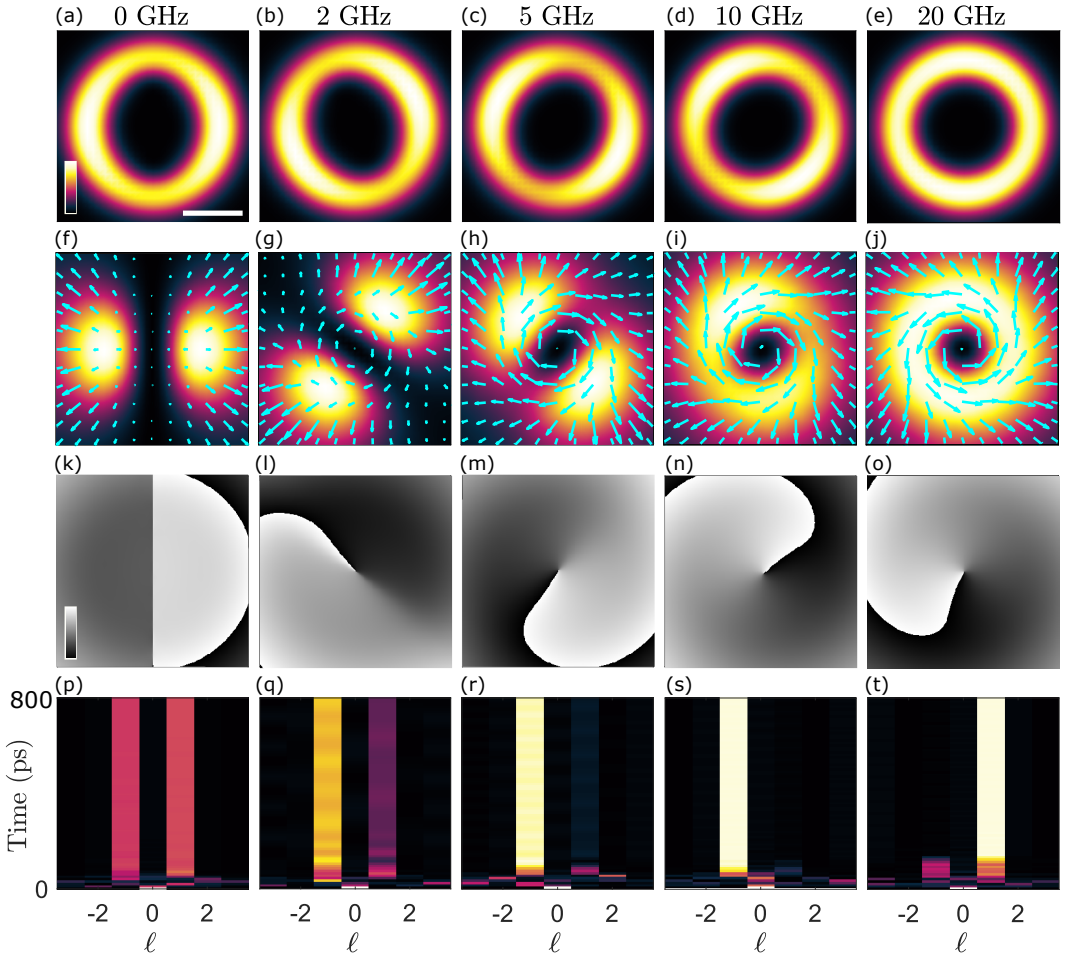

FIGURE 6.3: For trap rotation frequencies 0, 2, 5, 10 and 20 GHz, (a-e) active reservoir intensity, (f-j) real-space condensate PL intensity with superimposed probability current j_c in cyan, (k-o) real-space phase profiles and (p-t) distribution of condensate orbital angular momentum (OAM) at each time step of the 2DGPE simulations. Profiles (a-o) all single-shot after 800 ps of numerical integration. Each intensity profile and OAM distribution is normalised independently and the phase profiles scaled between $-\pi$ and π radians. White scale-bar in (a) indicates 5 µm.

subsection 6.4.3). As F is increased further, the central rotational flow becomes dominant with a weaker radial far-field flow, and the dark ridge vanishes as the intensity profile forms a single-lobe condensate with a dark core (the vortex). Interestingly, for large rotation frequencies, such as $F = 20$ GHz in Figure 6.3, the phase gradient and polariton flow about the vortex centre can either co-rotate or counter-rotate with the optical trap rotation. This is a result of the uniform ring-like trapping potential that presents to be nearly stationary to the polaritons and as such, the first excited state condensate forms randomly and stochastically with either the same or opposite phase rotation as the trap.

As the dipole mode (Figure 6.3(f)) is the equally weighted superposition of the orthogonal vortex and antivortex modes, we analyse the distribution of orbital angular momentum (OAM) of the polaritons within a 10 µm radius of the condensate centre in

order to understand what fraction of the system is in each vortex state, where polaritons with an OAM of $\ell = 1$ are part of the vortex, and $\ell = -1$ belong to the antivortex state. In Figure 6.3(p-t), we show the normalised OAM distributions for each 10 ps time-step in the simulation. For the static optical trap, the polaritons equally occupy $\ell = \pm 1$, thus confirming that the condensate is in the dipole mode. As F increases, the occupation in the antivortex mode supersedes the occupation of the vortex mode, where at $F = 10$ GHz, all polaritons have $\ell = -1$, thus the condensate forms a perfect antivortex. The switch in rotation direction of the polariton flow at $F = 20$ GHz is also seen in Figure 6.3(t), where all polaritons are in the vortex state in this realisations. These initial results indicate that a polariton condensate vortex can indeed be induced through optical stirring, and its existence is evidenced by a dark void in real-space, a circular flow in probability current, a gradient flow of phase about a singularity and by a dominant non-zero OAM, where interestingly, the condensate fluid rotation counter-rotates with the pump dynamics for $F \leq 10$ GHz, but stochastically co-rotates or counter-rotates with the pump for $F = 20$ GHz. However, in experiment we only observe co-rotating vortices (shown in Figure 6.4), plus the condensate populates a single Gaussian ground state lobe for high rotation frequencies as opposed to the first excited vortex states as we see in these simulations. Although the 2DGPE models the polariton fluid well, in this instance the numerical pumping

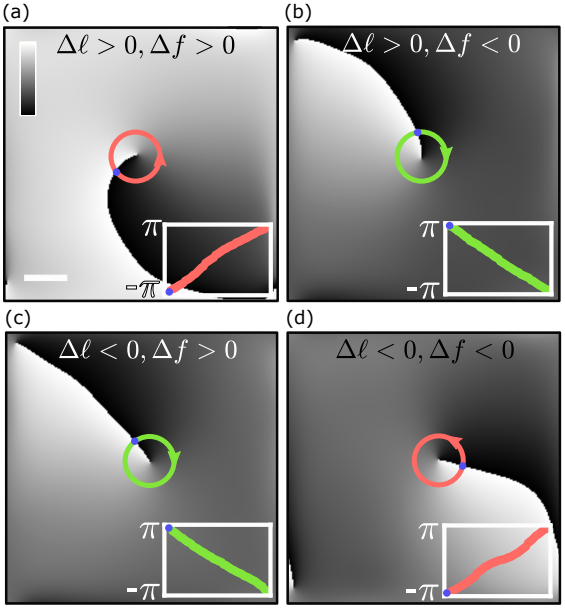

FIGURE 6.4: Experimental condensate phase maps for (a,d) anticlockwise and (b,c) clockwise pump rotation as a result of (a,c) $\Delta f = 4.6$ GHz and (b,d) $\Delta f = -3.7$ GHz with $\ell = \pm 1$ for the top and bottom panels respectively. The circular arrows around each singularity represent the path from which the phase is extracted in an anticlockwise direction, where the arrow represents the direction of the vortex phase winding and the blue dots indicate the point about which the profile is un-wound. The colour scale in (a) ranges between $-\pi$ and π, and the white scale bar corresponds to 2 µm, where both of which apply to all panels.

profile needs to be adjusted slightly in order to better fit the experimental findings.

6.4.2 Co-Rotating Polariton Fluid

As we do not always observe a co-rotating vortex in the simulations that follow the same pumping technique experimental pumping technique, nor do we observe a ground state condensate at high rotation frequencies, we adjust the numerical pump profile slightly to become more elliptical in shape by both stretching and compressing the pump in the top right panel of Figure 6.1 in the horizontal and vertical directions respectively, to form a new quasi-ellipse with a major diameter of 16 μm and a minor diameter of 12 μm. This ellipticity ensures that a dipole mode condensate forms at $F = 0$ GHz, and a ground state mode is trapped for large $|F|$. The updated pumping profile is used in the numerical integration of Eqs. 6.2-6.4 for $F = 0, 2, 4, 6$ GHz, where now the condensate fluid co-rotates with the pump profile, in agreement with experiment. Again, the intensity of the active exciton reservoir follows the ellipticity of the pump profile at $F = 0$ GHz, but as the pump rotation frequency increases, this ellipticity smears out and the reservoir intensity becomes more uniform (Figure 6.5(a-d)). The effect of this smearing is seen in the real-space PL intensity (Figure 6.5(e-h)), where the circulating polariton current builds with increasing F up to 4 GHz. However, in the snapshot of $F = 6$ GHz, we see that the less-elliptical trapping potential from the exciton reservoir confines the ground state condensate instead. We locate the centre of each vortex core at the minimum intensity location within the condensate, around which we take the azimuthal phase profile at a radius of 5 μm (red rings in Figure 6.5(i-l)), which we un-wind about ϕ, plot in Figure 6.5(m-p) and calculate the NRMSE. In the cases where there is no vortex core (e.g. Figure 6.5(a,d)), we take the phase profile about the centre of the trap profile. Additionally, we plot the energy dispersions for each rotation frequency (Figure 6.5(q-t)), where we observe a single first-excited-state energy mode at $F = 0$ GHz, which splits into two modes as F increases, up until $F = 6$ GHz where a single ground state mode is occupied by polaritons.

Using the criterion for a vortex of NRMSE ≤ 0.2 (as discussed in subsection 6.3.4), we analyse the experimental condensates over 100 unique realisations per rotation frequency and determine the fraction of realisations that present with a vortex. As we do not experimentally project the condensate to different angular harmonics, this is the best way to statistically analyse the experimentally observed vortices, and can directly compare it in theory (Figure 6.6(a,b)). The experimental data shown in blue follows a similar distribution to the theoretical data and remarkably, the probability of experimentally realising a vortex is close to unity over a similar region of F in both simulation and experiment. From the simulations results, we can project the condensate wavefunction onto the angular harmonics, so instead of setting some

arbitrary error threshold for confirming the presence of a vortex in the system, in Figure 6.6(b) we plot the average OAM per polariton $\langle \ell \rangle$ (again averaged over 40 realisations), where $|\langle \ell \rangle|$ is maximised at $|F| = 4$ GHz. The peaks (and troughs) in this

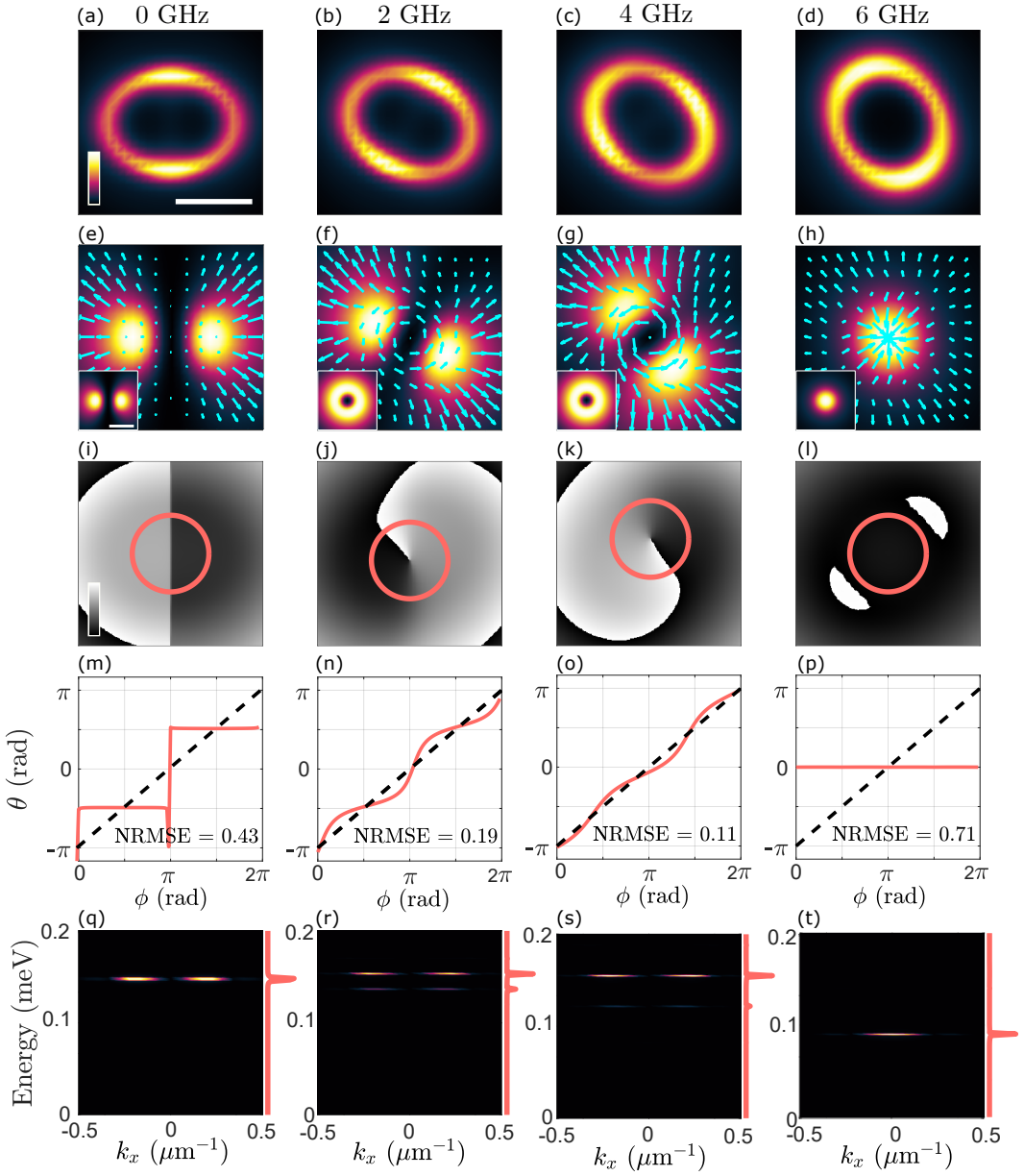

FIGURE 6.5: For trap rotation frequencies 0, 2, 4, 6, (a-d) active reservoir intensity, (e-f) single-shot real-space condensate PL intensity after 2.5 ns of numerical integration with superimposed probability current j_c in cyan and insets to show the time-integrated condensate intensity, (i-l) real-space phase profiles with a 10 μm diameter red ring about vortex core (or centre of trap if no condensate present), where (m-p) show the phase profiles about each red ring un-wound with $\phi = 0$ at $\arg(\psi) = -\pi$ compared to the perfect vortex profile indicated by dashed black lines. (q-t) Energy dispersion with vertical red line profiles to shown integrated energy intensity for each rotation frequency. Profiles (a-p) all single-shot realisations after 2.5 ns of numerical integration, aside from the insets in (e-h). Each intensity profile and OAM distribution is normalised independently and the phase profiles scaled between $-\pi$ and π radians. White scale-bar in (a) and inset of (e) indicate 10 μm.

plot are in accordance with the trend of Figure 6.6(a), showing that the criterion of NRMSE ≤ 0.20 for a vortex observation is appropriate for the experimental analysis. Additionally, we show the fraction of polartions with $\ell = 0, \pm 1$ in Figure 6.6(c), were at $F = 0$ GHz, the condensate consists of equal weightings of the vortex and antivortex (as we expected) and at $F = \pm 4$ GHz, $\ell = \pm 1$ is maximised such that $N_\ell \simeq 0.8$. However, even when N_ℓ is maximised, still 20% of polaritons are not in the (anti)vortex harmonic, which is why the average OAM per polariton in Figure 6.6(b) does not exceed a magnitude of 0.6. In Figure 6.6(d), we also show the energy spectrum over a range of F where we see that for a stationary trap, the polaritons dominantly occupy the first excited state of the system at ~ 37 GHz above the bottom

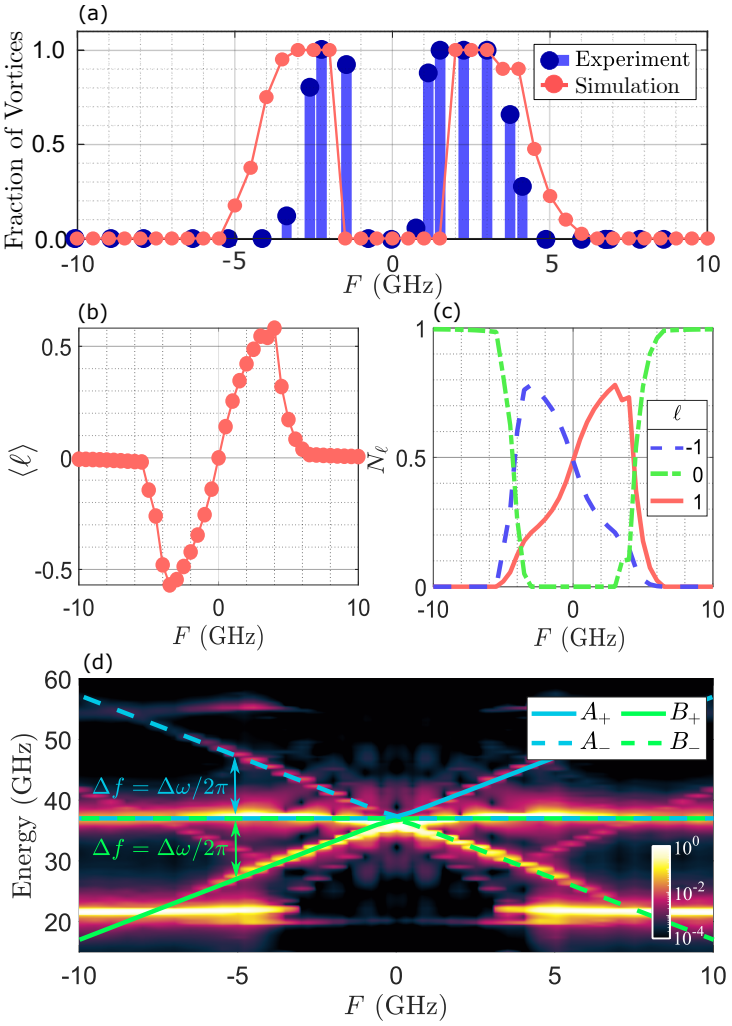

FIGURE 6.6: (a) Fraction of vortex states observed for (blue) in experiment over 100 realisations that display, and (red) in numerical simulation over 40 realisations, as a function of trap rotation frequency. (b) Average OAM per polaritons averaged at each rotation frequency averaged over 40 realisations, (c) number of polaritons with OAM of (red) $\ell = 1$, (blue) $\ell = -1$ and $\ell = 0$ averaged over 40 realisations in simulations at $t = 2.5$ ns. (c) Energy spectrum integrated over k_x from the dispersion over a range of F, with the $A_\pm$ ($B_\pm$) branches shown by dashed and solid blue (green) lines splitting away from the first excited energy state.

of the LP dispersion branch. However, as $|F|$ increases, we observe an additional two energy branches that split away from the bare excited state mode with an energy shift of $\Delta\omega$. As $|F|$ is increased further, polariton population in the ground state (at ~ 22 GHz) grows in agreement with experiment. We also observe very faintly (note the logarithmic colourscale) the second excited state of the trap around an energy of ~ 55 GHz with a minute occupation of polaritons. To investigate this energy splitting, and to understand why we can observe a co-rotating or a counter-rotating vortex, we explore the dynamics of the $\ell = \pm 1$ harmonic modes.

6.4.3 Discretised Gross-Pitaevskii Equation

Through describing the dynamics of this system solely in terms of the vortex and antivortex rotating components with $\ell = \pm 1$, we are able to explain the phenomena of the co-rotating and counter-rotating vortex, relative to the rotating pump. First, we must consider the linear regime of the Schödinger equation, describing the time periodic drive and negating the cavity losses,

$$i\hbar\frac{\partial\psi}{\partial t} = \left[\hat{H}_0 + \hat{U}(t)\right]\psi \tag{6.10}$$

where $\hat{H}_0$ is the unperturbed polariton system confined by some harmonic potential following,

$$\hat{H}_0 = -\frac{\hbar^2\nabla^2}{2m_p} + \frac{1}{2}m_p\omega_\parallel^2 r^2 \tag{6.11}$$

and $\hat{U}(t)$ is the perturbation potential that follows,

$$\hat{U}(t) = \lambda\cos^2\left(\frac{(\ell_1-\ell_2)\theta}{2} - \frac{(\omega_1-\omega_2)t}{2}\right). \tag{6.12}$$

For the unperturbed Hamiltonian (i.e. $\lambda = 0$), the solutions are the 2D harmonics $\hat{H}_0\phi_{n_x,n_y} = \hbar\omega_{n_x,n_y}\phi_{n_x,n_y}$, with eigenenergies $E_{x,y} = \hbar\omega_{n_x,n_y} = \hbar\omega(n_x + n_y + 1)$ [243]. Here, we assume that the polaritons are trapped deeply enough that they experience an effective harmonic potential of strength $\omega_\parallel$ determined by the time-independent term of the exciton reservoir.

In this perturbative approach, $\lambda = \lambda_R + i\lambda_I$ is a complex number that satisfies $|\lambda| \ll \hbar\omega_\parallel$ such that the $\hat{U}$ operator can be treated as a perturbation of the system. This is a valid assumption for intermediate rotation frequencies where the exciton reservoirs smear out over time, roughly forming a superposition of a time-independent unperturbed potential and a time dependent perturbing potential.

By only considering the $\ell = \pm 1$ angular harmonics, which are mainly all we observe in simulation and experiment at these intermediary rotation frequencies, the system

dynamics can be simplified to,

$$\psi = \xi(r)(c_+ e^{i\theta} + c_- e^{-i\theta})e^{-i2\omega_\parallel t} \tag{6.13}$$

where $\xi(r) = \frac{\beta^2}{\sqrt{\pi}} r e^{-\beta^2 r^2/2}$ is the radial solution to the unperturbed Schrödinger equation with $\beta = \sqrt{m_p \omega_\parallel / \hbar}$. The angular dependence of $\hat{U}$ couples the harmonics that differ by $\ell_1 - \ell_2$, where $\ell_1 - \ell_2 = 2$ couples the $e^{\pm i\theta}$ harmonics.

By substituting Equation 6.13 into Equation 6.10 and extracting across the spatial degrees of freedom, we obtain the coupled system of equations:

$$i\hbar \frac{\partial c_\pm}{\partial t} = \frac{\lambda}{4} c_\mp \exp\left[\mp i(\omega_1 - \omega_2)t \frac{\ell_1 - \ell_2}{|\ell_1 - \ell_2|}\right]. \tag{6.14}$$

Interestingly, these equations take the same form as those that describe Rabi flopping in a degenerate two-level system in the rotating wave approximation and have the exact solutions:

$$c_\pm(t) = A_\pm e^{-i(\pm\Delta\omega + \Omega_R)t/2} + B_\pm e^{-i(\pm\Delta\omega - \Omega_R)t/2} \tag{6.15}$$

where $\Delta\omega = (\omega_1 - \omega_2)(\ell_1 - \ell_2)/|\ell_1 - \ell_2|$ with a Rabi splitting of $\Omega_R = \sqrt{\Delta\omega^2 + \lambda^2/(4\hbar)^2}$. A schematic of the system's energy structure is shown in Figure 6.7 and the exponents of Equation 6.15 result in a four-way energy splitting, which we plot in blue and green on Figure 6.6(d) as frequency-based energy shift following,

$$f = \frac{1}{2\pi}\left[\pm\Delta\omega \pm \sqrt{\Delta\omega^2 + \lambda^2/(4\hbar^2)}\right]. \tag{6.16}$$

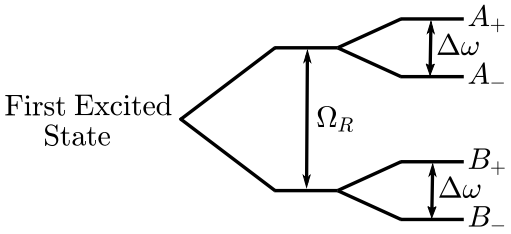

FIGURE 6.7: Energy structure of the system.

The sign of $\mathrm{Im}(\Omega_R)$ follows the sign of λ_I which determines if the frequency $A_\pm$ or $B_\pm$ has equal positive or negative imaginary components. If $\lambda_I > 0$, then the higher energy $A_\pm$ modes have lower losses (or narrower linewidths) and will be populated more strongly. Conversely, if $\lambda_I < 0$ then $B_\pm$ will have lower losses. Furthermore, the energy splitting between the pairs is precisely $\Delta E = \Delta f = 2\Delta F$, as we see in Figure 6.6(d).

This simple perturbative analysis shows that although the pump rotates in a definite direction, the condensates real-space (and phase-space) rotation direction cannot

simply be determined by the narrowest spectral peak. Instead, the condensate's rotation direction is determined by the different stability properties (i.e. nonlinear dynamics) of these high-gain modes, which we discuss in the following. We can write the discretised generalised GPE by including standard polariton condensate nonlinearities into Equation 6.14, which allows us to analyse more transparently whether the co-rotating or counter-rotating vortices (relative to the direction of F) stabilise the system, following:

$$i\frac{dc_{\pm}}{dt} = \left[ip + (\tilde{a} - i)(|c_{\pm}|^2 + 2|c_{\mp}|^2)\right] c_{\pm} + (1 - i\eta)c_{\mp}e^{\mp i\Delta\omega t}. \tag{6.17}$$

Here, p describes the net gain of the system, $\tilde{a}$ gives the renormalised nonlinear energy shift from removing the spatial dependence. Time is also scale in units of coupling strength like $t \to t/\lambda_R$ and defined as $\eta = \lambda_I/\lambda_R$. The condensate intensity and vorticity from numerically integrating Equation 6.17 are shown in Figure 6.8(a,b) respectively and indicate that the sign of the dissipative coupling term, η can flip the vortex rotation relative to the pump. In this figure, we fix $\tilde{a} = 1$ and $\Delta\omega = 1$, corresponding to an anticlockwise pump rotation. Interestingly, there is a bending of the boundary between blue and red regions in (b), which is attributed to the nonlinear energy term in Equation 6.17 becoming comparable to the linear coupling energy, making the co-rotating polariton fluid the most favourable macroscopic dynamics.

These results back up the experimental findings, which show a co-rotating polariton fluid with repulsive polariton interactions and the counter-rotating vortex seen in simulations with the purely LG-mode trap (Figure 6.3) is described using the discretised dissipative GPE by a negative dissipative coupling between the $\ell = \pm 1$ angular modes with that specific trapping potential. But as we have seen throughout this thesis, condensate dynamics strongly depend on the pumping profile, where minor changes to the system gain can drastically affect the resulting condensate.

6.4.4 Extracting Experimental Vortex Fractions

Although the ranges in rotation frequency in which a vortex presents itself do align in theory and experiment for the current definition of a vortex (NRMSE < 0.20), it seems quite arbitrary to have an error threshold to binarise the sighting of a vortex to "True" or "False" as the components of $\ell = \pm 1$ vary smoothly with F. As the system is in a continuous superposition of a vortex and antivortex state, we can instead compare the fractions of these modes in experiment too in order to find the average OAM per polariton and directly compare it to the theory. For future experiments, the optical set up could include an OAM sorting technique as described [224]. However, as this information has yet to be experimentally acquired in this investigation, we would need to numerically extract it by comparing the condensate phase-maps to the analytical

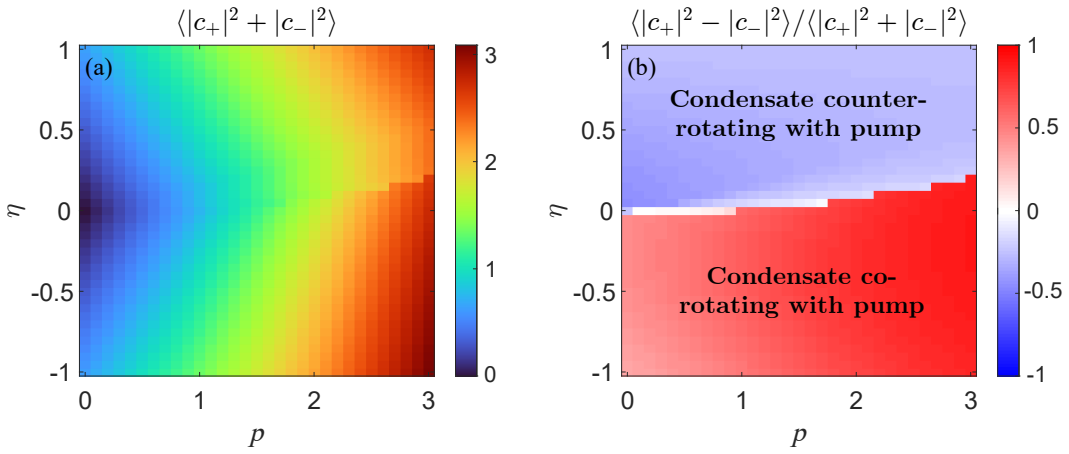

FIGURE 6.8: (a) Time-averaged intensity and (b) vorticity of the condensate by numerically solving Equation 6.17 as a function of power p and dissipative coupling strength η. Other parameters are $\tilde{\alpha} = 1$ and $\Delta\omega = 1$ (pump rotating counterclockwise). This figure was created by Helgi Sigurdsson.

combination of the vortex and antivortex wavefunctions, ψ_v and ψ_{av}, as well as the simulated condensate behaviour.

Trivially, the normalised distribution of OAM for $\ell = \pm 1$ gives exactly the vortex and antivortex fractions (v and $1 - v$) respectively, which means that by characterising the NRMSE of the analytical condensate wavefunction by varying v, we have the ability to extract the OAM distribution of $\ell = \pm 1$ from the experimental phase profiles. Firstly, we test this out with the analytical wavefunction and plot the mean and standard deviation of Δ from the extracted phase profiles about the centre of the system as a function of v, shown in red in Figure 6.9(e). We then compare this with the statistical analysis to Δ extracted from the 2DGPE simulations. An example of this analysis is shown for a simulation with $F = 4$ GHz in Figure 6.9(a-d). For each run of the simulation, we take the single shot phase profile at 10 different timesteps (Figure 6.9(a) corresponds to $t = 2.5$ ns), extract the 100-point phase profile at a radius of 5 µm about the phase singularity (Figure 6.9(b)) and calculate Δ (Figure 6.9(d)). Again, the zero-point of the azimuthal angle is chosen at each time step to lie on the phase discontinuity at $\arg(\psi) = -\pi$ and a global phase offset is chosen to minimise the NRMSE and $\langle\Delta\rangle$. The location of the phase singularity is given by the minimum intensity within the condensate and if no vortex exists, then the phase profile is taken about the centre of the system. Additionally the distribution of OAM in $\ell = \pm 1$ is determined using Eqs. (6.7,6.8), as shown in Figure 6.9(c) for $t = 2.5$ ns.

From this analysis of Δ and assuming that $N_1/N_{-1} \equiv v$, the extracted mean, standard deviation of Δ is plot as a function of v in Figure 6.9 (blue) to directly compare to the analytical wavefunction statistics (red). Note that it is not the rotation frequency on the x-axis here, but rather the fraction of the condensate in the vortex/antivortex modes. The analytical and numerical error match up closely, showing that the absolute phase difference and the standard deviation of the 100-point phase profile about a

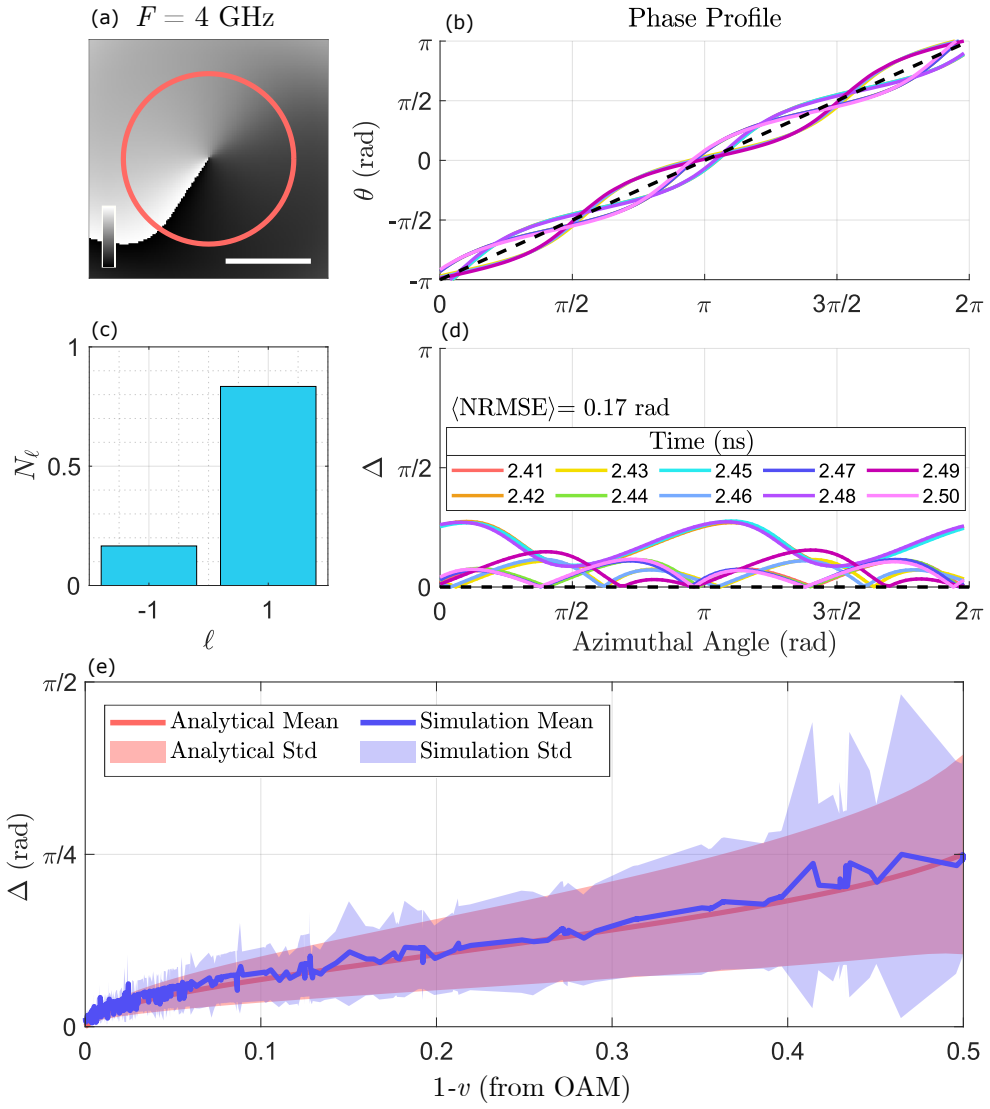

FIGURE 6.9: 2DGPE simulation results for $F = 4$ GHz showing (a) phase space at $t = 2.5$ ns with (red) 5 µm radius ring about phase singularity, (b) the extracted 100-point phase profile about ring at 10 different time steps between 2.41 ns to 2.50 ns, (c) extracted distribution of $\ell = \pm 1$ at $t = 2.5$ ns, (d) the absolute phase difference Δ between the phase profiles in (b) and the perfect vortex phase and (e) the mean and standard deviation of Δ as a function of antivortex ($\ell = -1$) fraction of the (red) analytical and (blue) simulated condensate wavefunction. White scale-bar in (a) indicates 5 µm.

vortex centre can be used to infer the vortex fraction of a condensate. A fitting is applied to the analytical errors of the mean $\langle\Delta\rangle$ and the mean with standard deviation $\langle\Delta\rangle \pm \sigma$ (red data in Figure 6.9(e)) in order to perform such an inference, following:

$$\langle\Delta\rangle = 7.05x^3 - 4.89x^2 + 2.16x + 0.04 \tag{6.18}$$

$$\langle\Delta\rangle + \sigma = 12.0x^3 - 8.04x^2 + 3.33x + 0.06 \tag{6.19}$$

$$\langle\Delta\rangle - \sigma = 2.90x^3 - 1.74x^2 + 0.99x + 0.02. \tag{6.20}$$

The distribution of OAM of the experimental data has yet to be analysed using this technique, but is simple enough carry out by taking a 100-point phase profile about each vortex in order to extract Δ and infer v by setting $x = v - 1$ when Δ is compared to a perfect vortex, and $x = v$ in comparison to the perfect antivortex.

6.4.5 Larger Quasi-Elliptical Pump

We also numerically investigate a larger trap that excites the ψ_{20} condensate when stationary (second excited state in x and ground state in y). This is achieved using the same LG-based trapping potential depicted in the top row of Figure 6.1, but with a diameter of 16 µm in experiment, and a combined LG-mode quasi-ellipse in simulation with major and minor diameters of 22 µm and 14 µm respectively. For varying trap rotation frequencies, the real-space and phase-space profiles of the condensates are shown in Figure 6.10. Here we see the ψ_{20} condensate mode in Figure 6.10(a,e), but as we increase F to 2 GHz and 5 GHz, we observe two vortices that co-rotate with the pump, as indicated by the probability current and phase-space profiles. However, when

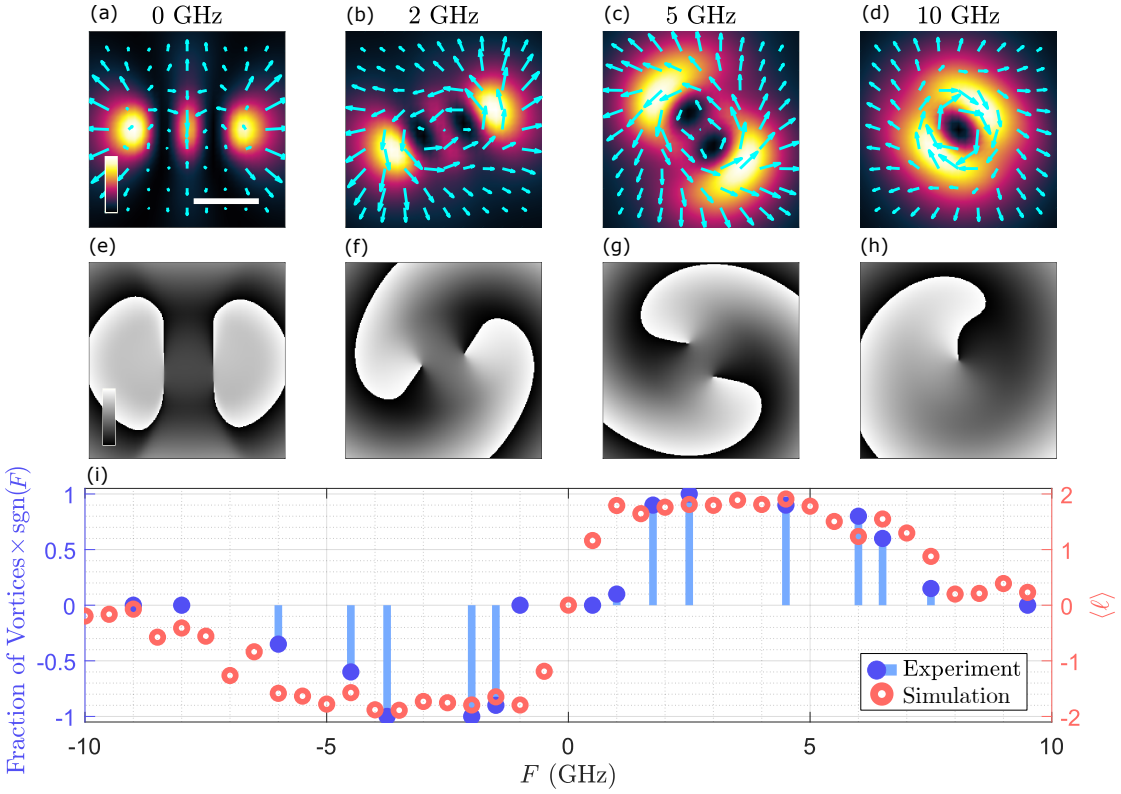

FIGURE 6.10: In simulations for trap rotation frequencies 0, 2, 5, 10 and 20 GHz, (a-d) real-space PL intensity superimposed with probability current j_c in cyan and (e-h) corresponding real-space phase-profiles. Each intensity and phase profile is normalised independently and the phase profiles scaled between $-\pi$ and π radians. The white scale-bar in (f) indicates 10 µm. (i) Average OAM per polariton within a 10 µm radius of the trap centres in (blue) experiment and (red) 2DGPE simulation using a 16 µm diameter pump, averaged over 40 realisations.

$F = 10$ GHz, the trapping potential becomes more uniform and less elliptical (as we saw in Figure 6.5(d)) and as a result, a lower mode becomes trapped leading to a single vortex at the centre of the system. However, as the reservoir is smeared out and more uniform in intensity, the single vortex at $F = 10$ GHz appears randomly and stochastically with $\ell = \pm 1$, where in Figure 6.10(d,h), we observe a counter-rotating singularly-charged vortex.

In Figure 6.10(i), we plot the average OAM per polariton (red) as a function of F for the numerically modelled condensate system, where $\langle \ell \rangle$ is averaged over 40 realisations. In blue, we also show the fraction of 100 experimental realisations where we observe a vortex multiplied by the sign of F, which follows the simulated trend of $\langle \ell \rangle$ very closely, where we observe two vortices in the system in almost every realisation in the region of roughly $|F|$ =1 GHz to 4 GHz. As the magnitude of F increases beyond 4 GHz, $\langle \ell \rangle$ converges to 0, as each realisation randomly presents with a vortex of $\ell = \pm 1$, and thus averages out over multiple realisations.

To summarise, single charged vortices can be induced into the polariton condensate system through optically stirring the condensate using a fast rotating (GHz rotation frequency) axially asymmetric quasi-elliptical optical pump profile for a small window of pump rotation frequencies. The winding number of each induced vortex is deterministically given by the rotation direction of the pump profile. When a larger pump profile is used (a stretched quasi-ellipse) two single-charged vortices are instead introduced into the polariton fluid. These results are observed experimentally and are corroborated by 2DGPE simulations.

6.5 Conclusions

We realise quantised vortices of polariton condensates induced by optical stirring using a rotating trap with broken axial symmetry. We map out regions where we observe a single-charged vortex that deterministically either co-rotates or counter-rotates with the rotating pump profile, where the region of trap rotation frequencies that lead to a deterministically rotating vortex coincide in simulation and experiment. To analyse the quantised vortices from the condensates in simulation, we project the condensate wavefunction onto angular harmonics and extract the number of polaritons with each value of OAM. We compare the extracted OAM to the phase profile about each vortex core, using the difference in phase at 100 points along the profile compared to the perfect vortex as a characterisation parameter. This characterisation allows us to potentially extract the distribution of the vortex and antivortex states from the experimentally obtained phase profiles, as ℓ is not directly measurable in the physical system.

Our findings demonstrate an unconventional GHz stirring method for the generation of stable quantised vortex states with a deterministic rotation direction. This is possible in the strong light-matter coupling regime due to the interactive nature of the quantum well excitons and ultrafast response time of polaritons to the excitation beam (on the order of picoseconds). Our results show that a time-periodic optical pump can fundamentality affect the condensate dynamics. Notably, we have shown that the condensate phase and energy spectrum strongly depend on the rotation frequency of the pump. We describe these phenomena using a discretised dissipative GPE model that considers only the $\ell = \pm 1$ angular condensate modes, which offers new perspectives on periodically driven polariton systems for Floquet engineering [244] in the strong light-matter coupling regime and spatio-temporal control of liquid light. With rapid experimental advancements allowing us to create extended coherent lattices of condensate [94, 78, 181], our technique could be used to engineer arrays of coupled vortices to study the complex interplay of polarisation, OAM, as well as explore the multiple phase degrees of freedom in the system in order to develop a programmable four-dimensional analogue simulator based on quantum fluids.

Chapter 7

Frustrated Geometries in Excited State Polariton Chains

7.1 Introduction

Polariton condensate systems have been extensively studied for their ability to minimise the XY Hamiltonian [54, 124, 106, 178, 2] with applications in solving graph-based mathematical problems [57, 4]. Although minimising the XY Hamiltonian is in general an NP-hard problem, there are still limitations in the complexity of a problem that can be mapped to this two-dimensional spin Hamiltonian characterised by a single complex number. All the aforementioned studies have considered the ground state condensate which is azimuthally homogeneous in density and phase and radially emits polaritons equally in all directions, resulting in a coupling strength between neighbours that depends solely on separation distance. However by exciting a system of first excited state condensates, additional degrees of freedom come into play such that two coupled excited state condensates can be characterised by four complex numbers. These excited state condensates emit particles anisotropically and as a results, the coupling strength is dependent on the geometric angle between the two trapped condensates.

Beyond the work in [2], a pair of annular traps with a larger diameter have been theoretically studied by Cherotchenko et al. in [235], which confine the first excited condensate mode in each trap. As the separation distance between the condensates is scanned, it is observed that the condensates pin to dipole modes either in parallel or perpendicular (head-to-tail) directions, with both in-phase and anti-phase alignment. In this chapter, the pair of first excited state condensates are extended to a continuous chain where the condensates are pinned to the dipole mode, and we observe geometric frustration in the case of an odd number of condensates, akin to that observed in [242]. This frustration is described by the system's Bloch mode with non-zero

quasimomentum, which results in an overall flow of a polariton current around the chain. Additionally, we investigate the effect on the pair of first excited state condensates which are pinned to the dipole modes by squeezing the annular trapping potential to an ellipse, where in both experiment and simulation we observe an energy splitting when the two dipoles are forced into a perpendicular alignment geometry.

As the first excited state condensate has additional degrees of freedom compared to the ground state condensate, the energy minimisation of the system goes beyond the XY Hamiltonian's two degrees of freedom, as two coupled excited state condensates are characterised by three relative phase terms, compared to the single term in the XY model. These additional degrees of freedom are defined in this chapter and are analysed for a continuous chain of FM and AFM coupled first excited state condensates. This continuous chain geometry is also studied using a Stuart-Landau network of dissipative coupled oscillators, where we report the first recorded observations of a frustrated mode with an even number of ferromagnetically coupled oscillators. This surprising observation is likened the "twisted state" of the Kuramoto model [202]. Designing an analogue simulator with these additional degrees of freedom will allow us to solve complex problems beyond those that are currently solvable using the XY Hamiltonian and the full characterisation of this complex spin system will put the excited state polariton simulator at the forefront of all optical heuristic solvers.

In this chapter, both the simulations and experiment were performed by me, although the optical setup was built by Lucy Pickup and I received assistance with optical alignment and image acquisition from Lucy Pickup, Julian Töpfer, Tamsin Cookson and Giannis Chatzopoulos. Additionally, I had regular discussions with the Hybrid Photonics Group as a whole about the simulation results, and particularly with Helgi Sigurdsson on the implementation of the GPE.

7.2 Relative Phases Between Two Condensates

The degrees of freedom that describe the first excited state condensate (whether in a dipole or vortex mode) are captured as the superposition of the $\psi_{10} = xe^{-\frac{x^2}{2}}$ and $\psi_{01} = ye^{-\frac{y^2}{2}}$ Hermite-Gaussian modes. These are scaled by some complex number c_x, c_y, which rotates the real-valued Hermite-Gaussian mode about the complex plane and scales it in amplitude. ψ_{10} and ψ_{01} are often referred to as "p-orbitals", where any first-excited state condensate can be described as $\psi = [P_x, P_y]$ from the horizontal and vertical p-orbital profiles through the condensate centre respectively, defined as:

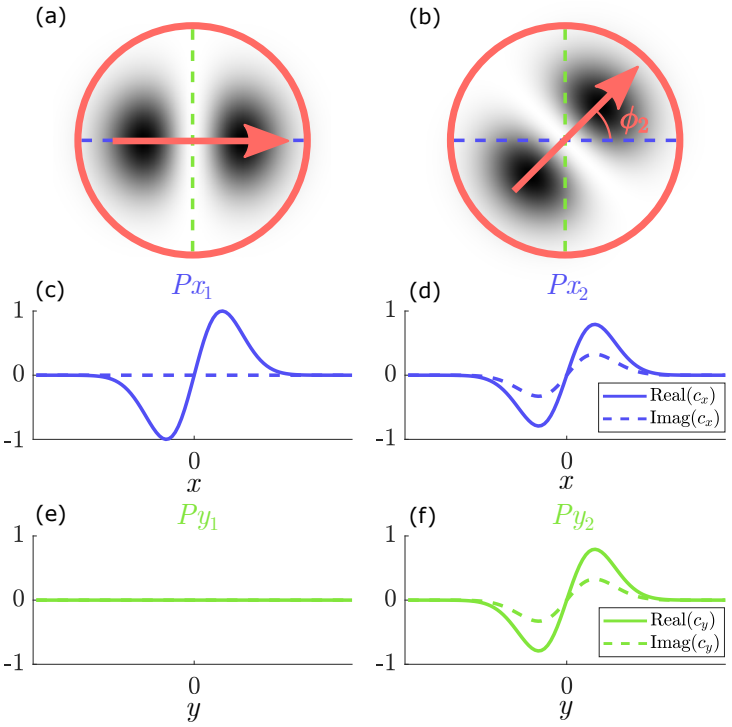

FIGURE 7.1: Schematic to show the relative phase characterisation between two first-excited state polariton condensates by analysing the x and y components of the doublet mode as complex numbers c_x and c_y respectively. These parameters describe the rotation of the p-orbital mode about the complex plane. Here, (a) shows the doublet intensity with a purely real p_x-orbital corresponding to $c_{x_1} = 1 + 0i$ and no amplitude in the p_y direction leading to $\phi_1 = 0$ rad. (b) shows a dipole mode intensity with $\phi_2 = \arctan(|c_{y_2}|/|c_{x_2}|) = \pi/4$ rotation and phases $\arg(c_{x_2}) = \arg(c_{y_2}) = \pi/8$.

$$P_x = c_x\psi_{10} = |c_x|e^{i\theta_x}\psi_{10} \tag{7.1}$$

$$P_y = c_y\psi_{01} = |c_y|e^{i\theta_y}\psi_{01} \tag{7.2}$$

where $c_x, c_y \in \mathbb{C}$ and $\theta_{x(y)} = \arg(c_{x(y)})$. As such, any first excited state condensate can be described simply by two complex numbers: c_x and c_y. For example, the real (solid) and imaginary (dashed) components of P_x and P_y of the dipole in Figure 7.1(a) are plot in Figure 7.1(c,e) respectively and show that $c_x = 1 + 0i$ (i.e. $P_x = \psi_{10}$) and $c_y = 0$ as the dipole is aligned along the x-axis. However, the second condensate (Figure 7.1(b)) is geometrically rotated with an angle $\phi_2 = \arctan(|c_{y_2}|/|c_{x_2}|) = \pi/4$ relative to the x-axis. P_{x_2} and P_{y_2} in Figure 7.1(d,f) thus show equal intensity in the x and y directions with $c_x = c_y = \frac{\sqrt{2}}{2}e^{i\pi/8}$.

To describe a system of interacting traps, we can compare each pair of coupled excited state condensates and project them onto the p_x and p_y orbital states giving a bi-spinor written as

$$\psi = [P_{x_1}, P_{y_1}, P_{x_2}, P_{y_2}] \tag{7.3}$$

where "1" and "2" denote the different condensates and the information of each state is encoded by four complex coefficients: $c_{x_1}, c_{y_1}, c_{x_2}$ and c_{y_2}, or equivalently, eight real numbers governing the amplitude and phase of the complex coefficients. When comparing two condensates, the relative coefficients are fully described by:

$$\Delta\theta_x = \theta_{x_2} - \theta_{x_1} \tag{7.4}$$

$$\Delta\theta_y = \theta_{y_2} - \theta_{y_1} \tag{7.5}$$

$$\phi_1 = \arctan\left(\frac{|c_{y_1}|}{|c_{x_1}|}\right) \tag{7.6}$$

$$\phi_2 = \arctan\left(\frac{|c_{y_2}|}{|c_{x_2}|}\right) \tag{7.7}$$

$$c_1 = \sqrt{c_{x_1}^2 + c_{y_1}^2} \tag{7.8}$$

$$c_2 = \sqrt{c_{x_2}^2 + c_{y_2}^2}. \tag{7.9}$$

Without loss of generality, we can scale the system such that the intensity of all condensates are equal in order to tackle the minimisation of a spin Hamiltonian [57] and apply a global phase offset, such that a single θ is set to zero (e.g. $\theta_{x_1} = 0$). Under these assumptions, the dipole alignment between a pair of condensates can be fully described by Eqs. (7.4,7.5) and $\Delta\phi = \phi_2 - \phi_1$.

7.3 Condensate Pinning

For a single annular trap, uncoupled to any other condensates, the first excited state will be occupied equally by two orthogonal dipole modes, thus resulting in a vortex with uniform intensity in a ring shape about a dark vortex core. This core houses a phase singularity with a phase winding of 2π which randomly and stochastically appears in a clockwise or anticlockwise direction (see Figure 6.2(a-c) for an example perfect vortex). However, when a second identical annular trap is introduced to the system, the density of both condensates orientate into two dipole modes consisting of the equal super position of the vortex and anti-vortex modes. In general, the neighbouring dipoles will align head-to-tail along the shortest path between the trap centres with either same or opposite phase alignment, resulting in destructive and constructive interference between the two dipoles respectively, analogous to σ-bonding of molecules in chemistry [235], provided that the system is pumped at or just above the power threshold. As with the ground state condensate pair in [2], for trap separation along the $x(y)$ axis, the FM and AFM coupling can be accessed through scanning the separation distance between the annular traps. Here, FM corresponds $\Delta\theta_{x(y)} = 0$ which now results in destructive interference between neighbours, and AFM coupling leads to alternating nearest neighbours being horizontally (vertically) flipped, such that $\Delta\theta_{x(y)} = \pi$ which results in constructive interference between neighbours.

Interestingly, at the midpoint separation distance between the purely FM and AFM dipole mode coupling, the two condensates can align in parallel with the same or flipped phase alignment, corresponding to in-phase and anti-phase molecular π-bonding [235].

The distance scan between two first excited state condensates confined within identical optical annular traps is performed theoretically using the generalised 2D GPE (see subsection 7.6.1). The separation distance between the two traps, which we label d, is considered between 10 μm and 28 μm in steps of 0.2 μm and averaged over 16 unique realisations. The real-space density and phase of two condensates with $d = 12$ μm is depicted in Figure 7.7(a,c). Here, the excited state condensates have pinned to the FM head-to-tail (σ-bond) configuration, resulting in a dark central interference fringe in real-space and a π phase jump at the centre of phase space. For each step of d, the horizontal cross section is taken through the centre of real-space along the line that connects the two trap centres. These cross sectional line profiles are averaged over 16 realisations and are stacked over all trap separation distances (shown in Figure 7.7(b)).

Here, it appears that the regions of d corresponding to FM condensate coupling (destructive interference) are twice as large as the regions of d corresponding to AFM coupling (constructive interference). In this scan, we do not see the π-bond condensate alignment, however from the power dependence of the system for each trap separation distance (shown in Figure 7.7(d)), it is interesting that the pump power for threshold condensation jumps in discrete steps as the system transitions from AFM and FM coupling (with increasing d). Note that the condensation threshold is defined as the pump power required for 1 polariton to exist in the condensate. For the ground state condensate studied in chapter 3, the transition between the AFM and FM regions (and vice versa) appeared blurred in real space, as both modes were partially occupied and although only one interference pattern was predominantly observed in real-space, over many realisations the dominant visible mode stochastically switched and averaged out forming a blurred region. In the case of the excited state condensate, as there is a jump in threshold power from the AFM to FM coupling, there exists a sharp clearly defined step between the two coupling regimes. However, the transition between the FM to AFM coupling regime share a similar threshold power, but as the FM coupling regime appears for a smaller separation distance with the same condensation power threshold, this mode has a slightly increased overlap with the gain and thus is the dominant visible mode in the transition from FM to AFM coupling.

7.4 Loop of Condensates

7.4.1 Small Polygon

Beyond two condensates, we expand the system to a loop of $N > 2$ traps in order to understand if the condensates still align in the head-to-tail configuration as we saw for $N = 2$. The loop is formed by arranging the traps in a regular polygon with a nearest neighbour separation of d. Interestingly, for a small number of traps, such as $N = 5$ in Figure 7.3, the condensates do not align in the head-to-tail configuration about the polygons perimeter, but in alternative configurations instead. At $d = 18$ µm for example, the condensates align in parallel, such that all condensates have the same phase and density profiles with $c_{y_1} = c_{y_2} = c_{y_i}$. By increasing the nearest neighbour separation to 20 µm, we do however see radial alignment of the condensates, which is not observed for $N > 5$ in these simulations. Here, the inner ring of dipole lobes interfere with some complex constructive interference pattern, while the outer lobes

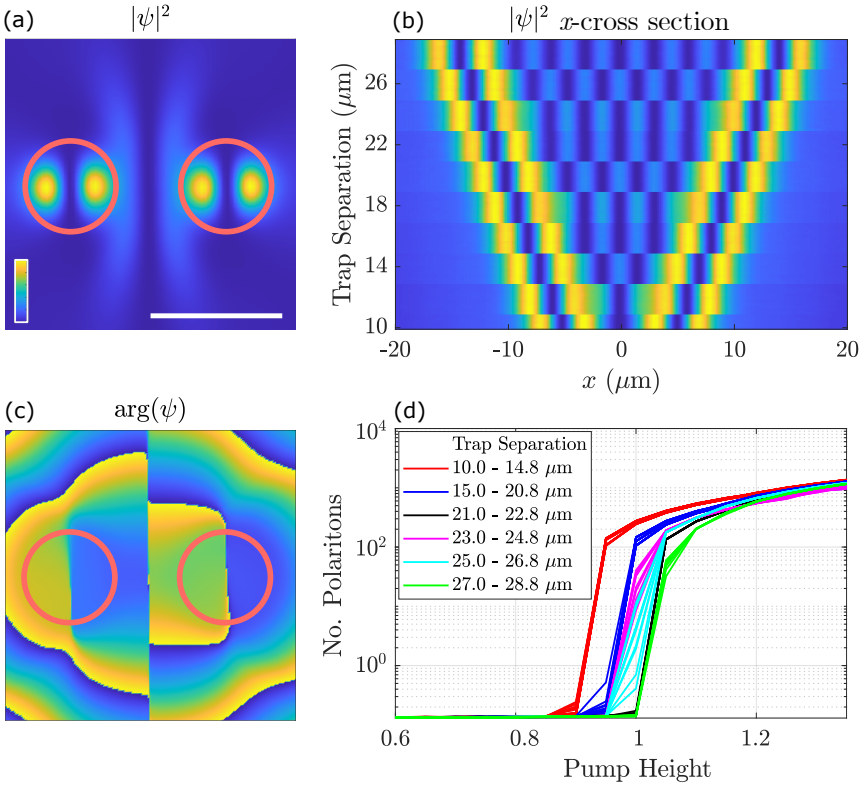

FIGURE 7.2: Simulations of two coupled optically trapped first-excited state condensates showing (a) real-space and (c) phase-space PL at a trap separation of $d = 12$ µm, (b) real-space x-cross section through the centre of the traps as a function of trap separation (averaged over 16 unique realisations), (d) the power dependence of the two trap system where each colour denotes a range in trap separation distances matching up to the coupling transitions in (b). (a,b) normalised to the same colour scale, with each cross-section in (b) normalised independently and (c) with sale colour scale ranging from -π to π radians. The overlayed red rings in (a,c) represent the pump profile. The white line in (a) corresponds to 10 µm.

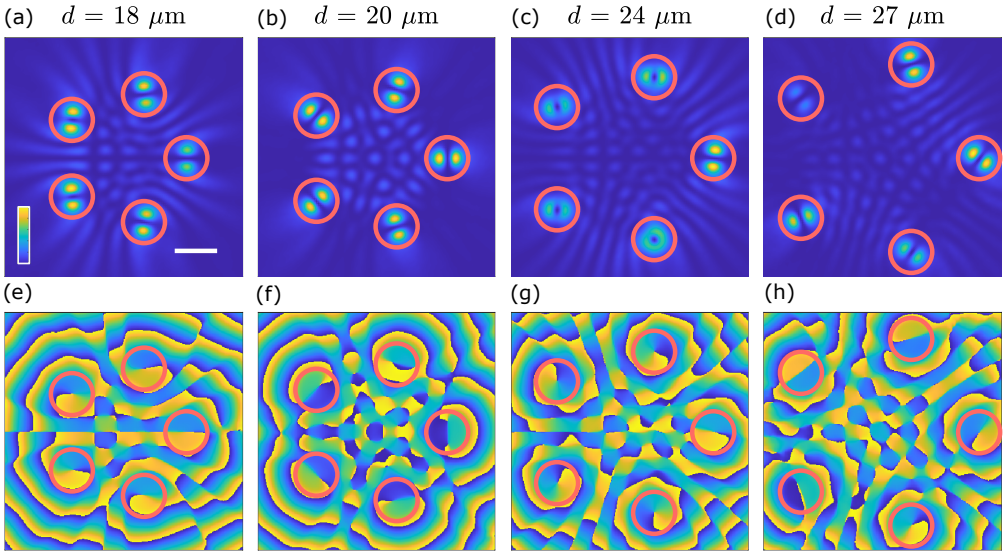

FIGURE 7.3: PL from $N = 5$ excited state condensates arranged in a regular pentagon with a first-nearest-neighbour distance of (a,e) 18 µm, (b,f) 20 µm, (c,g) 24 µm and (d,h) 27 µm, shown inn (a-d) real-space and (e-h) phase-space. The overlayed red rings represent the pumping profiles. The same colour scale is used throughout and is independently normalised in (a-d), and scaled between $-\pi$ and π in (e-h). The white line in (a) corresponds to 10 µm.

appear to not significantly interact as their relative separation is significantly greater than their inner radial counterparts in the limit of $N \leq 5$.

It is not surprising that we do not observe azimuthal alignment for $N = 5$ in this range of d, as for such a (relatively) small polygon, $\Delta\phi$ between nearest neighbours would be 0.4π, which is not close to either value of $\Delta\phi$ for the σ-bond or π-bond arrangement seen for just two condensates. Additionally, the coupling to condensates beyond first nearest neighbour is non-negligible for so few traps and affects the alignment of the condensates. This is indicated by the complex interference patterns at the centre of the polygons. For this small polygon, we also see the alignment of alternating-charge vortices with one dipole in Figure 7.3(c,g) and a combination of σ-bonding and π-bonding between nearest neighbours in Figure 7.3(d,h) as well as radial alignment. Clearly, such a polygon is not ideal for investigating the alignment between first nearest neighbours as the condensates are strongly dependent on the geometric angle between neighbouring traps.

7.4.2 Continuous Chain

In addition to the cross talk beyond first nearest neighbours in a geometric polygon of traps, it is also more complicated to extract the P_x and P_y profiles from condensates that are not arranged axially. In order to study the alignment of a loop of excited state condensates, the traps are instead aligned in a horizontally-separated chain configuration with continuous boundary conditions applied in the x-axis (i.e. the

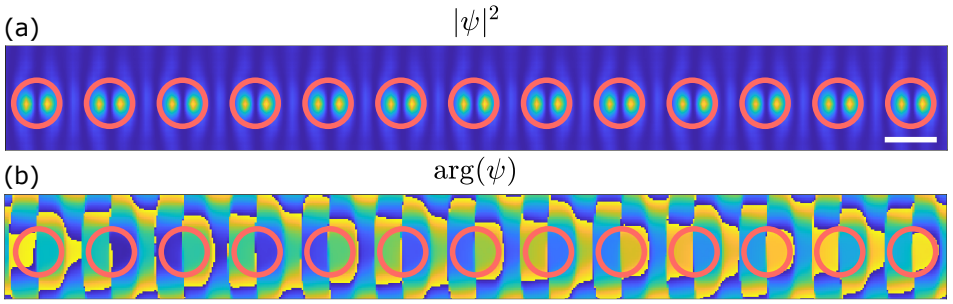

FIGURE 7.4: (a) Real-space PL intensity and (b) real-space PL phase of 13 condensates each trapped by an optical annulus (red rings), with a nearest neighbour separation of $d = 14$ µm (AFM coupling) and continuous horizontal boundary conditions. Numerically modelled using the 2DGPE. White scale bar in (a) represents 10 µm. Both follow the same colour scale but (a) is normalised between 0 and 1, and (b) between $-\pi$ rad and π rad.

decaying boundary conditions in the x-direction are removed), thus forming a continuous chain or "unraveled polygon". Trivially, FM first nearest neighbour coupling results in head-to-tail alignment with $\Delta\theta_x = \Delta\theta_y = 0$ across the chain. Additionally, when a chain is considered with an even number of AFM coupled traps, the condensates align head-to-tail with $\Delta\theta_x = \pi$ between nearest neighbours. The interesting case that we consider is for AFM nearest neighbour coupling between an odd number of traps in a continuous chain. For this, we consider $N = 13$ with $d = 14$ µm (AFM coupling) as shown in Figure 7.4. We then extract the relative phase and amplitude parameters (as defined in Eqs. (7.4-7.9)) between each pair of nearest neighbours by projecting the condensates onto the p-orbitals with $\psi = [P_{x_1}, P_{y_1}, \ldots, P_{x_{13}}, P_{y_{13}}]$. Figure 7.5(a) schematically shows the extraction of $\theta_{x_{13}} = \arg(c_{x_{13}})$ from the condensate order parameter and Figure 7.5(b) shows $\theta_{x(y)}$ for each condensate, where the negligible opacity of θ_y indicates σ-bonding across the chain, in addition to $\phi \simeq 0$ for all condensates in Figure 7.5(c).

Interestingly, we now see that $\Delta\theta_x = \pm\pi + \delta$ with $\pm$ alternating for each adjacent pair of condensates, where $\delta = \pm\pi/N$, and results in a phase winding of 12π about the continuous loop. This additional phase rotation of δ allows an odd number of AFM coupled condensates to arrange into a continuous chain and has previously been experimentally observed in ballistically expanding Gaussian condensates arranged in an AFM polygon, where the phase winding manifests as a vortex at the centre of the system [242]. Compared to the even-N FM chain, which exhibits $\delta = 0$, the non-zero phase shift of δ in the odd-N chain shows that there is a flow of polaritons, or "polariton current".

This polariton current around the chain can be interpreted by applying Bloch's theorem through describing the condensates in terms of Bloch modes with a quasimomentum of $q = 2\pi\ell/L$ for $\ell \in \mathbb{Z}$ (the phase winding number) with $|\ell| \leq N/2$ and $L = Nd$ (length of the continuous chain) [242]. In terms of the reduced Brillouin

zone, the $\ell = 0$ mode is occupied at $qd = 0$ when the condensates are FM coupled with $\Delta\theta_x = 0$ between all condensate pairs. For an even number of AFM coupled condensates, in general the $\ell = N/2$ mode is occupied at $qd = \pi$ and results in $\Delta\theta_x = \pi$. However, when N is odd, there is no Bloch mode at the edge of the Brillouin zone ($qd = \pi$) and so the polaritons condense into the states closest to the edge in order to maximise the gain with $\ell = \pm(N-1)/2$ giving $\Delta\theta_x = \pm(N-1)\pi/N$ between adjacent pairs, where $\pm$ indicates a polariton current in the $\pm x$ direction respectively.

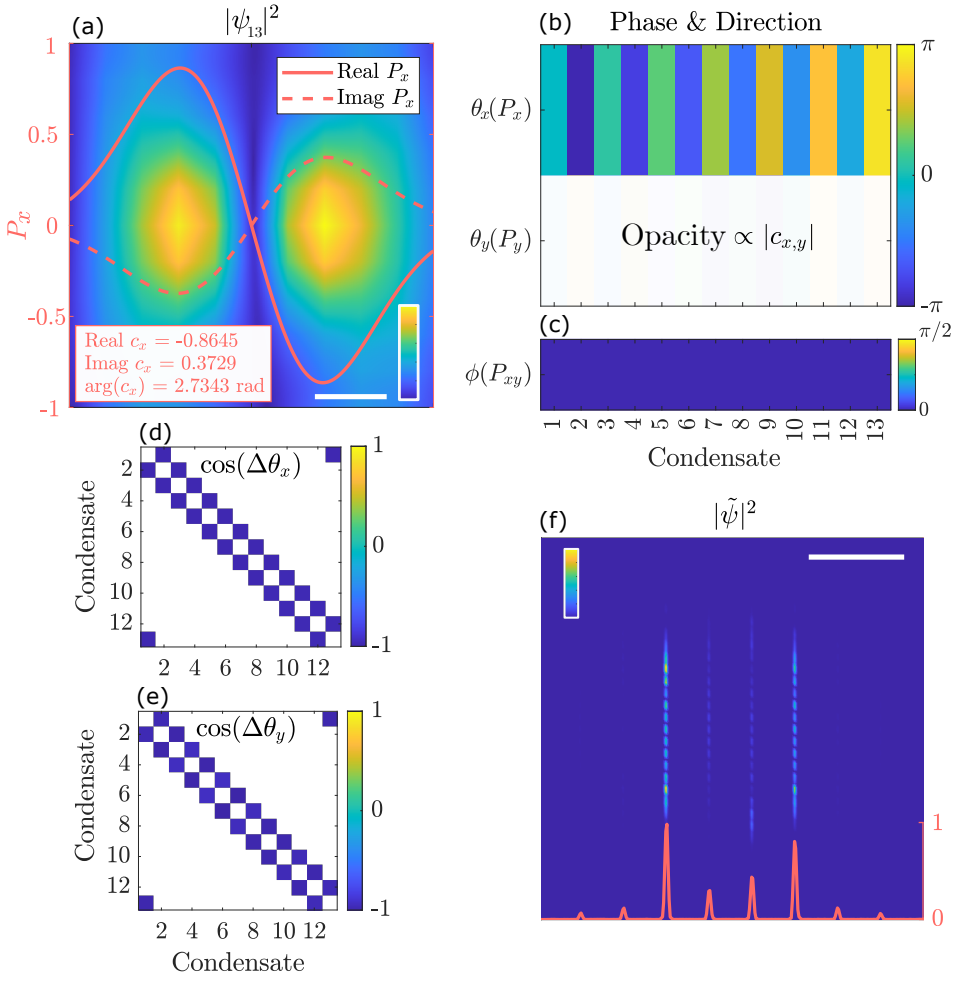

FIGURE 7.5: (a) Real-space PL intensity of the 13$^{\text{th}}$ condensate in an $N = 13$ chain of first-excited state condensates separated by $d = 14$ µm (AFM coupling) with continuous boundary conditions (i.e. forming a loop) on a normalised linear colour scale, with the x-line profile plot in red, where the solid and dashed lines represent the real and imaginary component of the P_x-orbital respectively and the corresponding c_x values shown in the bottom left corner. (b) the extracted $\theta_{x(y)}(P_{x(y)}) = \arg(c_{x(y)})$ and $\phi(P_{xy}) = \arctan(|c_y|/|c_x|)$ for each condensate in the chain, once the system has converged to a stable solution. The opacity of $\theta(P_{x(y)})$ is proportional to $|c_{x(y)}|$ respectively. (d-e) Show the cosine of the relative phases $\Delta\theta_x$ and $\Delta\theta_y$ between nearest neighbour condensates, where the opacity is proportional to the amplitude of the corresponding inter-condensate coupling strength. (f) shows the Fourier-space PL intensity of the chain with a dominant negative k_x corresponding to the current momentum in the $-x$ direction around the chain, as indicated by the red overlayed line profile. The white lines in (a,e) corresponds to 2 µm and 1 µm^{-1} respectively.

In the instance of Figure 7.5, $\ell = -6$ and $\Delta\theta_x = -12\pi/13 \simeq -2.90$ rad. We additionally show the cosine of the relative phases between nearest neighbours in Figure 7.5(d,e), which indicates that $\cos(\Delta\theta_x)$ and $\cos(\Delta\theta_y)$ are minimised to $\cos(-12\pi/13) \simeq -0.97$, where this parameter will converge towards -1 with the increase in N. Between all nearest neighbours, $\cos(\Delta\phi) \approx 1$ due to the σ-bonding of the condensates and corresponds to the weighting of the c_x component in the system compared to $\sin(\Delta\phi)$ for c_y.

As $\Delta\theta_x$ between each nearest neighbour pair is constant, the polariton current is also constant about the chain. In Figure 7.5(f), the brightest peak of Fourier-space shows that the dominant polariton momentum is in the $-x$ directions with a peak at $k_x = -0.68 \pm 0.06$ μm^{-1}. Using the Bloch analysis, the quasimomentum of the flowing polaritons is $q = 2\pi\ell/L = -0.414$ meV ps μm^{-1}, which corresponds to a wavenumber of $k = q/\hbar = -0.63$ μm^{-1}, thus showing that the dominant k-peak in Figure 7.5(f)

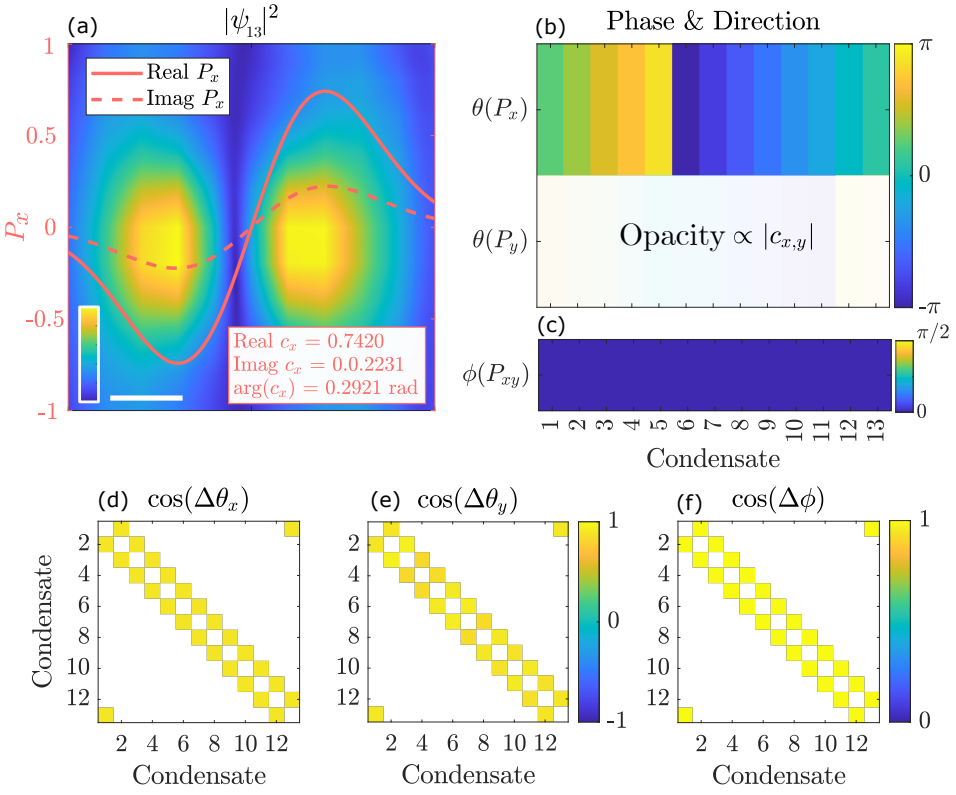

FIGURE 7.6: (a) Real-space PL intensity of the 13$^{\text{th}}$ condensate in an $N = 13$ chain of first-excited state condensates separated by $d = 17$ μm (FM coupling) with continuous boundary conditions (i.e. forming a loop) on a normalised linear colour scale, with the x-line profile plot in red, where the solid and dashed lines represent the real and imaginary component of the P_x-orbital respectively and the corresponding c_x values shown in the bottom left corner. (b) the extracted $\theta_{x(y)}(P_{x(y)}) = \arg(c_{x(y)})$ and $\phi(P_{xy}) = \arctan(|c_y|/|c_x|)$ for each condensate in the chain, once the system has converged to a stable solution. The opacity of $\theta(P_{x(y)})$ is proportional to $|c_{x(y)}|$ respectively. (d-f) Show the cosine of the relative phases $\Delta\theta_x$, $\Delta\theta_y$ and $\Delta\phi$ between nearest neighbour condensates, where the opacity is proportional to the amplitude of the corresponding inter-condensate coupling strength. The white line in (a) corresponds to 2 μm.

corresponds to the $\ell = -6$ quasimomentum and indicates a group current velocity of $v_g = \hbar k/m_p = -1.51 \pm 0.26$ µm ps^{-1}. Although $|\ell| = (N-1)/2$ has the highest gain with odd-N and alternating condensate alignment, it is possible for the condensates to condense with other non-zero quasimomenta available in the system, as shown in [242] for a polygon of $N = 5$ AFM coupled ballistically expanding polariton condensates. Interestingly, when we adjust the nearest neighbour separation to $d = 17$ µm (FM coupling), although in most instances $\Delta\theta_x = 0$ between neighbours, in some cases we observe a current with $|\ell| = 1$, as shown in Figure 7.6(b). Again, $c_{x,y}$ are extracted from fitting the horizontal and vertical cross sections of each condensate to $P_{x,y}$ orbitals respectively (Figure 7.6(a)). Here, the phase winds 2π around the continuous chain such that $\Delta\theta_x = 2\pi/13 = 0.48$ rad between each neighbour, leading to $\cos(\Delta\theta_x) = 0.89$ as shown in Figure 7.6(d). Again, the condensates exhibit σ-bonding along the chain, such that $|c_y|$ is negligible and $\phi \simeq 0$ for all condensates.

7.4.3 Twisted State

It is not just the cases of odd-N that exhibit $|\ell| \neq 0$, but also for even-N. For example, networks of identical Kuramoto oscillators have been studied with unit FM coupling to $\mu(N-1)$ nearest neighbours, where $\mu > 0.75$ guarantees that all oscillators will converge to a synchronised in-phase configuration with $\ell = 0$ [202]. Below this threshold however, the loop of oscillators can exhibit a constant relative phase difference between nearest neighbours of $\ell = 2\pi/N$, where ℓ again is the phase winding number about the continuous loop [202]. These solutions are known as "twisted states" and correspond exactly with what we observe in the continuous chain of excited state condensates in Figure 7.5 and Figure 7.6.

In order to understand the distribution of phase windings for condensates arranged in a chain, we study the system of sparsely connected Stuart-Landau oscillators (see subsection 7.6.2) to characterise the probability of each winding number occurring in a large chain of FM coupled oscillators. Here, we consider $N = 20, 40, 60, 80, 100$ with unit FM coupling between one to four nearest neighbours and plot the distribution of each winding number ℓ observed over 1000 unique realisations in Figure 7.7(a-d). For larger N, the spread in ℓ is greater, but reduces quickly as the number of nearest neighbour connections increases. When $N = 20$ for example, we observe $|\ell| = 0, 1, 2$ for first nearest neighbour connectivity, but this region decreases to $|\ell| = 0, 1$ when second nearest neighbour coupling is included to the system, as depicted in Figure 7.7(e-i) where the oscillators (circles) have unit FM coupling following the black graph edges and their steady-state phases are shown by their colour. In this analysis, $|\ell| = 2$ occurred in 0.1% of the cases for $N = 20$ with first nearest neighbour connectivity, so it is very unlikely to observe a phase winding greater than 2π in a smaller chain, which

is why only $|\ell| = 0, 1$ is observed for the $N = 13$ AFM excited state condensate chain in the GPE simulations.

To our knowledge, these are the first results investigating the twisted state of Stuart-Landau oscillators and comparing them to the sparse Kuramoto networks explored in [202]. As the phase winding about a twisted state corresponds to a phase singularity at the centre of the looped chain, large networks of sparsely connected

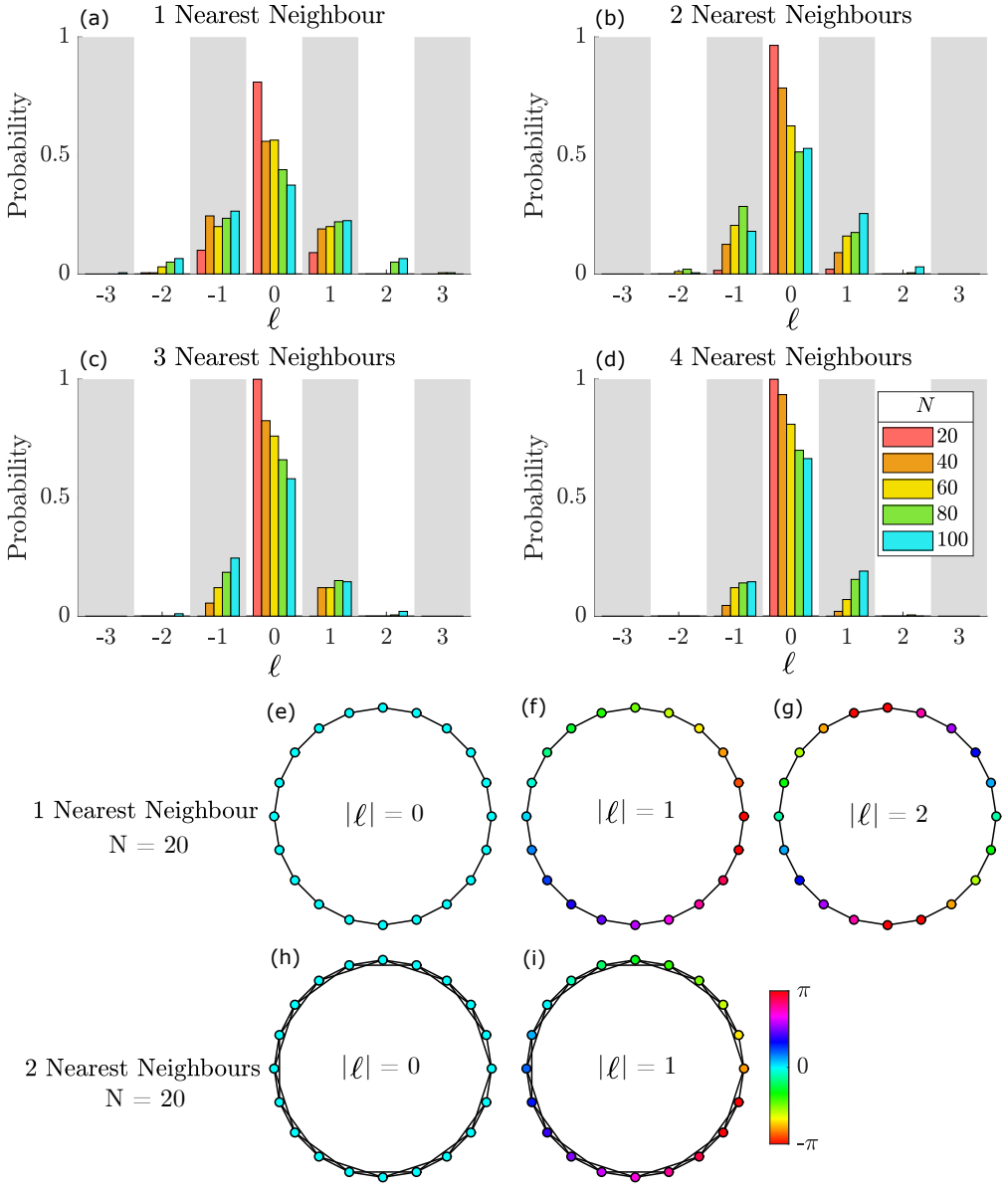

FIGURE 7.7: Distribution in winding number ℓ of a continuous chain of Stuart-Landau oscillators with (a-d) 1-4 nearest neighbour equal FM couplings respectively for $N = 20$, 40, 60, 80 and 100 shown in red, orange, yellow, green and blue bars respectively, over 1000 unique realisations for each N and number of nearest neighbours. For $N = 20$, an example of each stable phase solution is shown in graph format with (e-g) 1 nearest neighbour and (h,i) 2 nearest neighbour connections, showing all observed values of $|\ell|$ over 1000 realisations.

condensates could be used to investigate high-charge vortices in polariton condensate systems.

7.5 Coupled Ellipses

As shown in [235], a pair of optically trapped excited state condensates can align with σ (head-to-tail) or π (parallel dipole) bonding when confined in an annular trapped over varying separation distances. However, by giving the trap some ellipticity, we can force an excited state condensates into the dipole mode with the excited state along the traps major axis. For two dipole modes, we will no longer observe pinning into σ and π bonds, but rather the dipoles will take on any geometric angle $\Delta\phi$ dictated by the relative angle between the trap major axes.

We create two elliptical traps spatially separated by distance d that confine dipole modes in both simulation and experiment and consider $\Delta\phi = 0$ and $\Delta\phi = \pi$ rad. The simulation technique is identical to that used in section 7.3, but now the annular pumping profile in squeezed in one axis to form an ellipse with a 9.3 µm major axis and 7.3 µm minor axis and again the simulations are performed using the generalised 2D GPE (see subsection 7.6.1). In experiment, the elliptical pump profiles are formed using an SLM displaying a phase-modulating hologram calculated using the MRAF algorithm (see subsubsection 2.2.2.1), where the relative amplitude of the two ellipses in the target image are adjusted to give a similar PL intensity from each independent condensate when blocked in-turn with a knife edge. The experimental setup and technique is identical to section 3.2, other than a slight change in pump profile to form two elliptical traps, but is summarised again in section 7.7.

First we consider the elliptical traps separated along the x-axis, with their major axes aligned head-to-tail, through vary the separation between the trap centres d, where the experimental PL for $d = 30$ µm is shown in Figure 7.8(a). In both simulation and experiment, the system maintains a single first-excited state energy mode as d is scanned from 25µm to 60 µm (Figure 7.8(b)), where fluctuations in the experimental energy are a result of the fluctuations in total pump power from adjusting the relative pump intensities for each separation distance. With $\Delta\phi = 0$, this is fundamentally the same as scanning d with the two annular traps as in section 7.3. However, when the right trap is rotated by π rad such that $\Delta\phi = \pi$ between the two condensed dipole modes as shown in Figure 7.8(c) with $d = 30$ µm, the system energy splits by 0.09 meV in experiment (averaged over the range in d) and 0.05 meV in simulation (averaged over 40 realisations for each value of d), as shown in Figure 7.8(d), where the deviation between these two values is likely down to the slight difference in pumping geometries and pumping powers. Additionally, when the right trap is rotated by π rad, an additional interference fringe appears, where in Figure 7.8(a,c) the interference

between the condensates flips from destructive to constructive as a result of the increased distance between the closest condensate lobes.

As the dominant polariton flow from a dipole mode is along its major axis (as we saw previously from the dipole in Figure 6.3(f)), when the condensates are aligned head to tail, there is an equal flow of polaritons propagating from the left to right condensate and vice versa. However, when the right condensate is rotated, there is a strong flow of polaritons from the left to right condensates, as the dominant flow of the polaritons from the rotated condensate is in the vertical directions. This means the right condensate has a slightly higher gain than the left condensate and an energy splitting occurs as a result.

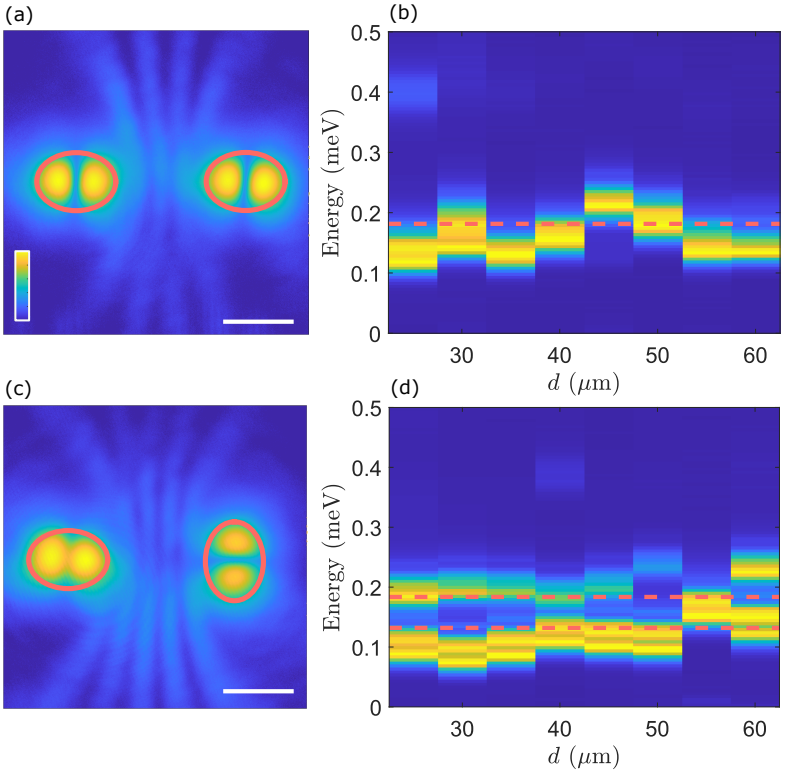

FIGURE 7.8: Experimental real-space condensate PL for two elliptical traps with a 11.2 µm major axis and 8.3 µm minor axis aligned (a) head-to-tail and (c) one trap rotated by π rad for a trap separation of $d = 30$ µm along the x-axis, both shown on a normalised logarithmic colour scale between 0.001 and 1. White line represents 10 µm and red ellipses indicate the shape of the optical traps. The experimental energy, relative to 1.4463 eV (∼0.8 meV above bottom of LP branch [3]), integrated over all k_x for varying trap separation and a relative trap rotation of (b) 0 rad and (d) π rad. Here the colour scale is linear and normalised between 0 and 1. The energy peaks from the equivalent numerical simulations of the GPE are shown by dashed red lines (averaged over 40 unique realisations), with energy realative to bottom of the LP branch.

7.6 Polariton Theory

7.6.1 2D GPE

The condensates are modelled using a mean-field theory approach to describe the condensate order parameter $\Psi(\mathbf{r},t)$ using the generalised 2D GPE coupled to two rate equations corresponding to the active and inactive exciton reservoirs (see section 2.1 for the derivation and details):

$$i\frac{\partial\psi}{\partial t} = \left[-\frac{\hbar\nabla^2}{2m_p} + G(n_A+n_I) + \alpha|\psi|^2 + \frac{i}{2}(Rn_A-\gamma)\right]\psi(\mathbf{r},t), \tag{7.10}$$

$$\frac{\partial n_A}{\partial t} = -(\Gamma_A + R|\psi|^2)n_A + Wn_I, \tag{7.11}$$

$$\frac{\partial n_I}{\partial t} = -(\Gamma_I + W)n_I + P(\mathbf{r}). \tag{7.12}$$

Here, m_p is the effective polariton mass at the bottom of the LP branch, G is the polariton-reservoir interaction strength, α is the nonlinear polariton-polariton interaction strength, R is the rate of stimulated scattering of polaritons from the active reservoir into the condensates, γ is the polariton decay rate, $n_{A,I}$ give the density of excitons in the active and inactive exciton reservoirs with decay rates of $\Gamma_{A,I}$ respectively, W is the conversion rate of excitons from the inactive to active reservoirs and $P(\mathbf{r})$ is the pump profile of the optical cavity excitation. In section 7.3 and section 7.4, the annular trap has a diameter of 9.3 μm and FWHM of 2.3 μm to match the diffraction limit in experiment. In section 7.5, the elliptical pump profiles have a 9.3 μm major axis and 7.3 μm minor axis, again with a 2.3 μm FWHM. All condensates are pumped equally in each simulation with a pumping power that excited the system to just above condensation threshold. A decaying potential is applied to the outer 10% of the system perimeter to block the continuous boundary conditions of the fast Fourier transform functions used in the numerics. However, to achieve the continuous chain (or loop), the decaying boundary conditions are removed in the x-direction.

The parameters in the GPE are chosen to match the properties of the InGaAs microcavity sample used in experiment, such that $m_p = 0.28$ meV ps^2, $\gamma = \frac{1}{5.5}$ ps^{-1}, $\hbar\alpha = 3.5$ μeV μm^2 and $G = 10\alpha$. The recombination rate of optically inactive excitons is taken to be much smaller than the condensate decay rate with $\Gamma_I = 0.01\gamma$, whereas the active reservoir exciton decay rate is comparable to the condensate decay rate ($\Gamma_A = \gamma$) due to the fast thermalisation to the exciton background [53]. Lastly, exciton feeding rates are found by fitting to experimental results, where we use $\hbar R = 98.9$ μeV μm^2 and $W = 0.035$ ps^{-1}.

7.6.2 Stuart-Landau Model

We apply the Stuart-Landau model to the sparsely connected networks of dissipatively coupled oscillators following:

$$\dot{\psi}_n = -[i\omega_n + |\psi_n|^2]\psi_n + \sum_{m=1}^{N} J_{nm}\psi_m \tag{7.13}$$

where $\psi_n \in \mathbb{C}$ gives the dynamics of oscillator n as a complex parameter with amplitude $|\psi_n|$ and phase $\arg(\psi_n)$. The Stuart-Landau model can be used to describe the dynamics of ground state polariton condensates [2], but can also more general describe any system of dissipative coupled nonlinear oscillator networks, where ω_n is the oscillators natural frequency and J_{nm} is the coupling strength between oscillators n and m. The simulations in subsection 7.4.3 consider uniform unit FM coupling with $J_{nm} = 1$ and identical Stuart-Landau oscillators, such that $\omega_n = \omega_m$. As such, a rotating gauge with a frequency of ω_n is chosen in order to set $\omega_n = 0$ without loss of generality.

7.7 Experimental Methods

The optically trapped dipole mode condensates are experimentally realised using a strain-compensated 2λ GaAs planar microcavity sandwiching an InGaAs QW core, as described in [3]. The sample is held in a cold finger cryostat and cooled to a cryogenic temperature using liquid helium. The sample is pumped nonresonantly with right-circularly-polarised light from a CW Ti:sapphire laser with a wavelength of 780 nm to match up with the first minimum in the reflectivity spectrum of the sample energetically above the reflectivity stopband. The laser is focussed on the surface of the sample using a high NA microscope objective at a point with a cavity detuning of ~ -5 meV. The excitation beam is periodically chopped using an AOM with a 5% duty cycle and 10 KHz repetition rate in order to avoid burning the sample. The PL emission from the sample is collected though the same objective that focusses the beam onto the sample and an 808 nm long-pass filter cuts out the excitation beam. The condensate PL is imaged in real-space and Fourier-space, and is also spectrally resolved with an 1800 grooves/mm grating in a 750 mm spectrometer centred at 857 nm in order to image the condensate dispersion for Figure 7.8(b,d). The optical setup is unchanged from Figure 3.1.

7.8 Next Steps

This project is not fully complete and there are still areas to expand upon and explore. My next steps are to further explore the alignment between multiple excited state condensates, and through following similar logic, reason and algebra to other works that realise spin Hamiltonians using optical annealing platforms [44, 54, 146, 245, 246, 247], I will realise the higher-order spin Hamiltonian that is minimised by excited state condensate networks. This will then be tested using the 2DGPE and a discretised version of the GPE describing each oscillator by its clockwise and anticlockwise rotating components as single point complex numbers, such as in Equation 6.17. From this point, I will characterise the system's ability to calculate the Hamiltonian's ground state and test its performance in real-world applications.

7.9 Conclusions

Through analysing coupled excited states of polariton condensates, we realise a potential test-bed for a 4D polariton simulator by describing the x and y condensate components as p-orbitals. Building off the work of Cherotchenko et al. in [235], not only do we observe σ-bonding between a pair of condensates, but also when we expand the system to a continuous chain (or loop) of many first excited state condensates with both FM and AFM nearest neighbour couplings. For an odd number of condensates that are AFM coupled to their nearest neighbours (i.e. show a flipped alignment in the case of just $N = 2$ traps), we observe a polariton current running along the looped chain, leading to a phase winding about the full loop of condensates. We describe this polariton flow similarly to the work of Cookson et al. in [242], by using Bloch theory where the circulating polaritons have a quasimomentum related to the phase winding.

Interestingly, we also observe a polariton current and phase winding around a continuous chain of FM coupled excited state condensates. In the majority of realisations, the relative p_x and p_y orbital phases are zero, but a small fraction of cases exhibit this frustrated geometry. We liken this result to the "twisted state" observed in the Kuramoto model and realise many different phase winding numbers in FM Stuart-Landau networks coupled only to the first few nearest neighbours.

Finally, we go back to the pair of coupled condensates, but pin the alignment of the two dipoles through introducing ellipticity to the optical traps. As a result, we observe both in simulation and in experiment a splitting in spectral energy as one trap is rotated by 90° from the σ-bonding configuration, which we relate to the unbalanced flow of polaritons axially between the condensate centres.

All in all, the findings of this chapter map out a potential platform for investigating a 4D polariton simulator using coupled excited state polariton condensates, showing that the geometry of excited-state condensates plays a significant role in the system's energy. Additionally, the twisted states of condensates have a potential use in studying high-winding number vortex states.

Chapter 8

Conclusions and Final Remarks

8.1 Conclusions

Exciton-polaritons show to be an ideal platform for analogue computing, where going beyond the binary limitations of the Ising machine, the liquid light simulator possesses a continuous phase degree of freedom in two dimensions, where to relative phase between coupled condensates orientate to maximise the crossover of the condensate with the optical gain (i.e. maximising the particle number), in turn minimising the XY Hamiltonian. The work in this thesis explores networks of synchronised ground state polariton condensates as a platform for the 2D liquid light analogue simulator in numerical simulation of the 2DGPE and in experiment, but also through describing the system as dissipative coupled Stuart-Landau oscillators. It is clearly shown how the optical pump profile plays a vital role in the condensate alignment and spectral energy of the system, where going beyond the stationary trap, quantum vortices with deterministic angular momentum are shown to appear in specific regions of pump rotation.

In chapter 3, it is shown how optically trapping same-energy condensates with identical pump potentials allows the system to operate in a synchronised regime, irrespective of the relative coupling strength between neighbouring traps. Here, regions of purely dissipative coupling are mapped out as a function of separation distance between two optically trapped condensates, and through describing the system as a network of dissipative Stuart-Landau oscillators, the system proves to be a robust analogue simulator for the randomly-coupled all-to-all connected XY Hamiltonian [2]. In chapter 7, the optical pump is expanded to trap the first excited state polariton condensates, where networks of which again occupy a single energy state and condensates align with first nearest neighbours along a chain in a head-to-tail configurations. As ellipticity is applied to the traps however, the condensate alignment is artificially controlled and an energy splitting occurs in response to the unbalanced

flow of polaritons. The additional degrees of freedom of the excited state condensates compared to the ground state studied in chapter 3 map out a new potential analogue simulator characterised by a 4D spin parameter. In a continuous loop of these excited state condensates, nontrivial polariton currents are observed and characterised as quasimomentum following Bloch theory, and are investigated in terms of twisted-states using Stuart-Landau networks.

In chapter 4, the synchronised network of nonlinear oscillators (which includes polariton condensates) is used to solve the NP-hard max-3-cut mathematical graph problem both in the numerical simulation of hundreds of coupled Stuart-Landau oscillators and in experiment for the AFM house graph of polariton condensates, through using a technique from semi-definite programming with specific real-world examples of image segmentation and circuit design. This work further explores how the coupled dissipative oscillator system can also solve the max-2-cut problem, which has previously been tackled using Ising machines, as well as approximating higher order cuts such as the max-4-problem. Experimentally realising an all-to-all connected polariton graph is a near-impossible task beyond a handful of condensates, which exist in a 2D planar cavity. To overcome this hurdle, chapter 5 explores the minor embedding technique from quantum annealing to map any all-to-all connected undirected graph of dissipative coupled oscillators to a standardised low-connectivity "triad" graph. The successful implementation of this technique in theory opens up a potential physical test-bed for an arbitrary XY Hamiltonian solver using continuous phase oscillators, such as polariton condensates, photon condensates and coupled laser arrays. These findings offer up the triad graph structure for an on-chip hardware architecture for robust annealing offer the XY Hamiltonian across a range of optical oscillator platforms.

In investigating a non-stationary condensate trapping potential, chapter 6 shows the first observations of inducing quantised vortices into a polariton system through periodic optical stirring with an axially asymmetric pump profile. Both in simulation and experiment, regions of rotation frequency are mapped out where deterministic vortex winding is observed. Interestingly, the system exhibits an energy splitting directly proportional to the rotation frequency and is described using Floquet theory and corroborates the our understanding of why we observe vortices both co-rotating and counter-rotating with the trapping potential.

All-in-all, synchronised polariton condensate networks show to be a promising platform for minimising the XY Hamiltonian, where the dynamical transients of the coupled condensate system allows for ultrafast annealing of the encoded XY Hamiltonian, such that NP-hard graph problems can be solved on the picosecond timescale. The work in this thesis maps out how the polariton simulator can be realised experimentally with a potential on-chip architecture and explores real-world mathematical problems that it can solve.

8.2 Next Steps

I am very fortunate to have received 12 months funding from the EPRSC Doctoral Prize, with which, I aim to continue researching the polariton analogue simulator as a postdoctoral researcher. My next project aims to bring together my expertise in developing the 2D analogue simulator and knowledge of excited state condensates in order to develop the theory of a 4D liquid light analogue simulator, following the relative phase parameters mapped out in chapter 7. This will put polariton systems at the forefront of analogue simulations by presenting the first four-dimensional analogue simulator. This will have the ability to solve more complex graph problems than those studied in this thesis, such as the max-5-cut problem. Additionally, by creating a fully controllable 4D analogue simulator, this platform has the potential to be used in realising the Yang-Mills theory, which is currently an unsolved problem in mathematics and is listed as a millennium problem due to its huge impact in physics.

8.3 Final Remarks

Overall, I have enjoyed my time as a PhD student, particularly before the pandemic when our incredibly sociable research group thrived with constant fruitful discussions on polaritonics at our many lunchtime and evening socials. However, working from home during lockdown was not a favourable period of my candidature, although I am thankful that I was able to continue working with no practical disruption to my research. As we are adjusting to the new-normal, it is brilliant to meet again in person for group meetings, and group morale is definitely on the up as we are finally meeting up socially again. As parting words to any new PhD students reading this thesis, my advice would be to enjoy yourself! It is so important to have fun alongside (and during) the hard work of a PhD. Say “yes” to that coffee break with a colleague, or lunch at Label Food, or the pub trip at the end of the working day, or the QLM social that you’ve just received an email about. Also, as a Southampton student who has been a member of five societies over the last eight years, I highly recommend joining a university society to make like-minded friends who don’t only talk about physics - trust me, I’m (almost) a doctor! Also, try to avoid a crossover between your candidature and a global pandemic.

References

[1] Kavokin, A., Baumberg, J. J., Malpuech, G. & Laussy, F. P. *Microcavities* (Oxford University Press, 2017). Google-Books-ID: cUi1DgAAQBAJ.

[2] Harrison, S. L., Sigurdsson, H. & Lagoudakis, P. G. Synchronization in optically trapped polariton Stuart-Landau networks. *Phys. Rev. B* **101**, 155402 (2020). URL https://link.aps.org/doi/10.1103/PhysRevB.101.155402.

[3] Cilibrizzi, P. *et al.* Polariton condensation in a strain-compensated planar microcavity with InGaAs quantum wells. *Appl. Phys. Lett.* **105**, 191118 (2014). URL https://aip.scitation.org/doi/full/10.1063/1.4901814. Publisher: American Institute of Physics.

[4] Harrison, S., Sigurdsson, H., Alyatkin, S., Töpfer, J. & Lagoudakis, P. Solving the Max-3-Cut Problem with Coherent Networks. *Phys. Rev. Applied* **17**, 024063 (2022). URL https://link.aps.org/doi/10.1103/PhysRevApplied.17.024063. Publisher: American Physical Society.

[5] Zory. *Quantum Well Lasers*, vol. Chapter 1 (Academic Press, 1993). ISBN: 978-0-12-781890-0.

[6] Dingle, R. & Henry, C. H. Quantum effects in heterostructure lasers (1976). URL https://patents.google.com/patent/US3982207A/en.

[7] Kroemer, H. A proposed class of hetero-junction injection lasers. *Proceedings of the IEEE* **51**, 1782–1783 (1963). Conference Name: Proceedings of the IEEE.

[8] Alferov, Z. I. & Kazarinov, R. F. Semiconductor laser with electric pumping. *Author's Certificate: N181737* **Application: N950840** (1963).

[9] The Nobel Prize in Physics 2000. URL https://www.nobelprize.org/prizes/physics/2000/ceremony-speech/.

[10] Alferov, Z. I. Nobel Lecture: The double heterostructure concept and its applications in physics, electronics, and technology. *Rev. Mod. Phys.* **73**, 767–782 (2001). URL https://link.aps.org/doi/10.1103/RevModPhys.73.767. Publisher: American Physical Society.

[11] Byrnes, T., Kim, N. Y. & Yamamoto, Y. Excitonpolariton condensates. *Nature Phys* **10**, 803–813 (2014). URL http://www.nature.com/articles/nphys3143.

[12] Gaponenko, S. V. *Optical Properties of Semiconductor Nanocrystals* (Cambridge University Press, 1998), 1 edn. URL https://www.cambridge.org/core/product/identifier/9780511524141/type/book.

[13] Born, M. & Oppenheimer, R. Zur Quantentheorie der Molekeln. *Annalen der Physik* **389**, 457–484 (1927). URL https://onlinelibrary.wiley.com/doi/abs/10.1002/andp.19273892002. _eprint: https://onlinelibrary.wiley.com/doi/pdf/10.1002/andp.19273892002.

[14] Hartree, D. R. The Wave Mechanics of an Atom with a Non-Coulomb Central Field. Part I. Theory and Methods. *Mathematical Proceedings of the Cambridge Philosophical Society* **24**, 89–110 (1928). URL https://www.cambridge.org/core/journals/mathematical-proceedings-of-the-cambridge-philosophical-society/article/wave-mechanics-of-an-atom-with-a-noncoulomb-central-field-part-i-theory-and-methods/C9417AC1CEC84B934C1EA4C4B8401FEF. Publisher: Cambridge University Press.

[15] Fock, V. Näherungsmethode zur Lösung des quantenmechanischen Mehrkörperproblems. *Z. Physik* **61**, 126–148 (1930). URL https://doi.org/10.1007/BF01340294.

[16] Ashcroft, N. W., W, A., Ashcroft, i. W. & Mermin, N. D. *Solid State Physics* (Holt, Rinehart and Winston, 1976). Google-Books-ID: 1C9HAQAAIAAJ.

[17] Myers, H. P. *Introductory Solid State Physics* (CRC Press, 1997). Google-Books-ID: bWC1DwAAQBAJ.

[18] Frenkel, J. On the Transformation of light into Heat in Solids. I. *Phys. Rev.* **37**, 17–44 (1931). URL https://link.aps.org/doi/10.1103/PhysRev.37.17. Publisher: American Physical Society.

[19] Wannier, G. H. The Structure of Electronic Excitation Levels in Insulating Crystals. *Phys. Rev.* **52**, 191–197 (1937). URL https://link.aps.org/doi/10.1103/PhysRev.52.191. Publisher: American Physical Society.

[20] Mott, N. F. On the absorption of light by crystals. *Proceedings of the Royal Society of London. Series A. Mathematical and Physical Sciences* **167**, 384–391 (1938). URL https://royalsocietypublishing.org/doi/10.1098/rspa.1938.0137. Publisher: Royal Society.

[21] David, A. & Miller, B. Optical physics of quantum wells. In Oppo, G.-L., Barnett, S. M., Riis, E. & Wilkinson, M. (eds.) *Quantum Dynamics of Simple Systems*, 239–266 (CRC Press, 2020), 1 edn. URL https://www.taylorfrancis.com/books/9781000111439/chapters/10.1201/9781003072973-9.

[22] Bastard, G., Mendez, E. E., Chang, L. L. & Esaki, L. Exciton binding energy in quantum wells. *Phys. Rev. B* **26**, 1974–1979 (1982). URL https://link.aps.org/doi/10.1103/PhysRevB.26.1974. Publisher: American Physical Society.

[23] Kapuscinski, P. *et al.* Rydberg series of dark excitons and the conduction band spin-orbit splitting in monolayer WSe2. *Commun Phys* **4**, 1–6 (2021). URL https://www.nature.com/articles/s42005-021-00692-3.

[24] Loh, K. P. Brightening the dark excitons. *Nature Nanotech* **12**, 837–838 (2017). URL https://www.nature.com/articles/nnano.2017.130.

[25] Winkler, R. Electron and Hole States in Quasi-Two-Dimensional Systems. In Winkler, R. (ed.) *SpinOrbit Coupling Effects in Two-Dimensional Electron and Hole Systems*, Springer Tracts in Modern Physics, 35–60 (Springer, Berlin, Heidelberg, 2003). URL https://doi.org/10.1007/978-3-540-36616-4_4.

[26] Gmitra, M. & Fabian, J. First-principles studies of orbital and spin-orbit properties of GaAs, GaSb, InAs, and InSb zinc-blende and wurtzite semiconductors. *Phys. Rev. B* **94**, 165202 (2016). URL https://link.aps.org/doi/10.1103/PhysRevB.94.165202. Publisher: American Physical Society.

[27] Hamilton, A. R. *et al.* The 0.7 anomaly in one-dimensional hole quantum wires. *J. Phys.: Condens. Matter* **20**, 164205 (2008). URL https://doi.org/10.1088/0953-8984/20/16/164205. Publisher: IOP Publishing.

[28] Li, X. F. & Yu, S. F. Modeling of Rabi splitting in quantum well microcavities using time-dependent transfer matrix method. *Opt. Express* **16**, 19285 (2008). URL https://www.osapublishing.org/oe/abstract.cfm?uri=oe-16-23-19285.

[29] Balili, R. B. Transfer matrix method in nanophotonics. *Int. J. Mod. Phys. Conf. Ser.* **17**, 159–168 (2012). URL https://www.worldscientific.com/doi/abs/10.1142/S2010194512008057.

[30] Savona, V., Andreani, L. C., Schwendimann, P. & Quattropani, A. Quantum well excitons in semiconductor microcavities: Unified treatment of weak and

strong coupling regimes. *Solid State Communications* **93**, 733–739 (1995). URL https://www.sciencedirect.com/science/article/pii/0038109894008655.

[31] Schneider, C. *et al.* Exciton-polariton trapping and potential landscape engineering. *Rep. Prog. Phys.* **80**, 016503 (2016). URL https://doi.org/10.1088/0034-4885/80/1/016503. Publisher: IOP Publishing.

[32] Bose. Plancks Gesetz und Lichtquantenhypothese. *Z. Physik* **26**, 178–181 (1924). URL https://doi.org/10.1007/BF01327326.

[33] Einstein, A. Quantentheorie des einatomigen idealen Gases. In *Sitzungsberichte der Preussischen Akademie der Wissenschaften*, vol. 1 (John Wiley & Sons, Ltd, 1925), 3 edn. URL https://onlinelibrary.wiley.com/doi/abs/10.1002/3527608958.ch27.

[34] Anderson, M. H., Ensher, J. R., Matthews, M. R., Wieman, C. E. & Cornell, E. A. Observation of Bose-Einstein Condensation in a Dilute Atomic Vapor. *Science* **269**, 198–201 (1995). URL https://www.science.org/doi/10.1126/science.269.5221.198. Publisher: American Association for the Advancement of Science.

[35] Davis, K. B. *et al.* Bose-Einstein Condensation in a Gas of Sodium Atoms. *Phys. Rev. Lett.* **75**, 3969–3973 (1995). URL https://link.aps.org/doi/10.1103/PhysRevLett.75.3969. Publisher: American Physical Society.

[36] Bradley, C. C., Sackett, C. A., Tollett, J. J. & Hulet, R. G. Evidence of Bose-Einstein Condensation in an Atomic Gas with Attractive Interactions. *Phys. Rev. Lett.* **75**, 1687–1690 (1995). URL https://link.aps.org/doi/10.1103/PhysRevLett.75.1687. Publisher: American Physical Society.

[37] Di Bari, P., Zwicky, R. & Akeroyd, A. Quantum Physics of Matter (PHYS2024) (2016). University of Southampton undergraduate course notes.

[38] Yamamoto, Y. QIS385 Bose-Einstein Condensation and Matter-Wave Lasers. URL https://www.nii.ac.jp/qis/first-quantum/e/forStudents/lecture/.

[39] Schroeder, D. V. *An introduction to thermal physics* (San Francisco, CA : Addison Wesley, 1999). URL http://archive.org/details/introductiontoth00schr_817.

[40] Petrov, D., Gangardt, D. M. & Shlyapnikov, G. V. Low-dimensional trapped gases. *Journal de Physique IV Proceedings* **116**, 5–44 (2004). URL https://hal.archives-ouvertes.fr/hal-00003349. Publisher: EDP Sciences.

[41] Kasprzak, J. *et al.* BoseEinstein condensation of exciton polaritons. *Nature* **443**, 409–414 (2006). URL https://www.nature.com/articles/nature05131. Bandiera_abtest: a Cg_type: Nature Research Journals Number: 7110 Primary_atype: Research Publisher: Nature Publishing Group.

[42] Penrose, O. & Onsager, L. Bose-Einstein Condensation and Liquid Helium. *Phys. Rev.* **104**, 576–584 (1956). URL https://link.aps.org/doi/10.1103/PhysRev.104.576. Publisher: American Physical Society.

[43] Tartakovskii, A. I. *et al.* Stimulated Polariton Scattering in Semiconductor Microcavities: New Physics and Potential Applications. *Advanced Materials* **13**, 1725–1730 (2001). URL https://onlinelibrary.wiley.com/doi/abs/10.1002/1521-4095%28200111%2913%3A22%3C1725%3A%3AAID-ADMA1725%3E3.0.CO%3B2-Z.

[44] Ohadi, H. *et al.* Nontrivial Phase Coupling in Polariton Multiplets. *Phys. Rev. X* **6**, 031032 (2016). URL https://link.aps.org/doi/10.1103/PhysRevX.6.031032. Publisher: American Physical Society.

[45] Töpfer, J. D., Sigurdsson, H., Pickup, L. & Lagoudakis, P. G. Time-delay polaritonics. *Communications Physics* **3**, 2 (2020). URL https://doi.org/10.1038/s42005-019-0271-0.

[46] Askitopoulos, A. *et al.* Polariton condensation in an optically induced two-dimensional potential. *Phys. Rev. B* **88**, 041308 (2013). URL https://link.aps.org/doi/10.1103/PhysRevB.88.041308. Publisher: American Physical Society.

[47] Askitopoulos, A. *et al.* Robust platform for engineering pure-quantum-state transitions in polariton condensates. *Phys. Rev. B* **92**, 035305 (2015). URL https://link.aps.org/doi/10.1103/PhysRevB.92.035305. Publisher: American Physical Society.

[48] Ohadi, H. *et al.* Spin Order and Phase Transitions in Chains of Polariton Condensates. *Phys. Rev. Lett.* **119**, 067401 (2017). URL https://link.aps.org/doi/10.1103/PhysRevLett.119.067401. Publisher: American Physical Society.

[49] Pickup, L. *et al.* Optical Bistability under Nonresonant Excitation in Spinor Polariton Condensates. *Phys. Rev. Lett.* **120**, 225301 (2018). URL https://link.aps.org/doi/10.1103/PhysRevLett.120.225301. Publisher: American Physical Society.

[50] Askitopoulos, A. *et al.* All-optical quantum fluid spin beam splitter. *Phys. Rev. B* **97**, 235303 (2018). URL https://link.aps.org/doi/10.1103/PhysRevB.97.235303. Publisher: American Physical Society.

[51] Ohadi, H. *et al.* Synchronization crossover of polariton condensates in weakly disordered lattices. *Phys. Rev. B* **97**, 195109 (2018). URL https://link.aps.org/doi/10.1103/PhysRevB.97.195109.

[52] Askitopoulos, A. *et al.* Giant increase of temporal coherence in optically trapped polariton condensate. *arXiv:1911.08981 [cond-mat, physics:physics]* (2019). URL http://arxiv.org/abs/1911.08981. ArXiv: 1911.08981.

[53] Wouters, M., Carusotto, I. & Ciuti, C. Spatial and spectral shape of inhomogeneous nonequilibrium exciton-polariton condensates. *Phys. Rev. B* **77**, 115340 (2008). URL https://link.aps.org/doi/10.1103/PhysRevB.77.115340.

[54] Berloff, N. G. *et al.* Realizing the classical XY Hamiltonian in polariton simulators. *Nature Mater* **16**, 1120–1126 (2017). URL https://www.nature.com/articles/nmat4971. Number: 11 Publisher: Nature Publishing Group.

[55] Lagoudakis, P. G. & Berloff, N. G. A polariton graph simulator. *New J. Phys.* **19**, 125008 (2017). URL https://doi.org/10.1088/1367-2630/aa924b. Publisher: IOP Publishing.

[56] Kalinin, K. P. & Berloff, N. G. Simulating Ising and n-State Planar Potts Models and External Fields with Nonequilibrium Condensates. *Phys. Rev. Lett.* **121**, 235302 (2018). URL https://link.aps.org/doi/10.1103/PhysRevLett.121.235302. Publisher: American Physical Society.

[57] Kalinin, K. P. & Berloff, N. G. Global optimization of spin Hamiltonians with gain-dissipative systems. *Sci Rep* **8**, 17791 (2018). URL https://www.nature.com/articles/s41598-018-35416-1.

[58] Landau, L. D. & Ginzburg, V. L. On the theory of superconductivity. *Zh. Eksp. Teor. Fiz.* **20**, 1064 (1950). URL https://cds.cern.ch/record/486430.

[59] Gross, E. P. Structure of a quantized vortex in boson systems. *Nuovo Cim* **20**, 454–477 (1961). URL https://doi.org/10.1007/BF02731494.

[60] Pitaevskii, L. P. Vortex Lines in an Imperfect Bose Gas. *Sov. Phys. JETP* **13**, 646 (1961). URL http://jetp.ras.ru/cgi-bin/dn/e_013_02_0451.pdf.

[61] Aranson, I. S. & Kramer, L. The world of the complex Ginzburg-Landau equation. *Rev. Mod. Phys.* **74**, 99–143 (2002). URL https://link.aps.org/doi/10.1103/RevModPhys.74.99. Publisher: American Physical Society.

[62] Fetter, A. L. Nonuniform states of an imperfect bose gas. *Annals of Physics* **70**, 67–101 (1972). URL https://www.sciencedirect.com/science/article/pii/0003491672903302.

[63] Proukakis, N. P. & Burnett, K. Generalized Mean Fields for Trapped Atomic Bose-Einstein Condensates. *J Res Natl Inst Stand Technol* **101**, 457–469 (1996).

[64] Proukakis, N. P. Beyond Gross-Pitaevskii Mean Field Theory. *arXiv:0706.3541 [cond-mat]* (2007). URL http://arxiv.org/abs/0706.3541. ArXiv: 0706.3541.

[65] Proukakis, N. P. & Jackson, B. Finite-temperature models of BoseEinstein condensation. *J. Phys. B: At. Mol. Opt. Phys.* **41**, 203002 (2008). URL https://doi.org/10.1088/0953-4075/41/20/203002. Publisher: IOP Publishing.

[66] Bogolyubov, N. N. On the theory of superfluidity. *J. Phys. (USSR)* **11**, 23–32 (1947). URL https://www.ufn.ru/dates/pdf/j_phys_ussr/j_phys_ussr_1947_11_1/3_bogolubov_j_phys_ussr_1947_11_1_23.pdf.

[67] Wouters, M. & Carusotto, I. Excitations in a Nonequilibrium Bose-Einstein Condensate of Exciton Polaritons. *Phys. Rev. Lett.* **99**, 140402 (2007). URL https://link.aps.org/doi/10.1103/PhysRevLett.99.140402. Publisher: American Physical Society.

[68] Amo, A. *et al.* Excitonpolariton spin switches. *Nature Photon* **4**, 361–366 (2010). URL https://www.nature.com/articles/nphoton.2010.79. Number: 6 Publisher: Nature Publishing Group.

[69] Bobrovska, N. & Matuszewski, M. Adiabatic approximation and fluctuations in exciton-polariton condensates. *Phys. Rev. B* **92**, 035311 (2015). URL https://link.aps.org/doi/10.1103/PhysRevB.92.035311. Publisher: American Physical Society.

[70] Landau, Lev D. On the Problem of Turbulence **44**, 339–349 (1944).

[71] Stuart, J. T. On the non-linear mechanics of hydrodynamic stability. *Journal of Fluid Mechanics* **4**, 1–21 (1958). URL https://www.cambridge.org/core/journals/journal-of-fluid-mechanics/article/on-the-nonlinear-mechanics-of-hydrodynamic-stability/4BF3BF108B737DFADA39853623313723. Publisher: Cambridge University Press.

[72] Stuart, J. T. On the non-linear mechanics of wave disturbances in stable and unstable parallel flows Part 1. The basic behaviour in plane Poiseuille flow. *Journal of Fluid Mechanics* **9**, 353–370 (1960). URL https://www.cambridge.org/core/journals/journal-of-fluid-mechanics/article/on-the-nonlinear-mechanics-of-wave-disturbances-in-stable-and-unstable-parallel-flows-B5A91F2ABD8B114DD10C94A9A8138CCC. Publisher: Cambridge University Press.

[73] Kuznetsov, Y. A. One-Parameter Bifurcations of Equilibria in Continuous-Time Dynamical Systems. In Kuznetsov, Y. A. (ed.) *Elements of Applied Bifurcation Theory*, Applied Mathematical Sciences, 77–115 (Springer, New York, NY, 2004). URL https://doi.org/10.1007/978-1-4757-3978-7_3.

[74] Röhm, A., Lüdge, K. & Schneider, I. Bistability in Two Simple Symmetrically Coupled Oscillators with Symmetry-broken Amplitude- and Phase-Locking. *Chaos* **28**, 063114 (2018). URL http://arxiv.org/abs/1712.01610. ArXiv: 1712.01610.

[75] Kuznetsov, Y. A. Andronov-Hopf bifurcation. *Scholarpedia* **1**, 1858 (2006). URL http://www.scholarpedia.org/article/Andronov-Hopf_bifurcation.

[76] Sheng Chen, G. & Liu, X. Chapter 6 - Friction Dynamics and Diagnosis of Rotor Systems. In Sheng Chen, G. & Liu, X. (eds.) *Friction Dynamics*, 247–298 (Woodhead Publishing, 2016). URL https://www.sciencedirect.com/science/article/pii/B9780081002858000067.

[77] Moon, J.-Y., Lee, U., Blain-Moraes, S. & Mashour, G. A. General Relationship of Global Topology, Local Dynamics, and Directionality in Large-Scale Brain Networks. *PLOS Computational Biology* **11**, e1004225 (2015). URL https://journals.plos.org/ploscompbiol/article?id=10.1371/journal.pcbi.1004225. Publisher: Public Library of Science.

[78] Töpfer, J. D. *et al.* Engineering spatial coherence in lattices of polariton condensates. *Optica, OPTICA* **8**, 106–113 (2021). URL https://www.osapublishing.org/optica/abstract.cfm?uri=optica-8-1-106. Publisher: Optical Society of America.

[79] Wertz, E. *et al.* Spontaneous formation and optical manipulation of extended polariton condensates. *Nature Phys* **6**, 860–864 (2010). URL https://www.nature.com/articles/nphys1750. Bandiera_abtest: a Cg_type: Nature Research Journals Number: 11 Primary_atype: Research Publisher: Nature Publishing Group.

[80] Galbiati, M. *et al.* Polariton Condensation in Photonic Molecules. *Phys. Rev. Lett.* **108**, 126403 (2012). URL https://link.aps.org/doi/10.1103/PhysRevLett.108.126403. Publisher: American Physical Society.

[81] Tanese, D. *et al.* Polariton condensation in solitonic gap states in a one-dimensional periodic potential. *Nat Commun* **4**, 1749 (2013). URL https://www.nature.com/articles/ncomms2760.

[82] Jacqmin, T. *et al.* Direct Observation of Dirac Cones and a Flatband in a Honeycomb Lattice for Polaritons. *Phys. Rev. Lett.* **112**, 116402 (2014). URL https://link.aps.org/doi/10.1103/PhysRevLett.112.116402.

[83] St-Jean, P. *et al.* Lasing in topological edge states of a one-dimensional lattice. *Nature Photon* **11**, 651–656 (2017). URL https://www.nature.com/articles/s41566-017-0006-2.

[84] Klembt, S. *et al.* Exciton-polariton topological insulator. *Nature* **562**, 552–556 (2018). URL https://www.nature.com/articles/s41586-018-0601-5.

[85] Cerda-Méndez, E. A. *et al.* Polariton Condensation in Dynamic Acoustic Lattices. *Phys. Rev. Lett.* **105**, 116402 (2010). URL https://link.aps.org/doi/10.1103/PhysRevLett.105.116402. Publisher: American Physical Society.

[86] Lai, C. W. *et al.* Coherent zero-state and pi-state in an excitonpolariton condensate array. *Nature* **450**, 529–532 (2007). URL https://www.nature.com/articles/nature06334. Bandiera_abtest: a Cg_type: Nature Research Journals Number: 7169 Primary_atype: Research Publisher: Nature Publishing Group.

[87] Kim, N. Y. *et al.* Dynamical d-wave condensation of excitonpolaritons in a two-dimensional square-lattice potential. *Nature Phys* **7**, 681–686 (2011). URL https://www.nature.com/articles/nphys2012.

[88] Isomae, Y., Sugawara, N., Iwasaki, N., Honda, T. & Amari, K. Phase-only spatial light modulator having high reflectance, high-definition pixels and high photo-durability. In *Digital Optical Technologies 2021*, vol. 11788, 191–196 (SPIE, 2021). URL https://www.spiedigitallibrary.org/conference-proceedings-of-spie/11788/117880T/Phase-only-spatial-light-modulator-having-high-reflectance-high-definition/10.1117/12.2595136.full.

[89] Sánchez-López, M. M. *et al.* Double-ring interference of binary diffractive axicons. *OSA Continuum, OSAC* **3**, 1679–1690 (2020). URL https://www.osapublishing.org/osac/abstract.cfm?uri=osac-3-6-1679. Publisher: Optical Society of America.

[90] Gerchberg, R. W. & Saxton, W. O. A practical algorithm for the determination of phase from image and diffraction plane pictures **35**, 275–284 (1971). URL https://asset-pdf.scinapse.io/prod/1484412996/1484412996.pdf.

[91] Pasienski, M. & DeMarco, B. A high-accuracy algorithm for designing arbitrary holographic atom traps. *Opt. Express, OE* **16**, 2176–2190 (2008). URL https://www.osapublishing.org/oe/abstract.cfm?uri=oe-16-3-2176. Publisher: Optical Society of America.

[92] Kreis, T. Digital holographic interference-phase measurement using the Fourier-transform method. *J. Opt. Soc. Am. A, JOSAA* **3**, 847–855 (1986). URL https://www.osapublishing.org/josaa/abstract.cfm?uri=josaa-3-6-847. Publisher: Optical Society of America.

[93] Liebling, M., Blu, T. & Unser, M. Complex-wave retrieval from a single off-axis hologram. *J. Opt. Soc. Am. A, JOSAA* **21**, 367–377 (2004). URL https://www.osapublishing.org/josaa/abstract.cfm?uri=josaa-21-3-367. Publisher: Optical Society of America.

[94] Alyatkin, S., Töpfer, J., Askitopoulos, A., Sigurdsson, H. & Lagoudakis, P. Optical Control of Couplings in Polariton Condensate Lattices. *Phys. Rev. Lett.* **124**, 207402 (2020). URL https://link.aps.org/doi/10.1103/PhysRevLett.124.207402.

[95] Espinosa-Paredes, G. Chapter 7 - Nonlinear BWR dynamics with a fractional reduced order model. In Espinosa-Paredes, G. (ed.) *Fractional-Order Models for Nuclear Reactor Analysis*, Woodhead Publishing Series in Energy, 247–295 (Woodhead Publishing, 2021). URL https://www.sciencedirect.com/science/article/pii/B9780128236659000079.

[96] Milnor, J. Attractor. *Scholarpedia* **1**, 1815 (2006). URL http://www.scholarpedia.org/article/Attractor.

[97] Robinett, R. D., III & Wilson, D. G. What is a limit cycle? *International Journal of Control* **81**, 1886–1900 (2008). URL http://www.tandfonline.com/doi/abs/10.1080/00207170801927163.

[98] Strogatz, S. *Nonlinear Dynamics and Chaos: With Applications to Physics, Biology, Chemistry, and Engineering*. Studies in Nonlinearity (Avalon Publishing, 2014). URL https://books.google.co.uk/books?id=JDQGAwAAQBAJ.

[99] Cross, M. C. & Hohenberg, P. C. Pattern formation outside of equilibrium. *Rev. Mod. Phys.* **65**, 851–1112 (1993). URL https://link.aps.org/doi/10.1103/RevModPhys.65.851. Publisher: American Physical Society.

[100] Acebrón, J. A., Bonilla, L. L., Pérez Vicente, C. J., Ritort, F. & Spigler, R. The Kuramoto model: A simple paradigm for synchronization phenomena. *Rev. Mod. Phys.* **77**, 137–185 (2005). URL

https://link.aps.org/doi/10.1103/RevModPhys.77.137. Publisher: American Physical Society.

[101] Matheny, M. H. *et al.* Exotic states in a simple network of nanoelectromechanical oscillators. *Science* **363** (2019). URL https://science.sciencemag.org/content/363/6431/eaav7932. Publisher: American Association for the Advancement of Science.

[102] Deng, H., Haug, H. & Yamamoto, Y. Exciton-polariton Bose-Einstein condensation. *Rev. Mod. Phys.* **82**, 1489–1537 (2010). URL https://link.aps.org/doi/10.1103/RevModPhys.82.1489.

[103] Plumhof, J. D., Stöferle, T., Mai, L., Scherf, U. & Mahrt, R. F. Room-temperature BoseEinstein condensation of cavity excitonpolaritons in a polymer. *Nature Materials* **13**, 247–252 (2014). URL https://www.nature.com/articles/nmat3825.

[104] Lagoudakis, K. G., Pietka, B., Wouters, M., André, R. & Deveaud-Plédran, B. Coherent Oscillations in an Exciton-Polariton Josephson Junction. *Phys. Rev. Lett.* **105**, 120403 (2010). URL https://link.aps.org/doi/10.1103/PhysRevLett.105.120403. Publisher: American Physical Society.

[105] Rayanov, K., Altshuler, B. L., Rubo, Y. G. & Flach, S. Frequency Combs with Weakly Lasing Exciton-Polariton Condensates. *Phys. Rev. Lett.* **114**, 193901 (2015). URL https://link.aps.org/doi/10.1103/PhysRevLett.114.193901. Publisher: American Physical Society.

[106] Kalinin, K. P. & Berloff, N. G. Polaritonic network as a paradigm for dynamics of coupled oscillators. *Phys. Rev. B* **100**, 245306 (2019). URL https://link.aps.org/doi/10.1103/PhysRevB.100.245306. Publisher: American Physical Society.

[107] Landau, L. D. (ed.) *On the problem of turbulence* (Gordon and Breach, New York, 1965). Publication Title: Collected Papers of L. D. Landau.

[108] Hakim, V. & Rappel, W.-J. Dynamics of the globally coupled complex Ginzburg-Landau equation. *Phys. Rev. A* **46**, R7347–R7350 (1992). URL https://link.aps.org/doi/10.1103/PhysRevA.46.R7347. Publisher: American Physical Society.

[109] Inagaki, T. *et al.* A coherent Ising machine for 2000-node optimization problems. *Science* **354**, 603–606 (2016). URL https://science.sciencemag.org/content/354/6312/603. Publisher: American Association for the Advancement of Science.

[110] Inagaki, T. *et al.* Large-scale Ising spin network based on degenerate optical parametric oscillators. *Nature Photonics* **10**, 415–419 (2016). URL https://doi.org/10.1038/nphoton.2016.68. Publisher: Nature Publishing Group.

[111] Reifenstein, S., Kako, S., Khoyratee, F., Leleu, T. & Yamamoto, Y. Coherent Ising Machines with Optical Error Correction Circuits. *Advanced Quantum Technologies* **4**, 2100077 (2021). URL https://onlinelibrary.wiley.com/doi/abs/10.1002/qute.202100077.

[112] Schmutzler, J. *et al.* All-optical flow control of a polariton condensate using nonresonant excitation. *Phys. Rev. B* **91**, 195308 (2015). URL https://link.aps.org/doi/10.1103/PhysRevB.91.195308. Publisher: American Physical Society.

[113] Su, R. *et al.* Room temperature long-range coherent exciton polariton condensate flow in lead halide perovskites. *Science Advances* **4** (2018). URL advances.sciencemag.org/content/4/10/eaau0244. Publisher: American Association for the Advancement of Science.

[114] Baas, A. *et al.* Synchronized and Desynchronized Phases of Exciton-Polariton Condensates in the Presence of Disorder. *Phys. Rev. Lett.* **100**, 170401 (2008). URL https://link.aps.org/doi/10.1103/PhysRevLett.100.170401. Publisher: American Physical Society.

[115] Eastham, P. R. Mode locking and mode competition in a nonequilibrium solid-state condensate. *Phys. Rev. B* **78**, 035319 (2008). URL https://link.aps.org/doi/10.1103/PhysRevB.78.035319. Publisher: American Physical Society.

[116] Christmann, G. *et al.* Oscillatory solitons and time-resolved phase locking of two polariton condensates. *New Journal of Physics* **16**, 103039 (2014). URL https://doi.org/10.1088%2F1367-2630%2F16%2F10%2F103039. Publisher: IOP Publishing.

[117] Ballarini, D. *et al.* Macroscopic Two-Dimensional Polariton Condensates. *Phys. Rev. Lett.* **118**, 215301 (2017). URL https://link.aps.org/doi/10.1103/PhysRevLett.118.215301. Publisher: American Physical Society.

[118] Kasprzak, J. *et al.* Second-Order Time Correlations within a Polariton Bose-Einstein Condensate in a CdTe Microcavity. *Phys. Rev. Lett.* **100**, 067402 (2008). URL https://link.aps.org/doi/10.1103/PhysRevLett.100.067402. Publisher: American Physical Society.

[119] Kim, S. *et al.* Coherent Polariton Laser. *Phys. Rev. X* **6**, 011026 (2016). URL https://link.aps.org/doi/10.1103/PhysRevX.6.011026. Publisher: American Physical Society.

[120] Nogrette, F. *et al.* Single-Atom Trapping in Holographic 2D Arrays of Microtraps with Arbitrary Geometries. *Phys. Rev. X* **4**, 021034 (2014). URL https://link.aps.org/doi/10.1103/PhysRevX.4.021034. Publisher: American Physical Society.

[121] Lagoudakis, K. G. *et al.* Probing the Dynamics of Spontaneous Quantum Vortices in Polariton Superfluids. *Phys. Rev. Lett.* **106**, 115301 (2011). URL https://link.aps.org/doi/10.1103/PhysRevLett.106.115301. Publisher: American Physical Society.

[122] Keeling, J. & Berloff, N. G. Spontaneous Rotating Vortex Lattices in a Pumped Decaying Condensate. *Phys. Rev. Lett.* **100**, 250401 (2008). URL https://link.aps.org/doi/10.1103/PhysRevLett.100.250401. Publisher: American Physical Society.

[123] Stepnicki, P. & Matuszewski, M. Tight-binding model for exciton-polariton condensates in external potentials. *Phys. Rev. A* **88**, 033626 (2013). URL https://link.aps.org/doi/10.1103/PhysRevA.88.033626. Publisher: American Physical Society.

[124] Kalinin, K. P. & Berloff, N. G. Networks of non-equilibrium condensates for global optimization. *New Journal of Physics* **20**, 113023 (2018). URL https://doi.org/10.1088%2F1367-2630%2Faae8ae. Publisher: IOP Publishing.

[125] Wales, D. J. & Doye, J. P. K. Global Optimization by Basin-Hopping and the Lowest Energy Structures of Lennard-Jones Clusters Containing up to 110 Atoms. *The Journal of Physical Chemistry A* **101**, 5111–5116 (1997). URL https://doi.org/10.1021/jp970984n.

[126] Backus, J. Can programming be liberated from the von Neumann style? a functional style and its algebra of programs. *Commun. ACM* **21**, 613–641 (1978). URL https://doi.org/10.1145/359576.359579.

[127] Edwards, J. & O'Keefe, S. Eager recirculating memory to alleviate the von Neumann Bottleneck. In *2016 IEEE Symposium Series on Computational Intelligence (SSCI)*, 1–5 (2016).

[128] Ibsen-Jensen, R., Chatterjee, K. & Nowak, M. A. Computational complexity of ecological and evolutionary spatial dynamics. *Proceedings of the National Academy of Sciences* **112**, 15636–15641 (2015). URL

https://www.pnas.org/content/112/51/15636. Publisher: National Academy of Sciences.

[129] Zhang, X. & Dincer, I. *Energy Solutions to Combat Global Warming* (Springer, 2016).

[130] Jayaraj, P. B., Rahamathulla, K. & Gopakumar, G. A GPU Based Maximum Common Subgraph Algorithm for Drug Discovery Applications. In *2016 IEEE International Parallel and Distributed Processing Symposium Workshops (IPDPSW)*, 580–588 (2016).

[131] Pierce, N. A. & Winfree, E. Protein Design is NP-hard. *Protein Engineering, Design and Selection* **15**, 779–782 (2002). URL https://doi.org/10.1093/protein/15.10.779.

[132] Goemans, M. X. & Williamson, D. P. Improved Approximation Algorithms for Maximum Cut and Satisfiability Problems Using Semidefinite Programming. *J. ACM* **42**, 1115–1145 (1995). URL https://doi.org/10.1145/227683.227684. Place: New York, NY, USA Publisher: Association for Computing Machinery.

[133] Zhang, S. & Huang, Y. Complex Quadratic Optimization and Semidefinite Programming. *SIAM Journal on Optimization* **16**, 871–890 (2006). URL https://doi.org/10.1137/04061341X.

[134] Such, F. P. *et al.* Deep Neuroevolution: Genetic Algorithms Are a Competitive Alternative for Training Deep Neural Networks for Reinforcement Learning. *CoRR* **abs/1712.06567** (2017). URL http://arxiv.org/abs/1712.06567.

[135] Yang, X.-S. *Nature-Inspired Optimization Algorithms* (Elsevier, Amsterdam, Netherlands, 2014).

[136] Tovey, C. A. Nature-Inspired Heuristics: Overview and Critique. In *Recent Advances in Optimization and Modeling of Contemporary Problems*, INFORMS TutORials in Operations Research, 158–192 (INFORMS, 2018). URL https://pubsonline.informs.org/doi/10.1287/educ.2018.0187.

[137] Aspuru-Guzik, A. & Walther, P. Photonic quantum simulators. *Nature Physics* **8**, 285–291 (2012). URL https://doi.org/10.1038/nphys2253.

[138] Sun, C. *et al.* Single-chip microprocessor that communicates directly using light. *Nature* **528**, 534–538 (2015). URL https://doi.org/10.1038/nature16454.

[139] Marandi, A., Wang, Z., Takata, K., Byer, R. L. & Yamamoto, Y. Network of time-multiplexed optical parametric oscillators as a coherent Ising machine. *Nature Photonics* **8**, 937–942 (2014). URL https://doi.org/10.1038/nphoton.2014.249.

[140] McMahon, P. L. *et al.* A fully programmable 100-spin coherent Ising machine with all-to-all connections. *Science* **354**, 614–617 (2016). URL https://science.sciencemag.org/content/354/6312/614.

[141] Kyriienko, O., Sigurdsson, H. & Liew, T. C. H. Probabilistic solving of NP-hard problems with bistable nonlinear optical networks. *Phys. Rev. B* **99**, 195301 (2019). URL https://link.aps.org/doi/10.1103/PhysRevB.99.195301. Publisher: American Physical Society.

[142] Pierangeli, D., Marcucci, G. & Conti, C. Large-Scale Photonic Ising Machine by Spatial Light Modulation. *Phys. Rev. Lett.* **122**, 213902 (2019). URL https://link.aps.org/doi/10.1103/PhysRevLett.122.213902. Publisher: American Physical Society.

[143] Böhm, F., Verschaffelt, G. & Van der Sande, G. A poor man's coherent Ising machine based on opto-electronic feedback systems for solving optimization problems. *Nature Communications* **10**, 3538 (2019). URL https://doi.org/10.1038/s41467-019-11484-3.

[144] Luo, S. *et al.* Classical Spin Chains Mimicked by Room-Temperature Polariton Condensates. *Phys. Rev. Applied* **13**, 044052 (2020). URL https://link.aps.org/doi/10.1103/PhysRevApplied.13.044052.

[145] Roques-Carmes, C. *et al.* Heuristic recurrent algorithms for photonic Ising machines. *Nature Communications* **11**, 249 (2020). URL https://doi.org/10.1038/s41467-019-14096-z.

[146] Nixon, M., Ronen, E., Friesem, A. A. & Davidson, N. Observing Geometric Frustration with Thousands of Coupled Lasers. *Phys. Rev. Lett.* **110**, 184102 (2013). URL https://link.aps.org/doi/10.1103/PhysRevLett.110.184102.

[147] Takeda, Y. *et al.* Boltzmann sampling for an XY model using a non-degenerate optical parametric oscillator network. In *Frontiers in Optics 2017 (2017), paper FM4E.3*, FM4E.3 (Optical Society of America, 2017). URL https://www.osapublishing.org/abstract.cfm?uri=FiO-2017-FM4E.3.

[148] Gershenzon, I. *et al.* Exact mapping between a laser network loss rate and the classical XY Hamiltonian by laser loss control. *Nanophotonics* 20200137 (2020). URL https://www.degruyter.com/view/journals/nanoph/ahead-of-print/article-10.1515-nanoph-2020-0137/article-10.1515-nanoph-2020-0137.xml. Place: Berlin, Boston Publisher: De Gruyter.

[149] Xu, X.-Y. *et al.* A scalable photonic computer solving the subset sum problem. *Science Advances* **6** (2020). URL

https://advances.sciencemag.org/content/6/5/eaay5853. Publisher: American Association for the Advancement of Science.

[150] Tradonsky, C. *et al.* Rapid laser solver for the phase retrieval problem. *Science Advances* **5** (2019). URL https://advances.sciencemag.org/content/5/10/eaax4530. Publisher: American Association for the Advancement of Science.

[151] Goemans, M. X. & Williamson, D. P. Approximation algorithms for Max-3-Cut and other problems via complex semidefinite programming. *Journal of Computer and System Sciences* **68**, 442 – 470 (2004). URL http://www.sciencedirect.com/science/article/pii/S0022000003001454.

[152] Garey, M. R. & Johnson, D. S. *Computers and Intractability: A Guide to the Theory of NP-Completeness* (W. H. Freeman & Co., USA, 1979).

[153] Harary, F. On the measurement of structural balance. *Behavioral Science* **4**, 316–323 (1959). URL https://onlinelibrary.wiley.com/doi/abs/10.1002/bs.3830040405.

[154] Barahona, F. On the computational complexity of Ising spin glass models. *J. Phys. A: Math. Gen.* **15**, 3241–3253 (1982). URL https://doi.org/10.1088%2F0305-4470%2F15%2F10%2F028.

[155] Harary, F., Lim, M.-H. & Wunsch, D. C. Signed graphs for portfolio analysis in risk management. *IMA J Management Math* **13**, 201–210 (2002). URL https://academic.oup.com/imaman/article/13/3/201/686406.

[156] Barahona, F., Grötschel, M., Jünger, M. & Reinelt, G. An Application of Combinatorial Optimization to Statistical Physics and Circuit Layout Design. *Operations Research* **36**, 493–513 (1988). URL https://pubsonline.informs.org/doi/abs/10.1287/opre.36.3.493.

[157] de Sousa, S., Haxhimusa, Y. & Kropatsch, W. G. Estimation of Distribution Algorithm for the Max-Cut Problem. In Kropatsch, W. G., Artner, N. M., Haxhimusa, Y. & Jiang, X. (eds.) *Graph-Based Representations in Pattern Recognition*, Lecture Notes in Computer Science, 244–253 (Springer, Berlin, Heidelberg, 2013).

[158] Barahona, F. Network Design Using Cut Inequalities. *SIAM J. Optim.* **6**, 823–837 (1996). URL https://epubs.siam.org/doi/10.1137/S1052623494279134.

[159] White, A. T. Chapter 8 Map-Coloring Problems. In White, A. T. (ed.) *Graphs, Groups and Surfaces*, vol. 8 of *North-Holland Mathematics Studies*, 101 – 124 (North-Holland, 1973). URL

http://www.sciencedirect.com/science/article/pii/S0304020808711368. ISSN: 0304-0208.

[160] Deb, S. K., Bhattacharyya, B. & Sorkhel, S. K. Development of Intelligent Mathematical Modeling for Facilities Layout Design. *Proceedings of the National Conference on Mathematical and Computational Models* 235–242 (2001). URL https://www.google.co.uk/books/edition/Proceedings_of_the_National_Conference_o/L375dEXnTCwC?hl=en&gbpv=1&printsec=frontcover.

[161] Yamamoto, Y. *et al.* Coherent Ising machinesoptical neural networks operating at the quantum limit. *npj Quantum Information* **3**, 49 (2017). URL https://doi.org/10.1038/s41534-017-0048-9.

[162] Hamerly, R. *et al.* Experimental investigation of performance differences between coherent Ising machines and a quantum annealer. *Science Advances* **5**, eaau0823 (2019). URL https://advances.sciencemag.org/content/5/5/eaau0823. Publisher: American Association for the Advancement of Science Section: Research Article.

[163] Reddy, A. N. K. *et al.* Phase-locking of lasers with Gaussian coupling. *arXiv:2106.02344 [physics]* (2021). URL http://arxiv.org/abs/2106.02344. ArXiv: 2106.02344.

[164] Vretenar, M., Kassenberg, B., Bissesar, S., Toebes, C. & Klaers, J. Controllable Josephson junction for photon Bose-Einstein condensates. *Phys. Rev. Research* **3**, 023167 (2021). URL https://link.aps.org/doi/10.1103/PhysRevResearch.3.023167. Publisher: American Physical Society.

[165] Frieze, A. & Jerrum, M. Improved approximation algorithms for MAXk-CUT and MAX BISECTION. *Algorithmica* **18**, 67–81 (1997). URL https://doi.org/10.1007/BF02523688.

[166] Vandenberghe, L. & Boyd, S. Semidefinite Programming. *SIAM Rev.* **38**, 49–95 (1996). URL https://epubs.siam.org/doi/10.1137/1038003. Publisher: Society for Industrial and Applied Mathematics.

[167] Rouco, J., Azevedo, E. & Campilho, A. Automatic Lumen Detection on Longitudinal Ultrasound B-Mode Images of the Carotid Using Phase Symmetry. *Sensors* **16**, 350 (2016). URL https://www.mdpi.com/1424-8220/16/3/350.

[168] Sharma, P. Image Segmentation \textbar Types Of Image Segmentation (2019). URL https://www.analyticsvidhya.com/blog/2019/04/introduction-image-segmentation-techniques-python/. Publication Title: Analytics Vidhya.

[169] Martin, D., Fowlkes, C., Tal, D. & Malik, J. A database of human segmented natural images and its application to evaluating segmentation algorithms and measuring ecological statistics. *Proceedings Eighth IEEE International Conference on Computer Vision. ICCV 2001* **2**, 416–423 (2001). URL https://ieeexplore.ieee.org/document/937655.

[170] Wang, X., Zhu, C., Bichot, C.-E. & Masnou, S. Graph-based Image Segmentation Using Weighted Color Patch. In *IEEE International Conference on Image Processing (ICIP)*, 4064–4068 (Melbourne, Australia, 2013). URL https://hal.archives-ouvertes.fr/hal-00833305.

[171] Felzenszwalb, P. F. & Huttenlocher, D. P. Efficient Graph-Based Image Segmentation. *International Journal of Computer Vision* **59**, 167–181 (2004). URL https://doi.org/10.1023/B:VISI.0000022288.19776.77.

[172] Peng, B., Zhang, L. & Zhang, D. A survey of graph theoretical approaches to image segmentation. *Pattern Recognition* **46**, 1020–1038 (2013). URL http://www.sciencedirect.com/science/article/pii/S0031320312004219.

[173] Boykov, Y. & Funka-Lea, G. Graph Cuts and Efficient N-D Image Segmentation. *Int J Comput Vision* **70**, 109–131 (2006). URL http://link.springer.com/10.1007/s11263-006-7934-5.

[174] Eriksson, A. P., Barr, O. & Astrom, K. Image segmentation using minimal graph cuts. In *SSBA Symposium on Image Analysis* (2006). URL https://eprints.qut.edu.au/108194/.

[175] Abdulqader, I. M. & Lim, K. C. Evaluation of Image Pixels Similarity Measurement Algorithm Accelerated on GPU with OpenACC. *Journal of Telecommunication, Electronic and Computer Engineering (JTEC)* **10**, 167–172 (2018).

[176] PCBcart. Multilayer PCB Benefits and Applications (2017). URL https://www.pcbcart.com/article/content/multilayer-PCB-benefits-and-applications.html.

[177] Sigurdsson, H., Kyriienko, O., Dini, K. & Liew, T. C. H. All-to-All Intramodal Condensate Coupling by Multifrequency Excitation of Polaritons. *ACS Photonics* **6**, 123–129 (2019). URL https://doi.org/10.1021/acsphotonics.8b01017. Publisher: American Chemical Society.

[178] Kalinin, K. P., Amo, A., Bloch, J. & Berloff, N. G. Polaritonic XY-Ising machine. *Nanophotonics* **9**, 4127–4138 (2020). URL https://www.degruyter.com/document/doi/10.1515/nanoph-2020-0162/html. Publisher: De Gruyter Section: Nanophotonics.

[179] Choi, V. Minor-embedding in adiabatic quantum computation: I. The parameter setting problem. *Quantum Inf Process* **7**, 193–209 (2008). URL https://doi.org/10.1007/s11128-008-0082-9.

[180] Choi, V. Minor-embedding in adiabatic quantum computation: II. Minor-universal graph design. *Quantum Inf Process* **10**, 343–353 (2011). URL https://doi.org/10.1007/s11128-010-0200-3.

[181] Harrison, S. L., Sigurdsson, H. & Lagoudakis, P. G. Minor embedding with Stuart-Landau oscillator networks. *arXiv e-prints* arXiv:2109.10142 (2021). _eprint: 2109.10142.

[182] Cai, J., Macready, W. G. & Roy, A. A practical heuristic for finding graph minors. *arXiv:1406.2741 [quant-ph]* (2014). URL http://arxiv.org/abs/1406.2741. ArXiv: 1406.2741.

[183] King, A. D. & McGeoch, C. C. Algorithm engineering for a quantum annealing platform. *arXiv:1410.2628 [quant-ph]* (2014). URL http://arxiv.org/abs/1410.2628. ArXiv: 1410.2628.

[184] Venturelli, D. *et al.* Quantum Optimization of Fully-Connected Spin Glasses. *Phys. Rev. X* **5**, 031040 (2015). URL http://arxiv.org/abs/1406.7553. ArXiv: 1406.7553.

[185] Perdomo-Ortiz, A. *et al.* Readiness of Quantum Optimization Machines for Industrial Applications. *Phys. Rev. Applied* **12**, 014004 (2019). URL https://link.aps.org/doi/10.1103/PhysRevApplied.12.014004.

[186] Zaribafiyan, A., Marchand, D. J. J. & Changiz Rezaei, S. S. Systematic and deterministic graph minor embedding for Cartesian products of graphs. *Quantum Inf Process* **16**, 136 (2017). URL http://link.springer.com/10.1007/s11128-017-1569-z.

[187] Boothby, T., King, A. D. & Roy, A. Fast clique minor generation in Chimera qubit connectivity graphs. *Quantum Inf Process* **15**, 495–508 (2016). URL http://link.springer.com/10.1007/s11128-015-1150-6.

[188] Lechner, W., Hauke, P. & Zoller, P. A quantum annealing architecture with all-to-all connectivity from local interactions. *Sci. Adv.* **1**, e1500838 (2015). URL https://www.science.org/doi/10.1126/sciadv.1500838.

[189] Puri, S., Andersen, C. K., Grimsmo, A. L. & Blais, A. Quantum annealing with all-to-all connected nonlinear oscillators. *Nat Commun* **8**, 15785 (2017). URL http://www.nature.com/articles/ncomms15785.

[190] Leib, M., Zoller, P. & Lechner, W. A transmon quantum annealer: decomposing many-body Ising constraints into pair interactions. *Quantum Sci. Technol.* **1**,

015008 (2016). URL https://doi.org/10.1088/2058-9565/1/1/015008. Publisher: IOP Publishing.

[191] Chancellor, N., Zohren, S. & Warburton, P. A. Circuit design for multi-body interactions in superconducting quantum annealing systems with applications to a scalable architecture. *npj Quantum Inf* **3**, 1–7 (2017). URL https://www.nature.com/articles/s41534-017-0022-6. Number: 1 Publisher: Nature Publishing Group.

[192] Leleu, T., Yamamoto, Y., Utsunomiya, S. & Aihara, K. Combinatorial optimization using dynamical phase transitions in driven-dissipative systems. *Phys. Rev. E* **95**, 022118 (2017). URL https://link.aps.org/doi/10.1103/PhysRevE.95.022118. Publisher: American Physical Society.

[193] Waldspurger, I., d'Aspremont, A. & Mallat, S. Phase recovery, MaxCut and complex semidefinite programming. *Mathematical Programming* **149**, 47–81 (2015). URL https://doi.org/10.1007/s10107-013-0738-9.

[194] Tamate, S., Yamamoto, Y., Marandi, A., McMahon, P. & Utsunomiya, S. Simulating the classical XY model with a laser network. *arXiv:1608.00358 [physics, physics:quant-ph]* (2016). URL http://arxiv.org/abs/1608.00358. ArXiv: 1608.00358.

[195] Goto, H., Tatsumura, K. & Dixon, A. R. Combinatorial optimization by simulating adiabatic bifurcations in nonlinear Hamiltonian systems. *Science Advances* **5** (2019). URL "https://advances.sciencemag.org/content/5/4/eaav2372.

[196] Kuramoto, Y. Self-entrainment of a population of coupled non-linear oscillators. In Araki, H. (ed.) *International Symposium on Mathematical Problems in Theoretical Physics*, Lecture Notes in Physics, 420–422 (Springer, Berlin, Heidelberg, 1975).

[197] Strogatz, S. H. From Kuramoto to Crawford: exploring the onset of synchronization in populations of coupled oscillators. *Physica D: Nonlinear Phenomena* **143**, 1–20 (2000). URL https://www.sciencedirect.com/science/article/pii/S0167278900000944.

[198] Pudenz, K. L. Parameter setting for quantum annealers. In *2016 IEEE High Performance Extreme Computing Conference (HPEC)*, 1–6 (2016).

[199] Pelofske, E., Hahn, G. & Djidjev, H. Advanced unembedding techniques for quantum annealers. In *2020 International Conference on Rebooting Computing (ICRC)*, 34–41 (2020).

[200] Strogatz, S. H. & Mirollo, R. E. Stability of incoherence in a population of coupled oscillators. *J Stat Phys* **63**, 613–635 (1991). URL http://link.springer.com/10.1007/BF01029202.

[201] Kuramoto, Y. Chemical Waves. In Kuramoto, Y. (ed.) *Chemical Oscillations, Waves, and Turbulence*, Springer Series in Synergetics, 89–110 (Springer, Berlin, Heidelberg, 1984). URL https://doi.org/10.1007/978-3-642-69689-3_6.

[202] Townsend, A., Stillman, M. & Strogatz, S. H. Dense networks that do not synchronize and sparse ones that do. *Chaos* **30**, 083142 (2020). URL https://aip.scitation.org/doi/full/10.1063/5.0018322. Publisher: American Institute of Physics.

[203] Feynman, R. P. Chapter II Application of Quantum Mechanics to Liquid Helium. In Gorter, C. J. (ed.) *Progress in Low Temperature Physics*, vol. 1, 17–53 (Elsevier, 1955). URL https://www.sciencedirect.com/science/article/pii/S0079641708600773.

[204] Fitzgerald, R. An Optical Spoon Stirs Up Vortices in a BoseEinstein Condensate. *Physics Today* **53**, 19–21 (2000). URL http://physicstoday.scitation.org/doi/10.1063/1.1310116.

[205] Madison, K., Chevy, F., Wohlleben, W. & Dalibard, J. Vortex Formation in a Stirred Bose-Einstein Condensate. *Physical review letters* **84**, 806–9 (2000).

[206] Lounasmaa, O. V. & Thuneberg, E. Vortices in rotating superfluid 3He. *PNAS* **96**, 7760–7767 (1999). URL https://www.pnas.org/content/96/14/7760. Publisher: National Academy of Sciences Section: Physical Sciences.

[207] Roditchev, D. *et al.* Direct observation of Josephson vortex cores. *Nature Phys* **11**, 332–337 (2015). URL http://www.nature.com/articles/nphys3240.

[208] Bardeen, J. & Stephen, M. J. Theory of the Motion of Vortices in Superconductors. *Phys. Rev.* **140**, A1197–A1207 (1965). URL https://link.aps.org/doi/10.1103/PhysRev.140.A1197. Publisher: American Physical Society.

[209] Rowell, J. M. Magnetic Field Dependence of the Josephson Tunnel Current. *Phys. Rev. Lett.* **11**, 200–202 (1963). URL https://link.aps.org/doi/10.1103/PhysRevLett.11.200. Publisher: American Physical Society.

[210] Josephson, B. D. Possible new effects in superconductive tunnelling. *Physics Letters* **1**, 251–253 (1962). URL https://www.sciencedirect.com/science/article/pii/0031916362913690.

[211] Van Waeyenberge, B. *et al.* Magnetic vortex core reversal by excitation with short bursts of an alternating field. *Nature* **444**, 461–464 (2006). URL http://www.nature.com/articles/nature05240.

[212] Kim, S.-K., Lee, K.-S., Yu, Y.-S. & Choi, Y.-S. Reliable low-power control of ultrafast vortex-core switching with the selectivity in an array of vortex states by in-plane circular-rotational magnetic fields and spin-polarized currents. *Appl. Phys. Lett.* **92**, 022509 (2008). URL http://aip.scitation.org/doi/10.1063/1.2807274.

[213] Miyahara, K., Mukaida, M. & Hohkawa, K. Abrikosov vortex memory. *Appl. Phys. Lett.* **47**, 754–756 (1985). URL https://aip.scitation.org/doi/10.1063/1.96028. Publisher: American Institute of Physics.

[214] Cowburn, R. P. Change of direction. *Nature Mater* **6**, 255–256 (2007). URL https://www.nature.com/articles/nmat1877. Bandiera_abtest: a Cg_type: Nature Research Journals Number: 4 Primary_atype: News & Views Publisher: Nature Publishing Group.

[215] Matthews, M. R. *et al.* Vortices in a Bose-Einstein Condensate. *PHYSICAL REVIEW LETTERS* **83**, 4 (1999).

[216] Yakimenko, A. I., Isaieva, K. O., Vilchinskii, S. I. & Ostrovskaya, E. A. Vortex excitation in a stirred toroidal Bose-Einstein condensate. *Phys. Rev. A* **91**, 023607 (2015). URL http://arxiv.org/abs/1408.3293. ArXiv: 1408.3293.

[217] Alexander, T. J., Sukhorukov, A. A. & Kivshar, Y. S. Asymmetric Vortex Solitons in Nonlinear Periodic Lattices. *Phys. Rev. Lett.* **93**, 063901 (2004). URL https://link.aps.org/doi/10.1103/PhysRevLett.93.063901.

[218] Ferrando, A., Zacarés, M., Córdoba, P. F. d., Binosi, D. & Monsoriu, J. A. Vortex solitons in photonic crystal fibers. *Opt. Express, OE* **12**, 817–822 (2004). URL https://www.osapublishing.org/oe/abstract.cfm?uri=oe-12-5-817. Publisher: Optical Society of America.

[219] van Nielen, N. *et al.* Electrons Generate Self-Complementary Broadband Vortex Light Beams Using Chiral Photon Sieves. *Nano Lett.* **20**, 5975–5981 (2020). URL https://doi.org/10.1021/acs.nanolett.0c01964. Publisher: American Chemical Society.

[220] Lagoudakis, K. G. *et al.* Quantized vortices in an excitonpolariton condensate. *Nature Phys* **4**, 706–710 (2008). URL http://www.nature.com/articles/nphys1051.

[221] Ma, X. & Schumacher, S. Vortex-vortex control in exciton-polariton condensates. *Phys. Rev. B* **95**, 235301 (2017). URL https://link.aps.org/doi/10.1103/PhysRevB.95.235301. Publisher: American Physical Society.

[222] Ma, X. & Schumacher, S. Vortex Multistability and Bessel Vortices in Polariton Condensates. *Phys. Rev. Lett.* **121**, 227404 (2018). URL https://link.aps.org/doi/10.1103/PhysRevLett.121.227404. Publisher: American Physical Society.

[223] Ma, X., Kartashov, Y. V., Gao, T., Torner, L. & Schumacher, S. Spiraling vortices in exciton-polariton condensates. *Phys. Rev. B* **102**, 045309 (2020). URL https://link.aps.org/doi/10.1103/PhysRevB.102.045309.

[224] Ma, X. *et al.* Realization of all-optical vortex switching in exciton-polariton condensates. *Nat Commun* **11**, 897 (2020). URL http://www.nature.com/articles/s41467-020-14702-5.

[225] Berger, B. *et al.* Formation dynamics of exciton-polariton vortices created by nonresonant annular pumping. *Phys. Rev. B* **101**, 245309 (2020). URL https://link.aps.org/doi/10.1103/PhysRevB.101.245309.

[226] Pukrop, M., Schumacher, S. & Ma, X. Circular polarization reversal of half-vortex cores in polariton condensates. *Phys. Rev. B* **101**, 205301 (2020). URL https://link.aps.org/doi/10.1103/PhysRevB.101.205301.

[227] Alperin, S. N., Berloff, N. G. & Berloff, N. G. Multiply charged vortex states of polariton condensates. *Optica, OPTICA* **8**, 301–307 (2021). URL https://www.osapublishing.org/optica/abstract.cfm?uri=optica-8-3-301. Publisher: Optical Society of America.

[228] Lagoudakis, K. G. *et al.* Observation of Half-Quantum Vortices in an Exciton-Polariton Condensate. *Science* (2009). URL https://www.science.org/doi/abs/10.1126/science.1177980. Publisher: American Association for the Advancement of Science.

[229] Manni, F. *et al.* Spontaneous self-ordered states of vortex-antivortex pairs in a polariton condensate. *Phys. Rev. B* **88**, 201303 (2013). URL https://link.aps.org/doi/10.1103/PhysRevB.88.201303.

[230] Sigurdsson, H., Egorov, O. A., Ma, X., Shelykh, I. A. & Liew, T. C. H. Information processing with topologically protected vortex memories in exciton-polariton condensates. *Phys. Rev. B* **90**, 014504 (2014). URL https://link.aps.org/doi/10.1103/PhysRevB.90.014504.

[231] Ma, X., Peschel, U. & Egorov, O. A. Incoherent control of topological charges in nonequilibrium polariton condensates. *Phys. Rev. B* **93**, 035315 (2016). URL https://link.aps.org/doi/10.1103/PhysRevB.93.035315.

[232] Barkhausen, F., Pukrop, M., Schumacher, S. & Ma, X. Structuring co- and counter-flowing currents of polariton condensates in concentric ring-shaped potentials. *Phys. Rev. B* **103**, 075305 (2021). URL http://arxiv.org/abs/2012.05565. ArXiv: 2012.05565.

[233] Sitnik, K. A., Alyatkin, S., Töpfer, J. D., Sigurdsson, H. & Lagoudakis, P. G. Spontaneous formation of time-periodic vortex crystals in nonlinear fluids of light. *arXiv:2110.15399 [cond-mat, physics:physics]* (2021). URL http://arxiv.org/abs/2110.15399. ArXiv: 2110.15399.

[234] Dall, R. *et al.* Creation of Orbital Angular Momentum States with Chiral Polaritonic Lenses. *Phys. Rev. Lett.* **113**, 200404 (2014). URL https://link.aps.org/doi/10.1103/PhysRevLett.113.200404.

[235] Cherotchenko, E. D., Sigurdsson, H., Askitopoulos, A. & Nalitov, A. V. Optically controlled polariton condensate molecules. *Phys. Rev. B* **103**, 115309 (2021). URL https://link.aps.org/doi/10.1103/PhysRevB.103.115309. Publisher: American Physical Society.

[236] Franke-Arnold, S. *et al.* Optical ferris wheel for ultracold atoms. *Opt. Express, OE* **15**, 8619–8625 (2007). URL https://www.osapublishing.org/oe/abstract.cfm?uri=oe-15-14-8619. Publisher: Optical Society of America.

[237] Courtial, J., Robertson, D. A., Dholakia, K., Allen, L. & Padgett, M. J. Rotational Frequency Shift of a Light Beam. *Phys. Rev. Lett.* **81**, 4828–4830 (1998). URL https://link.aps.org/doi/10.1103/PhysRevLett.81.4828. Publisher: American Physical Society.

[238] Kartashov, Y. V., Kartashov, Y. V. & Zezyulin, D. A. Rotating patterns in polariton condensates in ring-shaped potentials under a bichromatic pump. *Opt. Lett., OL* **44**, 4805–4808 (2019). URL https://www.osapublishing.org/ol/abstract.cfm?uri=ol-44-19-4805. Publisher: Optical Society of America.

[239] Brichkin, A. S. *et al.* Effect of Coulomb interaction on exciton-polariton condensates in GaAs pillar microcavities. *Phys. Rev. B* **84**, 195301 (2011). URL https://link.aps.org/doi/10.1103/PhysRevB.84.195301. Publisher: American Physical Society.

[240] Tassone, F., Piermarocchi, C., Savona, V., Quattropani, A. & Schwendimann, P. Bottleneck effects in the relaxation and photoluminescence of microcavity

polaritons. *Phys. Rev. B* **56**, 7554–7563 (1997). URL https://link.aps.org/doi/10.1103/PhysRevB.56.7554. Publisher: American Physical Society.

[241] Chen, M., Mazilu, M., Arita, Y., Wright, E. M. & Dholakia, K. Dynamics of microparticles trapped in a perfect vortex beam. *Opt. Lett., OL* **38**, 4919–4922 (2013). URL https://www.osapublishing.org/ol/abstract.cfm?uri=ol-38-22-4919. Publisher: Optical Society of America.

[242] Cookson, T. *et al.* Geometric frustration in polygons of polariton condensates creating vortices of varying topological charge. *Nat Commun* **12**, 2120 (2021). URL https://www.nature.com/articles/s41467-021-22121-3.

[243] Cohen-Tannoudji, C., Diu, B. & Laloë, F. *Quantum mechanics. 2* (Wiley, New York, 2005), nachdr. edn.

[244] Weitenberg, C. & Simonet, J. Tailoring quantum gases by Floquet engineering. *Nat. Phys.* **17**, 1342–1348 (2021). URL https://www.nature.com/articles/s41567-021-01316-x. Number: 12 Publisher: Nature Publishing Group.

[245] Struck, J. *et al.* Quantum Simulation of Frustrated Classical Magnetism in Triangular Optical Lattices. *Science* **333**, 996–999 (2011). URL https://science.sciencemag.org/content/333/6045/996.

[246] Honari-Latifpour, M., Mills, M. S. & Miri, M.-A. Combinatorial optimization with photonics-inspired clock models. *Commun Phys* **5**, 1–8 (2022). URL https://www.nature.com/articles/s42005-022-00874-7. Number: 1 Publisher: Nature Publishing Group.

[247] Mohseni, N., McMahon, P. L. & Byrnes, T. Ising machines as hardware solvers of combinatorial optimization problems. *Nat Rev Phys* **4**, 363–379 (2022). URL https://www.nature.com/articles/s42254-022-00440-8. Number: 6 Publisher: Nature Publishing Group.